Crystal Growth and Properties of Some Correlated Metal Oxides

A thesis

Submitted in partial fulfillment of the requirements

Of the degree of

DOCTOR OF PHILOSOPHY

by:

RABINDRANATH BAG

Registration ID : 20123219

Indian Institute of Science Education and Research,

Pune-411008, India

January, 2019

Dedicated to my Father...

Certificate

Certified that the work incorporated in the thesis entitled **"Crystal Growth and Properties of Some Correlated Metal Oxides"** Submitted by ***RABINDRANATH BAG*** was carried out by the candidate, under my supervision. The work presented here or any part of it has not been included in any other thesis submitted previously for the award of any degree or diploma from any other University or institution.

Pune
Date: March 30, 2019

(Dr. Surjeet Singh)
Thesis Supervisor

Declaration

I declare that this written submission represents my ideas in my own words and where others' ideas have been included, I have adequately cited and referenced the original sources. I also declare that I have adhered to all principles of academic honesty and integrity and have not misrepresented or fabricated or falsified any idea/data/fact/source in my submission. I understand that violation of the above will be cause for disciplinary action by the Institute and can also evoke penal action from the sources which have thus not been properly cited or from whom proper permission has not been taken when needed.

Pune
March 30, 2019

(RABINDRANATH BAG)
ID: 20123219

Acknowledgements

Working towards a doctorate degree in physics for the past six years was not just about physics but as much of an experience of a lifetime. There are many people who helped me, both academically and personally at various stages to achieve this. Here, I take the opportunity to express my deepest gratitude to all of them.

First and foremost, I would like to thank my PhD supervisor Dr. Surjeet Singh for his intellectual inspiration, integrity, enthusiasm and many enlivening and insightful discussions throughout this project. I feel deeply indebted to him for always encouraging me, helping me stay on the right research track and pointing out the obvious things that I was unable to see. He is one of the best teachers I have met in my academic career. He has also been a very supportive friend and helped me during some very tough times. I will never forget his support after my father's demise in the middle of my PhD journey. Honestly, it would not have been possible for me to continue this work without his immense guidance and support. In my view, my transformation from a student to a researcher, is mostly because of his continuous help and selfless guidance throughout this PhD journey. I am thankful to him for his patience and invaluable critical thinking while spending hours' with me to improve my presentation and writing skills. In fact, I had the most rewarding time working with my supervisor and I thank him for giving me this opportunity to work under his guidance.

I would like to acknowledge my research advisory committee (RAC) members, Dr. Pattayil Joy (NCL Pune) and Dr. Prasenjit Ghosh (IISER Pune). I thank them for their feedback and insightful suggestions during the annual meetings. It helped me improve my research work and provided a new perspective. I thank Dr. Sunil Nair (IISER Pune), also my RAC member at the beginning of my PhD for allowing me to perform some experiments in his busy lab.

I would like to thank Prof. Sudesh K. Dhar for giving me the opportunity to conduct low temperature (down to 0.06 K) specific heat experiments in his lab at TIFR, India. I am grateful for his advice and criticism while writing manuscripts. I am also thankful to Ruta Kulkarni for introducing me to the low temperature experimental set-up while visiting TIFR. I would like to acknowledge my collaborators Malvika Tripathi and Dr. Ram Janay Choudhary for performing XPS experiments at RRCAT, India and helping me analyse the experimental data. I would also like to acknowledge my collaborators, Soumitra Hazra and Dr. Rajeev N. Kini from IISER TVM, India. The experiments performed in their lab added an edge to support our new findings and helped in understanding the physics of spin-ladder system. I also thank Reshma Vijay Shinde for providing the data obtained in ICP-AES experiment at SAIF, IIT Bombay.

I was also fortunate to get the opportunity to work on different systems in collaboration with other groups. I thank Dr. Koushik Karmakar for introducing me the crystal growth and allowing me to study the properties of 'one dimensional spin chain' system at IISER Pune. I am thankful to Dr. Smita Chaturvedi and Prof. Sulabha Kulkarni at IISER Pune for introducing me in the field of 'Orthoferrite' nanoparticles. I am thankful to Chandan De and Prof. A. Sundaresan at JNCASR, India for providing the polycrystalline samples of 'Manganite' system to grow the single crystal. I should also thank to Kaustav De and Prof. Ruediger Klingeler (Heidelberg Univesity, Germany) for introducing the transition metal 'Titanate' system to grow the single crystals at IISER Pune. I would like to thank also Prof. Thorsten Schmitt (PSI, Switzerland) and Prof. Henrik M. Ronnow (EPFL, Switzerland) for performing the RIXS and INS measurements, respectively, on our crystals.

I wish to thank all the faculty members at the department of physics at IISER Pune. I especially thank Dr. Arijit Bhattacharyay and Dr. G. J. Sreejith for many insightful Physics discussions. I am grateful to Dr. Shivprasad Patil and Dr. G. V. Pavan Kumar for allowing me to be a student COSA member at IISER Pune and for their suggestions throughout this position. I would like to thank Dr. Shouvik Dutta and Dr. Apratim Chatterji for their enthusiasm in managing the bi-weekly get-togethers and annual departmental picnics, which helped the students and faculties to exchange their thoughts.

I would like to acknowledge the University Grant Commission (UGC) and IISER Pune for the research fellowship throughout my PhD. I would also acknowledge the Infosys foundation and Departmental Science and Technology (DST, India) for supporting my travels towards attending international conferences.

I am grateful to our technical staff members Nilesh Dumbre, Anil Prathamshetti, Parveen Nasa, Prashant Kale, Sudhir Lone, Yathis T Shakarappa and Santosh Khilare for their technical assistance in various stages during PhD. I am also thankful to all the administrative staff members and specially Prabhakar, Kalpesh, Dhanashree, Tushar, Nayana, Sayalee, Priyadarshini and Prabhas for their kind and continuous support throughout this journey. I would also like to thank the security, librarian, electrician and housekeeping staff at IISER pune for their help.

I would like to thank all the former and current lab-members: Dr. Koushik, Amartya, Pravu, Kshiti, Ajith, Devika, Varun, Deeksha, Rohisudev, Debaleena, Vinayak, Priyank, Harleen, Kalyani, Shivsagar, Dr. Luminita, Prachi, Saurabh, Dibyata, Navita, Anupam, Sanchayeta, Prakash, Haritha, Nupur and Dr. Sachin. I am thankful to all of you for always maintaining a friendly lab atmosphere, which is essential for an experimental lab. I enjoyed being together for all the fun, random discussions and the 'chai'. In particular, I have had many sweet memories with Kshiti and Navita, which will stay with me forever. Thank you, Navita, for the meal-time reminder, NCL-walks and empathy during my thesis writing. I am indebted to Dr. Luminita Harnagea for always inspiring me with her experiences and making me realizing my potential. I will never forget your homemade delicious cakes. I have seen few people with such enthusiasm and Hardwork.

I am very fortunate to have many good friends in IISER who have always been there whenever I needed them and I am really thankful to them for their selfless help and support. I would like to thank my colleagues: Soumendra, Sanku, Rejaul, Amandeep, Rohit (B), Harshini, Nishtha, Danveer, Aditya, Shishir, Kunal, Rohit, Ravi, Gunjan, Himani, Jyoti, Shalini, Neeraj, Aditi, Supratik, Amit, Shrreya, Devika, Avirup, Dr. Jitender, Shruti, Projjwal, Shatruhan, Sharma, Namrata, Sarath, Adarsh, Anweshi, Bani, Thathagata, Deepak, Jyotirmay, Mainak and many more.

I want to express my deepest gratitude to Suprakash Maharaj and Badal Maharaj for their selfless love and affection during my stay in 'Ramakrishna Mission Calcutta Students' Home' for three years while graduating. I consider this place as my 'second home', where I learned many important lessons. I would also like to thank Sameer Thukral for introducing me to Buddhism and the IISER Pathachakra members for their invaluable life lessons. I would like to thank all of my old friends, especially Sukdev, Aritra, Mithun, Pradeep, Biswanath, Snuhi, Dipanwita, Rupali and Anushree, who always pushed me up to do something good.

My heartfelt gratitude to all the teachers who have taught me from my school days to post-graduate education. I thank Kanai sir, Rabi sir, Nityanada sir, Bishnu sir, Pranab sir, A.D.C. sir, D.J. sir, S.B. sir, A.R.B. sir and U.N. sir. Without their blessings, support, motivation and encouragement, it would have been impossible for me to reach this stage.

Finally, I want to express my deepest and most sincere gratitude to my parents, sister, brother-in-law, brothers and my sister-in-law for their constant support, unconditional and immense love, encouragement and most importantly their enormous faith in me. My father, who is no more with us, would have been happiest person to see this achievement. I would like to thank my mother who has no school-life experience but managed to motivate me all the time. I must thank my sister under whose guidance I started my academic career and still find her the best teacher, guide and problem-solver in my life. I would like to thank all my best wishers.

Contents

Abbreviation

1D/2D/3D	One-dimensional/Two-dimensional/Three-dimensional
AIPES	Angle Integrated Photoelectron Spectroscopy
ARPES	Angle-Resolved Photo-Emission Spectroscopy
BSE	Back-Scattered Electrons
CW	Curie-Weiss
EDX	Energy-Dispersive x-ray
ENS	Elastic Neutron Scattering
ESR	Electron-Spin Resonance
FCC	Field Cool Cooling
FCW	Field Cool Warming
FZ	Floating-Zone
HAF	Heisenberg Antiferromagnetic
ICP-AES	Inductively Coupled Plasma Atomic Emission Spectroscopy
INS	Inelastic Neutron Scattering
LDD	Long-distance dimer
LRO	Long-range-order
NMR	Nuclear Magnetic Resonance
NQR	Nuclear Quadrupole Resonance
PPMS	Physical Properties Measurement System

RIXS	Resonant Inelastic x-ray Scattering
SEM	Scanning Electron Microscopy
THZ-TDS	Terahertz time-domain spectroscopy
TMO	Transition Metal Oxide
TqMAG	Torque Magnetometry
TSFZ	Travelling-Solvent Floating-Zone
VSM	Vibrating Sample Magnetometer
XPS	X-ray Photoelectron Spectroscopy
ZFC	zero-field cooling
ZFW	Zero-Field Warming
ZRD	Zhang-Rice dimer
ZRS	Zhang-Rice singlet

Abstract

This thesis deals with crystal growth, magnetic, and thermodynamic properties of two different classes of transition metal oxides, namely, $Sr_{14}Cu_{24}O_{41}$, which is canonical low-dimensional quantum magnet having an incommensurate chain-ladder structure; and orthoferrite $HoFeO_3$, which consists of two different magnetic sublattices.

Although $Sr_{14}Cu_{24}O_{41}$ has been extensively investigated in its pristine form, the effect of quantum impurities in chains and ladders of this composite system are scarcely reported. Being a low-dimensional system, the magnetic properties of $Sr_{14}Cu_{24}O_{41}$ are expected to be highly sensitive to the presence of impurities. In addition, due to mutually incommensurate chain and ladder sublayers, the phononic ground state of this composite system is expected to be very rich featuring "extra" quasi-acoustic modes. A thermodynamic investigation of these modes, and the pinning effect that various impurities may have on these modes has not been investigated to the best of our knowledge.

Here, we study the crystal growth of $Sr_{14}Cu_{24}O_{41}$ in the presence of various impurities. In particular, we investigate the distribution coefficient or homogeneity of an impurity in the grown crystal by examining the frozen-in molten-zone in our traveling-solvent floating-zone (TSFZ) growth experiments. The well-characterized crystals thus obtained are investigated further in details for their magnetic and phononic properties; and the effect of various impurities on these properties is described.

The orthoferrite $HoFeO_3$ constitutes the other extreme example of a transition metal oxide where not only the magnetic interactions are three-dimensional but the structure itself consists of two different interacting magnetic sublattices, which leads to a very rich magnetic behavior with multiple magnetic phase transitions, and sharp magnetization reversal transitions near room-temperature. Although there are some studies on the spin-reorientation transition in $HoFeO_3$, the detailed nature of this transition has

remained controversial. To add to this, a recent neutron study suggests the presence of new transitions not previously reported below the spin-reorientation transition. Additionally, the magnetic behavior of $HoFeO_3$ above room temperature is scarcely reported. Since, Fe sub-lattice orders antiferromagnetically around 640 K with a weak ferromagnetic component, we thought it would be interesting to investigate the magnetic behavior and anisotropy in $HoFeO_3$ above room-temperature.

We therefore carried out crystal growth of $HoFeO_3$ using the floating zone method. We carried out torque magnetometry study on the grown crystals to throw light on the controversy surrounding the spin-reorientation temperature and the weaker transitions reported recently. We studied the magnetic behavior above room-temperature which led to the discovery of interesting magnetization reversal phenomenon, which are expected to be technological important.

This thesis consists of eight chapters in total. The organization and a brief description of the subject covered under various chapters is as follows:

The chapter *one* starts with a general introduction to the transitional metal oxides (TMOs) followed by a brief introduction to low-dimensional quantum magnets including spin chains and spin ladders. Some basic aspects of the spin chain and spin ladder physics and their elemental excitations are discussed; alongside, the previous experimental work on the effect of impurities in spin chains are spin ladders is reviewed. This is followed by a detailed literature review on the structure and properties of $Sr_{14}Cu_{24}O_{41}$ and $HoFeO_3$.

The chapter *two* deals with details of various experimental techniques used during this thesis.

In chapter *three*, details of single crystal growth and characterization of $Sr_{14}Cu_{24}O_{41}$ and its doped variants, and $HoFeO_3$ are given.

The chapter *four* deals with the effect various impurities (Zn, Al and Ni) doped at the Cu site in $Sr_{14}Cu_{24}O_{41}$. We first show the presence low temperature long-distance dimers in the undoped compound. This is followed by a detailed magnetic analysis below 5 K to show that the so-called 'free' spins in the chains undergo a long-distance

dimerization as proposed recently. We then study the effect of magnetic and non-magnetic impurities on the ground state of $Sr_{14}Cu_{24}O_{41}$. We show how various impurities affect the low and high temperature dimers present in this system.

The chapter *five* is devoted to the effect of Co impurity at the Cu site in $Sr_{14}Cu_{24}O_{41}$. We show that of the various impurities investigated here, a Co impurity has the strongest effect on the magnetic properties due to the single ion anisotropy of the Co ion. We show that dilute Co impurity changes the isotropic magnetic behaviour of the undoped compound into an anisotropic one. Most interestingly, in presence of Co impurity an anisotropic suppression of the dimerization gap is observed.

The chapter *six* deals with the sliding phonon mode in $Sr_{14}Cu_{24}O_{41}$. As mentioned above, an acoustic or quasi-acoustic mode due to the incommensurate structure. We show that the low temperature specific heat of $Sr_{14}Cu_{24}O_{41}$ exhibits an excess contribution of non-magnetic origin around T = 10 K, whose magnitude depends on the growth conditions and post-growth treatment and impurities in the crystal. By performing terahertz time-domain spectroscopy (THz-TDS) experiment on three different crystals, namely, as - grown, O_2 - annealed and Al - doped, the presence of relative sliding motion of chain and ladder layers is established. The sensitivity of this sliding gap to the impurities is discussed.

In chapter *seven*, we use highly sensitive torque magnetometry study to show the presence of new magnetic transitions in $HoFeO_3$. We also show the presence of sharp magnetization reversal transitions above room temperature by performing high temperature magnetic measurement on the oriented single crystals.

The chapter *eight* provides a summary of the results obtained in this thesis and conclusions drawn from these results. Based on our results, a future plan is also proposed at the end this chapter.

List of Publications

Publications included in this thesis

1. *Travelling-solvent Floating-zone growth of the dilutely doped spin-ladder compounds $Sr_{14}(Cu, Co)_{24}O_{41}$.*, **Rabindranath Bag**, Koushik Karmakar and Surjeet Singh*,, Journal of Crystal Growth, Volume 458, 16-26 (2017).

2. *Magnetic phase transitions in $HoFeO_3$ single crystals grown using the optical floating-zone method*, **Rabindranath Bag**, and Surjeet Singh*,, AIP Conference Proceedings 1832, 100021 (2017).

3. *Effect of impurities on the long-distance and Zhang-Rice dimers in the quantum magnet $Sr_{14}Cu_{24}O_{41}$*, **Rabindranath Bag**, Koushik Karmakar, Sudesh Dhar, Malvika Tripathi, Ram Janay Choudhary and Surjeet Singh*,, Journal of Physics: Condensed Matter 31, 035801 (2018).

4. *Excess specific heat from the gapped sliding phonon modes in the incommensurate composite crystal $Sr_{14}Cu_{24}O_{41}$*, **Rabindranath Bag**, Soumitra Hazra, Rajeev N. Kini and Surjeet Singh*,, Phys. Rev. B 99, 054305 (2019).

5. *High temperature spin switching transition in orthoferrite $HoFeO_3$ single crystal*, **Rabindranath Bag*** and Surjeet Singh, to be submitted (2019).

6. *Investigation of magnetic phase transitions, spin-reorientation and magnetization reversal in orthoferrite $HoFeO_3$.*, **Rabindranath Bag**, Dibyata Rout and Surjeet Singh*, to be submitted (2019).

Publications not included in this thesis

1. *Crystal Growth of Spin Chain Compound Sr_2CuO_3 Doped with Quantum Defects: Zn, Co, Ni, and Mn*, Koushik Karmakar, **Rabindranath Bag** and Surjeet Singh*,Crystal Growth & Design, **15(10)**, 4843–4853 (2015).

2. *Ho induced enhanced functionality at room temperature and structural phase transition at high temperature in bismuth ferrite nanoparticles.*, Smita Chaturvedi, **Rabindranath Bag**, Vasant Sathe, Sulabha Kulkarni and Surjeet Singh*,, J. Mater. Chem. C, 4, 780–792 (2016).

3. *Impurities in weakly coupled quantum spin chains Sr_2CuO_3 and $SrCuO_2$,* Koushik Karmakar, **Rabindranath Bag**, Markos Scoulatos, Christian Rüegg and Surjeet Singh*,, Phys. Rev. B 95, 235154 (2017).

4. *Nanosize effect: Enhanced compensation temperature and existence of magnetodielectric coupling in $SmFeO_3$* Smita Chaturvedi, Priyank Shyam, **Rabindranath Bag**, M. Shirolkar, J. Kumar, H. Kaur, Surjeet Singh, A. M. Awasthi and Sulabha Kulkarni*,Phys. Rev. B 96, 024434 (2017).

5. *Highly tunable magnetic spirals and electric polarization in $Gd_{0.5}Dy_{0.5}MnO_3$.*, Chandan De, **Rabindranath Bag**, Surjeet Singh, Fabio Orlandi, P. Manuel, Sean Langridge, Milan K. Sanyal, C. N. R. Rao, Maxim Mostovoy and A. Sundaresan* (Accepted in Phys. Rev. Materials (2019)).

6. *Understanding the nature of charge density wave in $Sr_{14}Cu_{24}O_{41}$ using terahertz and femtosecond spectroscopy*, Soumitra Hazra, **Rabindranath Bag**, Surjeet Singh and Rajeev N. Kini* (To be submitted (2019)).

Chapter 1

Introduction

Transition metal oxides (TMOs) have continued to attract considerable attention since the discovery of high critical temperature superconductivity in the hole-doped cuprate La_2CuO_4 almost three decades ago. TMOs, in general, are characterized by strong electronic correlations where the interaction energy between the quasi-particles (the dressed-up electrons) exceeds their kinetic energy. Hence, they are called strongly correlated oxides or correlated oxides for short (for reviews, see Ref. [1, 2]). The strong electronic correlations render the 'free' electron theory completely inadequate to understand the collective emergent properties of these materials. In TMOs, the d electrons are subject to competing interactions: while the on-site Coulombic repulsion tends to localize these electrons at their respective lattice sites, the hybridization with the p-*orbitals* of oxygen enhances their kinetic energy which results in a tendency towards delocalization. The strong onsite Coulombic repulsion can in fact open up a gap in the d-band, splitting it into the upper and lower Hubbard bands. Depending on the position of oxygen 2p band vis-à-vis the Hubbard bands, the material is either an insulator of the charge-transfer type (2p band is located above the lower Hubbard band) or a Mott-Hubbard type (2p band is located below the lower Hubbard band) [3]. If U denotes the onsite Coulombic repulsion and W the single-particle bandwidth (proportional to the kinetic energy t) then in the limit U/W >> 1, the resulting ground state has an insulating nature. On the other hand, if U and W are comparable, the competition between localization and delocalization tendencies gives rise to a range of very interesting and technologically important properties, including, different types of magnetic orders, charge and orbital ordering, unconventional high-T_C superconductivity,

and various multiferroic orders, to name a few (see figure 1.1).

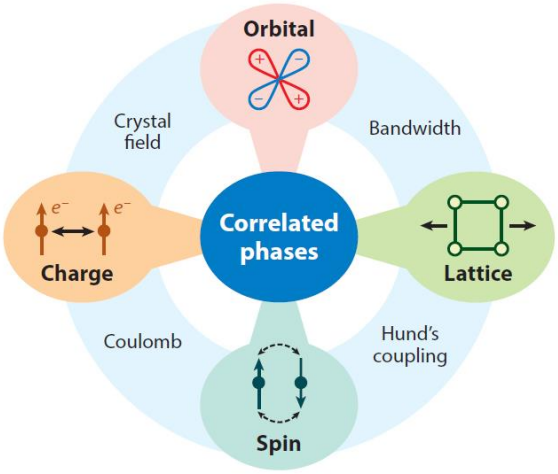

Figure 1.1: The spin, charge, orbital and lattice degrees of freedom are intercoupled and give rise to various correlated phases in transition metal oxides [4]

Due to these reasons, the TMOs are attractive not only for understanding fundamental issues but also for realizing multifunctional devices by manipulating various control parameters, including, coupled magnetic and electrical polarizations or by exploiting the high superconducting transition temperature found in superconducting cuprates. TMOs are, therefore, amongst the most important and challenging materials in the contemporary condensed matter physics. In this thesis we investigate two different classes of TMOs, namely, $Sr_{14}Cu_{24}O_{41}$, which is a low-dimensional quantum magnet of the cuprates family; and $HoFeO_3$, which is a member of the perovskite othoferrites family.

Our focus in the work related to $Sr_{14}Cu_{24}O_{41}$ is on understanding the effects of impurities on the magnetic ground state. The impurities or very small level of dopants in TMOs can alter their properties in unexpected ways. In superconducting cuprates, for example, the effect of impurities on the superconducting and magnetic properties has been widely investigated experimentally (for a review see Alloul et al. [5]). Perhaps due to the relative case with which the 1D models can be solved the impurities in spin chains and ladders generated considerable theoretical interest since the high-T_C days. However, experimental investigations of impurities in these systems are rather scarce, which has impeded the progress in theoretical research. This is partly related to the fact

that experimental realization of systems showing good one-dimensionality is limited; and, adding controlled level of impurities in bulk crystals of these materials is challenging. However, advances in materials synthesis and single crystal growth over the last two decades or so have changed this scenario.

Recently, for example, it has been shown that controlled level of dilute impurities of various kinds can be introduced in the bulk crystals of spin chain compounds Sr_2CuO_3 and $SrCuO_2$ the traveling solvent floating zone method [6, 7]. It was found that by doping various impurities in these antiferromagnetic Mott insulators, novel properties, characteristic of the doped impurities, can be induced. For example, while a Ni impurity opens a spin gap in the two-spinon continuum, a Co-impurity induces a long-range antiferromagnetic order with an Ising-like behavior [8, 9]. On the other hand, in the spin-ladder $SrCu_2O_3$, which can only be synthesized under high-pressure, a Zn impurity is shown to close the spin-gap by inducing an antiferromagnetic ordering [10, 11]. These examples suggest that doping dilute impurities in quasi-one-dimensional quantum magnets can induce unexpected properties. In this regard, the effect of impurities on the composite chain-ladder compound $Sr_{14}Cu_{24}O_{41}$ has not been properly investigated. In this thesis we investigate the effect of Zn, Ni, Co and Al impurities on the magnetic behavior of this quasi-one-dimensional system.

The second transition metal oxide investigated here is the orthoferrite $HoFeO_3$ which crystallize with the perovskite structure. Orthoferrites $RFeO_3$ (R is rare earth element) show several novel and technologically important properties, including spin switching [12], magnetization reversal [13], magneto-dielectric [14], magneto-optical [15] and multiferroic properties [16]. Interestingly, some of the orthoferrites show ultrafast spin-switching effect in their single-crystalline form. For example, $SmFeO_3$ and $NdFeO_3$ show spin-switching transition as a function of temperature and applied field; and, $TmFeO_3$ [17] exhibits a Laser-induced ultrafast spin reorientation. Motivated by these recent reports of ultrafast spin-switching, we investigated single crystals of the compounds $HoFeO_3$, and found sharp magnetization reversal transitions at and above room temperatures. We also carried out a detailed torque magnetometry study which revealed the presence of new phase transitions that were not previously reported due to

limitation of the conventional magnetization probes.

This expository chapter has two parts. The part I of this chapter, provides a survey of the important concepts required to understand and appreciate the low-dimensional quantum magnetism. Alongside, a detailed survey of the previous experimental works on spin chains and ladders with emphasis on the effect of defects or impurities is given. The part II of this chapter, therefore, provides an introduction to the properties and applications of orthoferrites relevant to the material covered under this thesis.

1.1 Low-dimensional quantum magnets

Low-dimensional magnets are the materials in which the spin-spin interactions are restricted to less than three dimensions (3D). The dimensionality of a system plays an important role in determining its magnetic ground state and excitations. The magnetic-lattice dimensionality (d) can be 3, 2 or 1, which corresponds to the three-dimensional arrays (3D), planar layers (2D) or one dimensional chains (1D) of spins as shown schematically in the figure 1.2.

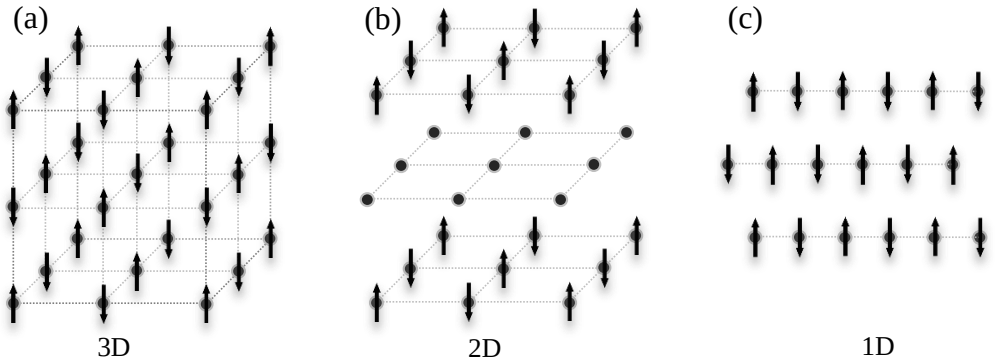

Figure 1.2: (a) Three-dimensional (3D) magnets; where aspin interacts to other spins along all three spatial dimensions (b) two-dimensional (2D) magnet with interactions constrained to plane due to presence of magnetic buffer layers (c) one dimensional (1D) magnet where a spin interacts only along the chain length.

Along with the magnetic-lattice dimensionality (d), the number of spin components (n) also play a crucial role in deciding the magnetic behaviour of such materials and is known as the spin dimensionality. Combining d and n, one can realize different types of

spin models as summarized in the table 1.1, where the spin-spin interactions are defined as the parameters J_x, J_y and J_z along the x, y and z directions, respectively. For d = 3, the 3D model shows a long-range magnetic ordering at a finite temperature (T > 0) irrespective of the spin dimensionality (n). On the other hand, the isotropic Heisenberg spins in 1D (d = 1, n = 3) and 2D (d = 2, n = 3) do not show any spontaneous ordering at any finite temperature, as shown by Mermin and Wangner [18]. This result is referred to as the Mermin-wagner theorem. However, in 2D (d = 2), the Ising spins (n = 1) show spontaneous order at a finite temperature as shown by Onsagar [19]. In 1973, Kosterlitz and Thouless showed that for 2D XY model (d = n = 2), there is a state below a critical temperature (T_{KT}) which is characterized by the so-called topological order of spin vortices. In this state, pairs of metastable vortices and antivortices are closely bound which eventually become free above the phase transition at T_{KT}, which is called the Kosterlitz-Thouless transition.

Table 1.1: S_x, S_y, and S_z denote the components of the spin operator S = (S_x, S_y, S_z), whereas J_x, J_y, and J_z are the interactions for different spin components, respectively. LRO- Long range ordering; The Kosterlitz-Thouless transition to topological order is denoted by KT [20, 21]

Spin Dimensionality (n)	Interacting Components	Name of Model	Lattice Dimensionality (d)		
			d = 3 (3D) (LRO)	d = 2 (2D) (LRO)	d = 1 (1D) (LRO)
n = 3 $S^2 = S_x^2 + S_y^2 + S_z^2$	$J_x = J_y = J_z$	Isotropic Heisenberg	yes	no	no
n = 2 $S^2 = S_x^2 + S_y^2$	$J_x = J_y$	Planar or XY	yes	KT	no
n = 1 $S^2 = S_z^2$	J_z	Ising	yes	yes	no

1.1.1 Spin chains

In a spin chain, the spin-spin interactions are restricted to one spatial direction. The individual spins may be constrained to point along a particular directions (Ising spins, n = 1), or may be free to point anywhere in a fixed plane (XY spins, n = 2) or are free to point anywhere in space (Heisenberg spins, n = 3). The spin quantum number (S) for each spin of the chain plays an important role in deciding the nature of ground state

and the magnetic excitations. For chains with Cu^{2+} ($3d^9$), the spin quantum number is S = 1/2, whereas with Mn^{2+} ($3d^5$), S = 5/2. In the S = 1/2 case, the quantum effects are prominent; whereas S = 5/2 behave more like a classical spin. In this thesis, we will focus on the spin-1/2 case. In the antiferromagnetic Heisenberg spin-1/2 chain, the presence of quantum fluctuations prevent long-range ordering even at T = 0. However, due to the presence of small interchain interaction, very often, these systems show three dimensional long-range ordering at the low temperature. For example, $KCuF_3$ behaves like a one-dimensional Heisenberg spin chain at high temperature, however, the presence of interchain interaction induces a long-range magnetic order below a Néel temperature of T_N = 39 K [22]. Whereas, $CsCoCl_3$ behaves almost as a one-dimensional Ising spin chain since the anisotropy constraints the spins to lie along a particular direction, but due to small interchain interaction it shows three dimensional long-range ordering below T_N = 21 K [23].

Magnetic Excitations: What makes the antiferromagnetic spin 1/2 chains more interesting is their magnetic excitations. In the AFM Heisenberg spin-1/2 chains, these excitations are known as *spinons* (fermions, spin-1/2) with a continuous dispersion relation [24]:

$$\hbar\omega = \pi|Jsin(qa)| \tag{1.1}$$

where J, a and q are the antiferromagnetic exchange coupling, lattice constant and the wave vector, respectively (as shown in figure 1.3). The bold line in figure 1.3 corresponds to equation 1.1, showing gapless nature of the excitations as at $q \rightarrow 0$, $\omega \rightarrow 0$. In an experimental realization, the neutron scattering on a one-dimensional system implies creation and annihilation of two spinons. Therefore, neutron experiment measures the momentum $q = q_1 + q_2$ with energy $\hbar\omega = \hbar\omega_1 + \hbar\omega_2$ associated with the creation and annihilation of pair of spinons. However, the experimental data shows two-spinon-continuum spectra with a modified dispersion relation as $\hbar\omega = 2\pi|Jsin(qa/2)|$ [25] (shown as shaded region in figure 1.3).

The spin excitation spectrum is gapless not only for S = 1/2 but for any half-integer

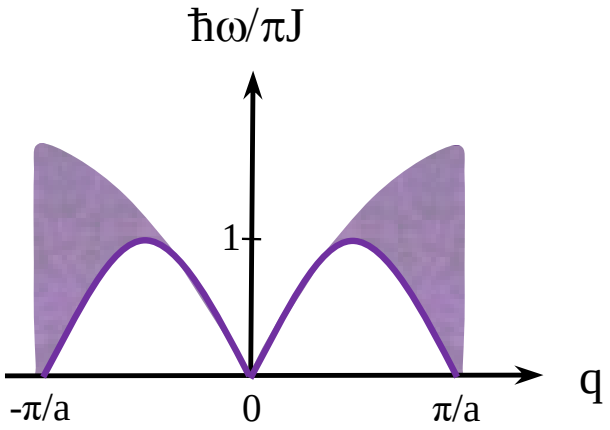

Figure 1.3: Dispersion relation for spinon excitations in a one-dimensional isotropic spin-1/2 HAF-chain (bold line). The shaded region shows the continuum of excitations according to the dispersion relation $\hbar\omega = 2\pi|Jsin(qa/2)|$; measured in a neutron scattering experiment [24, 25].

antiferromagnetic spin chain (i.e. S = 1/2, 3/2, 5/2, ...); whereas, the integer antiferromagnetic spin chains (i.e. S = 1, 2, 3, ...) show a gapped excitation spectrum. This was first conjectured by Haldane and the gap in the excitation spectra is referred to as the Haldane gap [26–28]. The Haldane conjecture has been experimentally verified for various Ni^{2+} (S = 1) chains including $CsNiCl_3$, Y_2BaNiO_5 and $Ni(C_2H_8N_2)_2NO_2ClO_4$ [29–32].

Spin-Peierls transition: Some one-dimensional chains are known to exhibit a gap in their excitation spectra due to the presence of magneto-elastic coupling which results in the formation of antiferromagnetic spin dimers with $S_{total} = 0$. This results due to the Spin-Peierls transition. Below the Spin-Peierls transition (T_{SP}), the distances between the neighbouring spins are no longer uniform but alternates. This leads to an alternation of the exchange coupling as J_1 and J_2; and, each pair of stronger coupled spins form a spin singlet below the transition temperature T_{SP}. The alternating chain has an energy gap due to the difference between the spin-singlet ground state and the excited spin-triplet state as shown in figure 1.4(b), schematically. From the experimental point of view, there are only very few materials, mostly organic compounds, TTF-$CuS_4C_4(CF_3)_4$ (T_{SP} = 12 K) and MEM(TCNQ)$_2$ (T_{SP} = 18 K), that show the

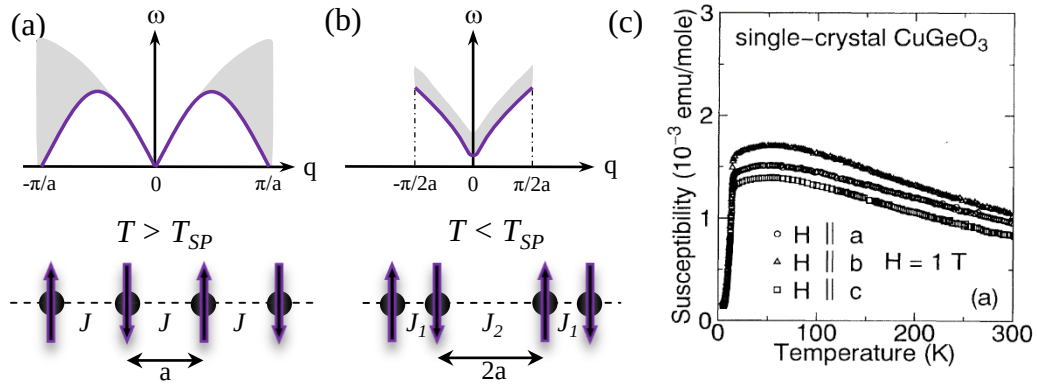

Figure 1.4: Schematic representation of the elementary excitations in (a) a uniform Heisenberg AFM chain (T > T_{SP}) shows a gap-less spectra and (b) alternative chain with alternating nearest neighbour interactions J1 and J2 (can be considered as Spin-Peierls phase (T < T_{SP})) shows gapped spectra [25] (c) Magnetic susceptibility of $CuGeO_3$ along three crystallographic directions show a rapid drop below T < T_{SP} = 14 K, due to opening of a gap [33]

Spin Peierls transition [34, 35]. But in a few inorganic spin 1/2 chains also, the spin-phonon coupling dominates over the interchain coupling to allow the SP transition to occur. The first observed Spin Peierls transition (T_{SP} = 14 K) in any inorganic compound is $CuGeO_3$ [33]. The magnetic susceptibility of $CuGeO_3$ shows a hump around T_{SP} = 14 K along the three crystallographic directions and below this temperature the susceptibility shows an abrupt fall due to opening of the spin gap as shown in figure 1.4(c).

1.1.2 Spin ladders

High-T_C superconductors are not a topic of this thesis but because of their general importance in the cuprates phenomenology and their relationship to the spin-ladders, we provide here a very brief introduction to the structural aspects of these materials to put their relationship with ladders into perspective. Within TMOs, the 2D magnets are often realized in systems with a general formula of the form A_2BO_4, where A is a non-magnetic cation and B is a magnetic cation. The most typical example of such materials are those crystallizing with the K_2NiF_4 type structure; where the magnetic ion (Ni) sits on a square lattice forming a 2D magnet [36, 37]. La_2CuO_4, which is an antiferromagnetic Mott insulator, is a prototypical example of it. It is generally

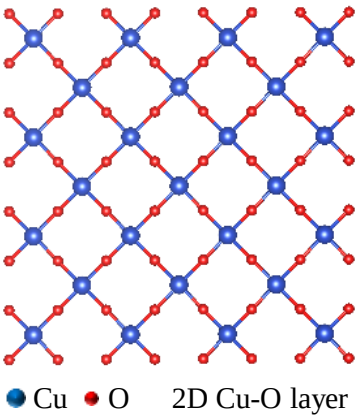

Figure 1.5: Cu-O layers in La_2CuO_4; The Cu^{2+} ions form a square 2D lattice.

considered as the parent compound of high-T_C superconducting cuprates. The Cu^{2+} ion has 9 electrons in the d *orbitals* ($3d^9$) and hence each Cu^{2+} (S = 1/2) interacts through a super-exchange interaction via an intervening oxygen ions as shown in figure 1.5. The non-magnetic La-O acts as a magnetic buffer layer between the CuO planes, which helps in realizing the 2D magnetism [38]. As a matter of fact, La_2CuO_4 is a member (n = ∞) of the homologous series $La_{4+4n}Cu_{8+2n}O_{14+8n}$; and it can be thought of as an infinite leg ladder.

Spin ladder is an intermediate structure between the one-dimensional (1D) chains and two dimensional (2D) layered magnets. A crossover from the 1D to 2D can be realized by assembling chains side by side such that the sideway coupling is comparable to the coupling within the chain. For example, a general n-leg ladder in the SrO-CuO system is of the form $Sr_{1-n}Cu_{n+1}O_{2n}$ as shown schematically in figure 1.6. Here n is the number of legs in the ladder which can either be an even-leg ladder (n = even) or an odd-leg ladder (n = odd), showing different interesting properties as described in the next section. In last few decades, the ladder systems have generated considerable interest as they provide a playground to understand the origin of unconventional superconductivity in cuprates. An advantage of ladder systems over the two-dimensional model is that these systems are relatively easier to study theoretically as they can be treated as quasi-one-dimensional.

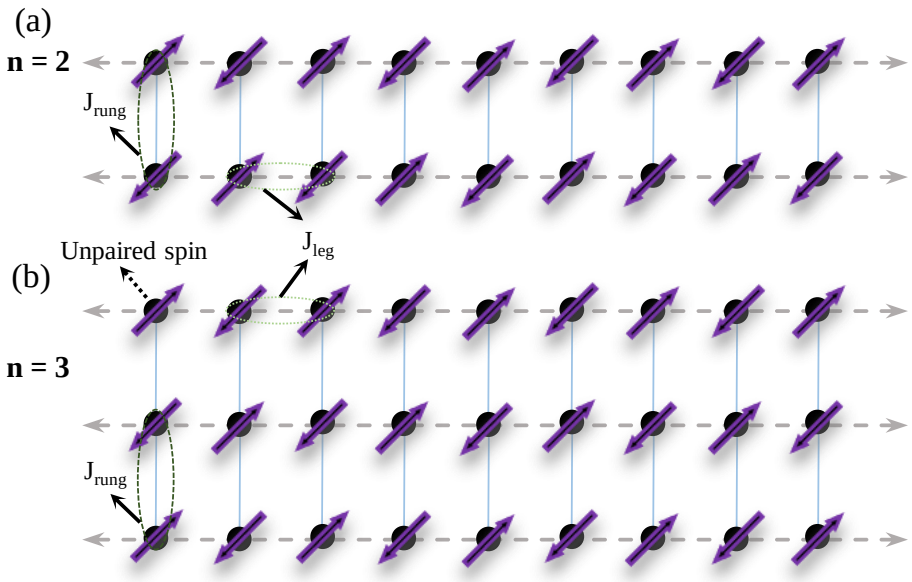

Figure 1.6: Schematic representation of the ladders with n = 2 and 3 legs. The coupling strength along the chains and perpendicular to chains are J_{leg} and J_{rung} respectively.

Even- and odd-leg ladders: The well-known examples of even- (n = 2) and odd-leg (n = 3) ladders are $SrCu_2O_3$ and $Sr_2Cu_3O_5$ respectively [11]. The copper-oxide sheets of these materials are shown in figure 1.7, showing 2-leg and 3-leg ladder structures. The even-leg ladders are expected to show a gapped excitation spectra whereas odd-leg ladders are gapless [39]. In figure 1.7(a), spin-1/2 two-leg ladder has a ground state consisting of spin singlets along the rungs of the ladder. It can be understood if one assumes that the rung coupling (J_{rung}) is greater than the leg coupling (J_{leg}) and hence to create an excitation from spin-singlet to spin-triplet state one must provide an energy similar to J_{rung}, which therefore represents the magnitude of the spin gap. However, for an even-leg ladder, the spin gap, appears for any non-zero value of J_{rung} [40]. On the other hand, an odd-leg ladder does not show any spin gap. A naive explanation for this is that on a given rung of a three-leg ladder, the adjacent spins will pair-up to form a spin-singlet leaving one of the spins free resulting in a gapless excitations akin to the gapless excitations of an AFM spin 1/2 chain.

The presence or absence of spin gap can be checked by performing magnetic susceptibility which is shown for $SrCu_2O_3$ and $Sr_2Cu_3O_5$ as examples in figure 1.8 [11].

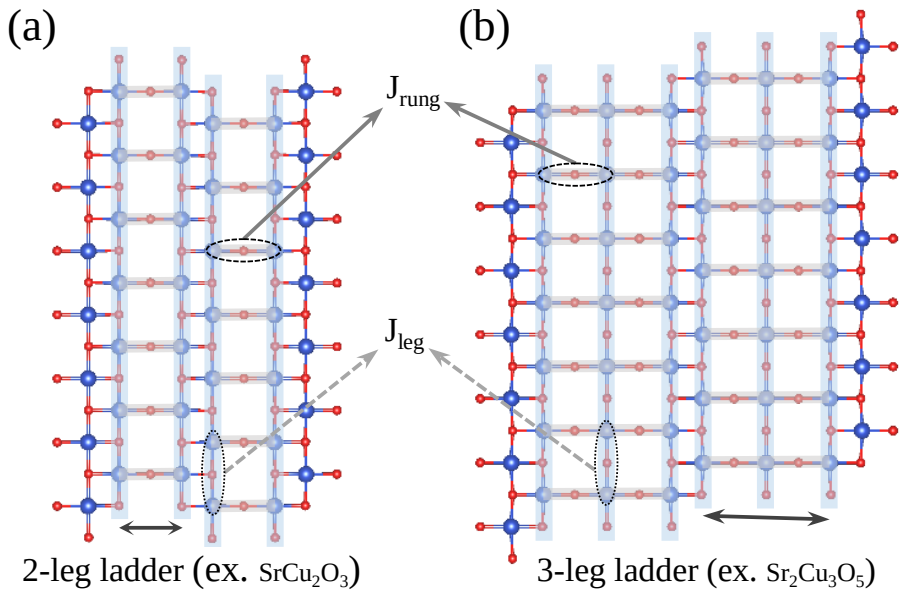

Figure 1.7: (a) 2-leg spin ladder; as in $SrCu_2O_3$ (b) 3-leg spin ladder; as in $Sr_2Cu_3O_5$. The Cu-O-Cu coupling along and perpendicular to the chains are denoted by J_{leg} and J_{rung} respectively.

After correcting for the low temperature Curie contribution from the measured magnetic

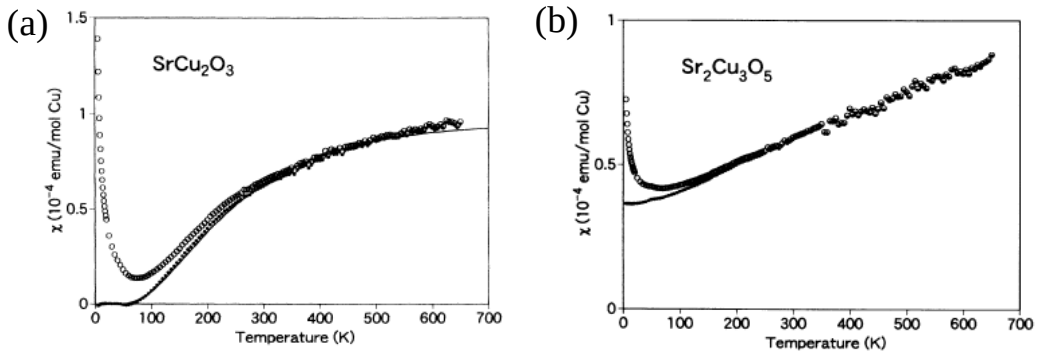

Figure 1.8: Temperature dependence of magnetic susceptibility of (a) two-leg ladder $SrCu_2O_3$ and (b) three-leg ladder $Sr_2Cu_3O_5$ are shown (adapted from Ref. [11]). The open circles represent the experimental raw data, while the data after subtraction of the Curie component are shown as closed circles. The solid line represents the calculated susceptibility.

susceptibility of $SrCu_2O_3$, the subtracted susceptibility shows an exponential behaviour ($T^{-1/2}\exp(-\Delta/T)$), suggesting the presence of an energy gap, Δ = 420 K. On the other hand, the Curie subtracted susceptibility of $Sr_2Cu_3O_5$ shows an upturn at low temperature clearly ruling out the presence of a spin gap in this compound.

1.1.3 Impurities in spin-1/2 chains and ladders

One of the motivations for studying the impurity effects in spin-1/2 chains is that due to the one dimensional nature of the magnetic correlations even dilute disorder results in profound effects on the magnetic properties of these materials. The simplest examples of one dimensional spin chains probably are Sr_2CuO_3 (linear chain) and $SrCuO_2$ (zigzag chain). The presence of large intrachain coupling ($J_{\parallel} \sim 2000$ K) along the chains provides a broad accessible temperature range to examine the effect of impurities experimentally [41]. Along with this, small inter-chain coupling ($J_{\perp} \sim 10$ K) in these materials allows accessibility to one dimensional behaviour over a wide temperature range [42]. Disorder in these systems has been shown to have a considerable effect on the low energy excitation spectra. For instance, by inducing only a dilute amount of Ni^{2+} (S = 1) impurity at the Cu site (S = 1/2) in $SrCuO_2$ opens a sizable gap in the excitation spectra, whereas a gapless excitation spectra has been observed for the pristine $SrCuO_2$ [43]. However, a similar level of non-magnetic Zn^{2+} (S = 0) impurity does not show any gap [44]. Thus, depending on the type of impurities, the excitations of a spin chain can be different.

In the spin peierls system $CuGeO_3$, it has been shown that the presence of various non-magnetic and magnetic impurities can suppress the spin-gap and induce an AFM ordering [45]. Hase et al. showed that the magnetic susceptibility of $CuGeO_3$ increases by doping Zn impurity at the Cu site and the peierls transition collapses above 3 % of Zn substitution [45]. Similarly, doping other impurities (for example, Mn and Ni) suppresses the peierls transition and reveals a Néel ordered state as shown in figure 1.9 [46].

The effect of non-magnetic Zn^{2+} impurity at the Cu-site of two-leg ladder material $SrCu_2O_3$ was reported by Azuma et al. [10]. The temperature dependent magnetic susceptibility data shows a rapid suppression of the spin gap with increasing doping concentration of Zn as shown in figure 1.10. The presence of an unexpected transition at low temperature for higher Zn concentration is observed around 8 K, which was later confirmed as the antiferromagnetic Néel ordering temperature by performing NMR by

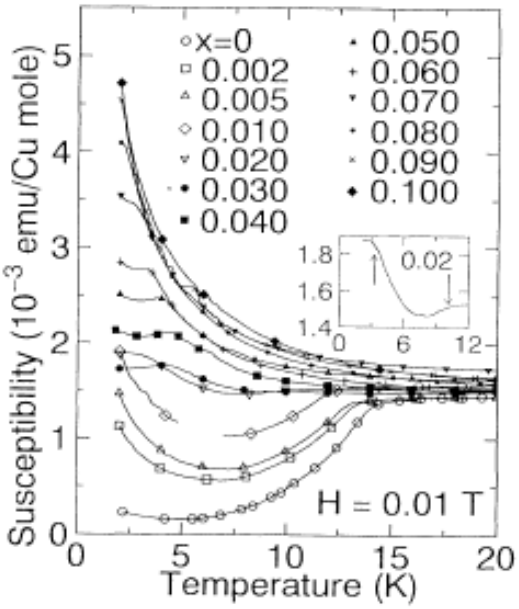

Figure 1.9: Temperature dependent magnetic susceptibility of Zn doped $Cu_{1-x}Zn_xGeO_3$ polycrystalline sample [adapted from Ref. [45]]. Above x = 0.02, a new transition (spin-glass [45], Neel ordering [46]) appear below T_{SP}

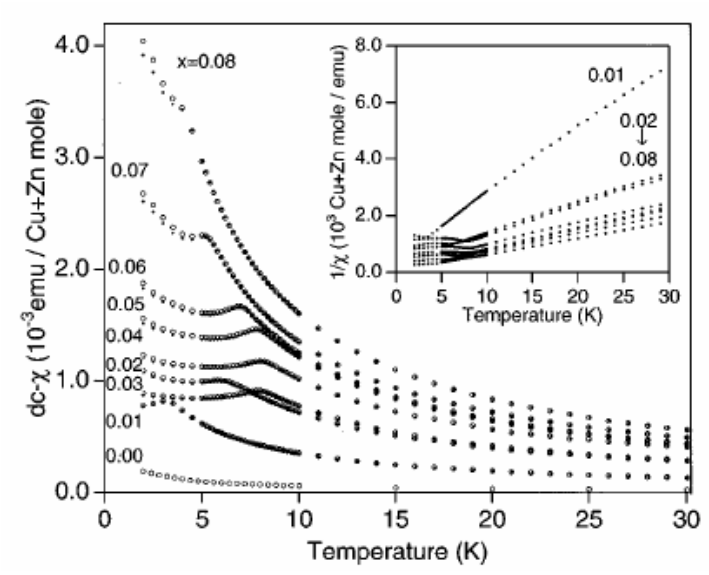

Figure 1.10: Temperature dependence magnetic susceptibility of $Sr(Cu_{1-x}Zn_x)_2O_3$ for various x measured by applying of magnetic field H = 100 Oe. Inset shows the inverse magnetic susceptibility for different doping concentration [adapted from Ref. [10].]

Fujiwara et al. [47]. A possible explanation for this phenomenon can be summarized as follows. The formation of spin singlets along the rungs is expected to be the most favourable ground state of a two-leg ladder system. Doping a spin zero impurity breaks the singlet rendering a Cu^{2+} S = 1/2 free which contributes to the magnetic susceptibility [10, 47, 48].

These examples show that a dilute level of impurity can quantitatively change the ground state of a ladder system [48]. Here, we have chosen to investigate the effect of impurities on the two-leg spin ladder compound $Sr_{14}Cu_{24}O_{41}$ and a major part of this thesis deals with studying the effect of various impurities at the Cu site of this materials. Although there are several studies on impurity effect at the Sr-site on this materials, studies dedicated to the Cu-site impurity effects in $Sr_{14}Cu_{24}O_{41}$ are rather scarce.

1.1.4 Hybrid chain-ladder compound $Sr_{14}Cu_{24}O_{41}$

$Sr_{14}Cu_{24}O_{41}$ is a composite chain-ladder compound showing several interesting properties due to its quasi-one-dimensional nature. Extensive studies have been done on this material since it was first reported by E. M. McCarron et al. in 1988 [49]. It has a unique crystal structure and exhibits properties, such as, spin dimerization [50], crystallization of charge holes [51], charge density wave [52] and metal-insulator transition upon doping with Ca and Co as shown by Uehara et al. [53]. The superconducting state has also been realized under pressure in $Sr_{14-x}Ca_xCu_{24}O_{41}$ (x = 13.6) under 3 and 4.5 GPa with critical temperatures 12 K and 9 K, respectively [54]. $Sr_{14}Cu_{24}O_{41}$ also shows an exceptionally high thermal conductivity despite an electrically insulating behaviour. This high thermal conductivity is due to the magnon mediated heat transport along the *c* - axis, parallel to the leg of the spin-ladder [55]. The presence of anisotropic thermal conductivity in this material provides a possible application for further miniaturization in the microelectronic devices [56]. An experimental evidence of long distance quantum entanglement in $Sr_{14}Cu_{24}O_{41}$ has also been furnished recently by performing low-temperature magnetic susceptibility and specific heat measurements [57].

1.1.4.1 Crystal structure of $Sr_{14}Cu_{24}O_{41}$

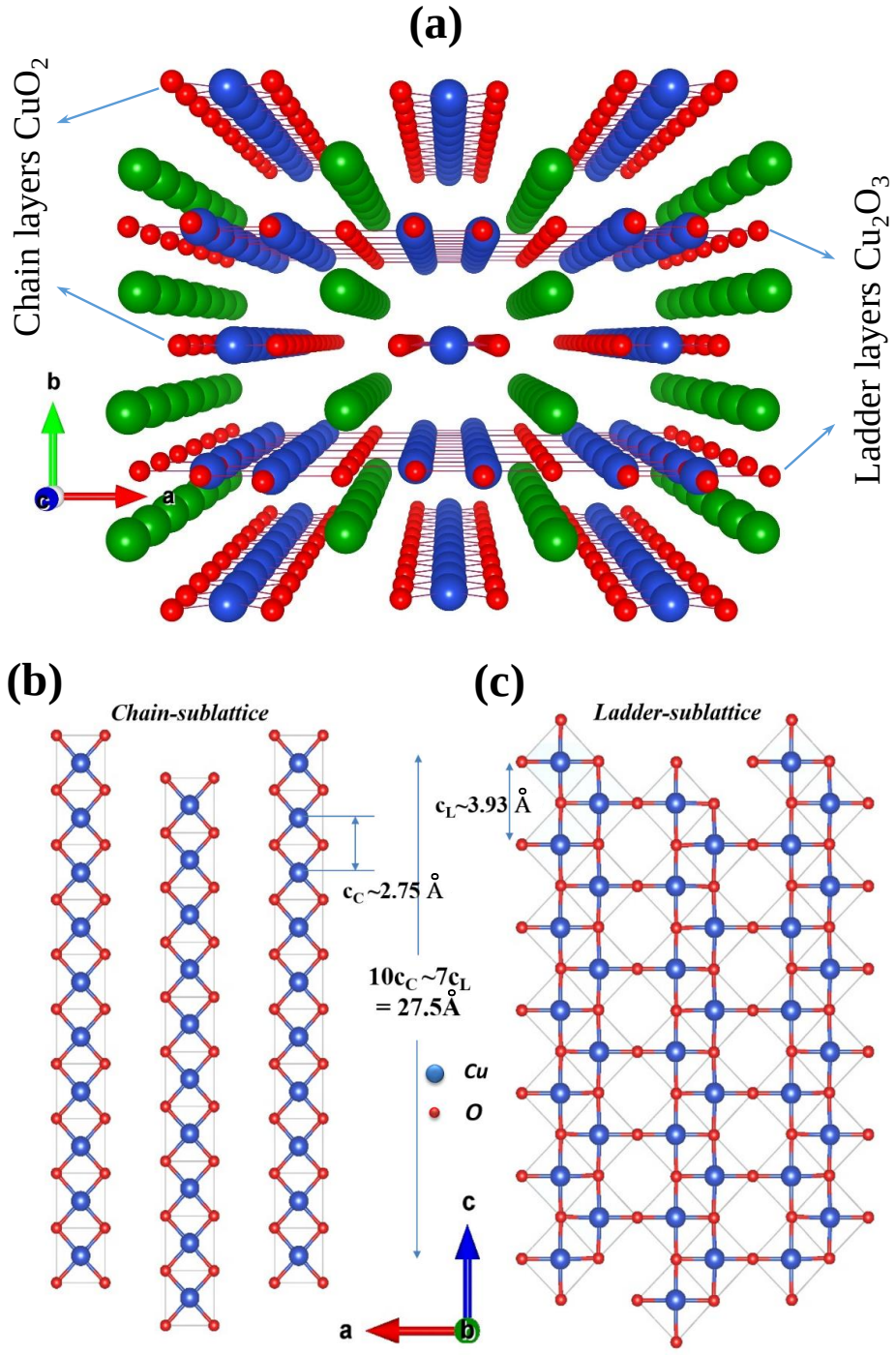

Figure 1.11: (a) Crystal structure of $Sr_{14}Cu_{24}O_{41}$ (orthorhombic) are generated by using VESTA; green, blue and red balls represent Sr, Cu and O atoms, respectively. (b) chain sublattice (CuO_2) (c) ladder sublattice (Cu_2O_3)

$Sr_{14}Cu_{24}O_{41}$ has a unique crystal structure as it consists of an alternate stacking of

layers containing CuO_2 chain and Cu_2O_3 2-leg ladder with an intermediate Sr layer along the crystallographic b - direction. The unit cell structure is shown in figure 1.11(a). The chain and ladder sublattices are shown separately in the ac - plane in figure 1.11(b, c). According to structural analysis [49], the space group of the ladder substructure is $Fmmm$ (face centered orthorhombic); and the space group of chain substructure is $Amma$ (A- centered orthorhombic). The chain sublattice is formed by an edge-sharing CuO_2 units along the crystallographic c - direction where the Cu-O-Cu angle is around 90^o. The ladder sublattice has a two-leg ladder structure with Cu-O-Cu angle of 180^o as shown in figure 1.11. The lattice constants along the a and b - axis (a = 11.47 Å, b = 13.35 Å) are identical for both sub-layers, but along the c - axis the Cu-Cu distance is differ by a factor of approximately $\sqrt{2}$ ($c_C \sim$ 2.75 Å, $c_L \sim$ 3.9 Å, c = 27.3 Å$\sim 7.c_L \sim 10.c_C$) [58]. The two sub-lattices are, therefore, structurally incommensurate along the c - axis. Incommensurability (IC) can be defined using the parameter, $\alpha = c_L/c_C$; where c_L and c_C are the nearest neighbour copper-copper (Cu-Cu) distances along the crystallographic c - direction of ladder and chain sublayers, respectively. More generally, the compound $Sr_{14}Cu_{24}O_{41}$ can be approximately described as a layered composite crystal with structural formulae $[CuO_2]_\alpha[Sr_2Cu_2O_3]$ where $\alpha \simeq 10/7$, which is a considered as a good approximation. In a real crystal, however, α takes a broad range of values, which is the hallmark of an incommensurate crystal [59].

Composite incommensurate structure The modulated structure of this composite spin-ladder system are addressed by a four dimensional superspace formalism as (h, k, l, m), where h, k, l and m are integers [60, 61]. The integers l and m correspond to the chain and ladder sublattice, respectively. The reciprocal lattice vector can be expressed as $q = ha^* + kb^* + lc_C{}^* + mc_L{}^*$. This can be further simplified by considering the chain as the base structure, $q = ha^* + kb^* + (l + m\alpha)c_C{}^*$, where $\alpha = c_L/c_C$ is defined in the previous section. In the early research work by McCarron et al. [49], the four dimensional formalism was not considered as they merely took into account the main reflections for the refinement. After that, to understand fully the superstructure symmetry of this composite compound, detailed studies have been carried out on the both

undoped and doped $Sr_{14}Cu_{24}O_{41}$ compounds by several research groups [61–64]. In the four dimensional formalism, each Bragg peak can be classified as follows: the main reflections from the chain CuO_2 sublayer are written as (h, k, l, 0); the reflections from the ladder sublattice $Sr_2Cu_2O_3$ as (h, k, 0, m); the common reflections from both chain and ladder as (h, k, 0, 0); and the indices (h, k, l, m) as the intrinsic satellite reflections corresponding to the mutual structure modulations between the two sublattices [64, 65]. Deng et al. [64] studied the structural evolution by introducing the Ca at the Sr- site. For high Ca substitution ($Sr_{1.8}Ca_{12.2}Cu_{24}O_{41}$), the CuO_4 unit in chains reduce their length to width ratio and the rung bond in ladders become straighter [64], and it is believed that the holes are transferred from the chains to ladders.

For a stoichiometry $Sr_{14}Cu_{24}O_{41}$ the expected value of α is equal to 10/7, whereas it can vary significantly depending on the oxygen off-stoichiometry as reported by Hiroi et al. [59]. It has been shown that α plays a significant role in the electronic, magnetic and vibrational properties of $Sr_{14}Cu_{24}O_{41\pm\delta}$, where δ is the deviation of oxygen from the ideal stoichiometric value [59]. This will be discussed in details further while introducing the properties of this material.

1.1.4.2 Distribution of holes in $Sr_{14}Cu_{24}O_{41}$

From the charge neutrality condition, one can easily see that the average valence of Cu ion is +2.25 state, which means that in a formulae unit (f.u.), out of 24 Cu, 18 Cu are in a +2 state (Cu^{2+}) and remaining 6 in +3 state (Cu^{3+}). This implies the presence of six intrinsically doped holes (per f.u.) without any chemical doping. Now, the question arises: where are these holes located? Some investigations on the undoped compound $Sr_{14}Cu_{24}O_{41}$ predicted that intrinsically doped holes enter the chain sublattice due to its larger O/Cu ratios [66, 67]. The BVS (Bond Valence Sum) calculations also suggested the presence of self-doped holes and confirm the higher BVS value for holes in the chains [66, 68]. Madelung energy calculations also support the presence of holes in the chain that are more electropositive in nature [69]. Although, this approach has been used by assuming arbitrary values of the initial parameters to achieve the lowest energy state, it nevertheless supports the presence of self-doped holes over the chain sublattice.

The distribution of holes upon doping Ca at the Sr site was also investigated using the BVS calculations based on the crystallographic data for Cu-O bond length as reported by Kato et al. [66]. It has been found that Ca substitution helps to transfer holes from the chains to ladders.

On the other hand, for fully doped material $La_6Ca_8Cu_{24}O_{41}$, the valence state of Cu is 2+, and hence there is absence of holes in this compound. The resistivity and magnetic measurements on doped samples $(La,Sr,Ca)_{14}Cu_{24}O_{41}$ revealed the distribution of holes in these samples [67]. However, polarization dependent Near Edge X-ray Absortion Fine Structure (NEXAFS) can directly probe the hole distribution between the ladders and chains. Nücker et al. carried out polarized NEXAFS experiments on a series of large single crystals of $(La,Y,Sr,Ca)_{14}Cu_{24}O_{41}$ and showed that the holes reside mainly in the chain sublattice [70]. Other experimental techniques including neutron scattering [50, 71–73] and optical investigations [74, 75] also suggest the presence of five holes in the chains and approximately one hole in the ladder sublattice of $Sr_{14}Cu_{24}O_{41}$.

Using elastic neutron scattering measurement on single crystal of $Sr_{14}Cu_{24}O_{41}$, Braden et al. reported the appearance of new peaks below 200 K, which they related to the charge ordering in the chain [76].The synchrotron X-ray measurements at low temperature (50 - 300 K) also revealed the presence of weak superlattice peaks, and the observed lattice periodicity as 4c, as shown in figure 1.14(C) [77]. This result leads to the hole count in the chain as 5 per formulae unit (f.u.). Kumagai et al. performed the NMR (nuclear magnetic resonance spectroscopy) experiments, which is a tool for direct observation of spin gap [78]. It has been found that the spin-gap for the chains is around 140 K. Below 200 K, two distinct resonance spectra are obtained, one corresponds to the magnetic Cu site and another due to the nonmagnetic Cu site. The results support the findings from INS study with a superlattice periodicity of 5c in the chain [78].

1.1.4.3 Physics of chain sublattice

Having two magnetic sublattices, it is important to understand the physics of these sublayers. Here we will first describe the magnetic structure of the chain sublattice,

followed by the magnetic structure in the ladder layer in the next section. In a chain sublattice, two types of copper ions are present: Cu^{2+} with spin S = 1/2 ($3d^9$); and a Cu^{2+} whose spin couples antiferromagnetically with spin of the doped hole which is delocalized over the four nearest neighbour oxygen atoms, to form a Zhang-Rice singlet (*ZRS*) [79]). In the *ZRS* singlet, the strong Cu-O hybridization delocalizes a hole on the square formed by O (2p orbital) atoms around the central Cu (3d orbital) ion as shown in figure 1.12.

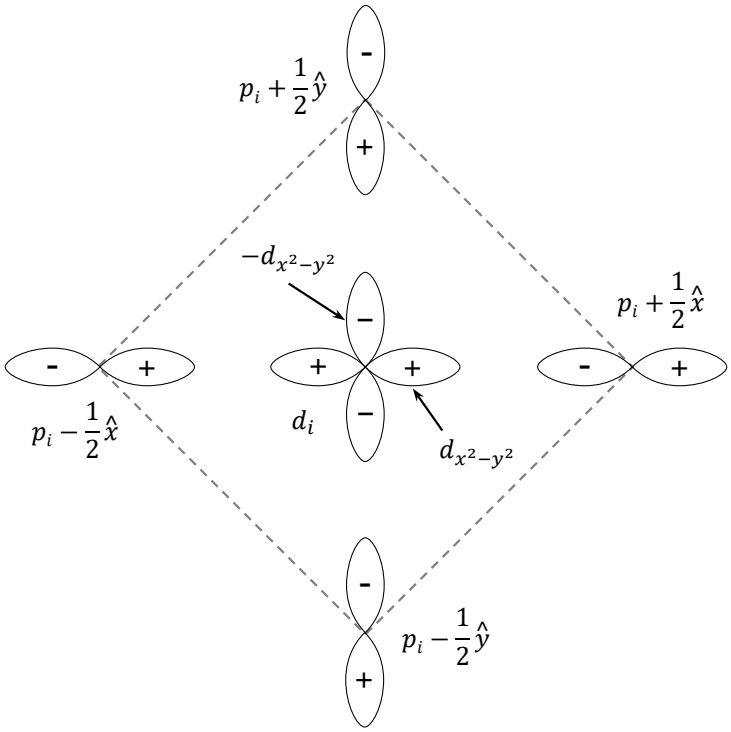

Figure 1.12: Schematic representation of the Cu-O hybridization of oxygen hole (2p orbital) and Cu hole (3d orbital). The + and - signs represent the phase of the wave functions [79].

High temperature Zhang-Rice dimers (*ZRD*) Another interesting phenomena that takes place in the chain sublattice is known as the charge ordering. It has been observed that the simple chain has a spin gap in its excitation spectrum which originates from a dimerized state [80]. As mentioned earlier, $Sr_{14}Cu_{24}O_{41}$ is inherently doped with six holes that reside on the chain sublattice [70]. While cooling down the system below 200 K, a superstructure occurs due to charge ordering in the chain sublattice.

The Cu^{2+} spins interact via an intervening *ZRS* along the chain to form spin dimer. Experimentally, the presence of a gap in the chain sublattice was first proposed by Matsuda et al. using magnetic susceptibility and ESR (electron spin resonance) probes [50]. The ESR measurements suggested that the ground state is a singlet with a large energy gap between the singlet and the first excited state. Later, by performing inelastic neutron scattering, Regnault et al. proposed a model of interacting antiferromagnetic dimers with intra- and interdimer distances equal to 2 and 3 times the Cu-Cu distance along the chain axis (*c* - axis) [81]. A schematic representation of the possible dimer formation in the chains are shown in figure 1.14. Here, it has been assumed that there are no holes in the ladders. The holes (Cu^{3+}) are drawn as square to symbolise Zhang-Rice singlets (*ZRS*) and the *ZRD* dimers are formed between two Cu^{2+} spins separated by a *ZRS*. The *ZRD* dimers nucleate around 80 K, where the magnetic susceptibility of undoped $Sr_{14}Cu_{24}O_{41}$ shows a broad maximum as shown in figure 1.13 [67].

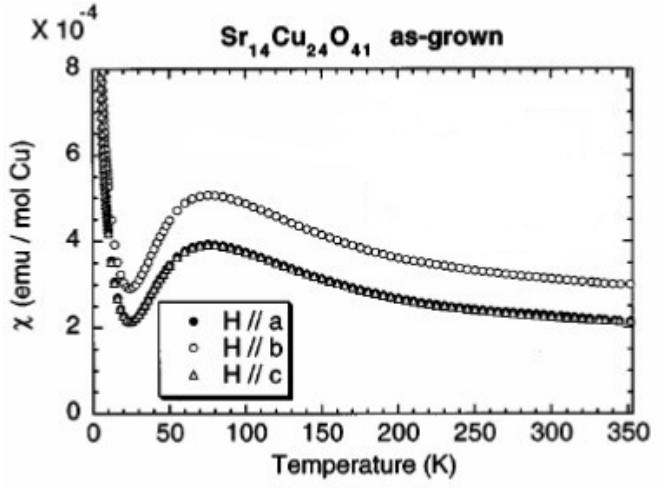

Figure 1.13: Temperature dependent magnetic susceptibility of the as grown crystal $Sr_{14}Cu_{24}O_{41}$. Adapted from Ref. [67].

Ideally, at low-temperatures the number of dimers in the chain is expected to be 2 per f.u. as shown in figure 1.14 (A). However, in real crystals, the number of dimers (N_d) per f.u. may not be exactly 2 for various reasons (including oxygen offstoichiometry [59]). This means that some of the spins in chain remain unpaired, these are referred to as the free spins. Hence below 20 K, a Curie-like rise in the magnetic susceptibility is observed [67, 82]. If we denote by N_S the number of free spins per f.u., then it is

evident that $N_S + 2N_d$ should not exceed 4, which is the number of Cu^{2+} spins per formula unit [83]. Therefore, the total magnetic susceptibility of $Sr_{14}Cu_{24}O_{41}$ can be expressed using four terms as:

$$\chi_{Total} = \chi_0 + \chi_{CW} + \chi_{chain} + \chi_{Ladder} \tag{1.2}$$

where the first term (χ_0) is temperature independent susceptibility, which includes the diamagnetic core term and Van Vleck paramagnetism. The second term represents the Curie contribution (χ_{CW}) due to presence of free-spins which gives rise to an upturn in χ below 20 K. The third and fourth terms are the chain and ladder contributions to the susceptibility, respectively. Due to the presence of large spin gap (400 - 500 K) in the ladder system [78, 84], the ladder contribution to the magnetic susceptibility below 300 K is almost negligible. Therefore, in the temperature range 2 - 300 K, the chain sublattice plays an important role in the magnetic properties. The dimer contribution to the susceptibility can be expressed by using Bleany-Bower [85] equation as:

$$\chi_{ZRD} = \frac{2N_d^{ZR}N_A g^2 \mu_B^2}{k_B T(3 + e^{-\frac{J_{ZR}}{k_B T}})} \tag{1.3}$$

where N_d^{ZR} is the number of dimers per formula unit and J_{ZR} represents the intradimer exchange via the *ZRS* singlet; N_A is the Avogadro's number, g is the Landé factor, μ_B is the Bohr magneton and k_B is the Boltzmann constant.

INS (inelastic neutron scattering) study on the undoped $Sr_{14}Cu_{24}O_{41}$ identified the gap excitation at the energy around 11 meV [73, 81]. Eccleston et al. showed that the excitation with an energy transfer of around 11.5 meV ($\simeq$ 132 K) arise from the dimer chain with an AFM intradimer coupling of 11.2 meV and a ferromagnetic interdimer coupling of 1.1 meV along the chain, and of 1.7 meV perpendicular to the chain (along *a* - direction) [81].

Low temperature long-distance dimer (*LDD*) More recently in the year 2015, Sahling et al. [57] suggested the presence of low-temperatures quantum entanglement

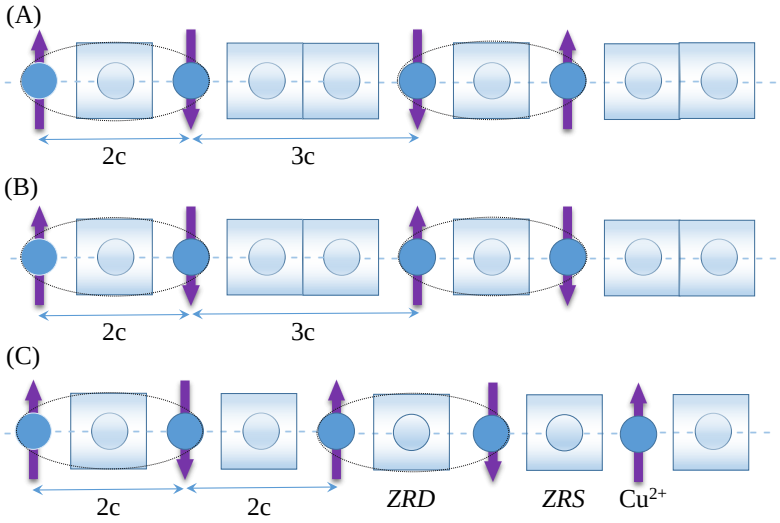

Figure 1.14: The magnetic ground state of the chain sublattice showing various possibilities for charge ordering of the holes. *ZRS* are represented as square with gradient colour. (A) and (B) models showing the 5c periodicity (3c + 2c) with six hole count proposed by INS [71, 81]. (C) Represents the periodicity of 4c with 5 holes count per f.u. in chain as proposed using synchrotron XRD and INS experiments [77].

in this material; i.e., below 2 K the unpaired spins in the chain sublattice form spin dimers over large-distances through an AFM interaction mediated via the intervening singlets (*ZRS*) in the chain. This is the first experimental realization of long-distance quantum entanglement in $Sr_{14}Cu_{24}O_{41}$. By performing low temperature magnetic susceptibility and the specific heat studies, Sahling et al. examined the quantum correlation between the unpaired spins in the chains separated by almost 100 Cu sites. They deduced the formation of long distance dimers (*LDD*) below T = 2 K. We shall denote the weak AFM exchange between these dimers by J_{LD}, where the subscript *LD* refers to the long-distances between the pairing spins. The *LD* dimer contribution can be expressed as

$$\chi_{LDD} = \frac{2N_d^{LD} N_A g^2 \mu_B^2}{k_B T(3 + e^{-\frac{J_{LD}}{k_B T}})} \tag{1.4}$$

where, N_d^{LD} and J_{LD}, are the number of *LDD* dimers and intradimer exchange, respectively. A schematic representation of long distance entanglement of unpaired spins separated by 200 - 220 Å, to form a long-distance-dimers via intervening *ZR* dimers and *ZR* singlets [57] is shown in figure 1.15. Hence, the modified total magnetic susceptibility

of $Sr_{14}Cu_{24}O_{41}$ can be expressed as follows

$$\chi = \chi_0 + \frac{N_S N_A g^2 \mu_B^2 S(S+1)}{3k_B T} + \frac{2N_A g^2 \mu_B^2}{k_B T} \sum_i \frac{N_{d_i}}{(3 + e^{-\frac{J_i}{k_B T}})} + \chi_{ladder} \tag{1.5}$$

Here, and in the rest of the thesis, $i = 1$ represents the high temperature *ZRD* dimers ($J_1 = J_1^{ZR}$, $N_{d1} = N_d^{ZR}$), and $i = 2$, the low temperature LDD dimers ($J_2 = J_2^{LD}$, $N_{d2} = N_d^{LD}$). The second term in equation 1.5 is the Curie contribution arising from the unpaired spins (N_S number of free spins per f.u. and S is the spin quantum number). In the next section we will provide the physics of ladder Cu_2O_3 subsystem of $Sr_{14}Cu_{24}O_{41}$.

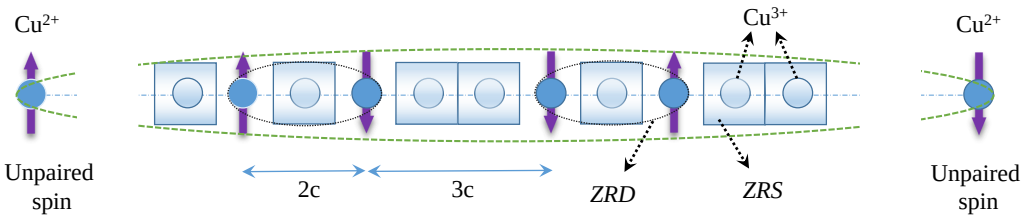

Figure 1.15: The schematic representation of long distance entanglement of unpaired spins that form long-distance-dimers (*LDD*) in $Sr_{14}Cu_{24}O_{41}$ below 2 K [57]

1.1.4.4 Physics of ladder sublattice

After giving the general review on the chain subsystem it is necessary to discuss the contribution of ladder subsystem the magnetic properties of this composite material. We will see that depending on the number of holes present in the ladder, $Sr_{14}Cu_{24}O_{41}$ and its doped variants show various physical phenomena starting from the charge density wave to superconductivity.

Gapped excitations: As mentioned in section 1.1.2, the ground state of an even-leg ladder should show a gapped excitation spectrum, which is what we expect for the two-leg ladder (Cu_2O_3) in $Sr_{14}Cu_{24}O_{41}$. By performing NMR and NQR experiments and investigating the spin dynamics of $Sr_{14}Cu_{24}O_{41}$, it has been shown that the spin-gap

of the ladders is Δ = 470 K [84]. Due to the presence of large spin gap, below room temperature the ladder contribution to the magnetic susceptibility is negligible. Nevertheless, considering the ladder contribution (χ_{ladder}) to the total magnetic susceptibility (equation 1.5), the last term can be expressed as $\chi_{ladder} = \frac{1}{\sqrt{T}} exp(-\frac{\Delta}{k_B T})$; where, Δ is the spin-gap of the two-leg ladder [11]. In this thesis, the temperature interval for the magnetic measurements ranges from 2 K - 300 K, hence the last term of the equation 1.5 can be disregarded unless otherwise stated. However, it is worth to mention here that by introducing La, Ca or Y at the Sr - site, the spin gap of the ladder decreases and interestingly the gap collapses for $Sr_1Ca_{13}Cu_{24}O_{41}$ [78, 84].

Charge density wave (CDW) As we have discussed in the section 1.1.4.2 that the distribution of self-doped holes in the parent compound $Sr_{14}Cu_{24}O_{41}$ plays an important role in determining the electronic properties. Vuletić et al. reported the presence of charge density wave (CDW) in the ladder subsystem by performing dielectric measurement [86]. The dc resistivity, low-frequency dielectric spectroscopy and optical spectroscopy measurements revealed that the CDW occurs below about 210 K with an energy gap of 130 meV. Later on, the proposed order is verified by performing the XAS (x-ray absorption spectroscopy) [51, 87] and RSXS (resonant soft x-ray scattering) [88, 89] by several groups. Below 210 K, in the CDW state, the holes are paired up along the rungs and these hole-pairs appear in every five ladder units ($5c_L$) along the legs of the ladder. This periodicity is broken above the CDW temperature as it is shown schematically in figure 1.16. The effect on Ca doping on the CDW ordering has been studied using dc resistivity and dielectric measurements by Vuletić et al. [86]. Introducing Ca at the Sr site suppresses the CDW transition temperature from 210 K with an energy gap of 130 meV (for $Sr_{14}Cu_{24}O_{41}$) to 10 K with a gap of 3 meV (for $Sr_5Ca_9Cu_{24}O_{41}$) [86]. The dc resistivity suggests that substituting isovalent Ca at the Sr site changes the electronic properties from insulating to metallic around room temperature due to redistribution of holes between chains and ladders [86, 91].

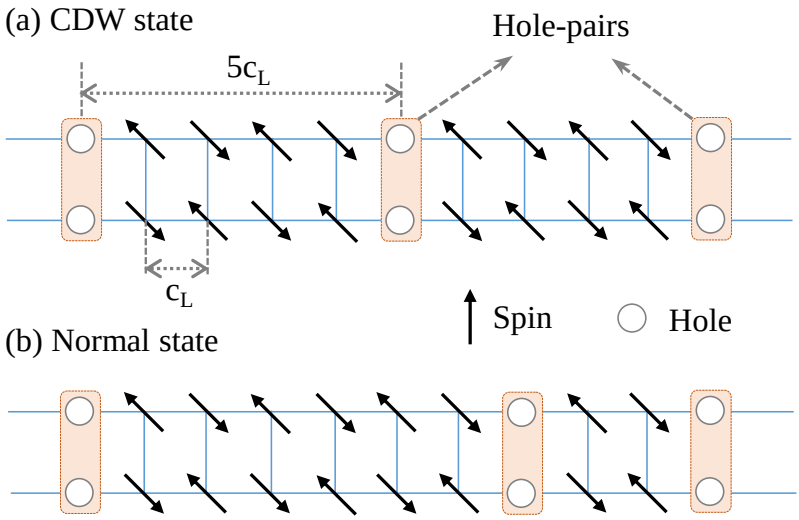

Figure 1.16: (a) the schematic representation of the hole-pair below the CDW ordering in ladder with periodicity of $5c_L$ (b) The normal insulating state of the hole pairs above the CDW transition in ladder, the periodicity has broken [90].

High-T_C superconductivity Doping an impurity in the spin ladders also results in many interesting phenomena. For instance, doping a 2-leg ladder with holes breaks the spin singlets releasing a free spin as shown in figure 1.17. In a two-leg ladder, it can be easily visualized that there is an energetic advantage for the doped holes to pair-up along a common rung. In the presence of an electric field, the hole-pair can move along the ladder as shown in figure 1.17. This might be a possible route to engineer superconductivity in a hole doped two-leg ladder as was theoretically predicted by Dagotto et al. [93, 94]. In this context, the compound $Sr_{14}Cu_{24}O_{41}$ is a suitable example for having two-leg spin ladder structure with a spin-gap above room temperature [84]. Indeed, superconductivity has been observed by doping Ca at the Sr-site ($Sr_{0.4}Ca_{13.6}Cu_{24}O_{41}$) under high pressure as reported by Uehara et al. [54]. The superconducting transition temperatures of 12 K and 9 K were reported under pressures of 3 GPa and 4.5 GPa respectively. The probable explanation of superconductivity in the hole doped ladder was given by Dagotto et al. [94]. By doping Ca^{2+} ion at the Sr^{2+} site in $Sr_{14}Cu_{24}O_{41}$, the holes are transferred from chains to ladders, which breaks the rung singlets in the ladder. It is believed that the hole-pairs that form as a result of this plays a crucial role in stabilizing the superconducting ground state (figure 1.17).

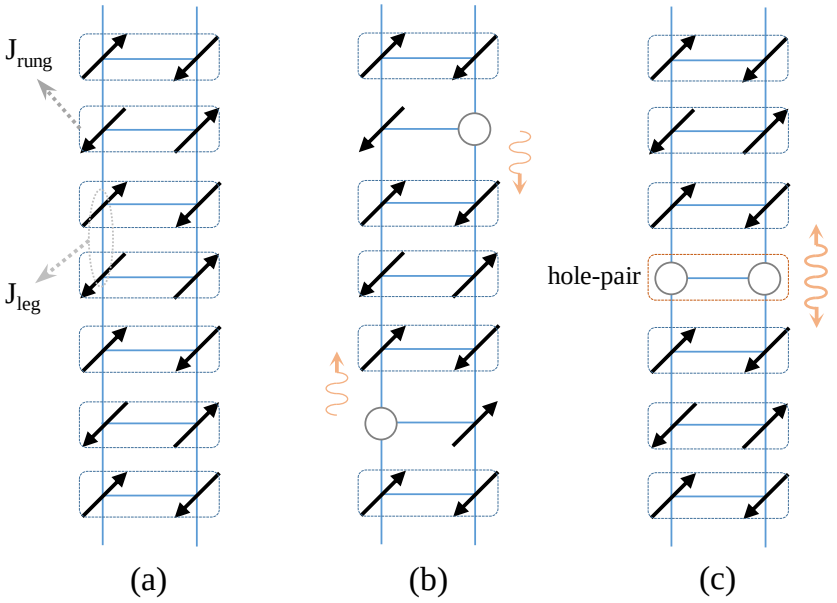

Figure 1.17: (a) The ground state of a two-leg ladder is represented schematically. A Spin-singlet forms between spin pairs on a common rung (b) Spin singlets are broken by adding holes. (c) To minimize the energy cost due to addition of holes, the holes form a bound-state on a common rung. The figure is reproduced from Ref.[92].

Anisotropic thermal conductivity $Sr_{14}Cu_{24}O_{41}$ exhibits highly anisotropic thermal conductivity. In figure 1.18(a), we show the thermal conductivity of a pristine compound $Sr_{14}Cu_{24}O_{41}$ crystal measured along crystallographic a, b and c - directions [95]. The maximum absolute value of the thermal conductivity is quite large (∼ 100

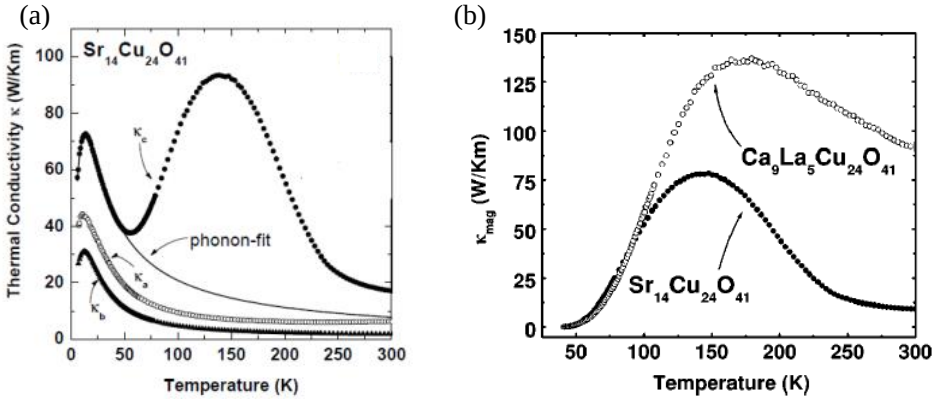

Figure 1.18: (a)Temperature dependent thermal conductivity along the three crystallographic directions a, b and c, (b) the magnonic thermal conductivity κ_{mag} of both $Sr_{14}Cu_{24}O_{41}$ and $La_5Ca_9Cu_{24}O_{41}$, adapted from Ref. [95]

$WK^{-1}m^{-1}$), which is comparable to the metallic thermal conductivity ($\sim$ 385 $WK^{-1}m^{-1}$ at T = 273 K for Cu metal [96]). It is noticeable that the thermal conductivity κ_c parallel to the chains and ladders shows double peaks behaviour and is higher in magnitude compared to the conductivity $\kappa_{a,b}$ perpendicular to the chain and ladder planes. The low temperature peak can be explained in terms of phonon thermal conductivity for all the directions. The second maximum in κ_c around 170 K is of magnetic origin. In principle, both the magnetic subsystems, chain and ladder, could contribute to the thermal conductivity. However, the chains are not responsible for carrying an extra amount of heat which can be explained as follows: the thermal conductivity of both $Sr_{14}Cu_{24}O_{41}$ (n_h = 6) and $La_5Ca_9Cu_{24}O_{41}$ (n_h = 1) are measured by Hess et al. [95]. It has been seen that for both the cases a large magnetic contribution in κ_{mag} is observed at high temperature (figure 1.18(b)). The magnetic thermal contribution is calculated by subtracting the phononic contribution. Interestingly, it is found that doped holes reduce the high temperature magnonic thermal conductivity as the magnon-hole scattering increases as shown in figure 1.18(b). In section 1.1.4.3, we have discussed that the chain sublattice shows charge ordering at low temperature for $Sr_{14}Cu_{24}O_{41}$, which is not the case for $La_5Ca_9Cu_{24}O_{41}$. As the magnetic thermal conductivity at low temperature is almost similar for both the compounds, hence the chains are unlikely to contribute to the thermal conductivity.

1.1.4.5 Sr-site doped (Sr,Ca,La,Y)$_{14}$Cu$_{24}$O$_{41}$

After discussing the physics of both chains and ladders, here we discuss the effect of doping in composite material $Sr_{14}Cu_{24}O_{41}$. The majority of studies on doping effect in $Sr_{14}Cu_{24}O_{41}$ have been focussed mainly on substitution at the Sr - site. The hole count in the chains changes with substitution of Ca, La or Y at the Sr site. For $La_6Ca_8Cu_{24}O_{41}$, the hole count is zero (n_h = 0) and hence 10 Cu^{2+} spins per f.u. are present in the chain. Magnetic susceptibility, specific heat and neutron scattering studies on $La_6Ca_8Cu_{24}O_{41}$ revealed the presence of long-range magnetic ordering around 12 K as reported by Matsuda et al. [97]. This suggests that the absence of holes in the chains does not favour singlet formation, and the magnetic modulated structure is favoured. But interestingly,

for $La_5Ca_9Cu_{24}O_{41}$ (n_h = 1), the chains show an antiferromagnetic long-range ordering around 10.5 K with ferromagnetic correlations within the chain [98]. The presence of smaller magnetic transition temperature for $La_5Ca_9Cu_{24}O_{41}$ can be correlated with the presence higher disorder (as the increased number of holes act as non-magnetic impurities) in the chains compare to the $La_6Ca_8Cu_{24}O_{41}$. It is also observed that the holes transfer from the chains to ladders upon isovalent Ca substitution at Sr - site causes a decrease in the electrical resistivity [70].

1.1.4.6 Cu-site doped $Sr_{14}(Cu,Zn,Ni,Al,Co)_{24}O_{41}$

Unlike Sr - site doping, there are very few reports on doping at the Cu - site. One probable reason behind this might be that it is not easy to dope an appreciable amount of other transition metal ions at the Cu - site. However, one can always try and substitute a very small concentration of transition metal impurities at the Cu - site. By substituting magnetic and non-magnetic impurities at the Cu-site, many interesting physical properties may emerge, as we discussed earlier in the context of $SrCuO_2$, Sr_2CuO_3 and $SrCu_2O_3$. How much, i.e., what concentration of a certain impurity can be added and how will that affect the properties can only be determined experimentally. Wang et al. investigated the effect of Co substitution on polycrystalline $Sr_{14}Cu_{24}O_{41}$ [99]. Using the convergent beam electron diffraction and selected area electron diffraction patterns, they predicted that the space group of the chain sublattice changes from *Amma* to *Ammm* above 10 % of Co-doping, while the space group of the ladder sublattice remains unchanged as *Fmmm*[99]. The substitution effect of non-magnetic impurities Zn, Ga, and Al have been studied by performing magnetic susceptibility measurements on powder samples which suggested that local moment induced by the non-magnetic impurities do not contribute to the Curie-Wiess term but the spin dimers in the chains are affected [100]. Ying Lin et al. investigated Co doping up to 18% and showed that the susceptibility and the value of Curie-Wiess constant C increases with increase in Co doping due to large moment of magnetic ion Co^{2+} [101]. In this study also polycrystalline samples were used. However, due to finite size effects in low-dimensional spin systems, the polycrystalline samples do not allow an adequate description of the effect of dilute impurities.

In this thesis, we will mainly focus on the substitution effects of magnetic and non-magnetic impuities at the Cu - site $Sr_{14}(Cu,M)_{24}O_{41}$; where M = Co, Ni, Zn and Al. To understand the physical and magnetic properties, we have grown the single crystals of $Sr_{14}(Cu,M)_{24}O_{41}$ by using the travelling-solvent floating-zone (TSFZ) method associated with a four mirrors optical image furnace.

1.2 Rare-earth Orthoferrite (RFeO$_3$)

Perovskite structure based rare-earth orthoferrites (RFeO$_3$; where R is a rare earth element or Y) are not only of fundamental interest, they also show several novel and technologically important properties, including spin-reorientation transition, spin-switching or magnetization reversal, magneto-dielectric effect, magneto-optical, and multiferroic properties [13–16]. Having both $4f$- element (rare-earth) and $3d$ transition element (Fe), these materials exhibit a rich physics. Recently, a range of technologically important properties, including, ultrafast spin switching, magnetization reversal, magneto-dielectric, magneto-optical, multiferroicity, and interesting exchange-bias effects has been reported for these compounds [12–17, 102, 103]. This has lead to a resurgence of interest in these materials with reports of magnetic excitations and spin dynamics in $YFeO_3$ [104], magnetoelectric coupling in $LuFeO_3$ [105], magnon-polaritons role in the propagation of THz waves in $TmFeO_3$ [106], exchange bias effect in $ErFeO_3$ [107, 108] and $SmFeO_3$ [109], giant reversible magnetocaloric effect in $GdFeO_3$ [110] and x-ray magnetic circular dichroism and x-ray magnetic linear dichroism to investigate the spin-reorientation transition in $TmFeO_3$ [111], to name a few.

1.2.1 Perovskites structure and properties

The crystal structure of rare-earth orthoferrites is based on the Perovskite ABO_3 structure; where A^{3+} and B^{3+} are the cations and O is typically an oxide (O^{2-}) or halide (X^{2-}) ions. Here, A^{3+} is either a tripositive rare-earth ion or Y^{3+} ion and B^{3+} is Fe^{3+} ion. The cubic structure of this unit cell consists of a BO_6 (here, FeO_6) octahedra as shown in figure 1.19. In general, in the unit cell, A ion sits at the corner position (0,

0, 0), B ion is at body-center position (1/2, 1/2, 1/2) and oxygen ion is at face centred positions (1/2, 1/2, 0), (1/2, 0, 1/2), etc.; as shown in figure 1.19.

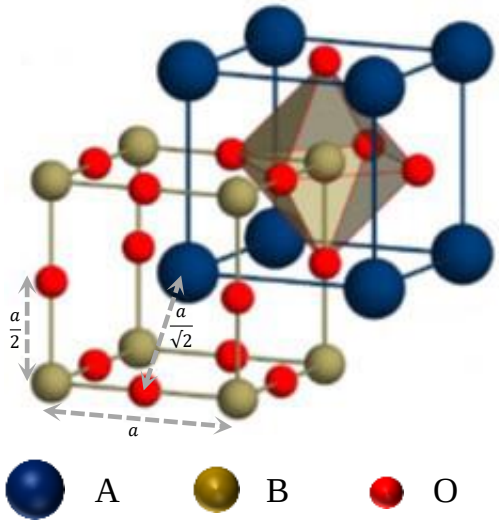

Figure 1.19: (a) The cubic unit cell of perovskite ABO_3 structure. Dimensions of unit cell and bond lengths are shown (adapted from [112])

Considering the A, B and O ions as hard spheres with ionic radii r_A, r_B and r_O, respectively, the tolerance factor $t = \frac{(r_A+r_O)}{\sqrt{2}(r_B+r_O)}$, can be derived from the relationship between the distances A-O ($a/\sqrt{2}$) and B-O ($a/2$), where 'a' is the unit cell parameter, as shown in figure 1.19. The ratio, t is equal to 1 for an ideal cubic structure [113]. However, due to size mismatch between the ionic radii of A and B cations (i.e. $t < 1$), a structural distortion is generated. There are different types of distortions that occur because of the flexibility of bond angles inherent to the perovskite structure. These include tilting of the octahedra BO_6, displacements of the cations (A and/or B) out of the centers of their coordination polyhedra. The orthoferrites RFeO$_3$ exhibit an orthorhombic, distorted perovskite structure (space group Pbnm).

RFeO$_3$ compounds feature two types of magnetic ions: rare-earth ion (R^{3+}) where 4f electrons contribute to the magnetic moment and Fe^{3+} where the magnetic moment arises due to the 3d electrons. The 3d electrons are spin-only type due to their quenched angular momentum, whereas 4f moments are derived from the total orbital momentum (J) which imparts to it a significant single-ion anisotropy which is at the heart of many

of the interesting physical effects mentioned above. A weak and antisymmetric superexchange Dzyaloshinsky-Moriya interaction (known also as *DM* interaction) is also present in these systems [114, 115]. The presence of this interaction induces a small canting of the Fe spins because of which a weak ferromagnetism (*WFM*) is developed below the Néel ordering temperature (T_N). The superexchange interaction involved between rare-earth (*R* - *R*) moments is much weaker. In fact, in those orthoferrites where R^{3+} is magnetic three types of interactions are present, namely, Fe^{3+} - Fe^{3+}, R^{3+} - R^{3+} and R^{3+} - Fe^{3+}; and, the strength of these interactions varies as: Fe^{3+} - Fe^{3+} < R^{3+} - Fe^{3+} < R^{3+} - R^{3+}.

As a result, the magnetic behaviour of orthoferrites is characterized by several magnetic phase transitions including the spin-reorientation and spin-switching. At high temperature these systems undergo a paramagnetic to weak ferromagnetic transition which marks as the onset of Fe moments. The Néel ordering temperature (T_N) is determined by the Fe^{3+} - Fe^{3+} interaction, and it lies in the temperature range 600 - 700 K. Upon cooling, the spin-reorientation (T_{SR}) transition occurs in most orthoferrites, which can be first-order or second-order and is believed to be due to R^{3+} - Fe^{3+} interaction. At the spin-reorientation transition (T_{SR}) the *WFM* associated with the Fe sublattice switches its orientation drastically. The rare-earth (*R*) moments order only at low temperature (below 10 K) due to the weak R^{3+} - R^{3+} exchange interaction.

In general, the spin reorientation transition (T_{SR}) can be induced by temperature and/or applied magnetic field. With reducing the temperature, the magnetic configuration in most cases changes from the Γ_4 to Γ_2 with possibly an intermediate Γ_{24} phase [116]. More specifically, Γ_4 and Γ_2 are defined by the magnetic space groups with configurations $\Gamma_4(G_x, A_y, F_z)$ and $\Gamma_2(F_x, C_y, G_z)$ respectively [117]. The value of T_{SR} in orthoferrites depends on the choice of *R* element [116]. For example, $SmFeO_3$ shows an easy axis rotation from *c* - axis (Γ_4) to *a* - axis (Γ_2) in the temperate range T_1 = 450 K to T_2 = 480 K as shown ion figure 1.8 [12]. On the other hand, $ErFeO_3$ shows a spin reorientation transition from T_1 = 88 K to T_2 = 97 K [118]. Similarly, $TmFeO_3$ shows this transition from T_1 = 82 K to T_2 = 92 K [119]. Here, T_{SR} is defined as $\frac{(T_1+T_2)}{2}$, where T_1 marks the onset of spin-reorientation and T_2 its completion while doping.

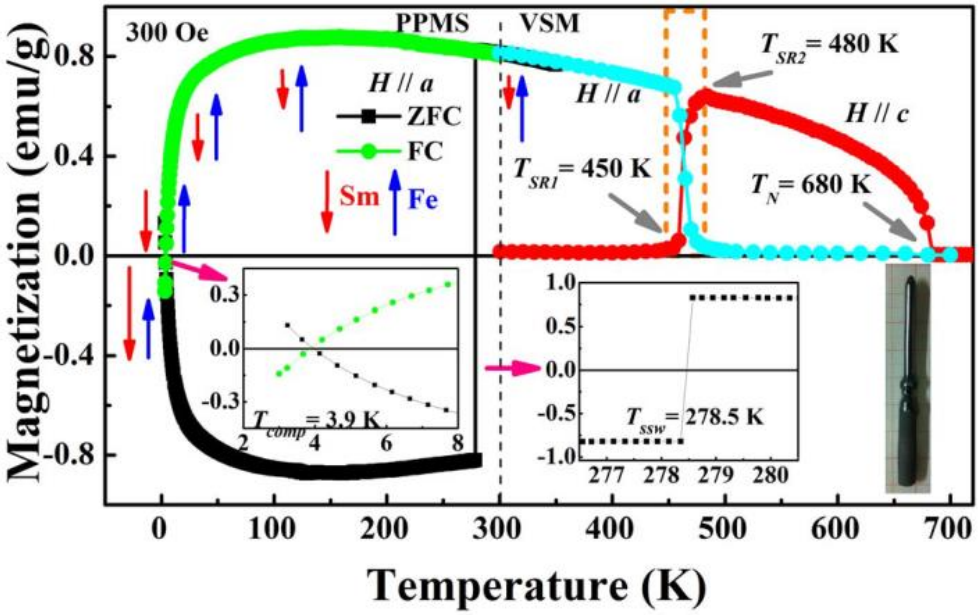

Figure 1.20: (a)Temperature dependent magnetization data, measured along different crystallographic axis (H || c and a) of single crystal $SmFeO_3$, showing T_{SR} and T_{SW} transitions (see the text for details), adapted from Ref. [12]

Apart from the spin-reorientation transition, some orthoferrites also show spin-switching or magnetization reversal below the spin-switching transition (T_{SW}) as reported for $SmFeO_3$ by Cao et al. [12]. They showed that in presence of a magnetic field H = 300 Oe, the magnetization of $SmFeO_3$ undergoes a sudden jump from a negative to positive value at T_{SW} = 280 K. This transition is first-order like, and in the presence of higher magnetic field strength, T_{SW} shifts towards lower temperatures. Similar type of first-order switching transition has also been observed in $NdFeO_3$ single crystals at lower temperature below 29 K [13].

1.2.2 Orthoferrite $HoFeO_3$

In case of $HoFeO_3$, Ho^{3+}, in particular, has one of the largest ionic magnetic moments (10 μ_B), which combines with its strong single-ion anisotropy, derived from the crystal electric field splitting of the lowest J = 8 multiplet to give rise to several interesting magnetic properties. Above room temperature $HoFeO_3$ (HFO) exhibits Nèel ordering at T_N = 643 K. In the antiferromagnetic state, Dzyaloshinskii-Moriya (*DM*) induced

canting of the Fe^{3+} moments results in a Weak Ferromagnetic (*WFM*) moment below the Néel ordering temperature. While cooling down the system, Fe^{3+} spins undergo a spin-reorientation transition (T_{SR}) in the temperature range from T_1 = 50 K to T_2 = 60 K.

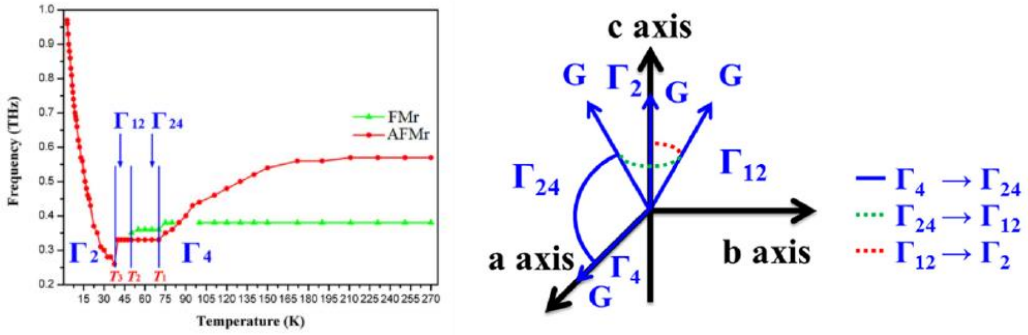

Figure 1.21: Terahertz time-domain spectroscopy study on $HoFeO_3$ showing the spin reorientations (T_{SR}) and magnetic phase transitions at low temperature, adapted from Ref. [12]

Below T_N, Fe - spins in HFO are aligned in a G-type AFM pattern along the crystallographic *a* - direction (G_x) with spins slightly canted, which results in a weak ferromagnetic (*WFM*) moment along the *c* - direction (F_z). This spin configuration, designated as $\Gamma_4(G_x, A_y, F_z)$, persists down to 60 K. Below T_1, the Fe spins rotate to show a *WFM* along the *a*- direction (F_x) with the magnetic space group $\Gamma_2(F_x, C_y, G_z)$ [117]. However, the behaviour of Fe spins in the T_{SR} region between T_1 and T_2 is not well understood.

Zeng et al. performed the Terahertz time domain spectroscopy (THz-TDS) on $HoFeO_3$ to investigate the spin reorientation region [120]. The anisotropic energy calculation from the THz data suggests that in the spin reorientation region two more magnetic transitions (Γ_{24}, Γ_{12}) are involved as the temperature decreases below 60 K. The sequence is plotted as $\Gamma_4 \longrightarrow \Gamma_{24}$, $\Gamma_{24} \longrightarrow \Gamma_{12}$ and $\Gamma_{12} \longrightarrow \Gamma_2$ as shown in figure 1.21 [120]. Very recently, Chatterji et al. [121, 122] also carried out temperature dependent neutron experiment and reported the presence of a new magnetic space group $\Gamma_1(A_x, G_y, C_z)$ between 55 K and 37 K along with Γ_4 (above 65 K) and Γ_2 (below 35 K) as shown in figure 1.22. This new magnetic space group Γ_1 arises from a non-abrupt

transition involving reorientation of Fe spin from being nearly parallel to *a* - axis to being parallel to *b* - axis and hence the weak ferromagnetism (*WFM*) is lost. Apart from this, two more new transitions are also reported at low temperature (~ 20 K and 10 K) as the *R* (Ho) interaction develops.

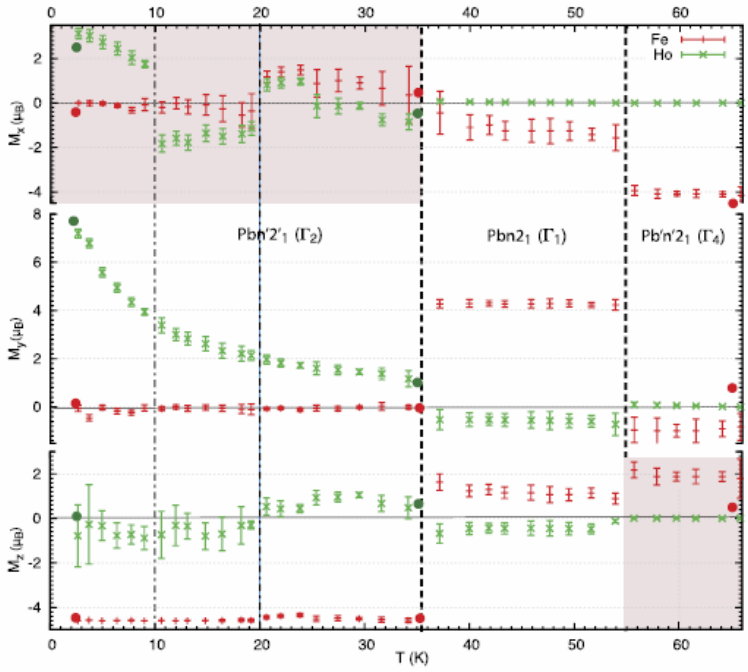

Figure 1.22: Temperature variation of the x,y, and z components of moment on Fe and Ho ions in HFO are shown in a temperature range 2.5 to 66 K derived from the INS study; x, y and z axes correspond to crystallographic *a*, *b* and *c* - axes, respectively, adapted from Ref. [121]

In this thesis, along with the magnetic study, we have also performed highly sensitive Torque magnetometry (TqMAG) measurement on single crystal specimens of HFO to investigate the spin-reorientation region and other weak transitions reported by Chatterjee et al. [121] at low temperatures. The torque data are discussed in details in chapter 7. In chapter 7, we also present our high-temperature magnetic properties (300 K to 950 K) on the single crystalline HFO specimen and observed the presence of so called spin-switching transition (T_{SR}) above room temperature, which was not reported previously.

Chapter 2

Experimental Methods

To investigate the effect of dilute impurities in solids one should have access to high-quality single crystals along with advanced experimental techniques to analyse their physical properties. In low-dimensional quantum magnets, in particular, the anisotropic nature of the physical properties necessitates the use of oriented single crystals. Accurate measurements of physical properties are crucial for advances in science, as they play a vital role in verifying or establishing new theoretical models. This chapter introduces the reader to various experimental techniques used in this thesis. These include probes for characterising the structure and quality of the grown crystals, namely, powder x-ray diffraction (PXRD), polarized optical microscopy; Scanning Electron Microscopy (SEM), Laue diffractometer; and bulk measurement techniques, including, physical properties measurement system (PPMS), Torque magnetometry measurement (TQM), Terahertz spectroscopy (THZ) and X-ray photoelectron spectroscopy (XPS) for their various physical properties.

2.1 Crystal growth

2.1.1 Four mirror image furnace

Although there are several crystal growth techniques available; in this thesis, the single crystals used were grown using the travelling solvent floating zone (TSFZ) method associated with a four-mirror optical image furnace (Crystal System Corporation, Japan).

Here, we provide a brief introduction of the crystal growth furnace used. The details of crystal growth for specific compounds investigated here are given in chapter 3.

Figure 2.1: (a) Four mirror optical furnace used in the growth experiments (IISER Pune). (b) Close-up image of the four mirrors is shown. (c) Photograph of the dynamical growth process showing feed, molten zone and seed crystal. (d) After the growth process of 5 % Co-doped $Sr_{14}Cu_{24}O_{41}$ crystal is shown inside the furnace.

Figure 2.1 shows the photograph of the optical image furnace used in this thesis. It consists of four semi-ellipsoidal mirrors with halogen lamps at their foci. The second focus of all the mirrors coincides on the vertical axis at the center of the furnace where the light flux converges after reflection from the mirrors. A large vertical temperature gradient along the axis facilitate growth of large and high quality single crystal from a polycrystalline cylindrical rod. The specifications of the image furnace used in this thesis are given in the table 2.1. For details, such as, working principle and various growth parameters, we refer the reader to chapter 3 of this thesis.

Table 2.1: Details of the image furnace used in growth of single crystals.

Parameter	Details
Model	FZ-T-10000-H-HR-I-VPM-PC
Input voltage : current	200 V (3-phase) : 40 A
Maximum lamp power	1500, 1000, 500, 300 and 150 W
Number of lamps	4
Number of mirrors	4
Maximum operating temperature	$\sim 2200^{\circ}$C
Maximum crystal growth length	150 mm
Growth speed	0.1 $\sim$ 300 mm/h
Rotations peed	3 $\sim$ 100 rpm
Maximum chamber pressure	0.95 MPa
Minimum chamber pressure	5×10^{-5} torr

2.2 Structural and compositional characterization

For structural and compositional analysis, thin sections were cut at different lengths of the grown crystal boule. These were characterized using powder x-ray diffraction (Bruker D8 advance), scanning electron microscope equipped with energy dispersive x-ray (EDX) analysis (Zeiss Ultra Plus) and polarized optical microscopy (Zeiss Lab A1, AXIO). The lattice parameters of the grown crystals were obtained from the powder diffraction pattern using the UNITCELL software. For magnetic and resistivity measurements, the crystals were oriented using the x-ray Laue diffraction technique (Photonics Science, UK). The temperature dependence of dc magnetization was measured using a vibrating sample magnetometer (VSM) probe in a Physical Properties Measurement System (PPMS) from Quantum Design, USA. In the next section we provide details of these characterization techniques.

2.2.1 Powder x-ray diffraction

Powder x-ray diffraction (PXRD) is generally used for phase identification of a crystalline material and for obtaining information on the unit cell parameters. X-ray diffraction on the samples was performed on powders obtained by crushing thin slices cut from the crystal boule. Before attempting a growth experiment, the phase purity of the polycrystalline sample was also examined using this technique. The experiments

were carried out using a 'Bruker D8 advance diffractometer', which consists of an x-ray source tube, sample platform (holder) and a detector for detecting diffracted x-rays from the sample. Figure 2.2 shows the 'Bruker D8 advance diffractometer' with monochromatic Cu-K_α source (wavelength, λ = 0.15418 nm; Power, P = 2.2 kW). The detailed specifications of the diffractometer are given in table 2.2.

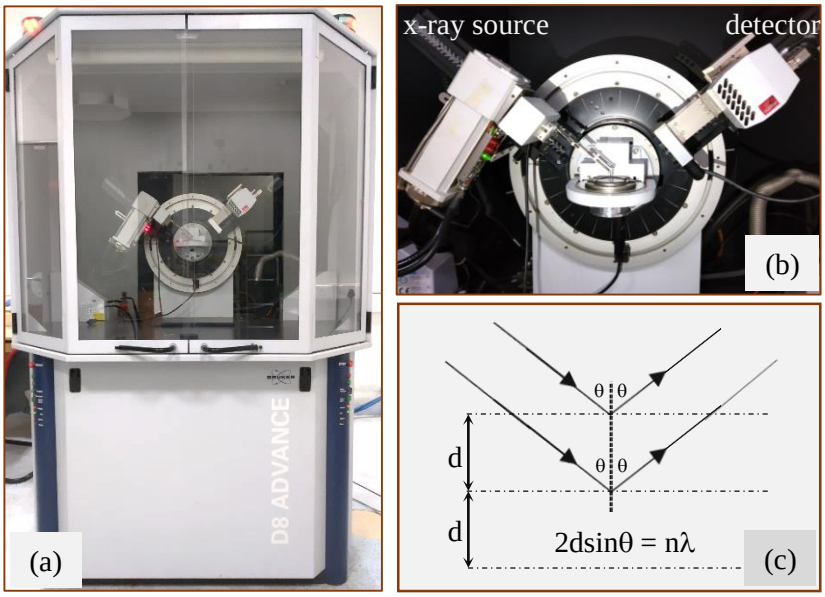

Figure 2.2: (a) Photograph of Brucker D8 x-ray diffractometer (b) Close-up view of x-ray source, sample holder and detector. (c) Bragg's law (2dsinθ = nλ): a schematic representation of x-ray diffraction; 'd' is interplanar distance of the crystal (see text for details).

A crystalline material can be thought of as a stack of lattice planes consisting of a periodic arrays of atoms. If the wavelength (λ) of the incident x-ray is comparable to the inter-planar distance (d) between the lattice planes then the diffracted x-ray shows a constructive interference according to the Bragg's condition: 2dsinθ = nλ; where, n is the order of diffraction and θ is the angle that the incident x-ray makes with the plane of the sample, as shown schematically in figure 2.2(c).

The experiments were done in the Bragg-Brentano geometry [123]. For phase confirmation the measured x-ray pattern was matched with the standard data available with the International Centre for Diffraction Data (ICDD).

Table 2.2: Specification of the powder x-ray diffractometer (Bruker D8) used in the laboratory.

Parameters	Details
Model	Bruker D8 Advance powder X-ray diffractometer, Germany
Geometry	Bragg-Brentano parafocusing geometry
Source	Cu$-K_\alpha$ (λ = 0.15418 nm; $P = 2.2k$W)
Detector	Solid state linear detector – Lynxeye

The unit cell parameters were calculated from the obtained diffraction pattern by using the UNITCELL software [124]. In some cases, the lattice parameters were estimated using the Rietveld methods. For these purpose, first, the pattern matching is performed, where the background and the unit cell parameters are refined, which was followed by the shape parameters [125]. Finally, the crystal structure and other informations were generated from the refined CIF (crystallographic information file) by using VESTA software [126].

2.2.2 Polarized optical microscopy

Polarized optical microscopy is one of the reliable characterization techniques to confirm the single crystalline nature of the grown crystals. For this technique a very flat and smooth surface is required. For this purpose, thin sections were cut at different lengths of the grown crystal boule by using a low-speed diamond saw (Buehler, USA). The sliced crystal pieces were polished using a silicon carbide (SiC) paper with progressively increasing grit sizes upto finest available grit size 1200 (i.e., granule size 15 μm). For polishing the orthoferrite crystals ($HoFeO_3$), water was used as a coolant. On the other hand, dry polishing was used for cuprates as they are sensitive to water. In figure 2.3, we show a representative polarized image of the frozen-in floating-zone (FZ) during the growth of an undoped $Sr_{14}Cu_{24}O_{41}$. Under steady state growth, the lamp power is rapidly reduced to quench the molten zone, which is called the frozen-in-zone, which was cut using the diamond saw vertically into two pieces. One of the flat surfaces is dry polished on the SiC grit papers and examined under an optical microscope using a

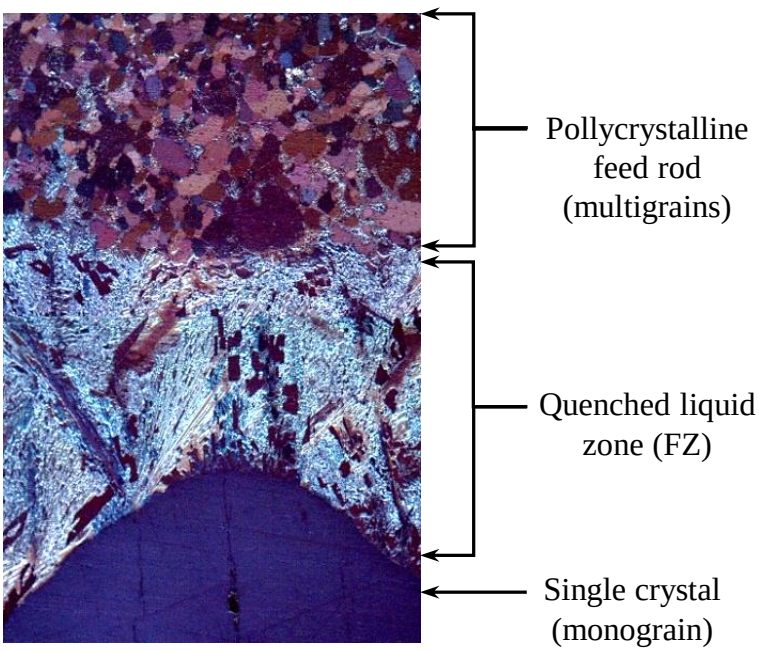

Figure 2.3: Optical image using polarised light of polished surface of the frozen-in-zone (FZ) during the growth of the undoped $Sr_{14}Cu_{24}O_{41}$.

polarized light. The optical polarized image shows that the polycrystalline feed rod consists of randomly oriented micron-size crystalline grains, whereas crystal region (lower part) shows a large mono-grain. The region sandwiched between the feed and crystal is the frozen-in-zone whose detailed compositional analysis is discussed in chapter 3.

2.2.3 Scanning electron microscopy

To study the morphology and composition of the grown crystals we used the scanning electron microscopy (SEM) and the energy dispersive x-ray spectroscopy (EDS), respectively. Sometimes EDS is also referred to as energy dispersive x-ray analysis (EDXA or EDX). In figure 3.9(a), the photograph of scanning electron microscopy (SEM, Zeiss Ultra Plus, Germany) is shown. In these experiments, a focussed electron beam is incident on the sample of interest. The incident electrons interact with the sample in various ways and produce variety of electrons and/or photons as shown schematically in figure 3.9(b). These emitted electrons are captured by a detector to generate an image and compositional information of the sample.

The signals used to characterise the samples are briefly described as follows: when an electron beam is made to incident on a sample, secondary electrons are ejected with relatively low energy. These secondary electrons provide information about the topography of the sample. Some of the electrons from the incident electron beams are, however, bounced back by the atomic electron cloud present in the sample. These are known as back scattered electrons (BSE) and the scattering cross section of these electrons depends on the atomic mass density. For instance, having large atomic density in the sample will produce more BSE and therefore a brighter image (high contrast resolution) will appear. For most of the samples, we have used BSE micrographs to determine if there were any segregations or secondary phases present.

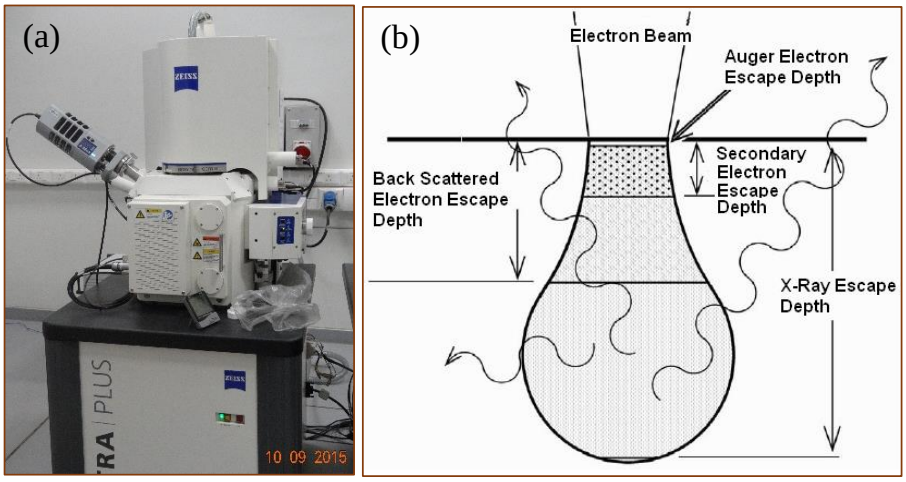

Figure 2.4: (a) Photograph of Scanning Electron Microscope (SEM). (b) Schematic representation of different emissions that occur due to the incidence of high-energy electron on a sample under high vacuum (taken from [127]).

When secondary electrons are emitted from the inner shells, the electrons from the outer shells fill up the empty shells. Due to this transition, the emission of x-ray photons with an energy equal to the difference between the energy levels occurs. The wavelengths of these emitted x-ray photons are a characteristic of the atom; and, therefore, by analysing these energies the elemental composition of the sample can be determined.

In this technique, the incident electron beam energy is crucial. The low-energy beams (5 - 10 keV) are more useful to determine the surface topography due to their low-penetration. Whereas, for EDS analysis higher energies are preferred. For instance,

EDS is carried out at 15-20 keV; but the optimum value of the excitation voltage depends on the atoms present in the sample. The drawback of using higher energies is that in some cases the incident electrons can damage the sample; but, even those cases where the sample being probed is resilient to high energies, the emergent beam is likely to be absorbed before reaching the detector. An empirical rule for choosing the excitation voltage is that it should exceed the energy corresponding to the highest excitation energy of the concerned sample. For example, in $Sr_{14}Cu_{24}O_{41}$, Sr possesses the highest excitation energy of 14 keV ($K_{\alpha 1}$), therefore, an excitation voltage ranging from $25-30$ keV has been used.

For SEM imaging, the surface to be examined is well polished to have a mirror finished appearance. Some representative SEM images of the grown crystals and frozen-in-molten zones are shown in chapter 3 where the crystal growth and characterizations of the crystals used in this thesis are presented.

2.2.4 Inductively coupled plasma - atomic emission spectrometry

Inductively coupled plasma - atomic emission spectrometry (ICP-AES) measurements were carried out at the SAIF (sophisticated analytical instrument facility) at IIT Bombay, India. ICP-AES is an emission spectrophotometric technique, which is based on the principle that the excited electrons in a sample, after excitation by high temperature argon plasma, emit photons of energy at a given wavelength. The energy of the emitted photon is unique to each element since it depends on the electronic configuration. Although each element emits energy at multiple wavelengths, in the ICP-AES technique it is most common to select a single wavelength (or a very few) for a given element. The intensity or the energy emitted at the chosen wavelength is proportional to the amount (concentration) of that element in the sample being analyzed. Thus, by determining which wavelengths are emitted by a sample and by determining their intensities, one can qualitatively and quantitatively find the elements in the given sample relative to a reference standard [128].

2.2.5 Laue diffractometer

Table 2.3: Specification of the Laue x-ray diffractometer used

Parameters	Details
Model	Photonic Science Laue diffractometer, UK and France
Target	Tungsten (Model)
Wavelength, λ	0.35 Å– 2.5 Å(Power = 15 W)
Collimator	Microfocal brush collimator (spot size = 0.5, 1, 1.5 mm)
Detector	GdOS (Gadolinium oxysulphate) scintillator flim followed by digital optical camera
Measurement distance	4.5 cm
Measurement time	30 – 1000 s

Before performing any physical or magnetic characterizations, the crystals were oriented using a Laue diffractometer (Photonic Science, UK). Figure 2.5 shows the diffractometers with a mounted crystal on the goniometer and the specifications details of the used Laue diffractometer are given in table 2.3. In this technique, a focussed 'white'

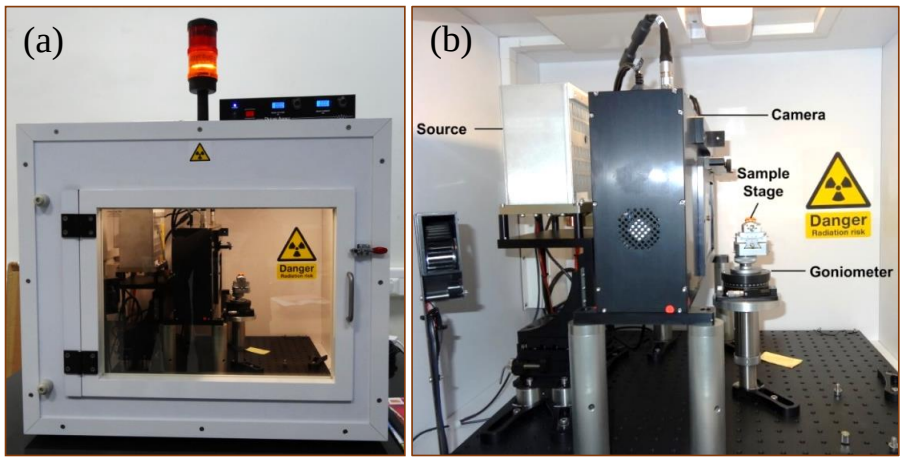

Figure 2.5: (a) Photograph of the Laue diffractometer (b) A close-up view of the source, detector, sample and goniometer inside the diffractometer.

x-ray beam (wavelength, $\lambda \simeq 0.35$ Å – 2.5 Å) is used as an incident beam, which is obtained from the bremsstrahlung radiation off the target. The Laue spots are collected on a 2D camera (scintillator detector) after back reflections of the incident x-rays from the crystallographic surface. Use of 'white' x-ray helps satisfy the Bragg conditions; and, different sets of parallel planes are captured as Laue spots on the camera at various angles. We use the 'Orient-Express' software to generate the simulated Laue spot for the

given crystallographic information. By analysing the measured Laue spots along with the simulated pattern from 'Orient-Express' software, the crystallographic orientation of the desired crystal is obtained with a accuracy of ± 2°.

2.3 Physical properties measurement system

The magnetic and transport properties of the oriented crystals were measured in PPMS (physical properties measurement system), Quantum Design, Model 6000, USA. PPMS consists of a super insulated Dewar which encloses the sample chamber and a superconducting magnet surrounded by liquid helium bath. The sample chamber is completely isolated (or sealed) from the external environments; the magnetic field and temperature can be varied according to the experimental requirements. The superconducting magnet submerged in the liquid helium bath, provide magnetic fields ranging between ± 9 Tesla. The minimum temperature that can be reached using an Evercool-II He refrigerator is 1.9 K; and, the maximum temperature that can be achieved by using a heater (VSM oven attachment) is upto 1000 K. The bulk properties including the magnetization, specific heat, resistivity and the torque magnetometry can be performed. The details of these probes are given further.

2.3.1 Magnetic characterization

2.3.1.1 Low temperature vibrating sample magnetometer

Magnetic measurements were carried out using a VSM (vibrating sample magnetometer) probe associated with the PPMS. The magnetization is measured as a function of temperature from 1.9 K to 400 K in the presence of a constant applied magnetic field and also as a function of magnetic field (from - 90 kOe to + 90 kOe) at a fixed temperature.

The oriented crystal sample is mounted on a high quality quartz sample holder by using non-magnetic GE varnish as a glue. This is shown in figure 2.6 (a). Figure 2.6

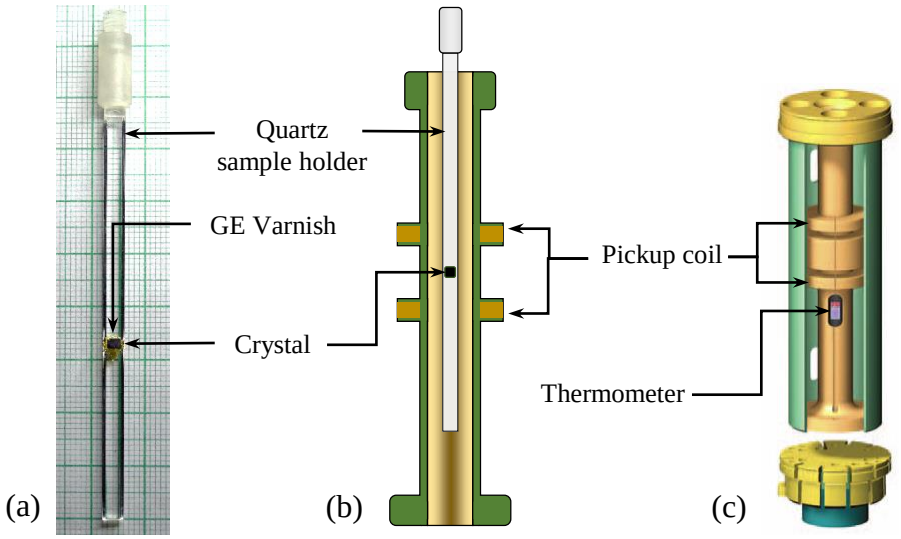

Figure 2.6: (a) The oriented crystal sample is mounted on the quartz sample holder by using GE varnish as a glue (b) The sample holder is placed inside the chamber and schematic view of the longitudinal section is shown. (c) The pickup coil-set of the VSM probe (adapted from PPMS manual, Quantum Design, USA [129]).

(b,c) shows schematics of this measurement technique. The sample holder is placed inside the chamber along with the VSM probe.

The VSM consists of a linear motor (not shown here) to vibrate the sample inside the pickup coil-set, and a voltmeter to detect the signal from pickup coil. The principle of operation of the VSM is based on Faraday's Law of induction. When the magnetic flux inside a conducting circuit changes, an emf is produced which is proportional to the time rate of change of the flux. The voltage induced across the ends of the VSM pick-up coil (V_{coil}) is given by:

$$V_{coil} = 2\pi f.C.m.A\sin(2\pi ft) \tag{2.1}$$

where m is the magnetic moment of the sample, C is a coupling constant, A is the amplitude of oscillation, and f is the frequency of oscillation [129]. When the sample is made to vibrate near the centre of the pick-up coil, the induced voltage generated from the change in magnetic flux is detected synchronously. Since the induced voltage is proportional to the magnetisation of the sample, a standard calibration is used to convert induced voltage from an unknown sample in the equivalent electromagnet units.

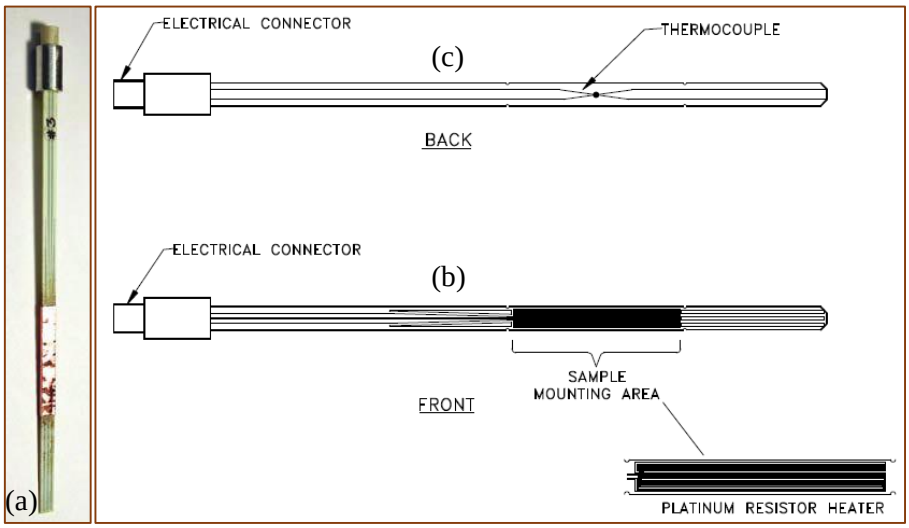

Figure 2.7: (a) The photograph of the VSM Oven sample holder ('heater stick') (b) The front side: a Platinum resistive heating elements are designed lithographically around the sample mounting area (c) Thermocouple embedded on the back side of the heater stick (adapted from VSM Oven manual, Quantum Design, USA [130])

2.3.1.2 High temperature VSM oven

The VSM Oven option attached to the PPMS provides a way to measure the magnetization in a controlled temperature range from 300 K up to 1000 K. VSM Oven consists of a heated sample holder (specially designed by Quantum Design) and VSM sample rod with electrical feedthrough, and the standard VSM detection coilset. To operate the VSM Oven, we need both the standard VSM option and a high-vacuum option.

In figure 2.7 (c and b), we show schematics of the sample holder which is specially designed for high temperature magnetic measurements. A Platinum resistive heating element is embedded lithographically on a custom-designed sample holder, known as 'heater stick'. The temperature around the sample region is measured using a thermocouple embedded on the back side of the heater stick and a thermistor at the top connector of the heater stick corrects for heating of the cold junction. The oriented crystal sample is placed on the lithographically patterned surface of the heater stick as shown in figure 2.7(a). The sample is attached to the heater stick with the help of an alumina-based cement, which provides the maximize thermal contact and helps to glue

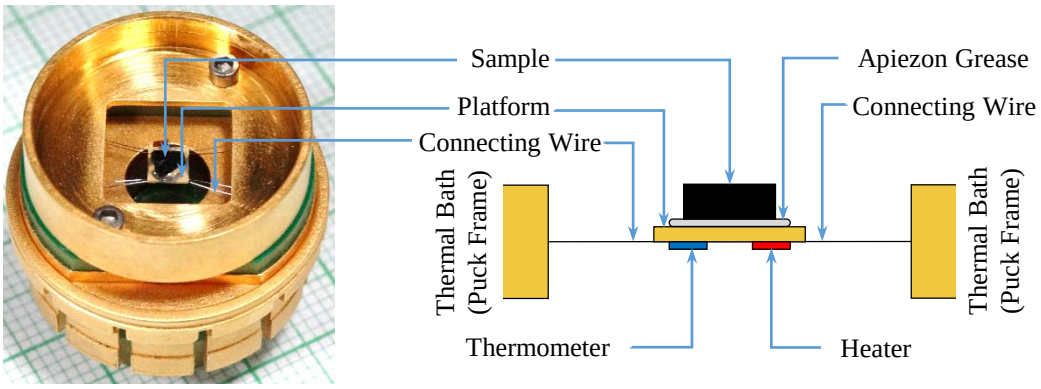

Figure 2.8: (left) Photograph of the calorimeter puck with a crystal sample mounted on the sample platform using Apiezon N grease (right) Schematic representation of the sample platform (see the text for details).

the sample to the heater stick. For a thermal isolation purpose, the heated region, including the sample, is wrapped with low emissivity copper foil which minimizes the heat leak from sample to the surrounding coilset. This helps in maintaining a constant sample temperature and also reduces the thermal gradient between the heater stick and the sample. During the high temperature VSM Oven measurement, the PPMS sample chamber is maintained under a high vacuum state ($< 10^{-4}$ torr).

2.3.2 Specific heat

In Quantum Design PPMS, the specific heat is measured by controlling the heat provided to the sample and monitoring the corresponding change in the temperature. To get a good thermal contact, the sample is mounted on the platform (attached to the calorimeter) using a thin layer of Apiezon N grease as shown in figure 2.8. Inside the calorimeter, the sample platform is suspended by 8 connecting wires made by Au-Pd alloy. These wires provide the electrical current to the heater and sensor placed at the sample platform.

A cleaved thin crystal sample, typically 3 - 4 mm $\times$ 3 - 4 mm $\times$ 1 mm in size is used to measure the specific heat. For low temperature specific heat measurement (below 200 K), Apiezon N grease is used, and for higher temperature Apiezon H grease is used to get a good thermal coupling between the sample and platform. At the beginning of each experiment, addenda (grease + platform) measurement is performed and then

the sample is mounted with the same grease and total heat capacity (sample + grease + platform) is measured. The sample heat capacity is obtained after subtracting the addenda from the corresponding total heat capacity. According to the heat capacity option attached to PPMS, a sample with a mass from 2 - 200 mg can be mounted on the sample platform [131]. However, we have typically used a crystal sample of mass not exceeding 30 mg. During the measurement, high vacuum is necessary so that unaccounted heat losses via conduction will be less. The measurements were done using the relaxation technique where both the thermal relaxation of the sample platform to the bath temperature and the relaxation time between the sample and sample platform is taken into account while fitting the temperature versus time response before, during, and after a heat pulse is applied.

2.3.3 Resistivity

In PPMS, the ETO (electrical transport option) supports the measurements of Resistance, IV characteristic and differential resistance. We measured the resistivity of grown crystals as a function of temperature. Although ETO option is capable of measuring both four-terminal and two-terminal resistances, we have only used the four-probe method. In this method, separate voltage and current terminals are used. The voltage terminals are placed in between the current terminals, which excludes the voltage drop due to contact resistance. To get more accurate values of resistivity, we used rectangular shaped samples with a good aspect ratio as shown in figure 5.8. Three crystals together can be loaded on a resistivity puck as shown in figure 5.8.

During this thesis, the resistivity measurement of some of the samples was also carried out using a DC four-probe home-built set-up down to the liquid nitrogen temperature (77 K). In each case, the sample to be measured was electrically contacted using four Au or Cu-wires glued to the sample surface using a conducting silver epoxy. In the home built set-up, the sample was cooled (or heated) by slowly lowering (or rising) it into a liquid nitrogen dewar. In this set-up, the sample temperature was measured using a platinum (Pt-100) temperature sensor mounted close to the sample. DC current

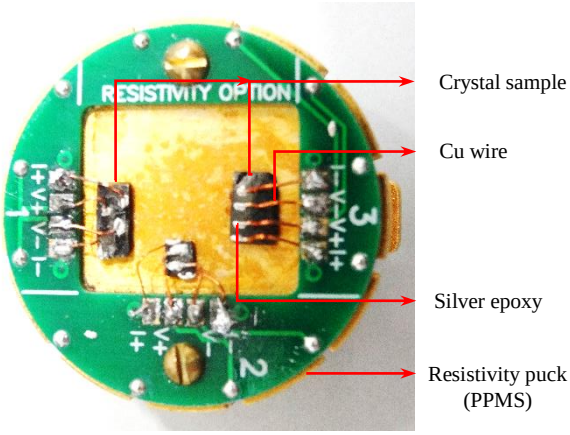

Figure 2.9: Representative image of a PPMS resistivity puck, where three crystal samples are shown. These samples are electrically contacted using the Cu-wires and silver epoxy.

of 100 μA was provided using a Keithley 6221 DC and AC current sourcemeter, and the voltage across the sample was measured using a Kiethley 2182A Nanovoltmeter.

2.3.4 Torque magnetometer

We used the highly sensitive torque magnetometer (TqMAG) associated with the PPMS to determine the behaviour of Fe - spins in the single crystalline $HoFeO_3$. In the presence of a magnetic field ($\vec{B}$), the angular-dependent magnetic torque experienced by the sample can be expressed as $\vec{\tau} = \vec{m} \times \vec{B}$; where '$\vec{m}$' is the magnetic moment of the sample.

The torque magnetometer operates in conjunction with the PPMS horizontal rotator or vertical rotator option and the user bridge board that is a component of the PPMS resistivity option. The torque magnetometer option features microfabricated, silicon, torque-lever chips as shown in figure 2.10. The torque magnetometer uses a piezoresistive technique to measure the torsion or twisting of the torque lever about the lever's symmetry axis, rather than flexion or bending to minimize the gravitational effect. The torque-lever chip consists of a continuous constantan, piezoresistive path incorporating two grids patterned on the legs of the torque lever chip [132].

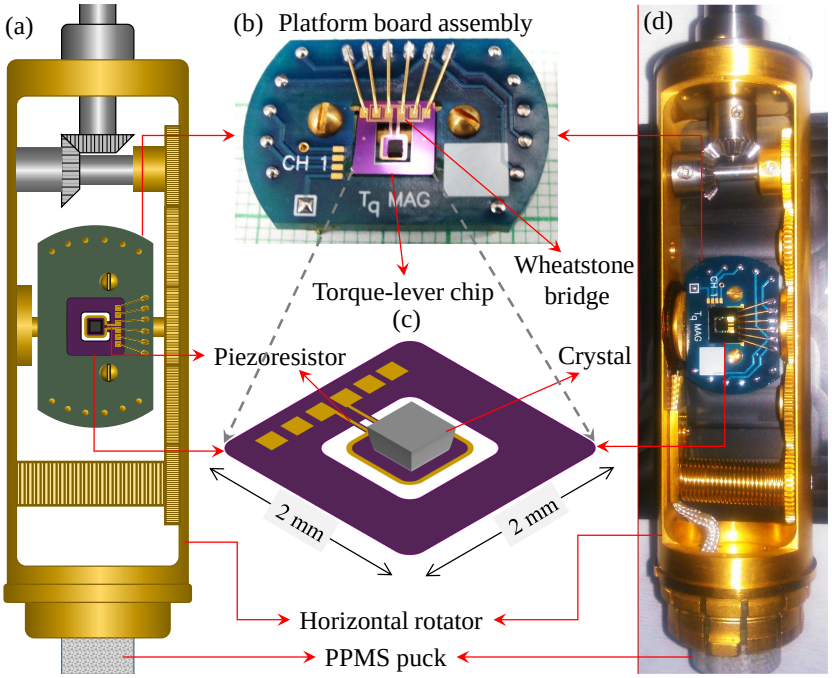

Figure 2.10: (a) Schematic representation of the torque measurement option containing (b) platform board assembly and (c) torque-lever chip along with the crystalline sample (d) photograph of torque option, PPMS, Quantum Design.

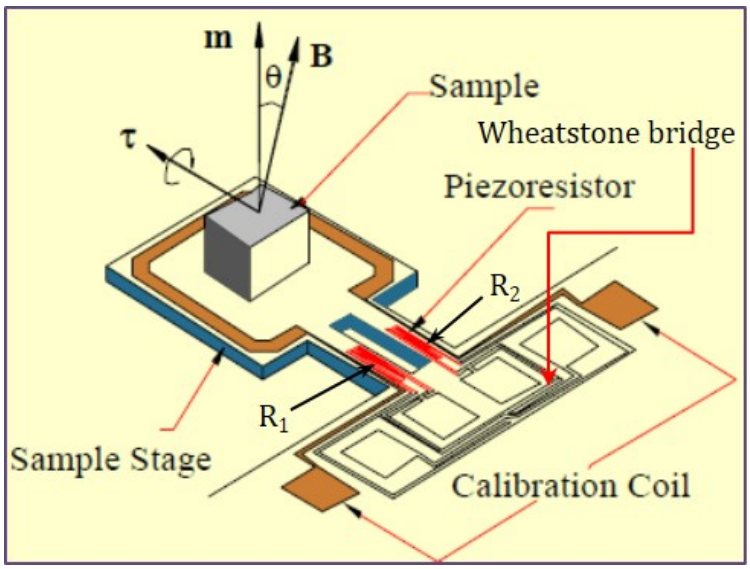

Figure 2.11: Principle operation of the torque measurement, torque ($\vec{\tau} = \vec{m} \times \vec{B}$; θ is the angle between the magnetic moment of the sample and the applied field (adapted from Ref. [132]).

Figure 2.12: (a) The photograph of UGC-DAE-CSR photoelectron spectroscopy beamline (b) Experimental station of angle integrated photoelectron spectroscopy (AIPES) beamline, Indus, RRCAT, Indore, India.

During the measurement, an oriented crystalline sample is mounted on the torque-lever chip and the chip is mounted on the PPMS rotator option (see figure 2.11). The torque-lever twists when an external magnetic field is applied. The change in resistance, $\Delta(R_1 - R_2)$, of the piezoresistor grids is measured using a Wheatstone bridge with a high degree of sensitivity. The measured ΔR is proportional to the torque experienced by the sample. The ΔR to τ conversion is done by calibrating the torque chip by passing a known current through the calibration coil lithographically embedded in the torque lever chip [132].

2.4 X-ray photoelectron spectroscopy

X-ray photoelectron spectroscopy (XPS) is a surface-sensitive quantitative spectroscopic technique that measures the elemental composition of a given sample [133]. Angle integrated photoelectron spectroscopy (AIPES) beamline at Raja Ramanna Centre for Advanced Technology (RRCAT, Indore, India) is designed to utilize photons in the energy range from 10 to 200 eV. The beamline operates in presence of ultra high vacuum more than 10^{-9} bar. The toroidal grating monochromators (TGM) is used to get a good photon flux and moderate resolution which are the basic requirements to study the XPS. The photograph of AIPES beamline at RRCAT is shown in figure 2.12(a) and a closer view of the experimental station of XPS is shown in panel (b). The optical

components of the beamline consist of a pre-mirror to focus the incident radiation and a post-mirror to focus the monochromatic beam on the sample. The specification details are gathered from the official website (http://www.rrcat.gov.in) and tabulated in table 2.4. We have used this technique to find out the valence state of Co in $Sr_{14}(Cu,Co)_{24}O_{41}$ crystals. X-ray photoelectron spectroscopy experiments were carried out on the single crystalline sample at the synchrotron Indus beamline BL-2 AIPES at RRCAT, Indore, India.

Table 2.4: Specification of the AIPES beamline at RRCAT, Indore, India

Parameters	Details
Source	Bending magnet
Acceptance	10 mrad (H) x 2.5 mrad (V)
Pre Mirror	Pt-coated toroidal mirror demagnification 2 : 1
Monochromator	Toroidal grating monochromator (TGM-2600)
Energy range	10 - 200 eV
Post Mirror	Pt-coated toroidal mirror
Spot size	Typically 1 mm (H) x 1 mm (V)
Experimental station	UHV compatible angle integrated photoelectron spectrometer

2.5 Terahertz spectroscopy

Terahertz spectroscopy (THz) on single crystals was performed at IISER TVM, India. For Terahertz Time-Domain Spectroscopy (THz-TDS) experiments, the THz signals were generated using ultrafast photoexcitation of low-temperature grown GaAsBi epi-layers; and were detected using a photoconductive antenna. Measurements were performed by mounting the sample on the cold-finger of an optical closed-cycle refrigerator. Transmittance were obtained by taking the ratio between magnitude of fast-Fourier transformed sample and the reference amplitudes.

Chapter 3

Crystal Growth and Characterization

This chapter is concerned with crystal growth of correlated oxides by the floating zone technique using a four mirror image furnace. The discovery of correlated materials showing interesting and potentially useful properties is important for scientific progress. To understand the properties of such complex materials, their availability as high-quality single crystals is essential. There are several crystal growth techniques for obtaining high-quality single crystals of the materials of interest. During this thesis, we used the travelling-solvent floating-zone method associated with a four mirror image furnace. To grow a high-quality, large-size, and homogeneous crystals in an image furnace, the first crucial step is to find out the optimum growth parameters, including growth speed, rotation rate, gas pressure and growth environment. These parameters also affect the eventual crystal quality and hence properties.

Here, we present the crystal growth of lightly-doped quasi-one dimensional, composite chain-ladder compound $Sr_{14}Cu_{24}O_{41}$. Various kinds of dilute magnetic and non-magnetic impurities are introduced in the structure. The details of single crystal growth in the presence of various impurities is presented. We also discuss why travelling-solvent floating-zone (TSFZ) is the most appropriate growth technique to obtain these compounds as large single crystals. Thereafter, starting from the basic principle of TSFZ growth process, we give details of crystal growth parameters and structural characterizations. Finally, we analyse the growth experiments to understand the different growth parameters including growth speed, rotation rate, lamp power dependence of the floating zone stability and floating zone composition of the grown crystals.

3.1 Crystal growth from melt

The choice of technique used for crystal growth of a given material depends strongly on the melting behaviour and vapor pressure of the components that make up the material. From the nature of solid-liquid phase transition, the crystal growth techniques have been classified as: growth from melt, solution-growth, vapor-phase growth, etc. The solution and vapor phase growth techniques are mostly used to avoid the decomposition of the material. However, crystal growth from the melt is often the most convenient method of obtaining large crystals, which can be employed in studying optical, electronic, and magnetic properties. Materials with controllable vapor pressure and congruent melting behaviour are most suitable for melt growth. In the present work, we will mainly focus on the optical floating zone (FZ) technique as we have grown the crystals using this technique. However, we will also briefly described the other melt-growth techniques before embarking on the floating-zone technique. This will enable us to appreciate the advantages of TSFZ technique over other growth techniques.

3.1.1 Melting behaviour

In single crystal growth the first thing one needs to know is the melting behaviour of the compound whose crystal needs to be grown. The melting behaviour of known compounds can be obtained from their associated phase diagram, which is a graphical representation of the relationship between composition, temperature and structure of various distinct phases of a system. There are two types of melting behaviours: congruently melting and incongruently melting. Schematically, the binary phase diagrams showing congruent and incongruent melting behaviour are shown in figure 3.1(a) and (b), respectively. In these diagrams, the solidus line is defined as the temperature below which the substance is stable in the solid state, whereas the liquidus line is the temperature above which the substance is stable in the liquid state.

As shown in figure 3.1, a congruently melting compound of composition α is characterised by a common equilibrium point of solid and liquid phase at the melting temperature (T_{MP}).The congruently melting behaviour compound can be readily grown

from a stoichiometric melt.

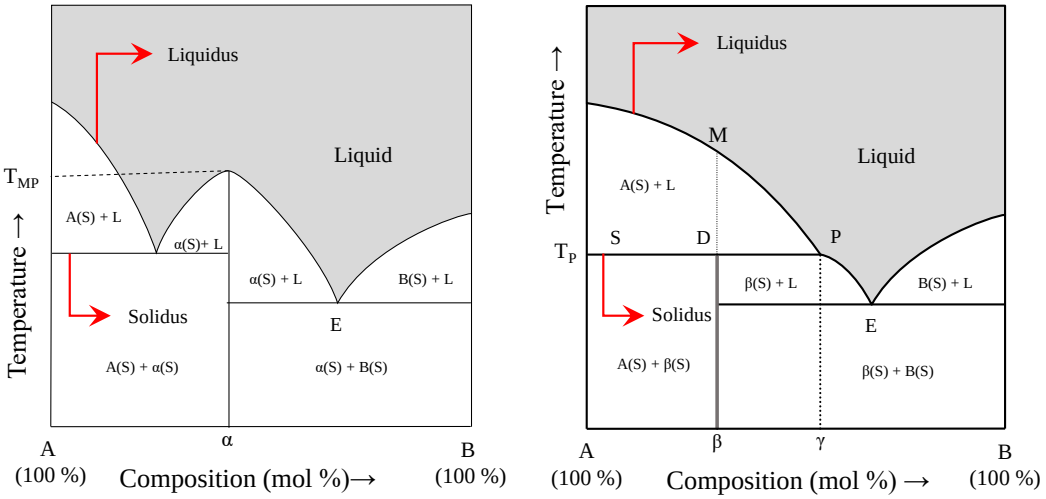

Figure 3.1: Left panel shows a binary phase diagram of components A and B with a composition of α of congruently melting behaviour. Right panel shows a binary phase diagram with a composition β of incongruently melting behaviour ($\beta \rightleftharpoons A(S)+\gamma(L)$).

The incongruent behaviour typically involves a peritectic decomposition at the peritectic temperature (T_P). In figure 3.1(b), it is shown that upon heating, the compound β decomposes peritectically into a solid A and a melt of composition γ. The temperature at which this decomposition takes place is called as peritectic temperature T_P. The compound β is therefore called an incongruently melting compound. Crystals of such compounds can in principle be obtained using the melt techniques; however, the melt in this case has a stoichiometry different from that of the incongruently melting compound whose crystal has to be grown.

3.1.2 Flux growth technique

'Flux growth' refers to the crystal growth from high temperature solutions (HTS). This method can be used to grow single crystals of a wide range of materials. In this method, the components of the desired material are dissolved in a solvent at a suitably high temperature, which is known as the flux. Upon slow cooling, the crystals of the material nucleate at multiple sites and grow progressively upon further cooling in a slow and controlled manner. An advantage of this technique is that the crystals are grown below

the actual melting temperature of the material. Therefore, materials that melt incongruently, or exhibit a phase transition below the melting temperature can also be grown using this method. Due to low growth temperature and very slow cooling rates involved, the obtained crystals are also less strained. Not only oxides but nitrides, borides and carbides can also be grown by this technique [134].

One of the disadvantages of this method is that the grown crystals are typically very small in size ($\sim$ mm dimension), which makes it difficult to perform inelastic neutron experiments where large crystal mass is required to get a good signal noise ratio. A further disadvantage is the unavoidable presence of impurities from the flux in the grown crystals [134, 135]. A very good temperature control is also important, since fluctuations of temperature are reflected in the final quality of the grown crystals [135].

3.1.3 Bridgman growth technique

This technique involves a relative translation of a conical shaped crucible holding the melt into a region of almost linear temperature gradient in a tubular furnace [136]. This results in a directional solidification of the melt. In this process, the crystal nucleates at the tip of the crucible, and grows in size as the crucible is made to slowly traverse through the temperature gradient. This method is very crucial in growing large single crystals of congruently melting materials. However, the choice of crucible material is often an important consideration; this is particularly important when the material to be grown has a high melting temperature.

3.1.4 Czochralski growth technique

In the Czochralski method, large single crystals are grown by slowly pulling a single crystalline seed out of the stoichiometric melt held in a water cooled hearth. In its simplest form, the technique consists of a water cooled hearth which contains the material to be crystallized surrounded by a heater or set of Ar gas arcs capable of melting the charge. A seed crystal (attached to a pulling rod) is lowered until the end of the seed crystal is dipped into the melt while the melt temperature is carefully adjusted until a

meniscus is supported by the end of the seed. Once a thermal steady state has been achieved, the pulling rod is slowly lifted and rotated, and crystallization onto the end of the seed occurs. Similar to Bridgman technique, a large-size crystal can be grown using the Czochralski technique. But this technique is mainly suitable for the intermetallic compounds that melt congruently.

3.1.5 Optical floating-zone growth technique

The crucible-free zone melting process was first introduced by W. G. Pfann at the Bell Laboratories [137], which was later awarded a US patent [138]. This technique eliminates the problems resulting from the use of crucibles. The floating zone technique is also effective in those cases where no crucible material is suitable due to high reactivity. The crystals grown by this technique are generally large (cm - dimension) and can also be easily extracted since there is no crucible or flux involved. This technique can be successfully employed to grow high-quality and large single crystals of incongruently melting compounds.

3.1.6 Details of optical floating zone technique associated with an image furnace

Four mirror image furnace We used a four-mirror optical-floating-zone Furnace (Model: FZ–T–10000–H–HR–I–VPM–PC, Crystal System Corporation, Japan). A schematic drawing of the vertical section of the furnace is shown in figure 3.2. The image furnace consists of four semi ellipsoidal mirrors with halogen lamps fitted at their foci. The second focus of each reflector is common and all the energy flux of the lamps, after reflections from the walls of the reflectors, converges at their common foci and melts the materials whose crystal needs to be grown. A large vertical temperature gradient helps in a rapid expulsion of heat at the lower interface to crystallize the material. In a typical crystal growth experiment, a molten zone is formed between the polycrystalline feed and the seed rods. The process is then continued by moving the molten-zone slowly upwards. This is achieved either by moving the mirror-stage up or

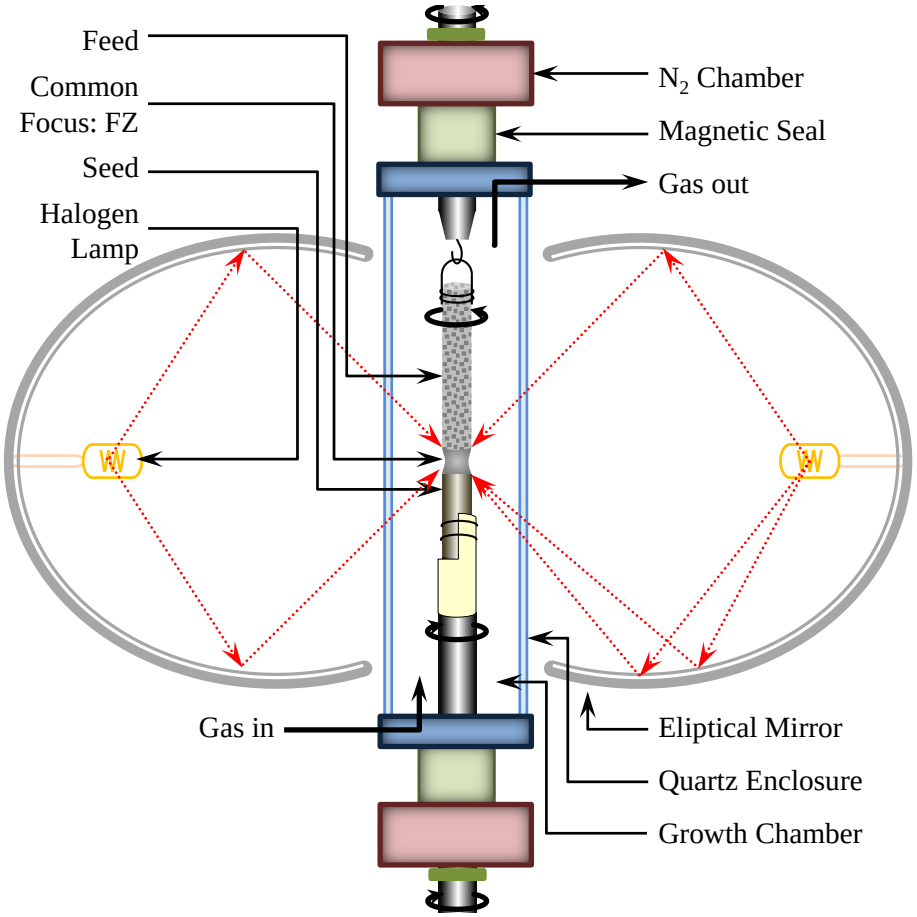

Figure 3.2: The vertical section of a four mirror image furnace is shown schematically to understand the working principle.

by lowering the feed and seed rods. When this process is carried out at a sufficiently slow speed, the polycrystalline feed is transformed into a single crystal. The feed rod is suspended from the upper shaft of the furnace by using a nickel wire, and the seed rod is clamped to the lower shaft on an alumina holder using Ni wire as shown in the figure 3.2. Since nickel has a low vapour pressure and it remains non-reactive upto very-high temperatures, nickel wire is used to fix the feed and seed rods. To start the growth for the first time, a portion cut from the polycrystalline feed rods itself is used as a seed. Otherwise, a single crystal cut from a previously grown crystal boule is used as a seed rod. The sample is protected by a large diameter, high-quality quartz tube that remain transperent to near-infrared and visible radiations. It prevents any evaporant settling on the mirror and also allows to control the growth atmosphere and gas pressure around the growing crystal. The upper and lower shafts are sealed into the chamber through

magnetic fluid seal to ensure high-purity of the chamber atmosphere and at the same time to allow for free rotation of the shafts. This type of magnetic fluid sealing can sustain upto 10 bar of high differential pressures and thus, our image furnace is limited to pressures less than 10 bar of atmospheric pressure. To obtain higher pressure in the growth chamber an equal pressure of N_2 is also applied outside the magnetic seal as shown in schematically in figure 3.2.

Feed rod preparation The first step in crystal growth by floating-zone (FZ) technique is the preparation of appropriate polycrystalline feed and seed rods. First, the material to be grown is prepared in the powdered form using the conventional solid-state synthesis route. The synthesized powder is then pressed in sealed rubber tubes by hydrostatic pressing under 700 bar pressure in a mechanical press to obtain cylindrical rods. These rods are used as feed and seed rod for crystal growth by the FZ technique. The ideal shape of feed rod is a cylindrical shape with a constant diameter and density along the length of the rod to prevent uncontrollable changes of the melt volume and the curvatures of the solid-liquid interfaces.

Growth parameters In floating zone technique, several growth parameters including the movement speed and rotation speed of both feed and seed rods, crystallization rate, growth atmosphere, gas pressure, temperature and shape of the molten zone are important for a successful growth. Optimizing these parameters is crucial for achieving growth stability and, consequently, a large and high quality single crystal. Therefore, one has to have the sufficient knowledge of the possible effects of these parameters and any correlations between them. These parameters need to have also adequate control of the overall growth procedure for which practical experience is vital.

3.2 Single crystal growth of $Sr_{14}(Cu,M)_{24}O_{41}$; M = Co, Zn, Ni and Al

Single crystals of $Sr_{14}Cu_{24}O_{41}$ and its doped variants: $Sr_{14}(Cu_{1-x}Co_x)_{24}O_{41}$ (x = 0.01, 0.03, 0.05 and 0.1), $Sr_{14}(Cu_{1-y}Ni_y)_{24}O_{41}$ (y = 0.0025 and 0.01), $Sr_{14}(Cu_{1-z}Zn_z)_{24}O_{41}$ (z = 0.0025 and 0.01) and $Sr_{14}(Cu_{1-a}Al_a)_{24}O_{41}$ (a = 0.0025 and 0.01) were grown in a four-mirror optical floating-zone furnace (Crystal System Corporation, Japan) using the traveling-solvent floating-zone growth method. Here, polycrystalline rods of $Sr_{14}Cu_{24}O_{41}$ and its doped compounds for the growth experiments were synthesized by the standard solid-state reaction route. Starting materials were in powder form and to remove moisture, we preheated $SrCO_3$ at 600°C for 24 hours. Powders of $SrCO_3$ (Alfa-Aesar 99.99 %) and CuO (Alfa-Aesar 99.995 %) and an appropriate oxide precursor of the impurity to be doped were weighed according to the required stoichiometry. The oxide precursors for Co, Ni, Zn and Al and their purities are as follows: Co_3O_4 (Alfa-Aesar 99.9985 %), NiO (Alfa-Aesar 99.995 %), ZnO (Alfa-Aesar 99.995 %) and Al_2O_3 (Alfa-Aesar 99.99 %). They were mixed thoroughly using an agate mortar and pestle. The mixture was then sintered in atmospheric air in the temperature ranging from 900 to 950 °C for a total of about 200 hours with several intermediate grindings. X-ray diffraction patterns were collected at various stages of the sintering process using the Bruker D8 Advance powder X-ray Diffractometer to confirm the phase formation. Once the desired phase was formed, the powders were packed, and sealed under partial vacuum in rubber tubes, which were cold-pressed in a hydrostatic bath under a pressure of about 700 bar. The compressed rods were removed fom the rubber tubes and subjected to a final heat treatment at 965 °C for 24 hours to obtain highly dense rods. These rods were used in the subsequent crystal growth experiments carried out using the travelling-solvent floating-zone (TSFZ) method.

3.2.1 Travelling solvent floating zone method

Here, we provide a brief explanation of the TSFZ technique, which has been successfully used for growing high-quality and cm-size single crystals of incongruently melting $Sr_{14}Cu_{24}O_{41}$ and its doped variants. To explain the TSFZ technique, we refere back to the phase diagram shown in figure 3.1(b). Here, the compound 'β' has an incongruently melting behaviour because upon heating it decomposes particularly into the solid A and a liquid (or melt) of composition γ. To grow single crystal of β, FZ growth from a

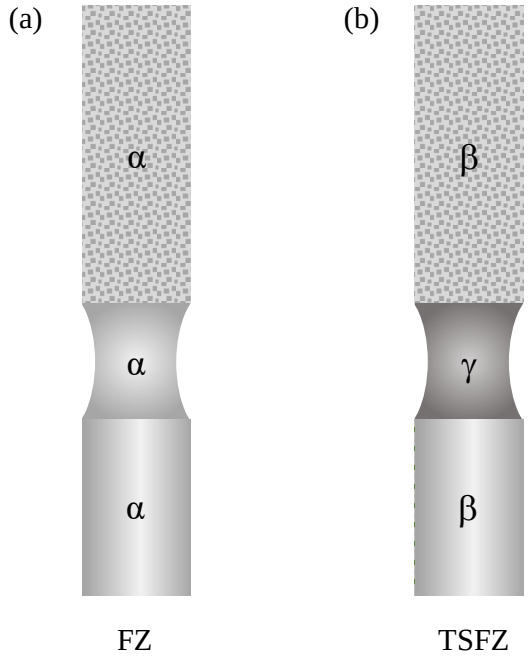

Figure 3.3: (a) Left panel shows FZ process dusring the growth of a congruently melting compound.(b) TSFZ process during the growth of an incongruently melting compound.

molten zone of the same concentration as the feed or seed will not give desired results. Thus, to grow this type of compound, one needs to introduce a 'solvent disk' of composition (γ) between the feed and seed rods. In the steady state, to produce the molten zone as the rods are made to travel downward, at the upper interface of the molten zone, the feed decomposes to solid A and liquid γ; and, simultaneously, the reverse reaction takes place at the lower interface, where the solid A and liquid γ re-combine to

crystallize the solid β; as shown in figure 3.3(b).

$$\beta(\text{Solid}) \underset{\text{Lower Interface}}{\overset{\text{Upper Interface}}{\rightleftharpoons}} \text{A (Solid)} + \gamma(\text{liquid}) \tag{3.1}$$

Thus the composition of solvent disk is extremely important to get a steady state in such experiments. Therefore, the solvent disk is prepared separately, using the solid state reaction route by taking the starting precursors in an appropriate ratio so as to match the composition of the associated peritectic point. The weight of the sintered solvent disk is taken to match the expected weight of the steady state molten zone. For above reasons, this technique is known as the travelling-solvent floating-zone (TSFZ) technique.

The spin ladder compound $Sr_{14}Cu_{24}O_{41}$ shows incongruently melting behaviour as shown in the binary SrO-CuO phase diagram 3.4. In the next section we will discuss the details growth procedure of the undoped and doped compounds $Sr_{14}Cu_{24}O_{41}$.

3.2.2 Binary SrO-CuO phase diagram

In the binary SrO - CuO phase diagram under ambient pressure, three incongruently melting compounds having compositions Sr_2CuO_3, $SrCuO_2$ and $Sr_{14}Cu_{24}O_{41}$ are known to exist [139–141]. A schematic view of the SrO-CuO binary phase diagram is presented in figure 3.4. Being incongruently melting in nature, the crystal growth of these compounds cannot be performed using the conventional melt growth technique, where the crystal is grown from the corresponding stoichiometric melt. In such cases, however, large single crystals can be obtained using the TSFZ method associated with an image furnace. The success of TSFZ method has been demonstrated in numerous cases including that of $Sr_{14}Cu_{24}O_{41}$ and its doped variants consisting of Ca and La doping at the Sr site [144, 145]. The Cu-site doped $Sr_{14}Cu_{24}O_{41}$ crystals in the present work are also grown using the TSFZ method. The details of the method are analogus to the one previously reported by us in the context of the compounds $SrCuO_2$ [146] and Sr_2CuO_3 [147]. The crystal growth conditions are tabulated in Table 3.1.

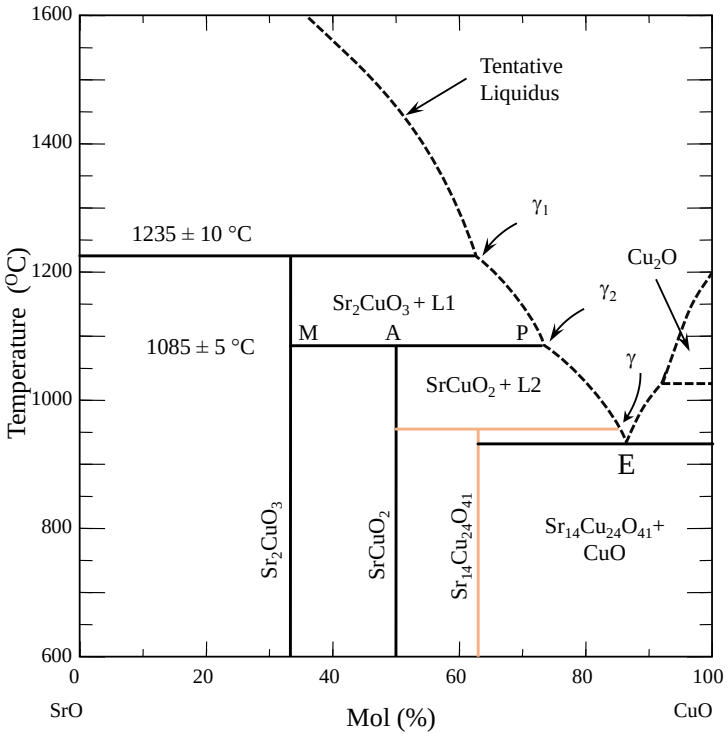

Figure 3.4: (a) Schematic binary phase diagram of the system SrO–CuO adapted from references [142] and [143].

3.2.3 Choice of solvent disk

Since the peritectic point associated with the decomposition of $Sr_{14}Cu_{24}O_{41}$ is located in the CuO rich region of the SrO - CuO phase diagram [139–141, 148], we carried out the initial growth experiments by melting a sintered CuO disk to form floating zone. A slight disadvantage of using CuO disk is that it takes longer to reach the steady state; therefore, in the subsequent growth experiments, the growth was initiated either by using a sintered pellet of approximate composition SrO 20 % and CuO 80 % or the frozen-in floating zone of a previous successful growth experiment (see, table 3.1).

The TSFZ growth process was initiated by melting a sintered solvent disk between the feed and the seed rods to form the initial or the first floating zone. In the growth of parent compound $Sr_{14}Cu_{24}O_{41}$, a preliminary experiment was carried out using a sintered CuO pellet as the solvent disk. In the subsequent growth experiments, the frozen-in last zone of the preceding growth was used to initiate the growth experiment. In the growth experiments of the doped crystals, sintered disks containing the corresponding

Table 3.1: Summary of the crystal growth experiments

#	Sample	Disk / weight Composition	Chamber Pressure (bar)	Feed Speed v_u (mm/h)	Growth Speed v_g (mm/h)	Growth Length (in mm)	Furnace Power(%)*	TSFZ stability
1.	Pure I	CuO /107 mg	1	0.90	1.0	10	29.5	Unstable
2.	Pure II	CuO /78 mg	2	0.95	1.00	40	33.0	Stable
3.	Pure III	CuO /116 mg	3	1.00	1.00	88	34.2	Stable
4.	Pure IV	FZ of #3	3	0.80	1.00	60	34.3	Stable
5.	Co1 %	FZ of #2 /116 mg	2.5	0.82	1.00	78	32.5	Stable
6.	Co3 %	Sr:(Cu+Co)=20:80 /139 mg	2	0.90	1.00	55	33.0	Stable
7.	Co10 % I	Cu:Co=90:10 /88 mg	3	0.80	1.00	91	34.5	Stable
8.	Co10 % II	FZ of #7 /151 mg	3	0.70	1.00	52	33.3	Stable
9.	Co5 % I	FZ of #8 /172 mg	3	0.85	1.00	74	34.5	Stable
10.	Zn0.25 % I	Sr:(Cu+Zn)=18:82 /380 mg	3	0.90	1.00	85	34.4	Stable
11.	Zn0.25 % II	Sr:(Cu+Zn)=18:82 /268 mg	3	0.90	1.00	96	34.5	Stable
12.	Zn1 % I	CuO /400 mg	3	0.90	1.10	110	32.4‡	Stable
13.	Al0.25 % I	CuO /334 mg	3	1.00	1.00	73.4	35.4	Stable
14.	Al0.25 % II	CuO /235 mg	5	1.00	1.00	41.3	37.7	Stable
15.	Al1 % I	CuO /334 mg	3	1.00	1.00	73.4	35.4	Stable
16.	Ni0.25 % I	Sr:(Cu+Ni)=18:82 /238 mg	3	0.90	1.00	95	34	Stable
17.	Ni0.25 % II	Sr:(Cu+Ni)=18:82 /215 mg	3	0.90	1.00	98	33.8	Stable
18.	Ni1 % I	Sr:(Cu+Ni)=18:82 /128 mg	3	0.90	1.00	100	41†	Stable
19.	Ni1 % II	Sr:(Cu+Ni)=18:82 /209 mg	3	0.90	1.00	100	43†	Stable

$v_u \rightarrow$ feeding speed; $v_g \rightarrow$ growth speed; * 4 x 500W Lamp; ‡ 4 x 1kW Lamp; † 4 x 300W Lamp

amounts of dopant were used. In majority of our experiments, the furnace was powered using four halogen lamps of maximum power rating 500 W each. In some cases lamps of lower power were also used (see, table 3.1 for details). The stable growth condition was achieved at around 34 % of the total furnace power.

3.2.4 Growth atmosphere

It is known from several previous works that the growth atmosphere plays a crucial role during the crystal growth experiments of $Sr_{14}Cu_{24}O_{41}$ and its Ca and La doped variants. In particular, the stability of the floating zone and the phase purity of the grown crystal depends on the oxygen pressure in the growth chamber[141, 144]. It has been shown, that in the growth experiments of the compounds $Sr_{14-x}Ca_xCu_{24}O_{41}$, the phase purity of the grown crystals for x > 9 could only be acheived by using high oxygen pressures exceeding 5 bar (e.g., the composition corresponding to x = 12 could only be grown as a single phase compound under an oxygen pressure of 12 - 13 bar) [144, 149, 150]. As far as the pristine $Sr_{14}Cu_{24}O_{41}$ is concerned, in a recent study, it has been reported to grow successfully under 2 bar oxygen pressure [150]. In an another relatively older report, 5 bar of oxygen pressure had been used successfully [151]. In table 3.1, the O_2 pressure used during various growth experiments in the present work is shown. All the crystals were successfully grown in the pressure range 2 - 3 bar except experiment #1, where 1 bar O_2 pressure was used; however, the floating zone at this pressure could not be stabilized. In each experiment, prior to pressurizing the growth chamber, a continuous oxygen flow for 12 - 14 hrs was used to ensure high-purity of the growth atmosphere. From the single phase nature of the grown crystals, it can be inferred that the pressure range used in our crystal growth experiments is adequate for doping Co, Ni or Zn at the Cu site at least upto the doping levels investigated here. This should be contrasted with the doping of Ca or La at the Sr site where increasingly higher oxygen pressures in the growth chamber were required with increasing doping level. One can understand this difference by considering the ionic size mismatch, which is quite significant in the case of doping at the Sr site; and also the level of doping, which is rather low in our

experiments compared to Ca and/or La doping at the Sr site .

3.2.5 Crystal growth speed

The TSFZ process involves a continuous decomposition of the feed rod at the upper interface of the molten zone. Simultaniously, crytstallization takes place at the lower interface of the zone. Under a steady state, the rate of crystalliztion at the lower interface has to match the rate of decomposition at the upper interface in order to maintain the quantity of liquid in the molten zone. Also, the FZ composition in a TSFZ process differs from both the feed and the growing crystal. These considerations make it necessary to run the growth process sufficiently slowly, for the composition and volume of the FZ to remain invariant all throughout the growth experiment. In our experiments, the growth speeds used were around 1 mm/h or less(see Table. 3.1). To control the size of the grown crystal and that of the molten zone, the feed rod is often lowered at a speed slower than the growth speed by 0.1 - 0.2 mm/h. The feed and the seed rods were rotated in opposite directions at rotation speeds ranging from 20 - 30 rpm. This was done to improve the temperature uniformity and compositional homogeneity of the floating zone.

3.3 Characterizations

Representative images of the doped $Sr_{14}Cu_{24}O_{41}$ crystals grown in the present work are shown in figure 3.5. The shiny surfaces of the grown crystals and their elliptical shaped cross-sections (not shown) were indicative of a good crystal quality. The elliptic cross-section is a hallmark of the single crystal of $Sr_{14}Cu_{24}O_{41}$ grown using the floating-zone method.

3.3.1 PXRD and variation of lattice parameters with doping

The grown crystals were examined using the powder x-ray diffraction. Some representative powder patterns are shown in Figure 3.6. Such patterns were recorded on the

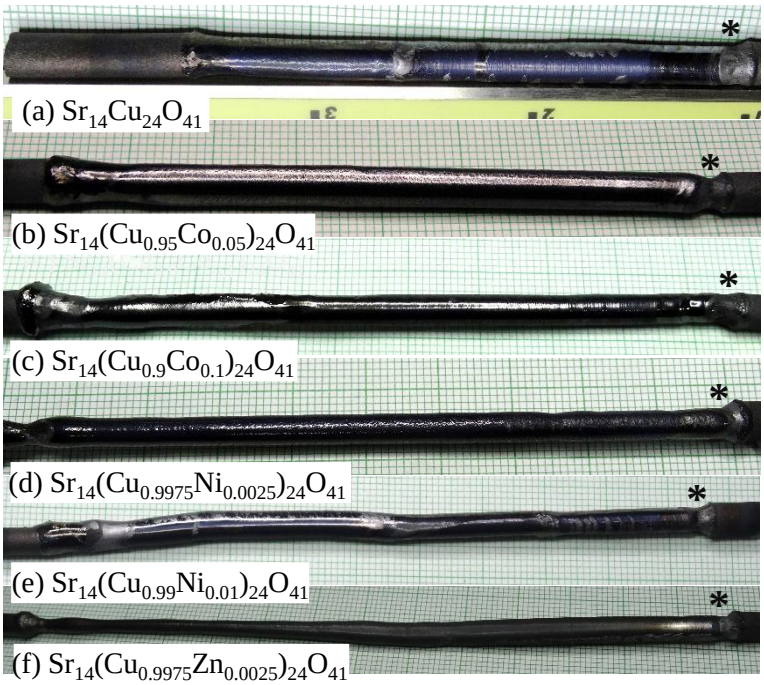

Figure 3.5: Representative images of the as grown crystals (a) $Sr_{14}Cu_{24}O_{41}$, (b) $Sr_{14}(Cu_{0.95}Co_{0.05})_{24}O_{41}$, (c) $Sr_{14}(Cu_{0.9}Co_{0.1})_{24}O_{41}$, (d) $Sr_{14}(Cu_{0.9975}Ni_{0.0025})_{24}O_{41}$,(e) $Sr_{14}(Cu_{0.99}Ni_{0.01})_{24}O_{41}$ and (f) $Sr_{14}(Cu_{0.9975}Zn_{0.0025})_{24}O_{41}$. '$*$' indicates the solidified TSFZ at the end of the crystal growth experiments.

powders obtained by crushing the crystal pieces cut from the as-grown crystal boules. The x-ray diffraction patterns show that the crystals are phase pure and that all the diffraction lines could be indexed based on the orthorhombic structure (space group Fmmm) [152]. In particular, no observable change of the crystal symmetry in the XRD patterns of any of our doped crystals, up to the highest doping level, could be observed. The lattice parameters were obtained using the UNITCELL program and are given in table 3.2. The variation of the *a*, *b* and *c* parameters, and the unit cell volume V of the Co-doped crystals is shown in figure 3.7. The effect of Co-doping on the lattice parameters is anisotropic -while along the *b*-axis, the lattice parameter decreases by about 0.21 %, along the *c*-axis it expands by about 0.18 % for the maximum Co concentration. Along the *a*-axis also the lattice parameter decreases, the decrease however is comparatively much smaller (0.04 % for Co10 % sample). Overall, the unit cell volume decreases with increasing Co-concentration as shown in figure 3.7.

Since the ionic radius of Co^{2+} in a 4-fold coordination (0.58 Å) is larger that that

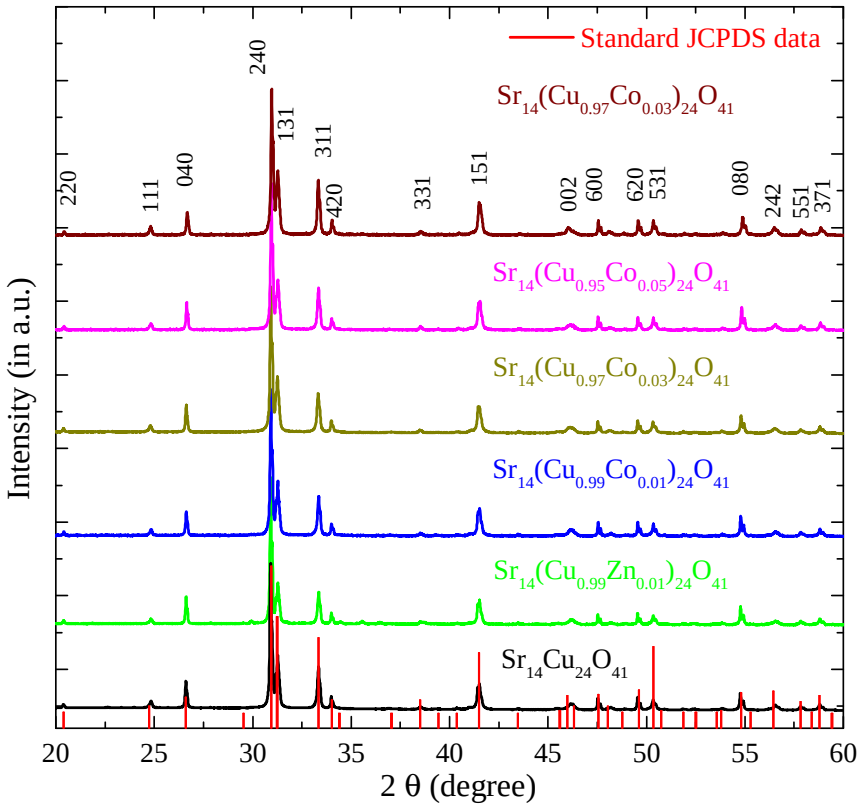

Figure 3.6: Representative powder x-ray diffraction patterns of the grown crystals.

of Cu^{2+} (0.57 Å) and Cu^{3+} (0.54 Å), substitution of Cu^{2+} / Cu^{3+} by Co^{2+} should only result is an increase of the unit cell volume, which is contrary to the experimental data. On the other hand, Co^{3+} is slightly smaller than either of Cu^{2+} or Cu^{3+} [153], hence, Co^{3+} substitution should result in a slight decrease of the unit cell volume. From the observed decrease of the unit cell volume, therefore, one can tentatively conclude that the doped Co-ions are incorporated in the structure as Co^{3+}. The +3 assignment of the oxidation state is also in agreement with the XPS results of ref. [154] on the polycrystalline samples with Co-concentrations upto 18 %. The analysis of the magnetic susceptibility data of Co-doped crystals also corroborate the +3 oxidation state of the doped Co-ions [155]. These observations, concerning the oxidation state of Co are, however, in apparent contradiction with the fact that Co^{3+} ion generally prefers a higher coordination number than the square-planar coordination present in $Sr_{14}Cu_{24}O_{41}$. To the best of our knowledge there is no known compound with Co^{3+} in the square-planar coordination.

The anisotropy of the lattice parameters upon Co-doping is also interesting and need

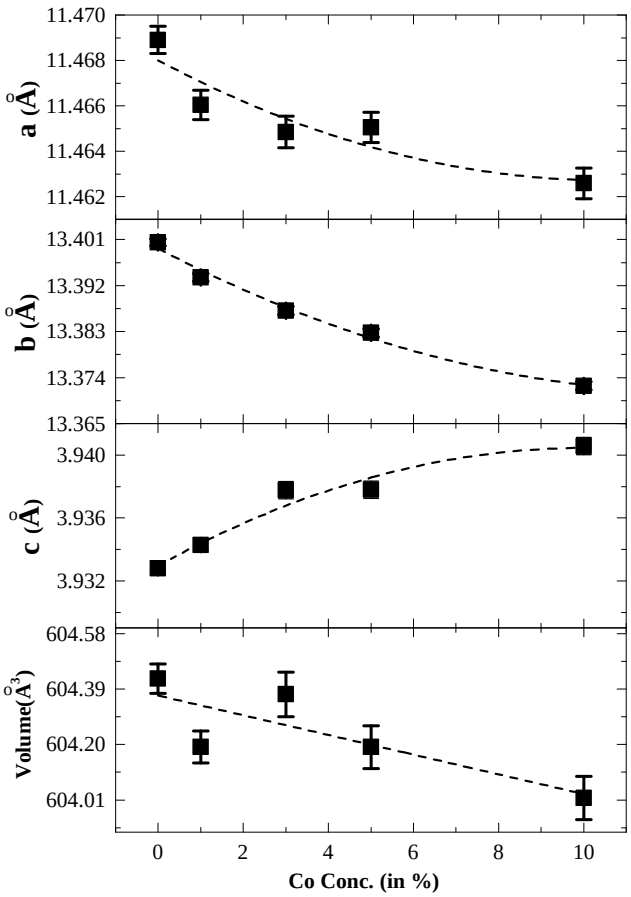

Figure 3.7: Lattice parameters and unit cell volume shown as a function of x in $Sr_{14}(Cu_{1-x}Co_x)_{24}O_{41}$ series of grown crystals.

Table 3.2: Lattice parameters of the grown crystals

Sample	a (Å)	b (Å)	c (Å)	cell volume (Å^3)
$Sr_{14}Cu_{24}O_{41}$	11.4689(6)	13.4004(8)	3.9327(3)	604.42(5)
$Sr_{14}(Cu_{0.99}Co_{0.01})_{24}O_{41}$	11.4660(6)	13.3936(8)	3.9343(3)	604.19(5)
$Sr_{14}(Cu_{0.97}Co_{0.03})_{24}O_{41}$	11.4648(7)	13.3871(8)	3.9378(5)	604.37(7)
$Sr_{14}(Cu_{0.95}Co_{0.05})_{24}O_{41}$	11.4651(7)	13.3827(8)	3.9378(5)	604.19(7)
$Sr_{14}(Cu_{0.9}Co_{0.1})_{24}O_{41}$	11.4626(7)	13.3724(8)	3.9406(5)	604.02(7)
$Sr_{14}(Cu_{0.99}Zn_{0.01})_{24}O_{41}$	11.4695(7)	13.3971(8)	3.9316(3)	604.12(6)
$Sr_{14}(Cu_{0.99}Ni_{0.01})_{24}O_{41}$	11.4942(7)	13.3658(8)	4.026(3)	618.52 (6)
$Sr_{14}(Cu_{0.99}Al_{0.01})_{24}O_{41}$	11.4503(7)	13.3761(8)	3.9402(3)	603.50(6)

further attention. Apparently, anisotropic lattice parameter variation in cuprates upon doping at the Cu-site is not uncommon. For instance, a careful study by Tarascon et al. [153] on doped $YBa_2Cu_3O_{7-\delta}$ (YBCO) revealed anisotropic variation of the lattice parameters upon doping with Al, Fe and Co at the Cu-site which are shown to be incorporated in the lattice as tri-positive ions. In YBCO, however, the unit cell volume increases with increasing doping level despite the fact that Al, Fe and Co, in the doped tri-positive state, have smaller ionic radii compared to the Cu^{2+}/Cu^{3+} ions. This anomalous increase of the cell volume had been attributed to an increase in the oxygen content, since the doped tri-positive ions selectively replace Cu^{2+} from the chain sublattice of YBCO.

In $Sr_{14}Cu_{24}O_{41}$, a similar mechanism may also be at play because, even though the unit cell volume shows a decrease, the lattice constant along the *c*-axis tends to increase upon Co-doping which cannot be understood on the basis of ionic size considerations alone. Indeed, the $Sr_{14}Cu_{24}O_{41}$ samples are known to show oxygen off-stoichiometry, however, their oxygen content variation is not as pronounced as that of the YBCO samples. In the study by Hiroi et al. [156], oxygen stoichiometry in $Sr_{14}Cu_{24}O_{41}$ is reported to vary from 40.3 to 41.9, beyond this range the structure does not remain stable. In another words, the maximum oxygen off-stoichiometry that $Sr_{14}Cu_{24}O_{41}$ can support is about 2 % of the ideal oxygen content, which is rather small compared to YBCO where this number can easily be as high as 10 %. Thus, unlike YBCO where doped Co^{3+} can selectively replace Cu^{2+} in the chains by increasing the oxygen content, in $Sr_{14}Cu_{24}O_{41}$, due to its limited oxygen uptake capacity, the situation is more complex. Remember, in $Sr_{14}Cu_{24}O_{41}$ the majority of holes are localized over the chains, therefore, the doped Co^{3+} ions can either replace Cu^{3+} directly in the chain which will leave the oxygen stoichiometry unchanged, or they may replace Cu^{2+} in either the chain or the ladder sublattice. Due to the similar x-ray photon scattering cross-section of Cu and Co, from the powder x-ray diffraction alone it is nearly impossible to tell which site the doped Co-ions will prefer in $Sr_{14}Cu_{24}O_{41}$. This problem is further compounded by the fact that the chain and the ladder sublattices show incommensurate structural modulation which makes the rietveld refinement of powder x-ray pattern rather ambiguous. Precise

TGA experiments in combination with other local structural probes (for example, x-ray absorption spectroscopy) should be carried out in order to address these questions.

3.3.2 Laue diffraction

The crystallographic orientations of the minor and major axes of the elliptic sections were confirmed using the Laue diffraction to be parallel to the *b* and the *a*-axis, respectively. The crystals were formed to cleave easily. Figure 3.8 shows a typical Laue

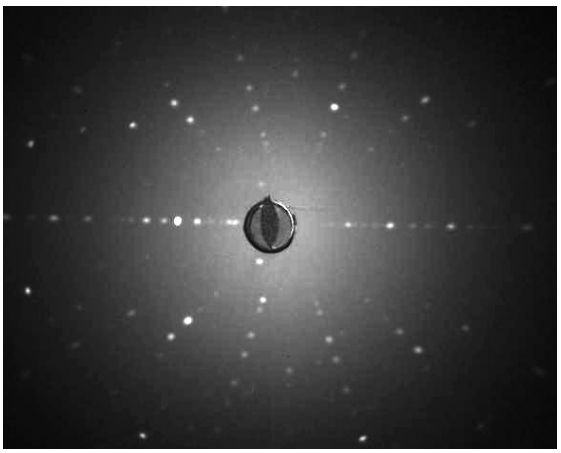

Figure 3.8: x-ray Laue diffraction image of a cleaved surface (*ac* - plane) of $Sr_{14}Cu_{24}O_{41}$ crystal specimen.

pattern obtained on a cleaved crystal section, captured in the back reflection geometry. The symmetry of the Laue spots confirms that the orientation of the surface is perpendicular to the *b*-axis of the crystal. Similar Laue diffraction patterns from other growth experiments indicate that in majority of our experiments, the crystallographic *c*-axis tends to coincide with the growth axis (i.e. the vertical furnace axis).

3.3.3 Optical & Scanning Electron Microscopy

Thin sections, cut from different positions of a crystal boules, were examined using the optical microscopy under the polarized light, back-scattered electronic (BSE) images and EDX analysis. Prior to SEM/EDX, these sections were dry-polished in air using silicon-carbide papers of progressively increasing grit-size to get mirror-finished surfaces. In table 3.3, average Co-concentration measured experimentally is compared

with the nominal values for three growth experiments. The experimentally determined

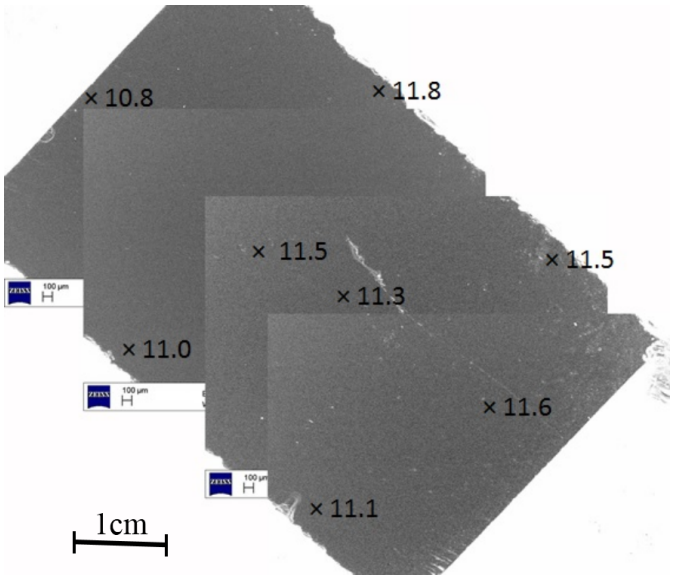

Figure 3.9: Back scattered scanning electron microscopy images of the longitudinal section of a 10 % Co doped $Sr_{14}Cu_{24}O_{41}$. Co concentration (in %) indicated at the positions marked 'x'. The section was cut at a distance of 80 mm from the beginning of the growth.

Co concentrations in each case are in close agreement with their respective nominal compositions within the error limits of the EDX probe (about 1 %). The 10 % Co-doped crystal boule (#8 in table 3.1) was examined rigorously using the EDX and magnetic susceptibility probe for variations of Co-concentration along the crystal length. The SEM images and the EDX analysis carried out on a longitudinal section of this crystal are shown in Figure. 3.9.

The points where the EDX analyses were performed and the corresponding Co concentrations are also shown in the figure. From these numbers we obtained an average Co-concentration of 11.3 ± 0.3 %. This value is in a reasonable agreement with the nominal Co concentration. Later in the manuscript, we will discuss the assessment of Co concentration along the length of this crystal using the magnetic susceptibility as a probe.

Table 3.3: Amount of Co concentration present in the crystal at *x* mm from the beginning of the growth

Sample	Nominal(%)	Actual(%)	*x* (mm)
$Sr_{14}(Cu_{0.97}Co_{0.03})_{24}O_{41}$	3	3.4	75-81
$Sr_{14}(Cu_{0.95}Co_{0.05})_{24}O_{41}$	5	5.2	70
$Sr_{14}(Cu_{0.9}Co_{0.1})_{24}O_{41}$	10	11.3	50

Table 3.4: Doping concentration (x_M) of the grown crystals were characterized by using ICP-AES

Sample	Sr (/f.u.)	Cu (/f.u.)	Dopant (M / f.u.)	Nominal (M in %)	Actual (x_M in %)
$Sr_{14}(Cu_{0.9975}Zn_{0.0025})_{24}O_{41}$	14	23.6	0.112	0.25	0.47
$Sr_{14}(Cu_{0.99}Zn_{0.01})_{24}O_{41}$	14	25.9	0.217	1.00	0.08
$Sr_{14}(Cu_{0.9975}Al_{0.0025})_{24}O_{41}$	14	26.2	0.024	0.25	0.09
$Sr_{14}(Cu_{0.99}Al_{0.01})_{24}O_{41}$	14	26.6	0.061	1.00	0.23
$Sr_{14}(Cu_{0.9975}Ni_{0.0025})_{24}O_{41}$	14	25.5	0.080	0.25	0.31
$Sr_{14}(Cu_{0.99}Ni_{0.01})_{24}O_{41}$	14	25.7	0.267	1.00	1.02
$Sr_{14}(Cu_{0.99}Co_{0.01})_{24}O_{41}$	14	26.1	0.264	1.00	1.00

3.3.4 Inductively Coupled Plasma- Atomic Emission Spectroscopy (ICP-AES)

Inductively Coupled Plasma- Atomic Emission Spectroscopy (ICP-AES) at the Sophisticated Analytical Instrument Facility (SAIF), Indian Institute of Technology, Bombay is used to determine the actual dopant concentration in the 1% Zn, Ni and Al doped crystals. The results are tabulated in table 3.4. For the Ni and Co doped crystals, the concentration determined using ICP agreed nicely with the nominal value. But in the case of Zn, the actual Zn concentration is found to be 0.008 ± 0.001/Cu; and for the Al-doped crystal this was around 0.0025 ± 0.001/Cu, indicating a very limited solid-solubility of Al in the crystals grown using the floating-zone method. Henceforth, the actual concentration is designated as x_M, where M can be Zn, Ni, Al or Co. Because of low doping levels there is no straight forward method of checking whether the doped impurities are substitutional or interstitial.

3.3.5 Compositional and microstructure analysis of the TSFZ

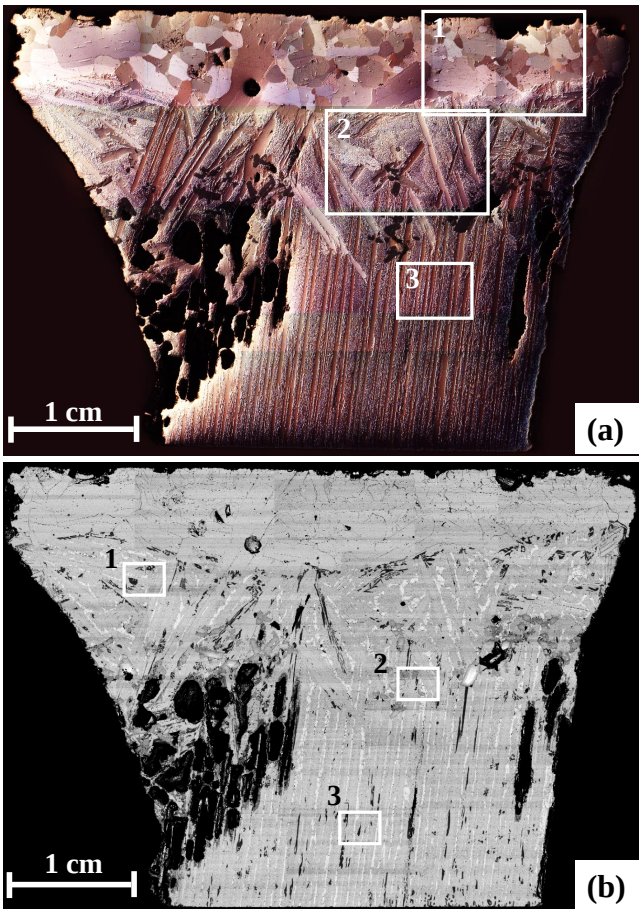

Figure 3.10: (a) Optial polarized image and (b) SEM (Back Scattered) image of frozen in zone and adjacent feed in the growth of $Sr_{14}(Cu_{0.95}Co_{0.05})_{24}O_{41}$ (this image is obtained by superposing several images spanning the entire specimen surface.)

To gain further insight into the TSFZ process, in some of the crystal growth experiments of doped $Sr_{14}Cu_{24}O_{41}$, we analyzed the quenched floating zone under the steady state condition, i.e., the stage during the TSFZ process when no further changes are required in the growth parameters and the growth experiment proceeds uninterrupted for days. The quenching was done by stopping the rotations of the feed and the growing crystal and quickly reducing the furnace power to $\sim$ 25 % below the steady state value. This led to the freezing of the molten zone in a small time interval of 20 - 30 seconds. Thereafter, the power was allowed to decrease to zero slowly over a period of 5 - 6 hours. The quenched zone was cut parallel to its length, and then dry-polished

using the silicon carbide papers of decreasing particle size down to about 10 μm to obtain a mirror-finished surface. The polished surface was examined using an optical microscope under polarized light and a SEM aided with an EDX probe. Figure 3.10 shows the optical (panel *a*) and SEM (panel *b*) images of the frozen-in zone and the part of the feed rod in immediate contact with the TSFZ. These images are a collage of many higher magnification images, some of which are shown in figures 3.11 and 3.12 as representatives. These are chosen to represent three different regions of the TSFZ, labeled '1', '2' and '3' in figures 3.10*a* and 3.10*b*. Region '1' highlights the interface between the feed and the TSFZ, region '2' is the upper region of the zone and region '3' lower region.

3.3.5.1 Melt-feed interface

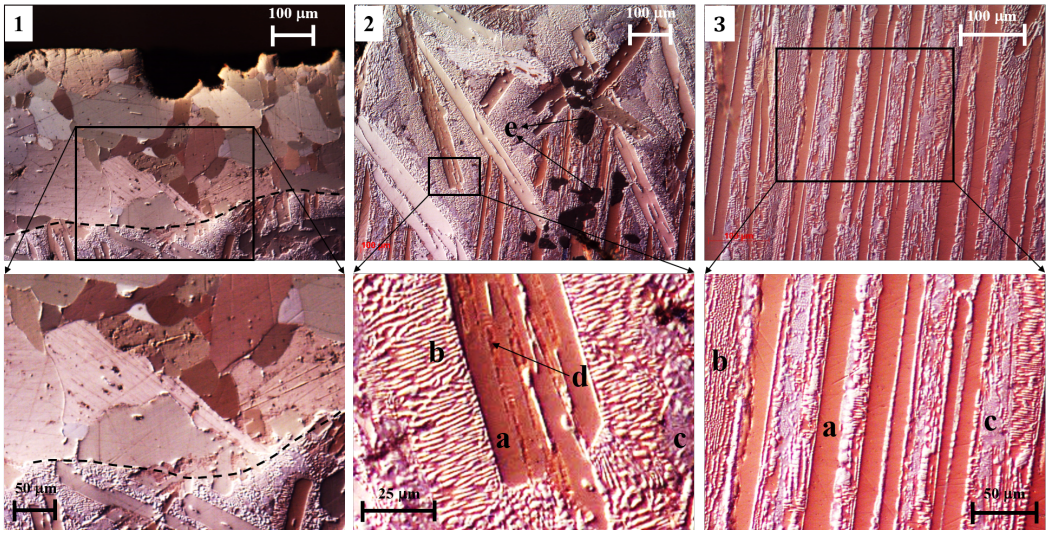

Figure 3.11: Optial polarized images of different sections of the frozen in zone shown in fig 3.10. Panels '1', '2' and '3' are the regions labelled as 1, 2 and 3 in figure 3.10*a*.

Before we go into specific details of the microstructure of the TSFZ, let us first comment on some more common observations. As shown in figure 3.11 (panel '1'), the interface between the feed and the molten-zone is found to be rather sharp with no signs of melt penetrating the feed rod due to the capillary action. This is due to the high-density of the feed rods employed in the growth experiments. The feed rods, as mention previously, were sintered in air at a temperature about 10 ^{0}C or so below the peritectic

melting point, which resulted in the high-density. This was not the case, for instance, in the TSFZ growth experiments of Sr_2CuO_3 reported previously where the melt from the molten zone penetrated the feed rod up to a considerable distance [147]. The peritectic melting temperature of Sr_2CuO_3 is about 1250 ^{0}C; but the highest temperature used for sintering the feed rods used in the growth experiments was significantly lesser (about 1100 ^{0}C), which did not allow densification to reach values close to the theoretical density. There, the higher temperatures were avoided since the alumina crucible employed tends to react with the compound at higher temperatures. In the present case, however, since the peritectic point itself is near 975 ^{0}C (see, figure **??**), obtaining high densities was straight forward. The high density of the feed rod is evident from its microstructure shown in panel '1' of figure 3.11, which is reminiscent of a melted alloy. The grains are large, 100 μm or bigger in size without pores.

3.3.5.2 Voids in the FZ

Having a sharp interface has interesting consequences for the microstructure of the TSF; however, before we turn our attention to that let us quickly comment on the presence of voids in the quenched zone. We found out that the voids invariably appeared in almost all the cases that we inspected. Similar observation was also recorded in the growth experiments of Sr_2CuO_3 [147] and $SrCuO_2$ [146]. It should be emphasized that we found no evidence of bubbles either in the molten zone during the crystal growth process or in the grown crystals as revealed by their post growth analysis. The voids in the frozen-in zone therefore appear during the quenching process due to the dissolved oxygen gas in the melt [147].

3.3.5.3 TSFZ composition

An exaggerated view of regions (2) and (3) are shown, respectively, in panels '2' and '3' of figure 3.11. Both these regions are well inside the TSFZ. The composition of both the regions, as shown in Table 3.5, is found to contain SrO 25 % and (Cu, Co)O 75 %. The corresponding Co concentration as a percentage of the Cu atomic concentration is also shown in the table. We also examined TSFZ composition over several other areas

(not shown) and found it to be the same as over the areas (2) and (3) shown here. Two broad conclusions can be drawn from here: (i) the average TSFZ composition during the growth of $Sr_{14}Cu_{24}O_{41}$'s contains SrO : CuO in the ratio 1 : 3, and (ii) the Co concentration of the TSFZ ($\sim$ 4 %) is close to the nominal value ($\sim$ 5 %), therefore, the segregation coefficient of Co is $\leq$ 1. Since under the steady-state condition the composition of TSFZ should correspond to that of the associated peritectic point, we may infer that the composition of the peritectic point, associated with the decomposition of $Sr_{14}Cu_{24}O_{41}$, under 3 bar oxygen pressure, is around SrO 25 % and CuO 75 %. This matches with the composition reported by Liang et al. using the DTA analysis [139]. Unfortunately, in their experiments the atmosphere is not mentioned. They also reported the eutectic and the peritectic temperatures to be around 965 and 975 ^{0}C, respectively. In other reports on SrO - CuO phase diagram, the eutectic and peritectic points are not clearly distinguished (see, for example [148]). In our own experiments [155], we found the eutectic and peritectic points to be indistinguishable under air atmosphere. It is only when the oxygen atmosphere is used that the temperature difference between the eutectic and the peritectic point began to widen with increasing pressure.

3.3.5.4 Microstucture of TSFZ

Coming now to the details of the microstructure of the TSFZ. As shown in panel '3' of figure 3.11, the microstructure in lower parts of the TSFZ is stripe-like, consisting of large, near-vertical grains sizing up to several hundred μm in length and $\sim$ 20 μm in width. These grains are embedded in the matrix of eutectic regions as shown in an exaggerated view below panel '3' of figure 3.11. A closer view of the region (3), using the back scattered SEM images revealed the compositional details of the microstructure. One such representative image is shown in figure 3.12 (panel 3). The stripes (labeled as 'a') were found to have the composition of the phase $Sr_{14}(Cu,Co)_{24}O_{41}$; within the stripes one finds traces of Cu rich phase. These are black regions, labeled as 'd' and their composition is shown in Table 3.5. In fact, in the SEM image of the TSFZ in figure 3.10, one can see these as thin, black vertical streaks. Their relative volume is small. The details of the eutectic are shown in the lower panels of figure 3.12. The eutectic

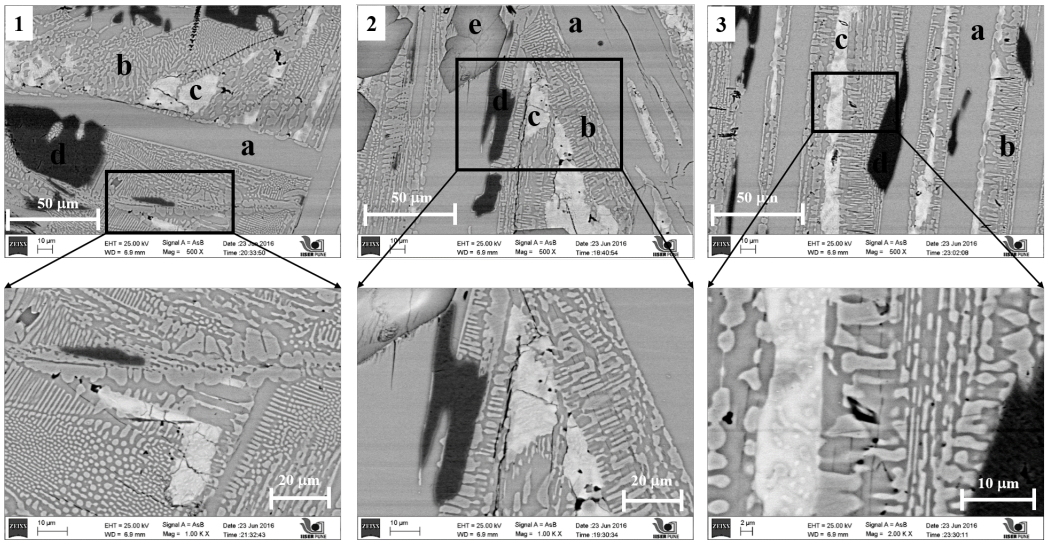

Figure 3.12: SEM (Back Scattered) images of the different sections of the frozen in zone of $Sr_{14}(Cu_{0.95}Co_{0.05})_{24}O_{41}$. Panels '1', '2' and '3' are the same as regions labelled 1, 2 and 3 in figure 3.10*b*.

consists of phases CuO and $Sr_{14}(Cu,Co)_{24}O_{41}$ as expected from the SrO - CuO phase diagram (figure 3.12). The eutectic composition is found to contain SrO 18 % and (Cu, Co)O 82 % (Co % with respect to Cu is shown in table 3.5). In addition to the well resolved eutectic, we also see thin white streaks; these are labeled as 'c' in figures 3.10*b*, 3.11 and 3.12. In figure 3.10*b*, they are barely resolvable due to poor contrast, but in figure 3.12 and 3.12, they are easily distinguishable. In panel '3' (and the panel below it showing an exaggerated view), these streaks are magnified. The average composition of these streaks obtained by area scan turned out to be the same as the eutectic composition. While more details are lacking and would require experiments at further higher magnifications, compositional analyses at various points over these streaks suggest the presence of submicron size grains of $Sr_{14}Cu_{24}O_{41}$ embedded a relatively higher CuO content matrise.

The microstructure of the upper part of the TSFZ is also characterized by the presence of stripes embedded in the eutectic mixture analogous to the lower region. However, here, the stripes are found to be randomly oriented as is evident from the optical image of the FZ shown in the panel (a) of figure 3.10. The composition of the stripes and the details of the eutectic mixture were also found to agree with those of the lower

Table 3.5: Compositional EDX analysis of different regions of Frozen-in Zone of the growth of $Sr_{14}(Cu_{0.95}Co_{0.05})_{24}O_{41}$ crystal

Regions of TSFZ	N	Average (Cu + Co) - atomic %	Standard Deviation	Average Co - % w. r. t. Cu	Standard Deviation
Region - *a*	43	62.3	0.3	6.23	1.1
Region - *b*	11	81.9	1.6	2.93	0.4
Region - *c*	12	75.4	0.9	0.39	0.1
Region - *d*	7	99.8	0.2	0.72	0.1
Region - *e*	6	3.9	0.4	17.48	7.8
FZ	26	74.3	0.7	3.74	0.2

'N' is the number of data points.

region of the TSFZ. Since their overall composition is also the same, the two regions appear to differ only with respect to the orientation of the stripes. What causes the stripe orientation to be different in the two regions? We believe that during the freezing of the molten zone, the orientation of the $Sr_{14}(Cu,Co)_{24}O_{41}$ stripes is governed by the substrate. The melt at the lower interface is supported on a single-crystalline substrate; therefore, in the process of freezing out of the zone, the stripes grow preferably along one direction guided by the orientation of the single crystalline substrate. At the upper interface, on the other hand, a polycrystalline solid is in contact with the melt, which results in the growth of randomly oriented stripes. One may ask why the volume of the lower region showing uniform stripes is larger than that of the upper region where stripes are crisscrossed. To understand this difference, one should probably consider the temperature gradient at the upper and the lower interfaces. At the lower interface the melt is in contact with a single crystalline support having higher thermal conductivity as opposed to a polycrystalline feed at the upper interface. It should be recalled that the single crystal of $Sr_{14}Cu_{24}O_{41}$ possesses a highly anisotropic thermal conductivity with high values along the chain/ladder direction which orient itself roughly parallel to the growth axis as revealed by the symmetry of the Laue spots (figure 3.8). As a result the temperature gradient at the lower interface is higher than at the upper interface. This difference of the temperature gradient at the two interfaces is further augmented by the fact that the growing crystal is more rigidly anchored to the water-cooled stainless lower shaft than the feed rod which is simply suspended to the upper shaft (also

water cooled) using a thin Ni-wire. Therefore, during the freezing out of the zone , the lower interface travels up faster than the speed at which the upper interface travels down, which explains why the portion of the TSFZ with vertically oriented stripes is larger in volume.

At the boundary where these two regions meet, small pockets consisting of micron-size grains, labeled as 'e' in figures 3.10*(a)* and 3.12 were also observed. The EDX analysis revealed the composition of these grains as SrO ~ 96 %, (Cu, Co)O ~ 4 %, with Co concentration relative to Cu ~ 18 % (see, table 3.5). In comparison with the nominal 5 % concentration in the phase $Sr_{14}(Cu,Co)_{24}O_{41}$, the Co-concentration in these Sr-rich grains is rather high. The detailed underlying structure of these grains is currently lacking and would require further investigations. The appearance at this phase at the boundary of the two regions of the FZ is rather interesting. What drives it formation and why it is located near the boundary are interesting questions for the future research.

To summarize, the microstructural details of TSFZ appear to be in a good agreement with the SrO - CuO phase diagram shown in figure 3.4. The appearance of thin Cu-rich streaks (phase labeled 'd') in the TSFZ is analogous to the observation of Cu-rich phase found also in the quenched zone during the crystal growth of Sr_2CuO_3 reported previously [147]. We believe that its occurrence has to do with small amount of Cu_2O present in the molten zone during growth, along with the dissolved oxygen gas. During quenching of the zone, not all the Cu_2O present in the melt recombines with the dissolved oxygen gas to give back CuO. As a result, some CuO_x remains, and so also the equivalent amount of trapped oxygen gas. While the residual CuO_x appears as thin, black streaks in the SEM images, the trapped oxygen gas gives rise to the voids.

3.3.6 Distribution coefficient

In a melt growth of doped crystals, uniformity of the dopant concentration along the crystal length is an important issue. The solute concentration in the grown crystal depends on the segregation or distribution coefficient (k). This can be understood from the

intersection points of isotherms with the liquidus and solidus lines in the binary phase diagram. The segregation or distribution coefficient (k) is defined as the ratio of concentration of the solute in the solid (C_S) to that in the liquid (C_L) as k = $\frac{C_S}{C_L}$. In the growth process it can be realized as the ration of dopant concentration in the crystal to that in the melt. In many cases the distribution coefficient is less than 1, which, implies that the dopant concentration in the grown crystals increases gradually over a good length of the growing crystal before reaching the equilibrium value corresponding to the composition of the feed. We have examined the microstructure of the TSFZ of the Co - doped grown crystal $Sr_{14}Cu_{24}O_{41}$ and found out the ratio (k) is almost equal to 1. Which means the doping concentration along the length of the grown crystal is uniform. This result is rather interesting because in the crystal growth of $SrCuO_2$ and Sr_2CuO_3, Co appears to have a distribution coefficient significantly smaller than 1[157]. The importance and the behaviour of this segregation or distribution coefficient in TSFZ process is reported in details elsewhere [158].

3.3.7 Variation of Co - concentration along the length of the grown crystal

In figure 3.14(a), we plotted χ as a function of Co-concentration at various temperatures by taking the values of χ for various Co concentrations from figure 3.13. The smooth curves in figure 3.14(a) were obtained by the polynomial fits of the data points. At low Co concentrations, the increase in χ with increasing Co concentration is almost linear; however, at higher Co-concentrations the increment became sub-linear. The curvature of the χ Vs. x plots is more pronounced at low temperatures and for crystal with higher Co - concentrations. This is because at higher concentrations, the probability of Co-clustering becomes higher. Antiferromagnetic interaction between the Co spins in the clusters will cause the magnetization to decrease below the extrapolated linear behaviour shown using the broken lines.

We used the smooth isotherms of figure 3.14(a), which gives susceptibility for any Co concentration and vice versa, to test the uniformity of Co-concentration along the

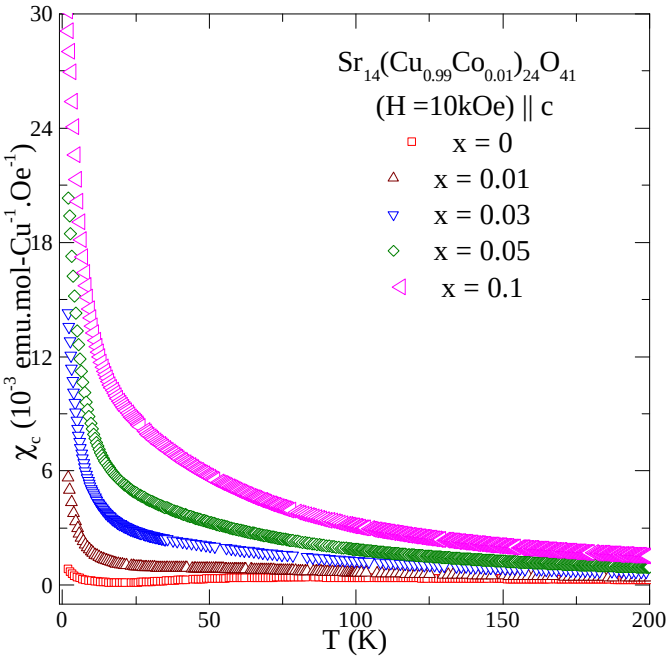

Figure 3.13: Magnetic susceptibility along the *c* - axis of the various Co doped $Sr_{14}Cu_{24}O_{41}$ crystals.

length of a crystal. For this purpose, a grown crystal containing nominal 10 % Co-concentration (# 8 in table 3.1) was cut along its length at 9 different places spanning the entire crystal boule length. The magnetizations of these crystal pieces were measured from 2 K to 300 K under 10 kOe magnetic field applied along the c-axis.figure 3.14(b) shows the susceptibility (y-axis) at various positions of the crystal boule (x-axis) at different temperatures. From these plots we see that at any given temperature (say 2 K), the susceptibility remains constant along the length of the crystal. The constant magnitude of susceptibility, at a given temperature, across the crystal length confirms the spatial uniformity of Co concentration over the entire length of the grown crystal. In a melt growth of doped crystals, uniformity of the dopant concentration along the crystal length is an important issue. The solute concentration in the grown crystal depends on the segregation or distribution coefficient (k) which is defined as the ratio of dopant concentration in the crystal to that in the melt. If the distribution coeeficient happens to be significantly less than 1, then the dopant concentration in the grown crystals increases gradually over a good length of the growing crystal before reaching the equlibrium value corresponding to the composition of the feed. From the data plotted in figure 3.14, the

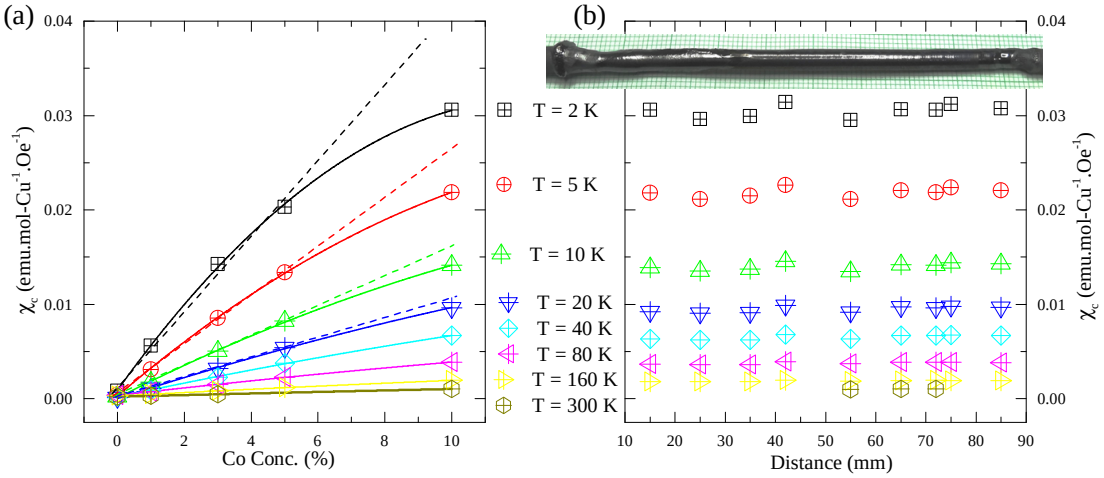

Figure 3.14: (a) c - axis magnetic susceptibility (χ_c) shown as a function of Co - concentration, (b) Susceptibility of a 10 % Co - doped crystal boule at various positions along its length (the origin being the starting point of the growth). The image of the crystal is shown as a reference for the positions measurements.

distribution coefficient of Co in the present case appears to be close to 1 in argument with the analysis of solidified TSFZ. This result is rather interesting because in the crystal growth of $SrCuO_2$ and Sr_2CuO_3, Co appears to have a distribution coefficient significantly smaller than 1 [147].

3.4 Single crystal growth of $HoFeO_3$

3.4.1 Synthesis of feed and seed rods

The seed and feed rods were prepared using the solid state reaction route. High purity Ho_2O_3 (99.9 %) and Fe_2O_3 (99.98 %) were used as the starting precursors. The precursors were weighted according to the stoichiometry mixed thoroughly and sintered from 1000° - 1400° C for 24 hours with intermediate grindings and taking powder XRDs (see figure 3.15). An impurity phase of Ho_2O_3 (marked as '$*$' in figure 3.15) was present in the starting reaction, whereas, this impurity is completely removed by increasing the sintering temperature above 1400° C. The cylindrical rods (feed and seed) were prepared under isostatic cold-pressing at 700 bar which were subsequently sintered at 1425° C for 24 hours to ensure the formation of dense rods.

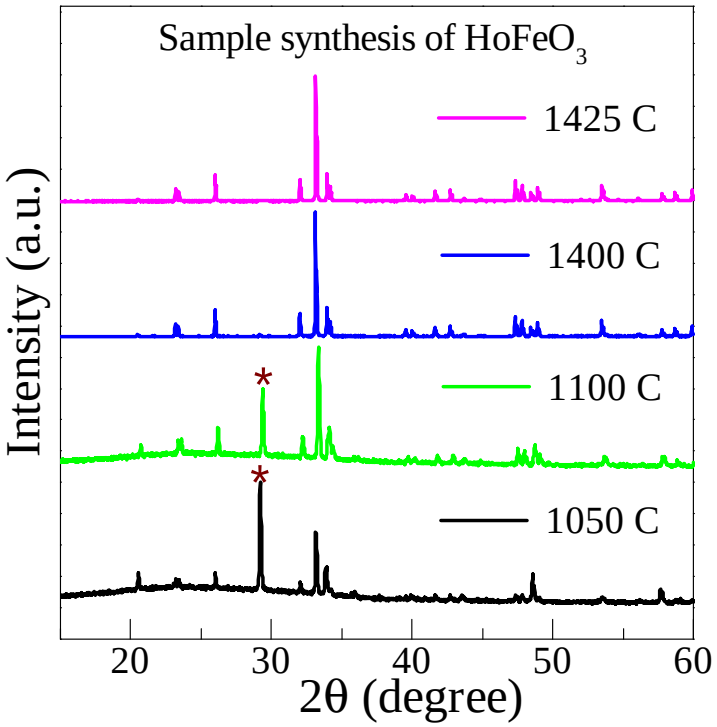

Figure 3.15: Powder XRD patterns of the polycrystalline $HoFeO_3$ after sintering at different temperatures; $*$ represents the presence of impurity phase Ho_2O_3.

The single crystals of $HoFeO_3$ (HFO) were grown in the four-mirror optical floating-zone furnace (Crystal System Corporation, Japan) under two different atmospheric environments; Air (HFO SC1) and Ar (HFO SC2) atmospheres. Being congruently melting, a higher growth speeds of around 5 mm / h were used to grow the crystals after forming a molten-zone simply by melting the lower end of the feed rod. The details of growth parameters are summarized in Table 3.6.

3.4.2 Single crystal growth

The images of the grown crystals (HFO SC1 and HFO SC2) are shown in figure 3.16. The shiny surfaces of the grown crystals are indicative of their high quality.

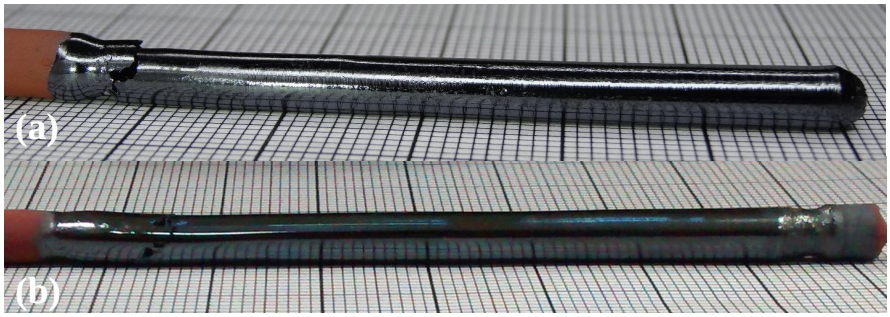

Figure 3.16: (a) Air grown (HFO SC1) (b) Ar grown (HFO SC2) crystals of $HoFeO_3$.

Table 3.6: growth parameters of crystal growth of $HoFeO_3$

Growth Parameters	**Air grown** (HFO SC1)	**Ar grown** (HFO SC2)
Feed movement speed (v_u)	4.5 mm / h	6 mm / h
Seed movement speed (v_l)	4.5 mm / h	5 mm / h
Feed rotation speed (ω_u)	20 rpm	20.1 rpm
Seed rotation speed (ω_l)	20 rpm	20.1 rpm
Lamp Power (150 W x 4)	63.2 %	56.7 %
Growth Length	50 mm	65 mm
Flow rate of gas	3 lit / min	1 lit / min

3.4.3 Characterization

3.4.3.1 Powder x-ray diffraction

The powder x-ray diffraction was carried out on the powders obtained by crushing a thin crystal section cut from the crystal boule. High temperature (HTXRD) was also carried out for investigating the phase stability at high temperatures.

In figure 3.17 (a), the PXRD pattern of both the grown crystals (HFO SC1 and HFO SC2) were shown in comparison with the standard JCPDS data (00-046-0115) and observed no extra peak which confirms the phase purity (*Pbnm* space group (62)) of the grown crystals. Similar measurements on an oriented single crystal specimen with *ac* - plane as the plane of diffraction is shown in figure 3.17 (b). As expected, only the (0 k 0) peaks, characterise of the [1 0 1] family of lattice planes, are observed. Although, it is a crude method but the presence of only (0 2 0) and (0 4 0) peaks suggests the high-quality of the crystal and the crystal orientation.

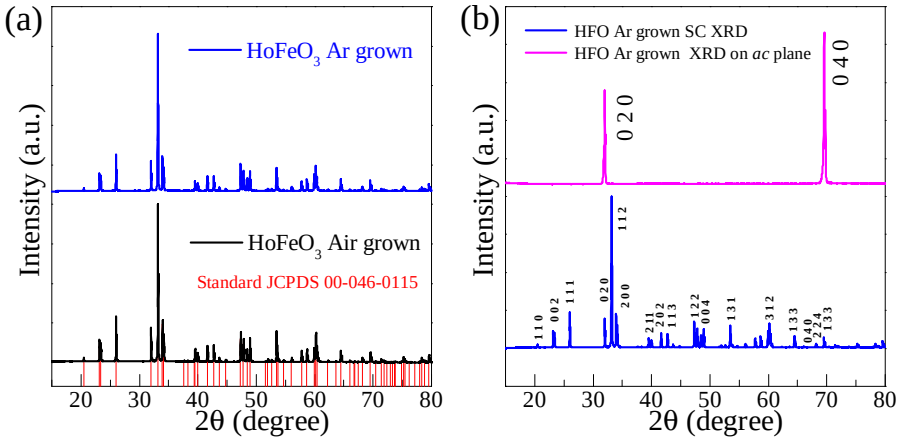

Figure 3.17: (a) XRD of Air (HFO SC1) and Ar (HFO SC2) grown single crystals. The standard data from JCPDS file are also shown. (b) Single crystal XRD from the *ac* - plane of HFO SC2.

To find out the crystal structure, a long XRD scan (10 - 12 hours) at room temperature is taken on the crystal powder. Rietveld refinement was performed with the orthorhombic unit cell (space group *Pbnm*) on the PXRD pattern. The obtained unit cell parameters are: a = 5.28092(6) Å, b = 5.59342(2) Å, c = 7.60677(1) Å, and χ^2 = 4.61. A representative refinement on the XRD data of HFO SC1 is shown in figure 3.18 (a); and the crystal structure obtained from the associated crystallographic information file (cif) is shown in figure 3.18 (b).

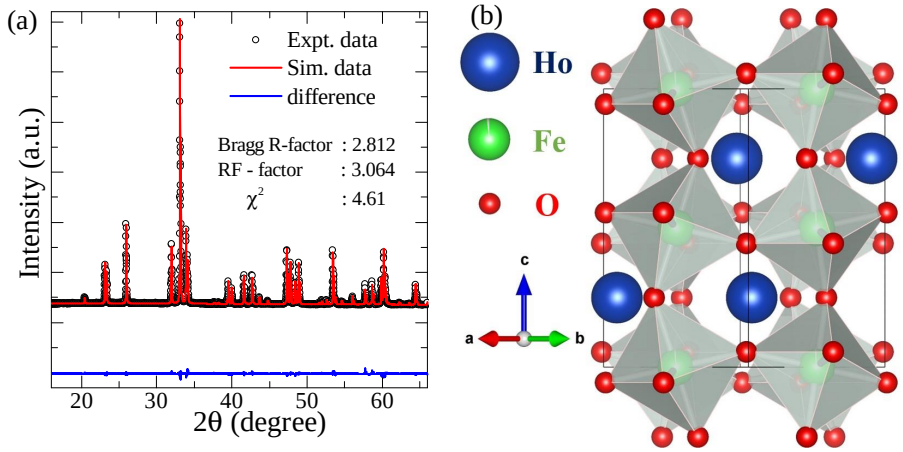

Figure 3.18: (a) Rietveld refinement on the XRD of HFO SC1 crystal. (b) Crystal structure is calculated from the crystallographic information file (cif) using VESTA software.

HTXRD: We carried out high temperature x-ray diffraction (HTXRD) on both the grown crystals in presence (or absence) of high vacuum. The HTXRD was carried out by mounting the sample in the form of fine powder on a platinum plate to get uniform heating. In the observed XRD pattern the strong peaks (denoted as #) are due to platinum (Pt) sample holder. The heating and cooling data upto 1020 K in air are shown in figure 3.19. No appearance of any extra peak (or any deconvolution of peak)

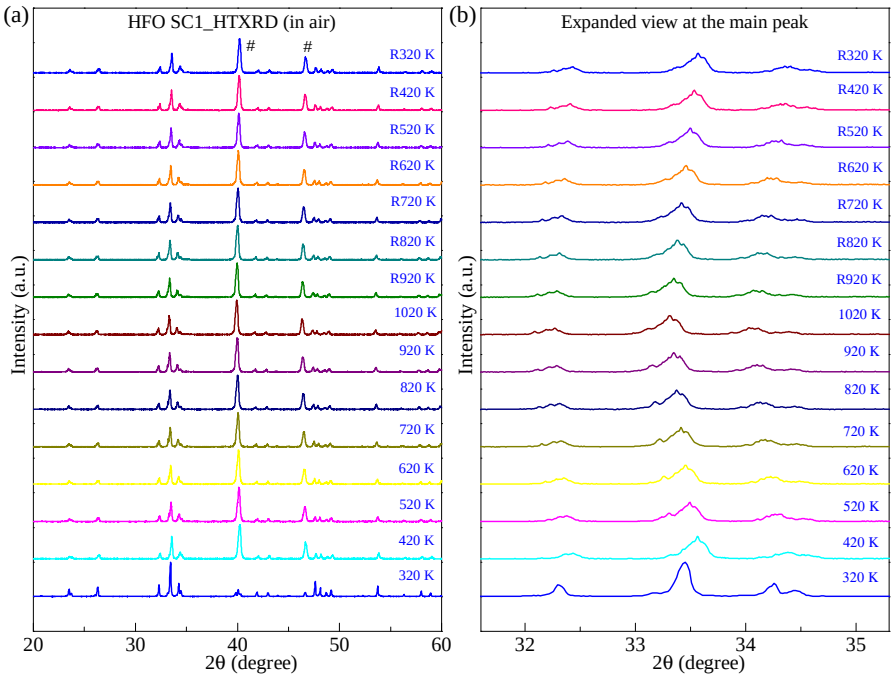

Figure 3.19: (a) HTXRD in air of HFO SC1 crystal. (b) Expanded view of (a); 'R' refers to reverse of heating (or cooling); '#' denotes the presence of platinum (Pt) peak

upto 1020 K in air (as shown in figure 3.19 (a)), suggests that the structure is very stable and remains *Pbnm* only. An expanded view around the main peaks ($2\theta \simeq 32 - 35$) is shown separately in figure 3.19 (b); a slight shifting towards lower angle suggests the expansion of the cell volume with increasing temperature. Upon cooling down to room temperature (denoted as 'R' for reverse direction, for cooling), the peak position returns to the same angle.

We also examined the stability of *Pbnm* phase by heating upto 1000 K under high vacuum and observed similar behaviour as during air-heating. The results are shown in figure 3.20, where only heating data are shown. In chapter 7, we have characterized

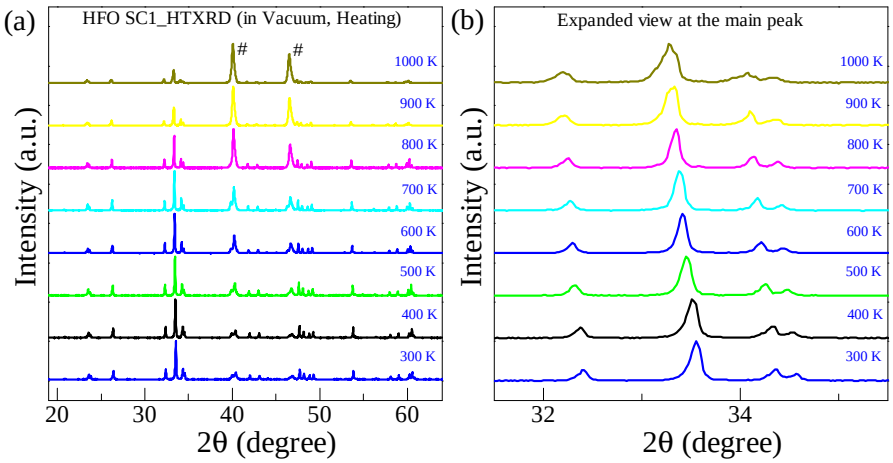

Figure 3.20: HTXRD patterns of HFO SC1 crystal while heating upto 1000 K under vacuum; '#' denotes the presence of platinum (Pt) peaks.

the high temperature magnetic behaviour by heating under vacuum. Therefore, it was necessary to know if these systems are structurally stable above room temperature under vacuum. A similar behaviour is also observed for the Ar-grown crystal, HFO SC2 (not shown here).

3.4.3.2 Laue diffractometer

The crystal were oriented using the Laue diffraction technique. Two representative Laue images, obtained from the cleaved surfaces of HFO (Air and Ar grown) crystals are shown in figure 3.21. The Laue spots are captured in the back reflection geometry

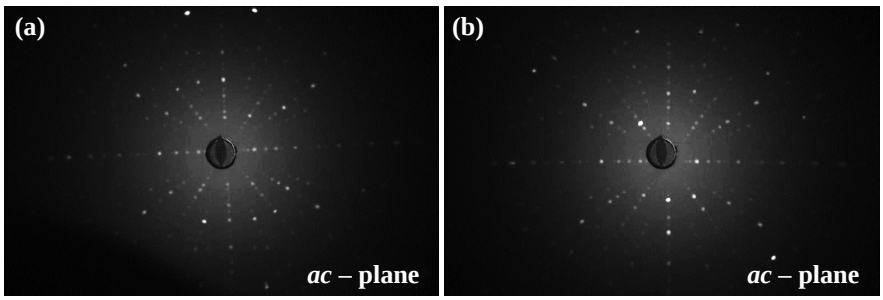

Figure 3.21: (a) Laue diffraction pattern of *ac*-crystallographic plane of HFO SC1 and (b) HFO SC2 crystals specimens.

and the four-fold symmetry clearly reveals that the cleaved surface is [1 0 1].

3.4.3.3 Scanning electron microscopy

Scanning electron microscope (SEM) is used for compositional analysis of the grown crystals. The crystal boule was cut at different lengths to obtain their slices that were polished and examined under both polarized and scanning electron microscopes. The

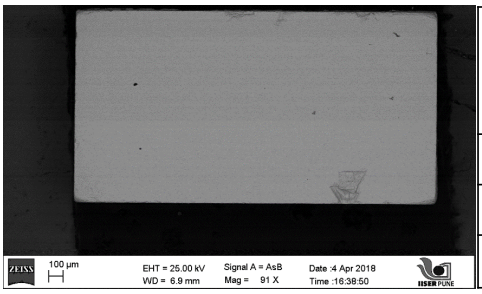

#	Ho (at. %)	Fe (at. %)	O (at. %)
1	13.80	13.88	72.32
2	13.89	13.86	72.26
3	13.93	14.52	71.55

Figure 3.22: (left panel) The scanning electron microscopy ('AsB' back scattered) image of a polished *ac* - plane of HFO SC2 crystal; (right panel) the compositional analysis using EDS is shown in atomic percentage (Ho : Fe = 1 : 1).

polished surface was subjected to compositional analysis using EDX. A representative SEM image is shown in figure 3.22, where the compositions measured at three different regions is also shown. The EDX composition suggests that the grown crystals are highly homogeneous with Ho and Fe ratio equal to the expected value of 1 : 1 within the error limits of the EDX technique.

3.5 Summary

In summary, we have successfully grown large and high-quality single crystals of incongruently melting compound $Sr_{14}Cu_{24}O_{41}$, doped with Co, Zn, Ni and Al at the Cu-site using the TSFZ method, and the congruently melting compound $HoFeO_3$ using the FZ technique. The compositions of the crystals grown and reported in this present work are: $Sr_{14}(Cu_{1-x}Co_x)_{24}O_{41}$ where x = 0, 0.01, 0.03, 0.05 and 0.1; $Sr_{14}(Cu_{1-y}Zn_y)_{24}O_{41}$ where y = 0.0025, 0.01; $Sr_{14}(Cu_{1-z}Ni_z)_{24}O_{41}$ where z = 0.0025 and 0.01 and $Sr_{14}(Cu_{1-a}Al_a)_{24}O_{41}$ where a = 0.0025 and 0.01. We characterized these crystals by optical microscopy under polarized light, scanning electron microscopy, powder x-ray diffraction and magnetization experiments. We show that the crystals of high-quality with well-developed facets

could only be grown under high oxygen pressure. 3 bar oxygen pressure is found to be sufficient for doping Co, Ni, Zn and Al in $Sr_{14}Cu_{24}O_{41}$, at least upto the concentrations tried in the present work. The magnetic susceptibility of Co-doped crystals was measured along the crystallographic *c*-axis. We showed that the *c*-axis susceptibility scales with Co-concentration. The scaling is found to be linear at low Co-concentrations but becomes sublinear at low temperatures and high doping concentration (> 5 %), suggesting a possible clustering of the Co-ions. From the plot of χ_C as a function of Co-concentration, we show that the doping level remains uniform across the entire crystal boule length. The composition uniformity of a 10 % Co-doped crystal was also confirmed by performing EDX analysis on centimeter size longitudinal-section. In crystals with low dopant concentration (< 1 atomic %), the uniformity is inferred from SEM/EDX investigation of the solidified floating zone, where no signs of dopant accumulation could be found. Similarly, HFO crystals were found to be of high-quality. HTXRD measurements revealed that the perovskite structure of HFO remains stable up to temperatures as high as 1020 K in air as well as under high vacuum. Using EDX analysis, Ho to Fe ratio in these crystals is found to be 1:1 within the error limit of the EDX technique.

3.6 Appendix

During the course of this thesis, we grew several congruently melting compounds that are not included in this thesis These include the maganites ($Gd_{0.5}Dy_{0.5}MnO_3$, grown in collaboration), Titanates ($MTiO_3$; M = Ni and Co, grown in collaboration). In figure 3.23(a), we show some representative images of the as-grown single crystals of $Gd_{0.5}Dy_{0.5}MnO_3$, $CoTiO_3$ and $NiTiO_3$. Since these compounds are not directly related to the main topic of my thesis, we have not included here the details of their growth process.

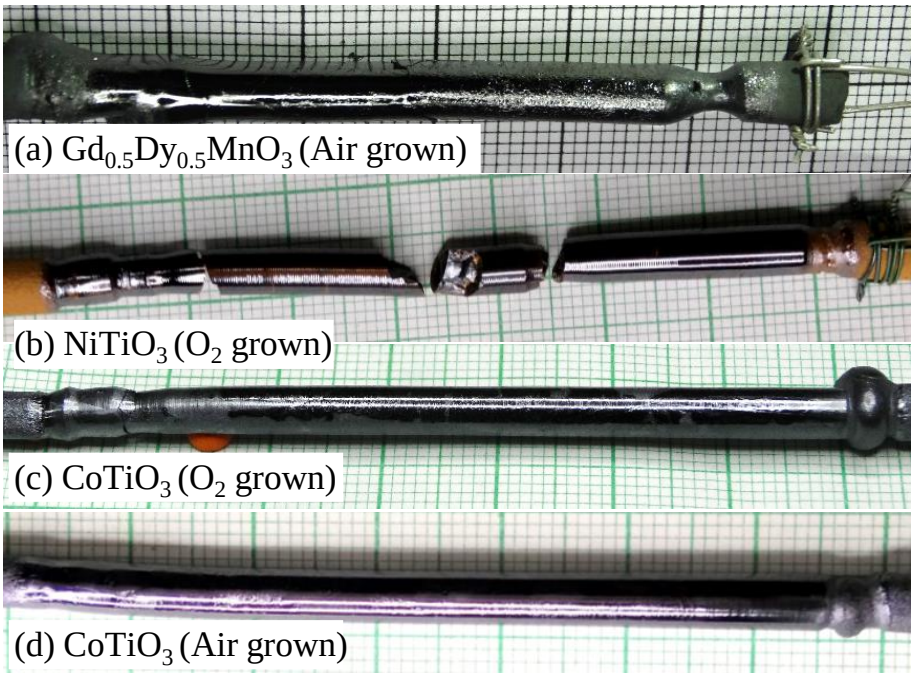

Figure 3.23: Representative images of some congruently melting oxides grown during this thesis.

Chapter 4

Effect of Zn, Ni and Al impurities on the magnetic ground state of composite chain-ladder quantum magnet $Sr_{14}Cu_{24}O_{41}$

4.1 Introduction

Impurities in spin 1/2 chains and ladders can have profound effects on their spin excitations and ground state properties [5, 159]. Recently, a number of studies have focused on this issue and shown that interesting and rather unexpected properties emerge in the presence of dilute impurities. It has been shown, for instance, that less than 1 % of Zn or Ni impurities can open a sizable gap in the spin excitation spectrum of spin chain systems $SrCuO_2$ and Sr_2CuO_3 [8, 9, 43, 160]; a Co impurity, on the other hand, leaves the excitations gapless but induces a strong Ising-like anisotropy, and a long-range magnetically ordered ground state [9]. In the 2-leg ladder cuprate $SrCu_2O_3$, less than 5 % of Zn impurity closes the spin-gap and induces a bulk antiferromagnetic ordering of the Cu spins[161]. In the spin chain compound $CuGeO_3$, which undergoes a spin-Peierls transition upon cooling below T = 15 K [162], the impurities were shown to suppress the Peierls transition and replace it by a long-range antiferromagnetic ordering [163, 164].

In this chapter, we will discuss the effect of Zn, Al and Ni impurities doped at the Cu site in $Sr_{14}Cu_{24}O_{41}$. We first show that at low temperatures, T $\lesssim$ 5 K, the "free" spins in the chains indeed undergo a long-distance dimerization as proposed previously [57]. We then study the effect of impurities on the two types of dimers in the chains, namely, the dimers that nucleate at relatively higher temperature (T $\lesssim$ 100 K), and the long-distance dimers that emerge at low-temperatures (T $\lesssim$ 5 K). We probe the effect of Ni impurity on the long-distance dimers by measuring the specific heat down to a temperature of T = 0.06 K.

The chapter has been organized as follows: in section 4.2 we provide the experimental details including the crystal growth and doping concentrations in the grown crystals. In the results and discussion section 4.3, we first present our analysis of the susceptibility data for the undoped sample $Sr_{14}Cu_{24}O_{41}$ in 4.3.1. The results for Zn, Ni and Al impurities at the Cu site are gathered in the section 4.4 under 4.4.1 for Zn, 4.4.2 for Ni and 4.4.3 for Al. The low temperature specific heat for undoped and Ni doped crystal are discussed in section 4.4.4 and finally we summarized our findings in the section 4.5.

4.2 Growth and doping concentration

4.2.1 Crystal growth and characterization

Single-crystals of $Sr_{14}Cu_{24}O_{41}$, and its doped variants $Sr_{14}(Cu_{1-x}M_x)_{24}O_{41}$ (M = Zn, x = 0.0025, 0.01; M = Al, x =0.0025, 0.01; M = Ni, x = 0.0025 and 0.01; and M = Co, x = 0.01, 0.03, 0.05 and 0.1) were grown using a four-mirror optical floating-zone furnace (Crystal System Corporation, Japan) by the Traveling-Solvent Floating-Zone (TSFZ) method. Details of the crystal growth and structural characterizations can be found in chapter 3. Crystals were oriented using the x-ray Laue diffraction technique (Photonics Science, UK). Magnetic measurements were carried out in the temperature range for 2 to 300 K, and by applying fields up to ±8 Tesla using the vibrating sample magnetometer (VSM) probe in a Physical Property Measurements System (PPMS).

Table 4.1: Doping concentration (x_M) of the grown crystals were characterized by using ICP-AES

Sample	Sr (/f.u.)	Cu (/f.u.)	Dopant (M / f.u.)	Nominal (M in %)	Actual (x_M in %)
$Sr_{14}(Cu_{0.9975}Zn_{0.0025})_{24}O_{41}$	14	23.6	0.112	0.25	0.47
$Sr_{14}(Cu_{0.99}Zn_{0.01})_{24}O_{41}$	14	25.9	0.217	1.00	0.08
$Sr_{14}(Cu_{0.9975}Al_{0.0025})_{24}O_{41}$	14	26.2	0.024	0.25	0.09
$Sr_{14}(Cu_{0.99}Al_{0.01})_{24}O_{41}$	14	26.6	0.061	1.00	0.23
$Sr_{14}(Cu_{0.9975}Ni_{0.0025})_{24}O_{41}$	14	25.5	0.080	0.25	0.31
$Sr_{14}(Cu_{0.99}Ni_{0.01})_{24}O_{41}$	14	25.7	0.267	1.00	1.02

Some of the magnetic measurements were also carried out using the SQUID magnetometer in a Magnetic Property Measurement System (MPMS), Quantum Design, USA (maximum field limit ±7 Tesla). Low-temperature specific heat (0.06 K < T < 2 K) was measured at the Tata Institute of Fundamental Research (TIFR) Mumbai in a dilution refrigerator, Quantum Design, USA. X-ray Photoelectron Spectroscopy (XPS) experiments were carried out at the synchrotron INDUS beamline BL-2 AIPES, Indore, India.

Inductively Coupled Plasma- Atomic Emission Spectroscopy (ICP-AES) is used to determine the actual dopant concentration in the 1% Zn, Ni and Al doped crystals. The results are tabulated in table 4.1. For the Ni doped crystals, the concentration determined using ICP agreed nicely with the nominal value. But in the case of Zn, the actual Zn concentration is found to be 0.008 ± 0.001/Cu; and for the Al-doped crystal this was around 0.0025 ± 0.001/Cu, indicating a very limited solid-solubility of Al in the crystals grown using the floating-zone method. The actual concentration is designated as x_M, where M = Zn, Ni and Al. Because of low doping levels there is no straight forward method of checking whether the doped impurities are substitutional or interstitial. Based on the comparable ionic radii of Zn^{2+}, Ni^{2+} and Cu^{2+}, we expect these impurities to substitute Cu in the structure. However, the same logic cannot be extended to the case of Al^{3+} since it is smaller in size and is a p-block element. In a previous study, on polycrystalline Al substituted $Sr_{14}Cu_{24}O_{41}$ sample, it was argued based on the lattice parameter variation that Al substitute Cu in the structure [100].

4.3 Undoped $Sr_{14}Cu_{24}O_{41}$

4.3.1 Magnetic susceptibility

The magnetic susceptibility χ(T) of $Sr_{14}Cu_{24}O_{41}$ along the crystallographic *a*, *b* and *c*-axis is shown in figure 4.1. It is evident from these plots that the magnetic behavior of $Sr_{14}Cu_{24}O_{41}$ is nearly isotropic. The small anisotropy between the in-plane and out-of-plane susceptibility, i.e., $\chi_a = \chi_c \lesssim \chi_b$ (here the subscript represents the crystallographic axis) is due to a slight anisotropy of the Landé g-factor as reported previously [165]. Below room-temperature, χ(T) of $Sr_{14}Cu_{24}O_{41}$ consists of a broad maximum near T_{max} = 80 K, followed by a sharp upturn below T_{min} = 20 K. Since the ladders in $Sr_{14}Cu_{24}O_{41}$ have a singlet ground state with a fairly large energy gap (Δ_l > 500 K) [166, 167], the magnetic behavior over the temperature range shown in figure 4.1 can be attributed mainly to the chain sublattice [165].

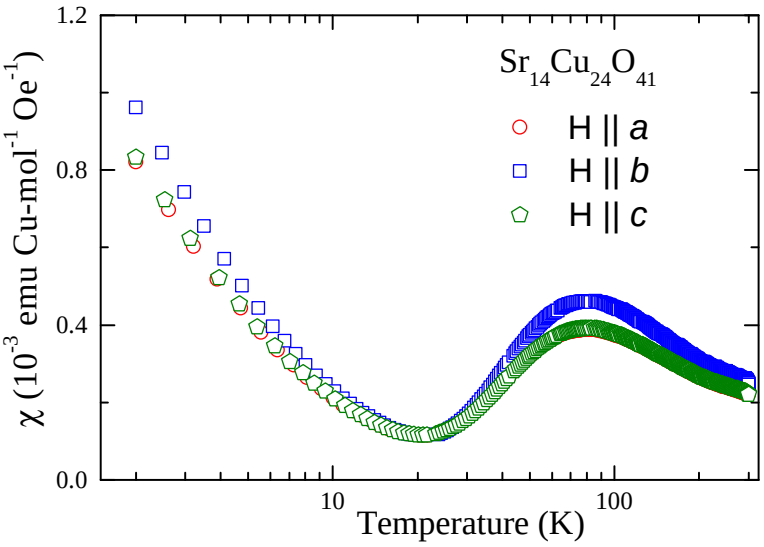

Figure 4.1: Temperature variation of susceptibility of a pristine $Sr_{14}Cu_{24}O_{41}$ single crystal along the crystallographic *a*, *b* and *c*-axis

$Sr_{14}Cu_{24}O_{41}$ is self-doped with six holes per formula unit (f.u.). A majority of these holes reside over the chain sublattice [168]. In the chain, the hole antialigns its spin to that of a native Cu^{2+} spin to form what is called the Zhang-Rice (ZR) singlet [169]. Thus, out of the 10 Cu sites per formula unit (f.u.) in the chain[67], 6 will be occupied by the ZR singlets and remaining 4 by S = 1/2 Cu^{2+} ions. The ground state of a chain

is proposed to have an arrangement as follows: $\cdots \circ \circ[\uparrow \bullet \downarrow] \circ \circ[\downarrow \bullet \uparrow] \circ \circ \ldots$, where the symbols $\bullet$ and $\circ$ represent, respectively, the intra- and interdimer ZR singlets in the chain, and $[\uparrow \bullet \downarrow]$ is a spin dimer in which the spins couple antiferromagnetically via the ZR singlet $\bullet$. Henceforth, we shall refer to the dimer $[\uparrow \bullet \downarrow]$ in the chain as a Zhang-Rice dimer (ZRD). This configuration of spins and dimers is, however, valid only if all 6 holes reside over the chain sublattice. However, in a real crystal due to small fraction of hole transfer from chains to ladders, some spins in the chains remain undimerized; these are referred to as the "free" spins.

We now return to understand various features observed in figure 4.1. The susceptibility maximum (χ_{max}) near T = 80 K is due to the nucleation of ZRD's, and the upturn below T_{min} = 20 K is typically attributed to the "free" spins. Our data are in fairly good agreement with previous single crystal reports [50, 80, 165]. Only at low-temperatures the value of χ is slightly different. For example, the value of χ_c near T_{min} = 20 K is $0.4 \times 10^{-3} \mu_B$/Cu for the single crystal used in Ref. [165], which is almost twice the value for our crystal at the same temperature. This difference is most likely related to the purity of starting precursors as discussed later [59].

In previous studies, the magnetic susceptibility of $Sr_{14}Cu_{24}O_{41}$ at low temperatures has been described using an antiferromagnetic (AFM) spin-dimer model [50, 59, 67, 80, 165, 170]:

$$\chi = \chi_0 + \chi_C + \chi_{dimer} \tag{4.1}$$

In this equation, χ_0 represents the temperature independent contribution due to core-diamagnetism and van-Vleck paramagnetism. The second term $\chi_C = C/(T - \theta_p)$ is the Curie-Weiss susceptibility due to the "free" spins. Here, the Curie constant is given by $C = N_A N_S g^2 \mu_B^2 S(S+1)/3k_B T$; where S is the spin quantum number, N_s is the number of free spins, N_A is the Avogadro number, g is the Landé factor, μ_B is the Bohr magneton, and k_B is the Boltzmann constant. The last term in the above equation represents the dimer susceptibility, χ_{dimer}, given by:

$$\chi_{dimer} = \frac{2N_d^{ZR} N_A g^2 \mu_B^2}{k_B T(3 + e^{-\frac{J_{ZR}}{k_B T}})} \tag{4.2}$$

where N_d^{ZR} is the number of ZRDs per f.u., and J_{ZR} is the intradimer exchange via the ZR singlet. The high temperatures data (T > 200 K) can also be included by including an extra describing the ladder susceptibility term in eq.4.1. Since the ground state of the ladders is a spin singlet, χ_{ladder} can be represented as $Ae^{-\Delta_l/k_BT}/\sqrt{T}$.

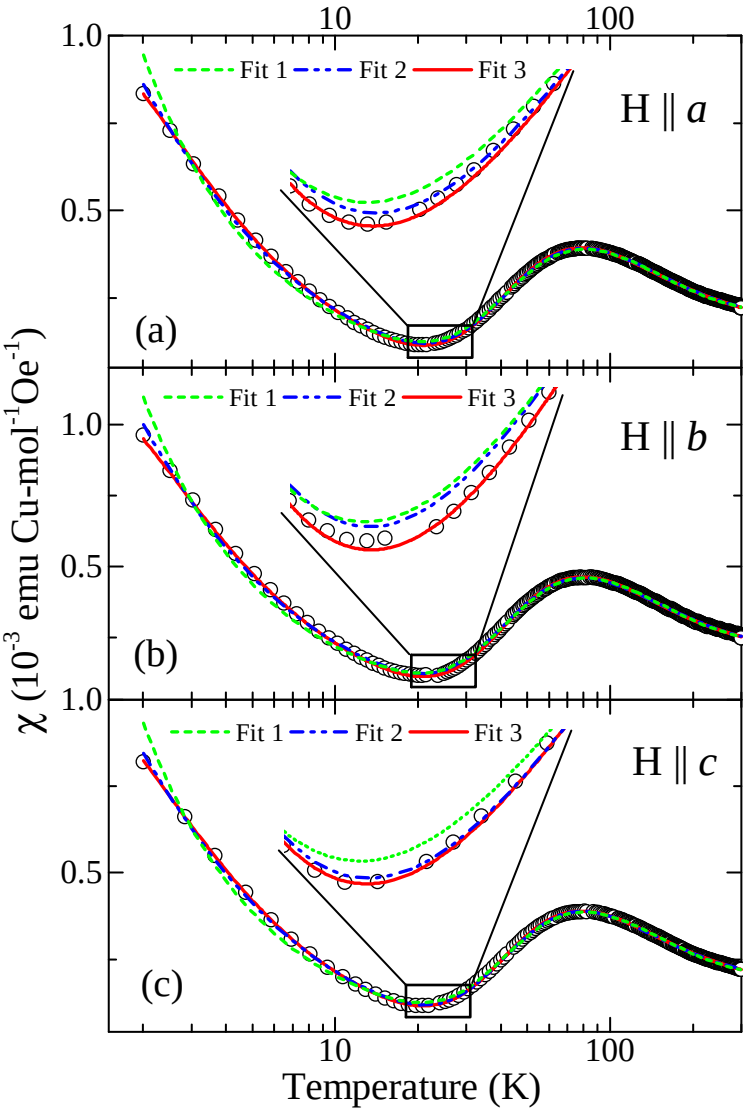

Figure 4.2: Temperature dependent magnetic susceptibility of pristine $Sr_{14}Cu_{24}O_{41}$ single crystal is shown as a function of temperature along three crystallographic axis. Fit 1, Fit 2 and Fit 3 refers to the three different fitting models (see text for details). Insets show the quality of fit at the low temperature region.

We fitted our susceptibility data along the three crystallographic orientations using equation 4.1, first by fixing $\theta_p = 0$ (this is called Fit 1); and then by varying θ_p (this is

called Fit 2). The value of g-factor in these fittings is kept fixed to 2.05 (a-axis and c-axis), and 2.25 (b-axis) based on a previous ESR study[171]. All other parameters were varied and their best-fit values are listed in Table 4.2. The results of similar analysis from previous studies on various polycrystalline and single-crystalline samples are also included in Table 4.2 for comparison. Consistent with previous works, our χ_0 values are two orders of magnitude smaller than the experimental χ. Being very small, sign of χ_0 does not affect the values of parameters in the dimer term. The value of J_{ZR} = 134 ± 2 K is in a fairly good agreement with previous single crystal reports. The value of N_d^{ZR} = 0.079 ± 0.002/Cu for Fit 2, and 0.075 ± 0.002/Cu for Fit 1. These values are slightly higher than those previously reported but do not overshoot the upper bound of N_d^{ZR} = 2/f.u. = 0.083/Cu. Finally, N_s for our crystal is smaller than the values previously reported, which in the polycrystalline sample [67] is almost 4 times the values found here for high-purity single crystals. The sum $N_s + 2N_d^{ZR}$, which should be 4 in the ideal case when all the holes are localized on the chain sublattice, varies from 3.61/f.u. to 3.79/f.u. for Fit 1 and it is ∼3.97/f.u. for Fit 2.

The quality of Fit 1 and Fit 2 can be judged from Fig. 4.2. Since $\chi_a = \chi_c$, data along the a-axis are not shown. Quite generally, we found that both the fits reproduce the qualitative behavior of $\chi(T)$ reasonably well, however, at low-temperatures both these fits are not satisfactory. For instance, Fit 1 is clearly not satisfactory below T = 5 K and deviates from the measured data near χ_{min}. On the other hand, while Fit 2 is more acceptable at low temperatures, it deviates from the measured data marginally around χ_{min}, as shown in the insets of figure 4.2. Moreover, in the absence of any magnetic ordering down to at least 60 mK [57], $\theta_p \sim 1$ to 2 K obtained in Fit 2 is difficult to explain. The failure of these fits suggest that the ground state of chains is more complex. Sahling et al. [57] suggested that at low-temperatures the "free" spins are quantum entangled; i.e., they form spin dimers over large-distances via an AFM interaction mediated via the intervening singlets in the chain. We shall denote the exchange between these dimers by J_{LD}, where the subscript LD refers to the long-distances between the pairing spins. The long distance dimers are designated as [↑ . . . ↓], where . . . represent the intervening sites. We, therefore, fitted the measured χ by

Table 4.2: Values of the various fitting parameters obtained by analyzing the susceptibility of a pristine $Sr_{14}Cu_{24}O_{41}$ single crystal specimen using the Fit 1 and Fit 2 (see text for details). Corresponding values from the previous reports in the literature are also included

Reports	Specimen type	χ_0 (10^{-5})	N_s (10^{-3}/Cu)	θ_p (K)	N_d^{ZR} (10^{-2}/Cu)	$N_s+2N_d^{ZR}$ (1/f.u.)	J_{ZR} (K)	g
Carter et al.[67]	Polycrystal	-	22.9	0.25	6.1	3.49	139	2.17
Klingler et al. [165]	H $\parallel c$	1.0	10.0	-	7.4	3.78	134	2.04
Matsuda et al.[50]	H $\parallel c$	0.5	15.4	-1.7	-	-	133	2.04
	H $\parallel b$	-	18.3	-1.7	-	-	-	2.26
	H $\parallel a$	-	15.8	-1.7	-	-	-	2.05
Hiroi et al.[59]	Polycrystal	4.4	6.6	0.2	6.7	3.4	131	2.2
Fit 1	H $\parallel c$	1.9	4.7(2)	NU	7.3(2)	3.61	134(2)	2.05
	H $\parallel b$	-2.7	4.6(2)	NU	7.7(2)	3.79	135(2)	2.25
	H $\parallel a$	1.7	4.7(2)	NU	7.4(2)	3.65	134(2)	2.05
Fit 2	H $\parallel c$	-2.2	6.6(2)	-1	7.9(2)	3.95	133(2)	2.05
	H $\parallel b$	-3.6	6.1(2)	-0.8	8.0(2)	3.98	133(2)	2.25
	H $\parallel a$	-1.6	6.4(2)	-0.9	7.9(2)	3.97	134(2)	2.05

Unit of χ_0 is emu Cu-mol^{-1}Oe^{-1}; The g value is fixed from the previous literature; NU refers to parameter not used in the fitting

Table 4.3: Fitting parameters obtained from an analysis of the susceptibility of undoped $Sr_{14}Cu_{24}O_{41}$ using the Fit 3 (see text for deatils)

Fit 3	χ_0 (10^{-5})	N_s (10^{-3}/Cu)	N_d^{ZR} (10^{-2}/Cu)	J_{ZR} (K)	N_d^{LD} (10^{-2}/Cu)	J_{LD} (K)	g
H ∥ c	-2.4	2.8(2)	7.9(2)	132(2)	0.17(5)	4(1)	2.05
H ∥ b	-5.4	2.5(2)	8.0(2)	133(2)	0.17(5)	4(1)	2.25
H ∥ a	-2.7	2.5(2)	8.0(2)	132(2)	0.17(5)	4(1)	2.05

χ_0 is in emu Cu-mol^{-1}Oe^{-1} unit; g-factor is kept fixed during the fitting, N_s is obtained from Curie constant C for spin 1/2

including an extra dimer term in eq.4.1 to account for the long-distance dimer (LDD), and by setting θ_p to zero, which is not required in this model. The modified equation for χ is now given by:

$$\chi = \chi_0 + \frac{C}{T} + \frac{2N_A g^2 \mu_B^2}{k_B T} \sum_i \frac{N_{d_i}}{(3 + e^{-\frac{J_i}{k_B T}})} \tag{4.3}$$

Here, N_{d1} is N_d^{ZR} and J_1 is J_{ZR}; and, N_{d2} and J_2 are corresponding parameters for the long distance dimers, where $N_{d2} = N_d^{LD}$ and $J_2 = J_{LD}$. The fitting done using equation 4.3 is called the Fit 3.

The results of Fit 3 are also included in figure 4.2. We found that the Fit 3 represents the experimental data more accurately than Fit 1 or Fit 2. The fitting parameters in Fit 3 are listed in table 4.7. The values of J_{ZR} and N_d^{ZR} are nearly the same as obtained earlier using the Fit 2. N_s has slightly decreased, which is understandable since some of the free spins have dimerized at low-temperatures. The value of J_{LD} is $\sim 4\pm2$ K and that of N_d^{LD} is ~ 0.0017/Cu. From these numbers we can estimate the quantity $N_S + 2N_d^{ZR} + 2N_d^{LD}$, which gives the effective number of spins 1/2 in the chain sublattice as 0.162/Cu = 3.88/f.u. $\approx$ 4/f.u. This value being not exactly equal to 4 suggests that a small fraction of holes resides over the ladder sublattice.

Table 4.4: M(H) of Pristine at T = 2.5 K under 80 kOe for H ∥ *c*

Present work	30 emu/Cu-mol
Kilingler et al. [165]	54 emu/Cu-mol
Matsuda et al. [50]	46 emu/Cu-mol

4.3.2 Isothermal magnetization

We now turn our attention to the isothermal magnetization of the pristine crystal measured at different temperatures. First, we will show the magnetization of the pristine $Sr_{14}Cu_{24}O_{41}$ at T = 2 K along three principal axes, in applied magnetic field upto H = 8 T. Then we will also discuss the magnetization at higher temperature along three crystallographic directions. The magnetization under highest applied magnetic field (H = 8 T) almost saturates to a value close to $5.5 \times 10^{-3} \mu_B$/Cu, where the previous reports are compared in Table.4.4.

4.3.2.1 Low temperature magnetization (T = 2 K)

To show further the poor applicability of Curie- or Curie Weiss law alone near T = 2 K, we first analyzed the T = 2 K isothermal magnetization of $Sr_{14}Cu_{24}O_{41}$ using the spin 1/2 Brillouin function with N_s as a free parameter as in eq. 4.4:

$$M(H) = \chi_0 H + N_s N_A g \mu_B B_{\frac{1}{2}}(y) \tag{4.4}$$

where, H is the applied field and S = 1/2; $y = g\mu_B HS/k_B T$ and $B_{\frac{1}{2}}(y)$ is the spin 1/2 Brillouin function. In this equation, a small contribution from χ_0 is also included in the first term. Since the contribution of ZRDs will be negligible at T = 2 K, eq. 4.4 should fit the 2 K isotherm if the "free" spins are not dimerized or magnetically ordered.

The results are shown in figure 4.3. The fitted curve (blue line of figure 4.3) deviates from the measured data over the whole range for both field orientations. The deviations are not very large but they are significant enough to suggest that eq. 4.4 is not sufficient to fit the M(H) data at 2 K satisfactorily, corroborating the need for considering an additional term to account for the weak AFM interaction between the 'free' spins.

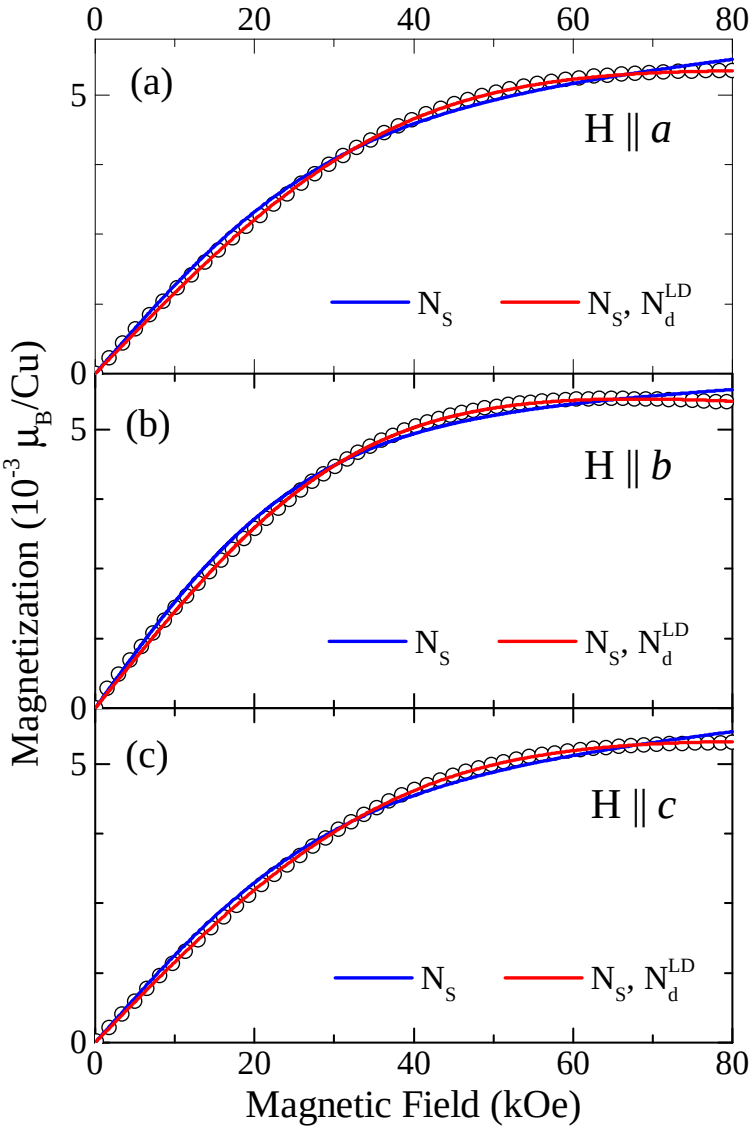

Figure 4.3: Isothermal magnetization at T = 2 K of pristine $Sr_{14}Cu_{24}O_{41}$ single crystal is shown as a function of applied magnetic field along three crystallographic axis. Blue and red lines are fit to the data correspond to the free spin contribution and dimer contribution along with the free spins, respectively (see text for details).

Therefore, a term accounting for LDDs is incorporated in eq. 4.4, and, an excellent fit to the data is obtained for all the field orientations as shown in figure 4.3.

For an antiferromagnetic spin dimers, the spin-gap, Δ, is a separation between the singlet (S = 0) and the excited triplet state (S = 1). For an isotropic spin-triplets, with applied magnetic field H, $\Delta_{1,-1}$ (H) = $\Delta_0 \pm \frac{g\mu_B H}{K_B T}$ and Δ_0 = Δ (0); The partition function for the spin-dimer can be written as,

$$Z(H,T) = 1 + e^{-\Delta_0 \beta}\left(1 + 2cosh\left(\frac{g\mu_B H}{K_B T}\right)\right) \tag{4.5}$$

and thus the magnetization M (dimer) is given by,

$$M(dimer) = \left(\frac{\delta F}{\delta H}\right)_T = 2N_d N_A g\mu_B \frac{\sinh\left(\frac{g\mu_B H}{K_B T}\right)}{1 + e^{-\frac{J}{K_B T}} + 2\cosh\left(\frac{g\mu_B H}{K_B T}\right)} \tag{4.6}$$

where, F = NK_BT lnZ(H, T), free energy;

Thus, the modified equation can be expressed as:

$$M_{Total}(H) = \chi_0 H + N_s N_A g\mu_B B_{\frac{1}{2}}(y) + 2N_{di} N_A g\mu_B \frac{\sinh\left(\frac{g\mu_B H}{K_B T}\right)}{1 + e^{-\frac{J_i}{K_B T}} + 2\cosh\left(\frac{g\mu_B H}{K_B T}\right)} \tag{4.7}$$

In the figure 4.3, the red line is the fitted line coming from the eq. 4.7, where, $N_{d2} = N_d^{LD}$ and $J_2 = J_{LD}$. At temperatures higher than 10 K, the ZRDs gain importance while the contribution of LDDs become very small. The fitting parameters are tabulated in table 4.5. M(H) fitting for higher temperatures is discussed in the next section with considering the high temperature ZRD dimer term; where, $N_{d1} = N_d^{ZR}$ and $J_1 = J_{ZR}$ in the eq. 4.7.

4.3.2.2 High temperature magnetization (T > 10 K)

The isothermal magnetization M(H) above 10 K along three crystallohraphic directions along with the fitted lines are shown in figure 4.4. Above 10 K, the number of free spins increases and the high temperature dimer contribution (*ZRD*) also becomes significant.

Table 4.5: Fitting parameters of isothermal magnetization (T = 2 K) parallel to chain/ladder of pristine crystal $Sr_{14}Cu_{24}O_{41}$

Specimen	Fitting Eq.	χ_0	N_S (/f.u.)	N_{d2}(/f.u.)	J_{LD} (K_B)
H ∥ *c*	Brillouin fit.	8.81 x 10^{-5} (v)	0.10 (v)	–	–
	Dimer fit.	-2.47 x 10^{-5} (f)	0.06(f)	0.03 (v)	3.04 (v)
H ∥ *b*	Brillouin fit.	-2.68 x 10^{-6} (v)	0.12 (v)	–	–
	Dimer fit.	-5.46 x 10^{-5} (f)	0.06(f)	0.04 (v)	2.07 (v)
H ∥ *a*	Brillouin fit.	8.81 x 10^{-5} (v)	0.10 (v)	–	–
	Dimer fit.	-2.74 x 10^{-5} (f)	0.06(f)	0.04 (v)	2.74 (v)

'f' stands for fixed value from MT; 'v' stands for variable parameter in MH.

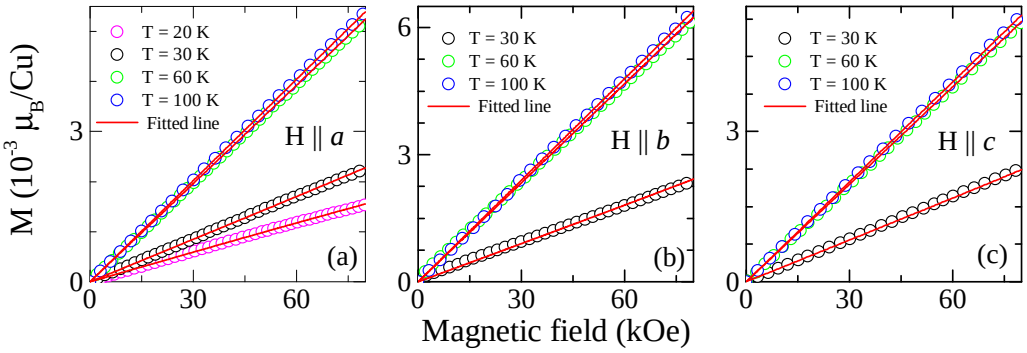

Figure 4.4: Isothermal magnetization of pristine $Sr_{14}Cu_{24}O_{41}$ at various temperature is shown as a function of applied magnetic field along three crystallographic axis. The data are fitted using the free spins Brillouin contribution.

In these fitting, the parameters N_d^{ZR} and J_{ZR} were fixed to their values obtained from the susceptibility ($\chi(T)$) analysis. The number of free spin parameter (N_S) is treated as a free parameter. The best-fit values of (N_S) along the three crystallographic axes for various temperatures are tabulated in the table 4.6.

Table 4.6: The value of fitting parameter N_S (number of free spins per Cu) using the Brillouin function for the pristine $Sr_{14}Cu_{24}O_{41}$ above 10 K.

Temperature	H ∥ *a*	H ∥ *b*	H ∥ *c*
T = 20 K	0.0063 (2)	–	–
T = 30 K	0.0068 (2)	0.007(1)	0.0063(2)
T = 60 K	0.0072 (2)	0.010(1)	0.0065(2)
T = 100 K	0.0085 (2)	0.013(1)	0.0069(2)

4.4 Effect of impurities in $Sr_{14}(Cu,M)_{24}O_{41}$; M = Zn, Al and Ni

We now present the effect of doping Zn, Ni and Al impurities on the magnetic behavior of $Sr_{14}Cu_{24}O_{41}$. For the convenience of our reader, we recollect here the various symbols that we will be using extensively in the subsequent sections: $\uparrow$ or $\downarrow$ for a Cu^{2+} spin 1/2; $\Uparrow$ for a Ni^{2+} spin 1; $\circ$ is for an inetrdimer ZR singlet; $\bullet$ is for an intradimer ZR singlet; $[\uparrow \bullet \downarrow]$ represents a ZR dimer (ZRD), and $[\uparrow \ldots \downarrow]$ is for a long-distance dimer (LDD).

The temperature dependent magnetic susceptibility, $\chi(T)$ of 0.25% and 1% Zn, Ni and Al doped crystals is shown in the each section along all the three crystallographic directions. But the results are summarized in figure 4.6, where only the data gathered by applying magnetic field parallel to the chains/ladder direction (i.e., H $\parallel$ c) are shown. The data for pristine sample are also included for comparison. The results for other orientations are also similar.

4.4.1 Zn impurity

We first consider the case of a Zn impurity which is expected to be in the Zn^{2+} ($3d^{10}$) state. Due to a completely filled d-shell, a Zn^{2+} ion is non-magnetic. In figure 4.5, we have shown the temperature dependent magnetic susceptibility from 2 K to 300 K along the three crystallographic directions. The measurement was carried out under an applied magnetic field of 10 kOe. Comparing with the susceptibility of the pristine crystal (4.1), 1 % of Zn impurity enhanced the magnetic susceptibility significanty.

In figure 4.6(a), we have shown the susceptibility of 0.25% Zn doped crystal (Zn0.25) and 1 % Zn doped crystal (Zn1) along with the pristine crystal for a comparison. The data are taken in presence of the magnetic field of 10 kOe parallel to the chain/ladder direction. It has been observed that $\chi(T)$ of 0.25% Zn doped crystal (Zn0.25) overlaps that of the undoped crystal except below T = 2.5 K where it begins to exceed marginally, as shown in the inset. This is an interesting result which suggests that at

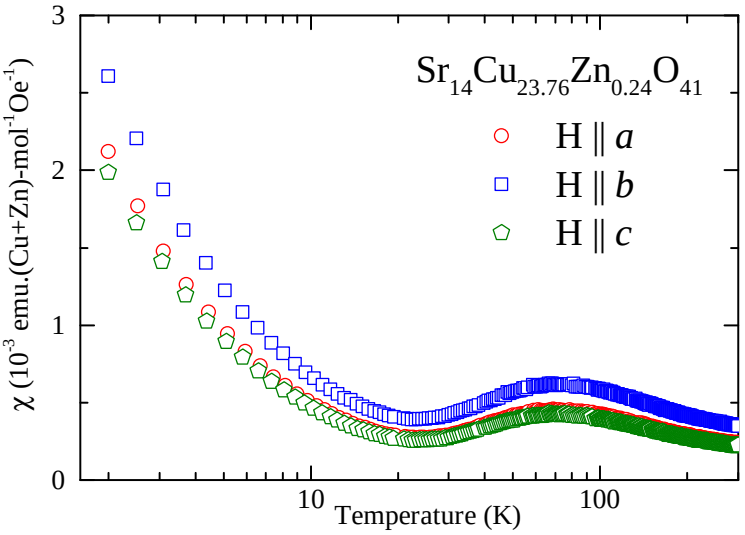

Figure 4.5: Temperature variation of susceptibility of 1 % Zn doped crystal along the crystallographic *a*, *b* and *c*-axis

low concentrations, the Zn ions substitute ∘ in the chain because in any other event (i.e., Zn substituting ↑ or •), "free" spins will be liberated which will enhance the Curie-tail.

When the doping concentration is raised to 1% (Zn1), the low-temperature susceptibility enhances by nearly 200 %. This strong enhancement suggests that at this higher doping concentration, Zn substitutes not only ∘ in the chain but also • and/or ↑ (or ↓) in [↑ • ↓]. In any of these events free spins will be liberated. However, which one of these is more favored can be understood by analyzing $\chi(T)$ quantitatively. We analyzed χ(T) of Zn0.25 and Zn1 crystals in the temperature range 10 K to 200 K using eq. 4.3 but without considering the LDD term, whose contribution above 10 K is expected to be negligible in any case. We excluded the temperature range below 10 K as the precise nature of the magnetic ground state in the presence of Zn is not known.

Before proceeding, we tested if fitting in 10 K to 200 K range give the same results as found earlier. For this purpose, we fitted $\chi(T)$ of undoped sample in this temperature range. We found same values of N_d^{ZR} and J_{ZR} as before (see tables 4.3 and 4.7). The value of N_s did increase slightly but this is not unexpected since the spins in the dimer [↑ . . . ↓] also contribute to N_s in this temperature range.

For Zn0.25, the parameters N_d^{ZR}, J_{ZR} and N_s are practically the same as for the undoped crystal, which is to be expected as the two data sets overlap in this temperature

range. In the Zn1 crystal, N_d^{ZR} has decreased from 0.078/Cu for the undoped crystal to 0.069/Cu. Simultaneously, J_{ZR} decreased from 132 to 125 K. A significant decrease in the values of these parameters provides a direct evidence that on increasing the doping level to 1%, the Zn impurity tends to break the dimers [↑ • ↓] in the chains. We note that for Zn1, the value of N_s has increased to 0.012/Cu. If we take into account the value of N_s of the undoped crystal, the effective increase in N_s (ΔN_s) due to Zn-doping in Zn1 is ∼0.006/Cu. Similarly, ΔN_d^{ZR} is ∼0.009/Cu. These values are in good accord with the actual concentration of Zn in the crystal as determined using the ICP technique.

Substitution of a divalent Zn impurity for a ZR singlet ∘ in the chain (which can be naively thought of as Cu^{3+}) is expected to transfer a hole from chains to ladders. But the excess holes in the ladder are expected to pair-up along the rungs[172], which will not contribute to the Curie-tail. This indeed is consistent with our experimental data on low level of Zn doping (Zn0.25 crystal). However, presence of holes in the ladders should suppresses the magnonic thermal conductivity because hole-pair on the rung of a ladder will effectively cut the ladder into two decoupled segments, preventing the magnetic excitations from propagating through. It has been shown in a previous work [56] that doping $Sr_{14}Cu_{24}O_{41}$ with Zn indeed suppresses the magnetic thermal conductivity significantly.

4.4.2 Ni impurity

We now consider the case of a Ni^{2+} ($3d^8$) impurity which can either be in a spin 0 (low-spin) or a spin 1 (high-spin) state. To determine the spin state of Ni, we estimated the excess susceptibility ($\Delta\chi$) due to Ni impurity by subtracting χ per Cu of 1% Ni doped crystal (Ni1) from that of the undoped crystal. The excess susceptibility, when plotted as $\Delta\chi^{-1}$ versus T, showed a fairly good linearity both above and below 60 ± 10 K, and with a mild curvature around this temperature, which is reminiscent of the χ_{max}. From the Curie-Weiss analysis of data above T = 150 K, we estimated the spin-state of Ni to be S = 1.

χ of Ni0.25 and Ni1 is analyzed along the same line as done previously for the Zn

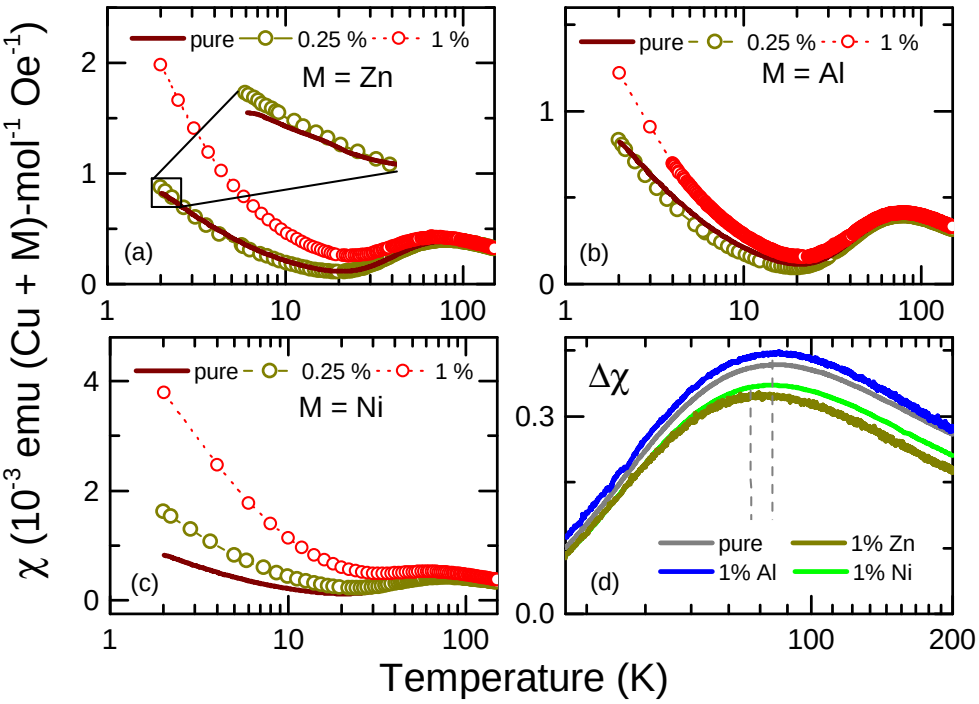

Figure 4.6: Temperature variation of susceptibility of (a) Zn, (b) Al and (c) Ni doped $Sr_{14}Cu_{24}O_{41}$ single crystals along the crystallographic c-axis; (d) the dimer contribution is shown for each dopant. In each panel data for the pristine crystal is shown for comparison.

doped crystals. χ(T) of Ni0.25, shown in figure 4.6, exhibits an enhanced Curie-tail at low-temperatures. In this case, fitting χ in the range T = 10 K to 200 K resulted in a good-fit with practically unchanged values of N_d^{ZR} and J_{ZR}, but with Curie constant increased from 0.22 (undoped) to 0.45 emu (Cu + M)-mol^{-1}Oe^{-1}K. Taking into account that the "free" spin density in the undoped sample is 0.0022/Cu, the net increase in the "free" spin density (ΔN_s) due to Ni doping comes out to be 0.0023/Cu, which agrees fairly nicely with the Ni concentration (x_{Ni}) in the crystal (0.0025/Cu).

This simple analysis suggests that Ni substitutes ∘ in the chains akin to the Zn case discussed above.

In figure 4.7, we have shown the magnetic susceptibility of 1% Ni doped (Ni1) along the three crystallographic directions. In Ni1, ΔN_d^{ZR} is 0.007/Cu, and ΔJ_{ZR} is about 4 K. From the decrease in values of these parameters, we can infer that at higher Ni concentrations the Ni impurity breaks the ZR dimers [↑ • ↓] analogous to the case

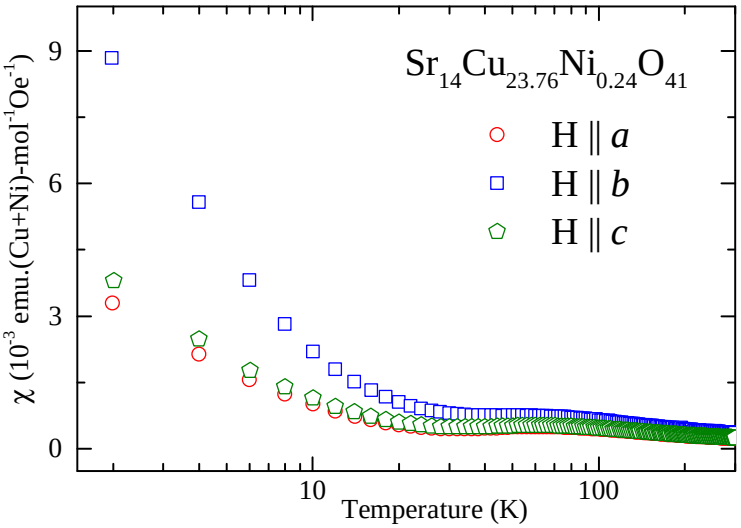

Figure 4.7: Temperature variation of susceptibility of 1 % Ni doped crystal along the crystallographic *a*, *b* and *c*-axis (H = 10 kOe).

of Zn. But a Ni impurity can break a dimer either by substituting ↑ (or ↓) in the dimer [↑ • ↓] as [⇑ • ↓] or [↑ • ⇓], where ⇑ represents the Ni spin. The other possibility is that it substitutes directly at the • site. In order to gain some insight into what is preferred in the Ni case we proceed as follows:

We know that for Ni1 $\Delta N_d^{ZR} = \sim 0.007$/Cu (see table 4.7), i.e., due to Ni doping the number of dimers have reduced. To began with, we presume that the probability of ⇑ substituting a • is relatively weak, i.e., the dimers break with the substitution of a ⇑ either at ↑ or ↓ in [↑ • ↓]. Whether this presumption is correct or not will become clear at the end depending on what we get.

After a dimer has been broken, we assume ↑ and ⇑ to be "free" to align with the field (i.e., the interaction between ↑ and ⇑, mediated via the ZR singlet is weak), and hence both spins will contribute independently to the Curie-tail. Their respective contributions can be calculated using the expression: $C = \eta N_A g^2 \mu_B^2 S(S+1)/3k_B T$, where S = 1 for ⇑ and 1/2 for ↑, and η is 0.007/Cu (= ΔN_d^{ZR}) for both. Form this calculation we obtained the Curie constant for ↑ ($C_\uparrow$) and ⇑ ($C_\Uparrow$) as 0.0026 and 0.007 emu mol^{-1} Oe^{-1} K, respectively.

Above we accounted for 0.007/Cu of Ni ions breaking the dimers. Since x_{Ni} is 0.01/Cu, we still need to account for the remaining 0.003/Cu of Ni ions. From the

previous analysis of Ni0.25 (or Zn0.25), we expect these Ni ions to substitute at ∘ site in the chains. The Curie constant due to these Ni ions ($C^{\circ}_{\Uparrow}$) can be calculated as above by substituting η = 0.003/Cu in the expression for C. We get, $C^{\circ}_{\Uparrow}$ = 0.003 emu Cu-mol^{-1}Oe^{-1}K.

Hence, the net Curie constant (C) due to Ni impurity in Ni1 will be $C_{\uparrow} + C_{\Uparrow} + C^{\circ}_{\Uparrow}$ = 0.0126 emu Cu-mol^{-1}Oe^{-1}K. The experimental value of this quantity can be obtained by subtracting from the Curie constant of Ni1 the Curie constant of the undoped crystal, as given in table 4.7. This is done to take into account the small number of "free" spins that are expected to be there even in the absence of Ni (as in the undoped crystal). Doing so gives ΔC_{exp} = 0.009 emu Cu-mol^{-1} Oe^{-1} K, which is comparable to the calculated value of 0.0126/Cu. Note that substitution of ⇑ for • in the dimer will further enhance the calculated Curie constant, making the disagreement between the calculated and experimental ΔC worse, which supports the presumption made at the beginning concerning the site preference of Ni.

From these reasonably credible analyses one can draw the following conclusions: (i) in terms of their doping habits, both, Zn and Ni impurities behave analogously, (ii) at low-doping concentration, at least up to 0.0025/Cu, both, Zn and Ni tend to replace the interdimer ZR singlet in the chain, (iii) at higher concentration, dimers [↑ • ↓] are broken, (iv) probability for substituting • in [↑ • ↓] is found to be smallest, which makes sense because there are only 2 sites in a f.u. occupied by •.

In a previous polycrystalline study [173], N_d^{ZR} was reported to decrease by almost 28%, and J_{ZR} to increase to about 10%. Both these values appear mutually inconsistent because a 28% decrease in N_d^{ZR} due to severing of dimers cannot simultaneously lead to an increases in the intradimer exchange. As the dimer breaking is expected to decrease the average value of J_{ZR} as is found to be the case here.

4.4.3 Al impurity

The Al impurity is expected to be in a +3 (spin 0) state. In figure 4.8, the magnetic susceptibility of 1% doped Al crystal (Al1) are shown along three crystallographic *a*,

Table 4.7: Fitting parameters obtained from an analysis of the c-axis susceptibility for Zn, Ni and Al impurities (see text for details)

Dopant (M)	x (%)	Fitting range (K)	χ_0 (10^{-5})	θ_p (K)	C ($10^{-2}/Cu$)	Spin (S)	$^{\diamond}N_s$ ($10^{-3}/Cu$)	N_d^{ZR} ($10^{-2}/Cu$)	J_{ZR} (K)
Undoped	0	10 - 200	-1.9	NU	0.22(2)	1/2	5.9(2)	7.8(2)	132(2)
Zn	0.25	10 - 200	-0.9	NU	0.18(2)	1/2	5.1(2)	7.8(2)	130(2)
Ni	0.25	10 - 200	-1.6	NU	0.44(2)	1	4.4(2)	7.8(2)	131(2)
Al	0.25	10 - 200	-1.5	NU	0.17(2)	1/2	4.6(2)	7.8(2)	128(2)
Zn	1	10 - 200	1.0	NU	0.45(2)	1/2	12.1(4)	6.9(4)	125(2)
Ni	1	10 - 200	0.8	NU	1.14(2)	1	11.4(4)	7.1(4)	128(2)
Al	1	10 - 200	-2.2	NU	0.29(2)	1/2	7.9(4)	7.5(4)	127(2)

χ_0 is in emu (Cu + M)-mol^{-1} Oe^{-1}, N_s is obtained from C; g-factor in these fittings is 2.05; NU stands for the parameters not used

b and c - axis. The measurement were carried out under an applied magnetic field of 10 kOe. As shown in figure 4.6, in Al0.25, $\chi(T)$ is nearly unchanged compared to the undoped sample. When the doping concentration is increased to 1%, the low-temperature enhancement is observed but it is much smaller than in the case of Zn. Since both Zn and Al are non-magnetic, the difference between these impurities could be due to a lower solubility limit of Al in the crystal as revealed by the ICP technique. In the Al1 crystal, the actual Al concentration (x_{Al}) is close to 0.25%.

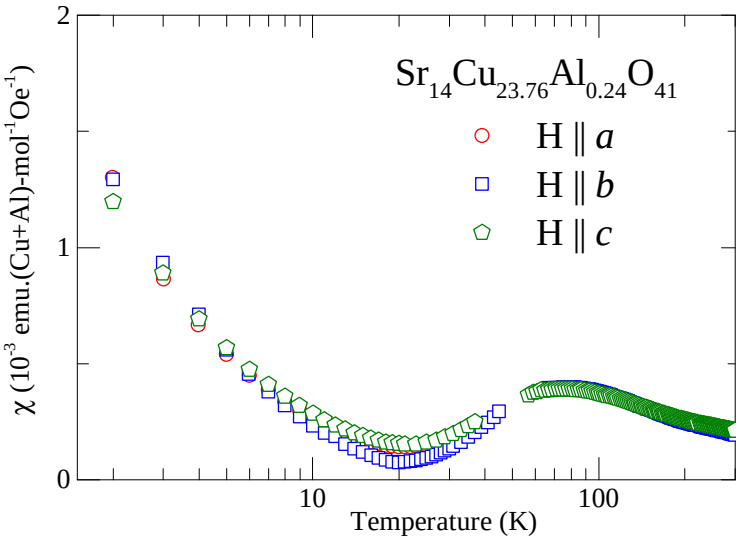

Figure 4.8: Temperature variation of susceptibility of 1 % Al doped crystal along the crystallographic a, b and c-axis. The measurements were carried out in presence of applied magnetic field H = 10 kOe.

Using the same analysis for treating $\chi(T)$ of crsytal Al1 as done previously for the Zn and Ni doped crystals, we found that the increment ΔN_s upon Al doping to be ~0.002/Cu, which is consistent with the value of x_{Al}. Changes in N_d^{ZR} and J_{ZR} upon Al doping are found to be marginal, which is also reflected in the fact that χ_{max} shifts only slightly upon Al-doping (panel d). Since Al impurity increases the Curie-tail without breaking the dimers (N_d^{ZR} and J_{ZR} are unchanged), one can tentatively conclude that unlike the divalent impurities, Zn and Ni, the tripositive Al impurity has a tendency to dope the ladders rather than the chains.

4.4.4 Specific heat study

4.4.4.1 Undoped and 0.25 % Ni doped

So far we concentrated on the effect of impurities on the ZRDs [↑ • ↓], but how their presence in the chains affect the LDDs [↑ . . . ↓] remains unevaluated. To understand this, we studied the specific heat of the undoped and Ni 0.25% doped crystal below T = 2 K. The results of the specific heat (C_p) measurements down to a temperature of 0.06 K are shown in figure 4.9.

We note that near T = 2 K, the value of C_p of the pristine $Sr_{14}Cu_{24}O_{41}$ is about 25 mJ Cu-mol^{-1}K^{-1}, which is higher than a value of 10 mJ Cu-mol^{-1}K^{-1} previously reported for the spin chain compound Sr_2CuO_3 [8]. The higher value of C_p in $Sr_{14}Cu_{24}O_{41}$ is due to the presence of "free" spins that undergo long-distance dimerization at low temperatures. This is manifested in the low-temperature specific heat in the form of a broad maximum centered around T = 0.9 K. Another noteworthy feature in the low-temperature specific heat is the presence of an upturn below T = 0.15 K. This feature is probably the high-temperature tail of the Schottky anomaly that peaks below T = 0.06 K. The Schottky anomaly arises from a small number of "free "spins that have not dimerized due to very large separations; the presence of a weak magnetic field in the cryostat tend to align these spins giving rise to a Schottky anomaly at very low-temperatures[57]. This interpretation gains more credibility once a small magnetic field is turned on. As shown in panel (b), under a small applied field of 2 kOe, the Schottky

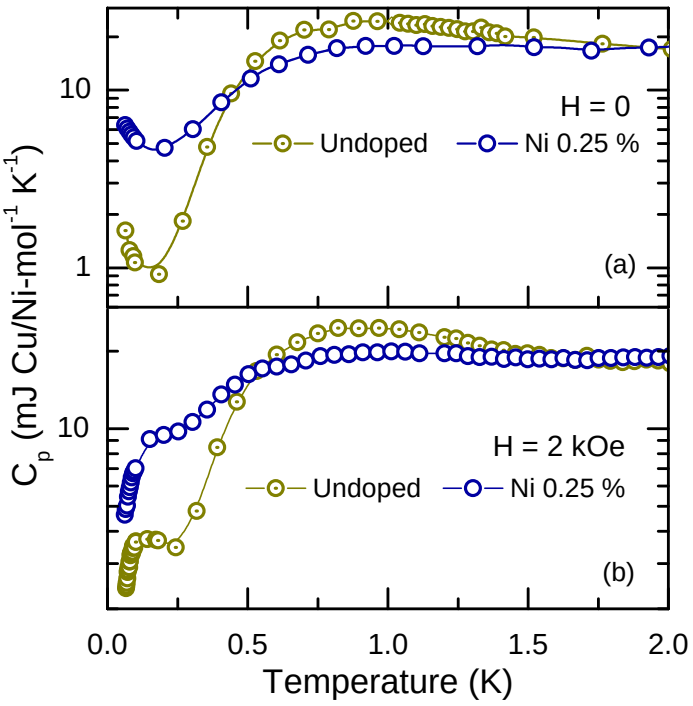

Figure 4.9: Temperature variation of specific heat (C_p) of pristine and 0.25% Ni doped $Sr_{14}Cu_{24}O_{41}$ single crystals: (a) under zero-field condition (H = 0), (b) under H = 2 kOe. Lines are drawn as a guide to the eye.

anomaly shifts considerably to higher temperatures, and is now peaked around T = 0.2 K. On the other hand, the applied field has no discernible effect on the position of 0.9 K anomaly associated with the long-distance dimers, which is not surprising given that the J_{LD} (4 ± 2 K) is too large compared to the magnitude of applied magnetic field.

4.4.4.2 Fitting procedure

We first estimated the specific heat due to phonon by approximating the total measured specific heat in the temperature range 10 K to 15 K as $C_p \sim C_{ph} \simeq T^3$, which fitted the data fairly well with β = 5.4 mJ mol^{-1} K^{-4} for the undoped crystal and 5.6 mJ mol^{-1} K^{-4} for the Ni-doped crystal. The subtracted data below T = 2 K is fitted to: (1) a Schottky contribution (C_{Sch}) due to a small number of spins that remain undimerized down to the lowest temperature (upturn at low temperatures), and (2) the dimer contribution (C_{dimer}) arising from the long-distance dimers (T = 0.9 K hump). Due to variable length of these dimers, the exchange J_{LD} is expected to have some sort of a distribution

associated with its values. Here, for simplicity, we approximate this distribution by a single value of $J_{LD} = \Delta$.

A quantitative analysis of the low-temperature C_p can be carried out following Sahling et al. [57]. They approximated the measured specific heat of an undoped $Sr_{14}Cu_{24}O_{41}$ by expressing it as $C_p = C_{ph} + C_{dimer} + C_{Sch}$, where C_{ph} represents the phononic contribution which can be approximated as βT^3; C_{dimer} is the dimer term which can be expressed as: $A(\Delta/k_BT)^{\frac{3}{2}}\exp(-\Delta/k_BT)$, and C_{Sch} is the Schottky contribution[174] of the "free" spins. Here, the coefficient A in the dimer term is simply N_d^{LD} times the gas constant (R), and Δ corresponds to the exchange J_{LD}. The subtracted specific heat data (C_p - βT^3) of undoped and the doped Ni0.25 crystal are shown in figure 4.10

4.4.4.3 Discussion

The low temperature upturn in the zero-field data could only be fitted by varying H which gave a value of about 450 Oe (denoted by H_{cal} in table 4.8). This value is high compared to the typical remnant field in a cryostat (H < 100 Oe). The corresponding value reported by Sahling et al. is about 150 Oe. However, we found that by considering two dimer terms instead of one not only the quality of fit below 0.5 K improves, the value of H_{cal} also decreases. This suggests that C_p at low temperatures (i.e, below about 0.5 K or so) is more complex. Interestingly, in the measurements done under 2 and 4 kOe the value of H_{cal} agrees well with the applied magnetic field.

In order to fit the data for the Ni-doped crystal below T = 0.5 K, we should consider not only the Schottky term due to S = 1/2 but also due to S = 1 (Ni spins), which make the fitting procedure more ambiguous due to a larger number of free parameters. Since in the present chapter our interest mainly pertains to the anomaly associated with the long-distance dimers, we fitted the data above T = 0.5 K using the dimer term alone. It should be noted that the same procedure may not work in the presence of a magnetic field since a substantial weight of the low-temperature Schottky term shifts to higher temperatures in the presence of an applied magnetic field. From table 4.8, one can quantify the effect of Ni doping on the long-distance dimer. From the fitting of the

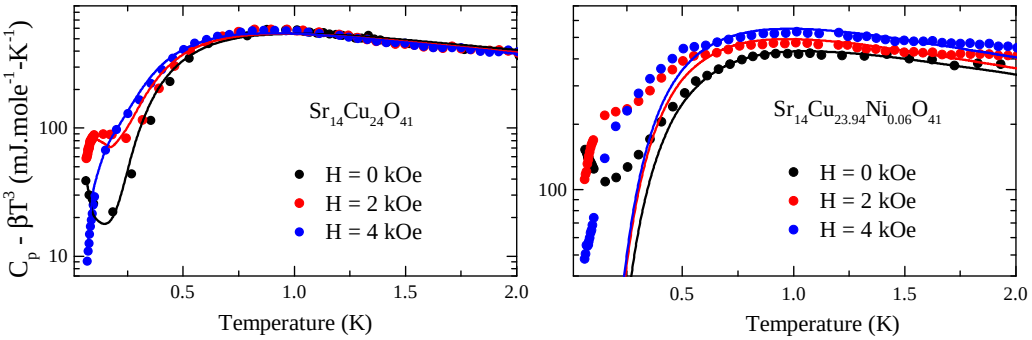

Figure 4.10: The low temperature specific heat (C_p) of an undoped and a 0.25% Ni doped $Sr_{14}Cu_{24}O_{41}$ single crystals measured under H = 0, 2 and 4 kOe. βT^3 is the phononic contribution which has been subtracted from Cp. Solid lines are fit to the data. The fitting procedure and the associated fitting parameters are described in the text

Table 4.8: Values of the fitting parameters corresponding to figure 4.10

Specimen	H (Oe)	H_{cal}	N_f (/f.u.)	A (/f.u.)	Δ (K)
Undoped	0	439	0.029	1330	1.50
	2000	1874	0.023	1319	1.42
(0.06 to 2 K)	4000	3383	0.020	1319	1.38
Ni0.25	0	–	–	1056	1.58
	2000	–	–	1201	1.46
(0.50 to 2 K)	4000	–	–	1341	1.47

zero-field data, we find ΔA (%) = 21 %. This suggests that 21 % of LDDs will be severed in the presence of Ni impurity.

Let us now turn our attention to how the T = 0.9 K anomaly associated with the long-distance dimers is affected due to a small amount of Ni doping. In figure 4.9, we notice that C_p of the Ni doped crystal exhibits the same qualitative features as found for the undoped crystal, but with the exception that the 0.9 K anomaly has been suppressed, and at the same time C_p at temperatures less than 0.5 K has been enhanced. The enhancement below 0.5 K can be attributed to the Ni spins and the new "free" spins that may have released due to a severing of the long-distance dimers upon Ni doping. The low-temperature C_p in this case is evidently more complex due to the presence of Ni spins (spin 1) in the chain. Since we do not know the exact ground state in the

presence of Ni spins, we defer a detailed investigation of C_p below 0.5 K for a future study and focus here on the suppression of the T = 0.9 K anomaly associated with the long-distance dimers, which is what we had started with.

From the magnitude of decreases in the height of T = 0.9 K anomaly, the suppression of long-distance dimers can be estimated to be $\approx 28\%$. A slightly more refined value of 21% is obtained by fitting C_p as discussed above. This suppression suggests a severing of the long-distance dimers. Given that the impurity concentration is merely 0.0025/Cu, which corresponds to nearly 1 Ni impurity for every 400 Cu sites in the chain sublattice, the severing appears to be quite significant for the dilute amount of impurity incorporated. However, the large separation (around 100 Cu sites on an average[57]) between the spins in the dimer [$\uparrow \ldots \downarrow$] implies that there is a fair probability of finding a Ni impurity in approximately one out of four randomly picked dimers in the chain, which is in agreement with the magnitude of suppression observed experimentally.

These considerations suggests that only those long-distance dimers that enclose a Ni impurity between the pairing spins as $\uparrow \ldots \Uparrow \ldots \downarrow$ are severed; and the dimers without a Ni impurity ([$\uparrow \ldots \downarrow$]) are not affected by their presence outside. What we can conclude from here is that while the dimer [$\uparrow \ldots \downarrow$] itself is sensitive to the presence of a Ni impurity, the long-distance quantum entangled ground state of the spin chains in $Sr_{14}Cu_{24}O_{41}$ appears to be quite robust to these impurities.

4.5 Summary

We show that the "free" spin picture previously proposed for the ground state of $Sr_{14}Cu_{24}O_{41}$ breakdown at low-temperatures. This however may not appear surprising as the undimerized spins in a chain are expected to interact weakly via the intervening singlets. But what is intriguing is that rather than freezing or ordering in some random pattern, a ground state consisting of long-distance dimers is favored [57]. Through our analysis of χ(T) and low-temperature M(H) data we confirm that this description indeed provides a satisfactory explanation of the observed magnetic behavior at low temperatures.

To explain the long-distance dimerization we argue that since the "free" spins in a chain are randomly located, the interaction J_{LD} between them will also vary depending on how far apart they are. In a scenario like this, as the sample is cooled the spins that are closest will be the first to dimerize; and, with further cooling the spins at the next higher separation will pair up, and so on and so forth. This process appears to be similar to the dissemination technique for the Random-singlet phase of a strongly disordered HAF spin 1/2 chain [175, 176].

We further investigated the effect of *four* different impurities, namely, Zn, Ni and Al on the ZRDs and LDDs. We found that Zn dopes at the site of an interdimer ZR singlet ($\circ$) thus leaving the ZRDs intact in agreement with Ref. [100] where N_d^{ZR} was reported to remain unchanged with small Zn doping. However, in 1% doped samples, we inferred breaking of ZRDs as the value of N_d^{ZR} and J_{ZR} decreased in agreement with Ref. [173].

The Ni impurity is expected to be in the high-spin ($S = 1$) state. We examined its effect on the two types of dimers: $[\uparrow \bullet \downarrow]$ and $[\uparrow \ldots \downarrow]$. At low Ni concentration, Ni impurity has little or practically no effect on the dimer $[\uparrow \bullet \downarrow]$. The increase in the 'free' spin density (ΔN_s) is found to agree fairly nicely with the actual Ni concentration (x_{Ni}) in the crystal as determined using the ICP technique. From this observation we inferred that at the lower concentration, similar to the Zn case, Ni impurity also substitutes ZR singlets $\circ$ in the chains. At 1% Ni doping, clear evidence of severing of the dimers $[\uparrow \bullet \downarrow]$ is found.

We found that the broad specific heat anomaly associated with LDDs is suppressed by about 25% upon 0.25% Ni doping. This suggests that LDDs are severed in the presence of Ni impurity; however, the dimers without the presence of an intervening Ni impurity remain intact. From this one can infer that the effect of Ni impurity is highly local as it severs only the dimer that it occupies. We, therefore, conclude that Ni impurity does not completely disrupt the quantum entangled ground state of the spins chains.

The case of trivalent Al^{3+} impurity turned out to be different from the divalent impurities Zn and Ni. We found that unlike Zn or Ni, the solid-solubility of Al in the crystal

is very limited. The crystal with 1% nominal Al concentration is found to contain about 0.25% of Al. However, what makes it different from the divalent Zn and Ni impurities is that Al prefers to dope the ladders than the chains.

Chapter 5

Anisotropic gap suppression in spin ladder $Sr_{14}Cu_{24}O_{41}$ upon Co-disorder

5.1 Introduction

In chapter 4, we presented the effect of Zn, Ni and Al impurities on the magnetic ground state of $Sr_{14}Cu_{24}O_{41}$. In particular, We studied the effect of these impurities on the two types of dimers in the chains, namely, the long distance dimers (LDD) which emerge at low-temperatures below 5 K, and high temperature Zhang-Rice dimers (ZRD) that nucleate around 100 K. Reports of doping at the Cu-site in $Sr_{14}Cu_{24}O_{41}$ are rather scarce [177–179], which is unusual given that Cu-site doping in the high-temperature superconductors has a long history (see, [5] for a review). Recently, it has been shown that a Co-impurity induces a long range antiferromagnetic ground state in the Heisenberg spin 1/2 chain compounds $SrCuO_2$ and Sr_2CuO_3; as opposed to a spin-gapped ground state induced by other impurities [161]. Such a contrasting effect of Co-impurity in these spin chain compounds motivated us to look at the effect of Co impurity on the ZRDs in $Sr_{14}Cu_{24}O_{41}$.

In this chapter, we will discuss the effect of Co impurity at the Cu site in $Sr_{14}Cu_{24}O_{41}$. The effect of Co impurity is investigated up to 10% of Co doping. The bulk behavior is found to be highly anisotropic even for the lowest 1 % Co doping in stark contrast with a nearly isotropic behavior of the pristine crystal. The intradimer excahnge associated with the high-temperature dimers is shown to exhibit an unusual anisotropic

suppression in the presence of Co doping. The details of the single crystal growth of $Sr_{14}(Cu_{1-x}, Co_x)_{24}O_{41}$ (x = 0, 0.01, 0.03, 0.05, 0.1) are presented in the chapter 3.

The plan of the chapter is as follows: we will first discuss the magnetic properties of the Co-doped crystals in section 5.2 including the magnetic susceptibility in 5.2.1, isothermal magnetization in 5.2.2, and followed by the anisotropic dimer gap suppression in 5.2.1.2. The XPS study and resistivity of the Co-doped crystals are presented separately under section 5.3 and 5.4 respectively. A summary of all the results and conclusions drawn from this work is gathered under section 5.5.

5.2 Magnetic characterization

5.2.1 Magnetic susceptibility

The effect of Co doping on the magnetic susceptibility (χ) is shown in figure 5.1. As shown, with merely 1% of Co doping, χ_c shows a 5-fold increase at low temperatures, which is higher than in the Ni case examined in the previous chapter 4. However, this is not the only difference between Co and other impurities investigated here. A more striking difference is related to the anisotropic behavior that emerges upon Co doping.

In figure 5.1, χ_a, χ_b and χ_c for 1, 3 and 10 % Co doping is shown. The susceptibility of pristine crystal is also shown for comparison. Since no qualitative change takes place between 3 to 10 % doping range, for brevity, we did not include the 5 % data in figure 5.1. We note that in the presence of a Co impurity, the sign of magnetic anisotropy has reversed, i.e., $\chi_b < \chi_a \lesssim \chi_c$, which is opposite to the pristine case where $\chi_b > \chi_a = \chi_c$. For the 1% sample, the ratio χ_c/χ_b is nearly 5 : 2, and for higher Co-concentrations, the anisotropy is even more pronounced with χ_c/χ_b at T = 2 K approaching values as high as 5 : 1 (10% Co). χ_a in each case shows a variation similar to that of χ_c but with a somewhat smaller magnitude. We argue that unlike a Cu^{2+} ion in oxides or hydrides, which exhibits a nearly isotropic spin 1/2, the unquenched residual orbital angular momentum in a Co ion can give rise to significant single-ion anisotropy [180, 181]. In the spin chains or spin ladders, due to low-coordination, the

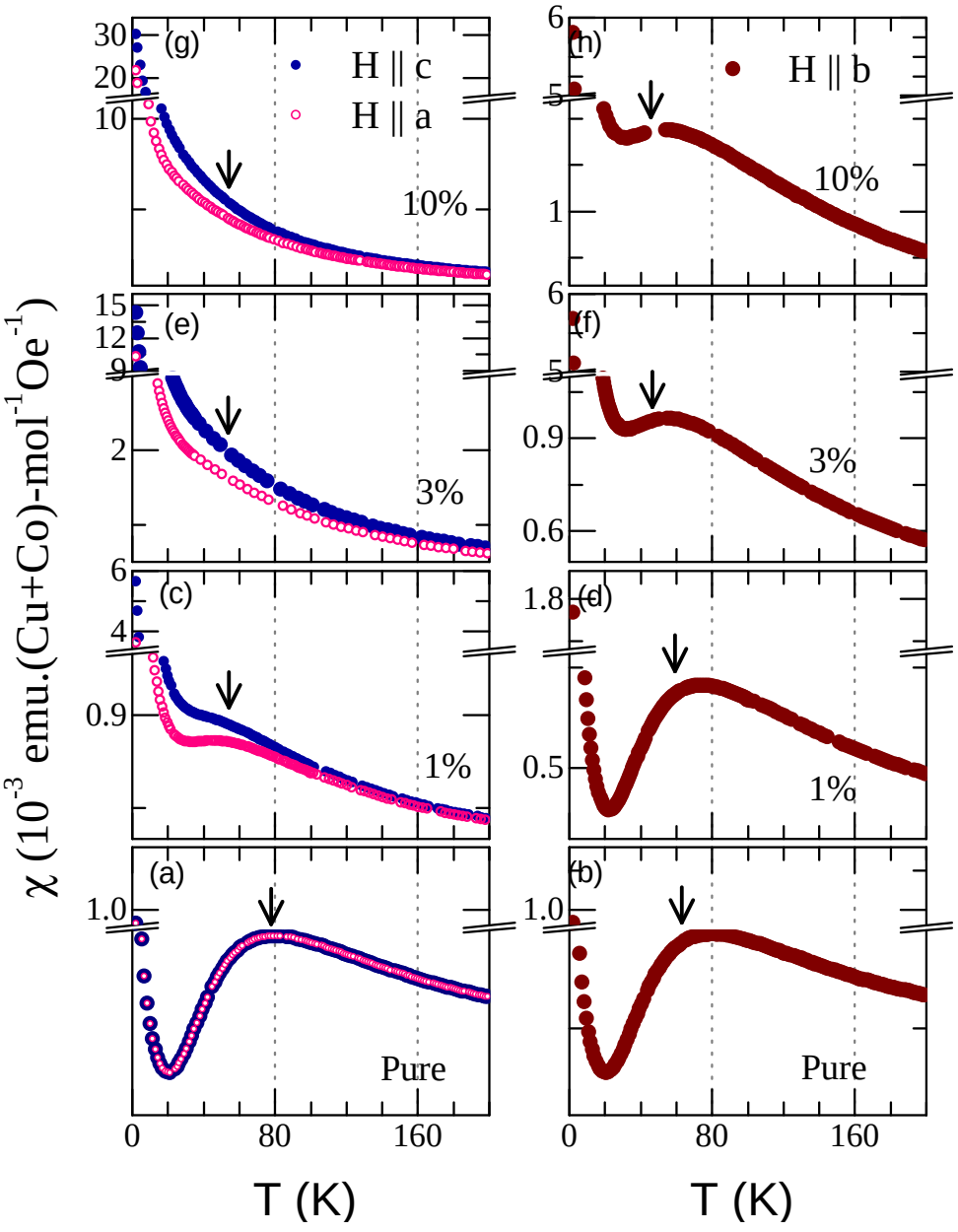

Figure 5.1: The susceptibility (χ) of various Co doped $Sr_{14}Cu_{24}O_{41}$ single crystals along the crystallographic *a*, *b* and *c*-axis is shown as a function of temperature. The corresponding data for a pristine $Sr_{14}Cu_{24}O_{41}$ specimen is also shown for comparison.

anisotropy at the impurity site percolates via the spin-spin interaction along the chain length, causing the bulk of the crystal to show an anisotropic response. Recently, we found that merely 1 % of Co doping in the spin chains $SrCuO_2$ and Sr_2CuO_3 induces a significant magnetic anisotropy in the bulk of the sample [9].

Interestingly, in the doping range from 3% to 10 %, the value of χ_b at 2 K increases only marginally with x_{Co} but over the same doping range the value of χ_c doubles in magnitude. Another striking feature of the data shown in figure 5.1 concerns the position and size of the susceptibility maximum (χ_{max}). While in the χ_b data, χ_{max} remains clearly discernible up to the highest Co doping (10%), along the c-axis (or a-axis), above 3% of Co-doping, χ_{max} is not easily discernible due to an overwhelming Curie-like background of the Co impurity spins.

5.2.1.1 Dimer susceptibility

Trial fits to the data using eq. 1.2, as done previously in the Zn and Ni case, did not give satisfactory results, particularly around χ_{max} in χ_c and χ_a. This suggests that Co doping, for as low as 1% concentration, has a significant effect on the magnetic ground state of $Sr_{14}Cu_{24}O_{41}$. To make an approximate estimate of the dimer contribution to the total susceptibility, we subtracted the low-temperature Curie-tail from the measured χ. This is done by fitting $\chi(T)$ in temperature range 2 K to 15 K using the Curie-Weiss law: $\left[\chi_0 + \frac{C}{T-\theta_P}\right]$ (where C is the Curie constant, θ_P is the Weiss temperature and χ_0 is the temperature independent diamagnetic core term). Since the ladder contribution below room temperature is negligible, one may consider that the subtracted susceptibility $\Delta\chi$ is due to the dimer contribution from the chain sublattice only. Using this approach for all the Co doped crystals, we obtained the spin dimer contribution to the chains from eq. 4.2 along both parallel (c-axis) and perpendicular (b-axis) to the chain as shown in figure 5.2.

Interestingly, along the c-axis, the susceptibility maximum shifts towards lower temperatures upon Co doping leading to a rapid suppression of the spin dimerization gap as discussed in the next section. However, along the b - axis, the position of dimer

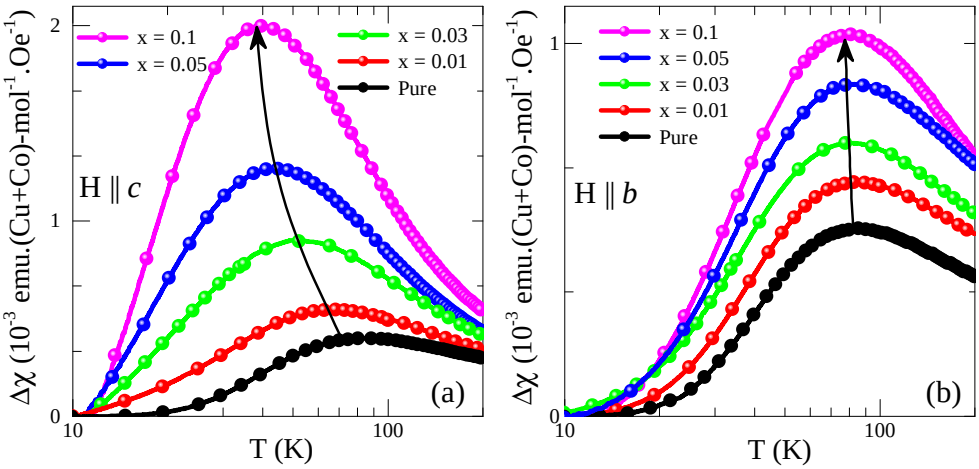

Figure 5.2: The subtracted spin dimer susceptibility of $Sr_{14}(Cu_{1-x}Co_x)_{24}O_{41}$, x = 0, 0.01, 0.03, 0.05 and 0.1 under applied magnetic field (a) parallel to the chain/ladder (H ∥ *c*) and (b) perpendicular to the chain/ladder (H ∥ *b*); Arrow guides the shifting of dimer maxima (T_{max}).

susceptibility maxima remained practically unchanged upon Co-doping upto the highest doping level as shown in figure 5.2(b). From the subtracted data ($\Delta\chi$), the peak position (T_{max}) of the dimer susceptibility for all the co-doped crystals is obtained.

5.2.1.2 Anisotropic suppression of the dimer gap

In figure 5.3, the variation of T_{max} is shown as a function of x_{Co} along *a*, *b* and *c*-axis. From the subtracted data ($\Delta\chi$), shown in figure 5.2, T_{max} is obtained. We found that along the *b*-axis, suppression of T_{max} is significantly smaller compared to that along the c (or a)-axis. Along these orientations T_{max} decreases rather sharply, and by a significantly larger value. Interestingly, independent of the crystal orientation, T_{max} tends to saturate beyond about 3% of Co doping. Since the intradimer exchange, or the spin dimerization gap (J_{ZR}), is proportional to T_{max} ($J_{ZR} \approx 5T_{max}/3$), based on the variation of T_{max} shown in figure 5.3, it can be inferred that the rate of suppression of J_{ZR} in the Co-doped samples is highly anisotropic. With initial Co doping, the dimerization gap along the *c*-axis or *a*-axis closes at a much faster rate (27 % per % of Co doping) than along the *b*-axis (2 - 3% per % of Co doping). However, as the concentration of Co is increased beyond ~3%, $\Delta T_{max}/\Delta x_{Co}$ becomes very small, indicating a saturation.

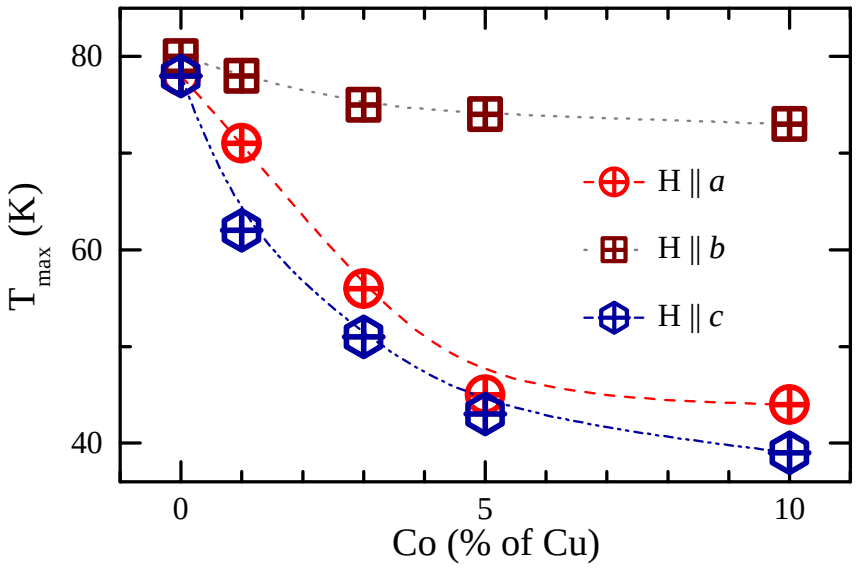

Figure 5.3: Variation of T_{max} ($\approx 3J_{ZR}/5k_B$) with Co concentration along the crystallographic a, b and c-axis showing an anisotropic suppression of the dimerization gap (see text for details).

This observation suggests that for Co doping higher than 3%, the Co impurity does not dope the chains, i.e., the concentration of Co in the chains saturate for $x_{Co} > 3\%$. We therefore believe that at higher concentrations, Co is doped in the ladder sublattice.

5.2.2 Isothermal magnetization

The isothermal magnetization $M_\epsilon(H)$ ($\epsilon = a$, b and c) at T = 2K for a 10 % Co doped crystal is shown in figure 5.4. Data for 1 %, 3 % and 10 % Co doped crystals are are shown with varying the applied magnetic field upto H = 80 kOe. For comparison, however, analogous data for the undoped crystal are also shown. In the undoped crystal, the magnetization behavior is isotropic in the ac-plane. A slight anisotropy with respect to the b-axis ($M_b \gtrsim M_a = M_c$), is consistent with the $\chi(T)$ data discussed earlier.

In 10% Co doped crystal, the magnetization in the ac-plane is different along the a- and c-axis. More importantly, the sign of magnetic anisotropy has reversed, such that, $M_b < M_a \lesssim M_c$, i.e., the b-axis is no longer the *easy* magnetization axis. A similar behavior is found for 1, 3 and 5 % crystals. In figure 5.5, we show the value of $M(H)|_{2K}$ at H = 80 kOe for 0, 1, 3, 5 and 10 % Co doped crystals. We found that along the

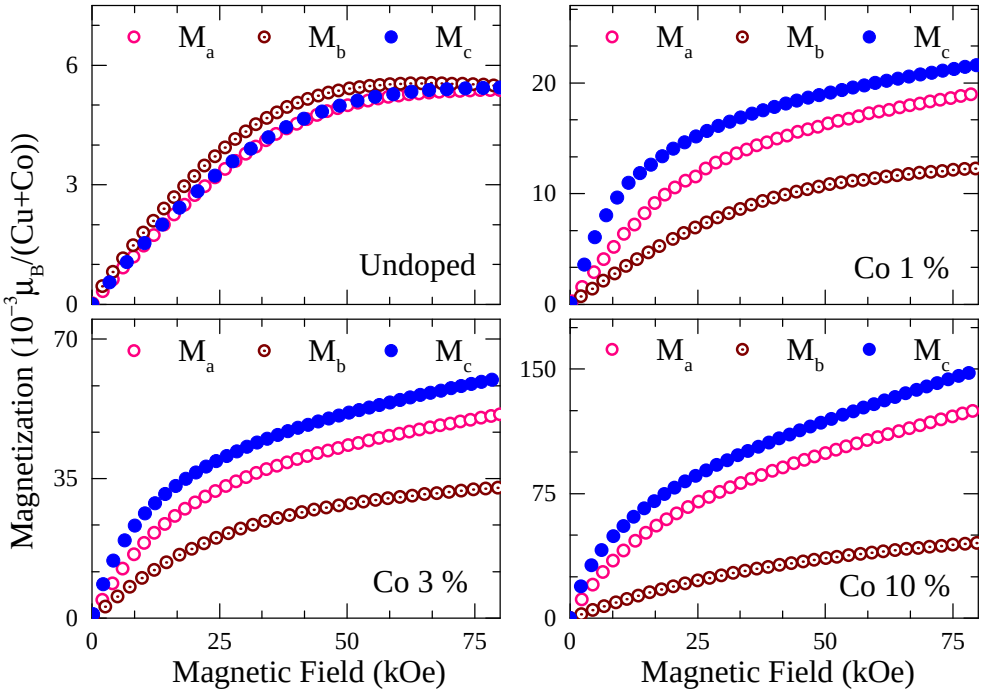

Figure 5.4: Isothermal magnetization along *a*, *b* and *c*-axis is shown as a function of applied magnetic field at T = 2 K for an undoped, 1 % Co , 3 % Co and 10% Co doped $Sr_{14}Cu_{24}O_{41}$.

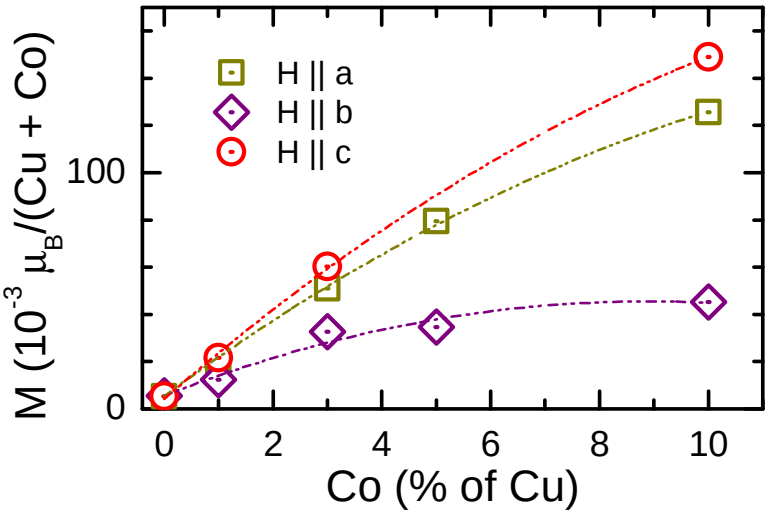

Figure 5.5: Magnetization under 80 kOe along *a*, *b* and *c*-axis plotted as a function of *x* in $Sr_{14}(Cu_{1-x}Co_x)_{24}O_{41}$.

b-axis, the magnetization initially increases with Co-doping but levels-off at higher Co concentrations (>3%). On the other hand, along the *a*- (or *c*-axis) it continues to grow almost linearly. We recall that above 3%, Co is not doped in the chains (inferred from the variation of T_{max} in the previous section). Therefore, the observed saturation of magnetization along *b*-axis above 3% doping suggests that the Co ions doped in the ladder have no spin component along the *b*-axis. On this basis one can hypothesize that Co spins in the ladder sublattice have a planar (*ac*-plane) anisotropy. At this point, it is worth mentioning that the anisotropy for Zn, Ni and Al doped crystals has the same sign as for the undoped crystal, but it is opposite for the crystals doped with Co.

5.3 X-ray photoelectron spectroscopy

While the magnetic behavior in the presence of Co impurity revealed useful information concerning the magnetic anisotropy induced by Co and its site-substitution preferences, the valence state of Co (i.e., whether it is in a +2 or a +3 valence state) still remains to be ascertained.

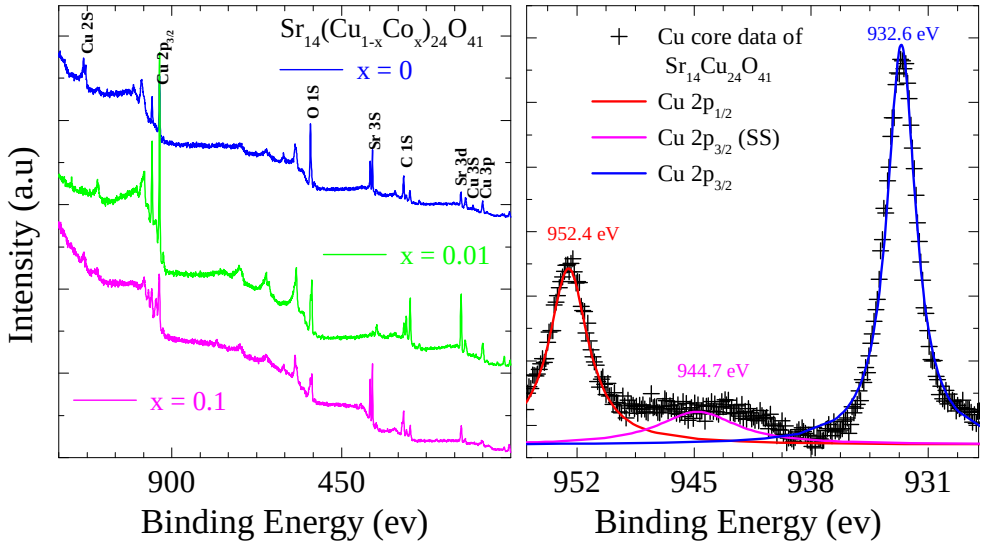

Figure 5.6: (Left panel) X-ray Photoemission Spectroscopy (XPS) survey data on $Sr_{14}(Cu_{1-x}Co_x)_{24}O_{41}$ where x = 0, 0.01 and 0.1; (Right panel) Lorentzian peak fit to find out the Cu 2p peaks of the pristine sample; SS stands for shake up satelite peak.

To ascertain the valence state of Co, we performed X-ray photoelectron spectroscopy (XPS) on the single crystal specimens (*ac*-plane) of pristine and doped samples. From the survey scan it was confirmed that no other elements except Sr, Cu, Co, O and C are present as shown in figure 5.6 (left panel). Calibration is done using the adventitious C 1S peak at 285.2 eV [133]. We used the least square curve fitting to evaluate the peak positions from the spectra. The spectral background was subtracted by Shirley method and then peaks were found using Lorentzian curve fitting procedure. In figure 5.6 (right panel), we have shown the Cu core data consisted of two main peaks at 954.2 eV (Cu $2p_{1/2}$) and 932.6 eV (Cu $2p_{3/2}$), and a smaller and broader satellite peak at 944.7 eV (Cu $2p_{3/2}$ satellite) in conformity with the standard data [182].

We used the same fitting procedure for the subtracted spectra of highest Co doped $Sr_{14}(Cu_{0.9}Co_{0.1})_{24}O_{41}$ sample. The XPS spectrum of a 10% Co-doped crystal showing Co-2p peaks is presented in figure 5.7. Due to low concentration of Co in the sample, the signal-to-noise ratio in our data is not particularly high. The crystals with lower Co-concentrations (not shown) suffered from even poorer signal-to-noise ratio and are therefore not considered further. Nonetheless, in the spectrum of 10% Co-doped crystal in figure 5.7, one can easily identify peaks at the binding energies close to 780 eV, 795 eV and 806 eV, with a broad and not so clearly discernible feature around 785 eV.

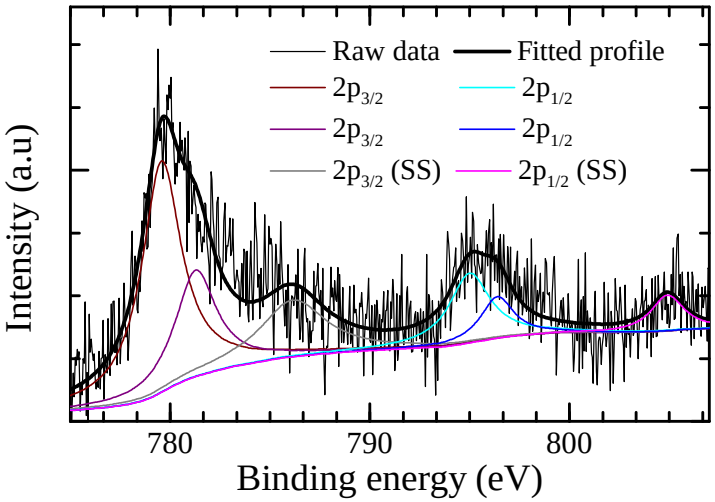

Figure 5.7: Co-2p core level spectrum showing $2p_{3/2}$ and $2p_{1/2}$ peaks and the shake-up satellite peaks for a 10% Co-doped $Sr_{14}Cu_{24}O_{41}$ single crystal. The lines are fit to the data (see text for details); SS stands for shake up satelite peak.

Co-2p core level spectrum is split in $2p_{3/2}$ and $2p_{1/2}$ features due to spin-orbit coupling. The asymmetry in the peak shape towards the higher binding energy side in both, $2p_{3/2}$ and $2p_{1/2}$ features, indicates the possibility of mixed valance state. Therefore, the whole spectrum is fitted with *six* Lorentzian peaks, and background is approximated by Shirley function. Comparing the binding energy positions with various valance states of Co as reported in available literature, we conclude that cobalt is present in two charge states: Co^{2+} and Co^{3+} (Refs. [183–185]). The estimated ratio Co^{3+}/Co^{2+} is approximately 3.5 : 1. The additional features labeled as SS correspond to the shake-up satellites of Co^{2+} and Co^{3+}. Thus, in the crystal doped with 10 % of Co, approximately 23% of the doped Co ions are inferred to be in a +2 state and 77% in +3 state. If we combine this with the result from a previous section that above approximately 0.003/Cu of doping concentration, Co is not doped in the chains, one can infer that in the 10% Co doped crystal, the ratio Co^{2+}/Co^{3+} in the chains is around 2.3 : 0.7.

5.4 Resistivity

In figure 5.8 (left panel), the temperature dependence of the resistivity ratio ρ(T)/ρ(300) along *c*- (parallel to ladders within the ladder planes) and *a*- (perpendicular to the ladders within the ladder planes) axis of the grown crystals $Sr_{14}(Cu_{1-x}Co_x)_{24}O_{41}$ where x = 0, 0.03, 0.05 and 0.1 are shown. The absolute resistivity ($\rho_a \simeq 3 \times 10^3$ Ω-cm, at T = 150 K) of the pristine crystal is in a good agreement with the previous reports [186], and shows a semiconducting behaviour. We observe that the magnitude of resistivity decreases with the increase in Co concentration and below 100 K (for 10 % of Co doped crystal) the *c*-axis resistivity ρ_c is lower than the *a*-axis resistivity ρ_a. Although there are several reports on the resistivity, but the doping effects of $Sr_{14}Cu_{24}O_{41}$ are focused on the substitution at the Sr-site [186–188]. Previously, Wang et al. reported the effect of Co - substitution at Cu-site [189], but these measurements were carried out on the polycrystalline samples where it is difficult to isolate the effect due to the grain boundaries.

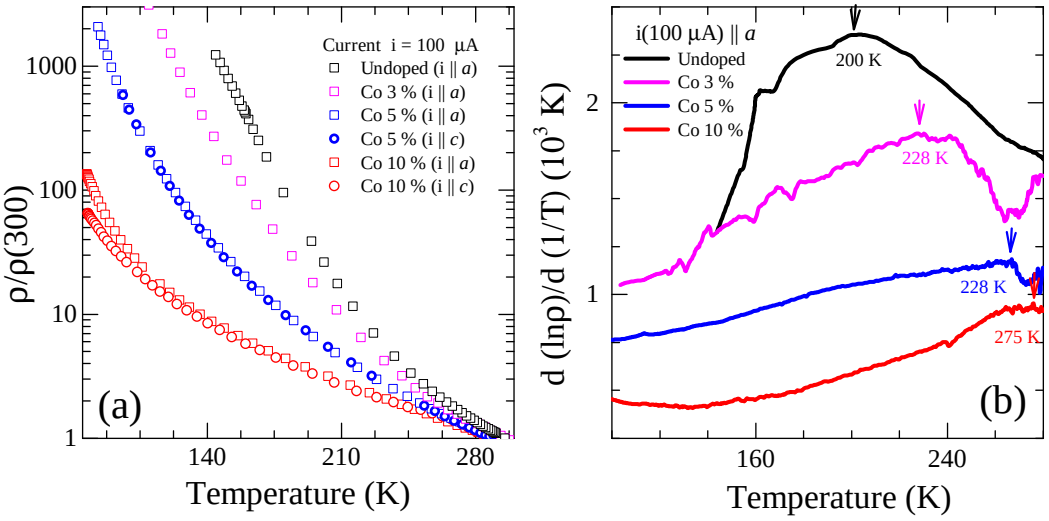

Figure 5.8: a) Resistivity ratio of the pristine and Co doped crystals along different crystallographic directions. b) The Arhenious plots are shown along the *a*-axis resistivity of the pristine and doped crystals, the corresponding peak temperature were also shown.

In figure 5.8(b), the temperature dependence of d(lnρ)/d(1/T) is shown for the Pristine (x = 0) and Co doped (x = 0.03, 0.05 and 0.1) crystals along the *a*- axis. For the undoped crystal, a broad peak is observed around $T_\rho \sim 200$ K in good agreement with previous report by T. Adachi et al. T_ρ is gradually shifted towards higher temperatures upon increasing the Co concentration. A similar $\frac{d(ln\rho)}{d(1/T)}$ behaviour was previously reported for the Sr- site doped compounds $(Sr_{1-x}A_x)_{14}Cu_{24}O_{41}$, where A = Ca, La and Y [188, 190]. Carter et al. interpreted this anomaly at T_ρ as a charge-ordering temperature below which all the holes present in the chains are ordered [188]. On the other hand, according to Adachi et al., T_ρ is not the charge ordering temperature since in this material the electrical conduction is mainly dominated by the ladders. They reported that the peak temperature T_ρ goes down with increasing the hole concentration in the ladder (as with Ca substitution at the Sr site which transfers some of the holes from chains to ladders [188]), while T_ρ goes up with decreasing the hole concentration upon La and Y doping at the Sr - site [190]. From this, they concluded that holes are localized in the ladder below the peak temperature T_ρ.

However, here we have substituted Co at the Cu - site and we observed the decrement of resistivity with increasing the doping concentration *x*. In figure 5.8 (b), it is

clearly visible that with only 3 % of Co substitution (x = 0.03), the peak temperature T_ρ shifted by 14 % towards higher temperature. Hence, for Co substitution, we see a contradicting behaviour where the magnitude of ρ decreases but simultaneously the anomaly at T_ρ shifts to higher temperatures. If we assume that the number of holes in ladder is increased by Co substitution then the question arises as to why T_ρ has also shifted towards higher temperatures? To understand this strange behaviour we have extracted the so called inflection temperature T_χ from the magnetic susceptibility data (shown in figure 5.9(a)). The inflection temperature T_χ is the deviation from T linear

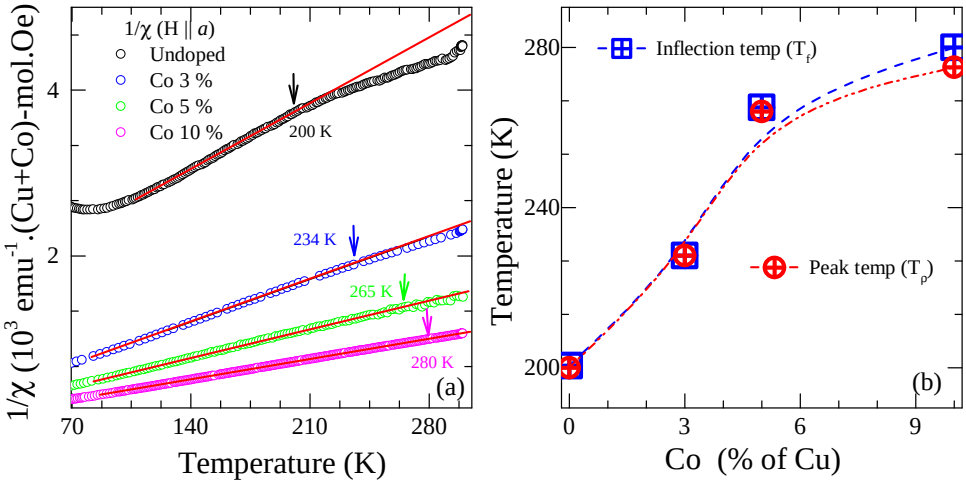

Figure 5.9: (a) Inflection temeprature were calculated from the linear deviation of the $1/\chi$ plots of pristine and Co doped crystals. (b) The Peak temperature were calculated from resistivity, nicely matching with the inflections temperatures obtained from $1/\chi$ plot.

relation from the $1/\chi$ vs T curve, as shown by the arrows in figure 5.9(a). The T_χ goes up with increasing the Co concentrations x. The values of T_χ and its x dependence have been found to match with those of T_ρ, as shown in the right panel of figure 5.9. We also see a good correlation between the values of T_ρ and T_χ. Both increase almost in the same manner with increasing Co concentration x, shown in figure 5.9(b). Thus, different from Sr-site doping, Co doping at the Cu-site not only decreases the absolute resistivity but also increases the temperature T_ρ (which shows a decreasing behaviour with decreasing ρ).

5.5 Summary

The strongest effect of doping on the magnetic behavior is observed in the presence of a Co impurity. Co-doping not only enhances the low-temperature Curie-tail but also results in a highly anisotropic magnetic behavior. We argued that this strong anisotropy, even for doping level as low as 1 %, is due to the single-ion anisotropy of the Co ion. We also found evidence to suggest that upon increasing the Co concentration beyond to ∼3% , the population of Co in the chain sublattice reaches a saturation level. Interestingly, the dimerization gap associated with the *ZRD*s showed a highly unusual behavior with a much higher suppression rate with Co doping in the ac-plane than along the b-axis. In a previous study [99], this interesting feature had remained hidden due to the powder nature of samples investigated. From our combined magnetization and XPS study presence of two types of Co ions is inferred: Co^{3+} in the ladders having a planar (ac-plane) anisotropy, and Co^{2+} in the chains with a spin component along the b-axis.

The resistivity of pristine sample shows a semiconducting behaviour but doping Co decreases the resistivity. Arhenius plot reveals an increment of the peak temperature T_ρ with Co doping along both the *a*- and *c*- axis. The electrical conductivity along chain/ladder is found to more compared to perpendicular to the chain. The inflection temperature T_f calculated from the magnetic susceptibility also increases with Co doping and shows a good agreement with T_ρ. From which we conclude that they both have a common origin which is related to the doping of Co in the ladder sublattice. But how is this related to the CDW ordering in the ladder sublattice remains unclear.

In summary, we investigated the effect of Co impurity on the magnetic behavior of the quantum magnet $Sr_{14}(Cu_{1-x}Co_x)_{24}O_{41}$ for x = 0, 0.01, 0.03, 0.05 and 0.1. We observed profound changes in the magnetic behavior in the presence of Co impurity. The effect of Co impurity turned out to be most unusual displaying a strongly anisotropic response, and with a dimerization gap that suppresses faster along the chain/ladder direction than perpendicular to it as a function of increasing Co concentration.

Chapter 6

Excess specific heat from the gapped sliding phonon modes in $Sr_{14}Cu_{24}O_{41}$

6.1 Introduction

Crystalline materials, regardless of their composition and symmetry properties, exhibit a universal phononic ground state consisting of three gapless acoustic modes whose contribution to the specific heat is well-known to vary as the Debye T^3 law [191]. However, in a composite crystal comprising two substructures that individually obey *full* translational symmetry but are mutually incommensurate (IC) along one or more directions, the phononic ground state can be highly unconventional due to the occurrence of new normal modes that arise from a relative sliding motion of these substructures past each other [192–195]. An “extra" acoustic or acousticlike mode has indeed been observed experimentally in a number of IC systems, including the IC chain compound $Hg_{3-x}AsF_6$ [196, 197], higher manganese silicides of the Nowotony chimney-ladder family [198], Rb-IV [199], n-alkane-urea composite crystals [200], and in some of the BSCCO superconductors [201, 202]. Within this, a particularly interesting behavior emerges when the IC substructures are in the form of oppositely charged sheets as the coulomb restoring force between these sheets, as they slide past each other, opens an energy gap rendering the sliding mode quasiacoustic or optical [203]. Such systems are interesting as they not only offer a tunable phonon gap which scales with the charge difference between the sliding layers, but also provide a platform for understanding the

gapped phononic excitations in a wider class of systems, including, disordered solids and glasses [204–206], filled skutterudites [207], and strong electron-phonon coupling superconductors [208].

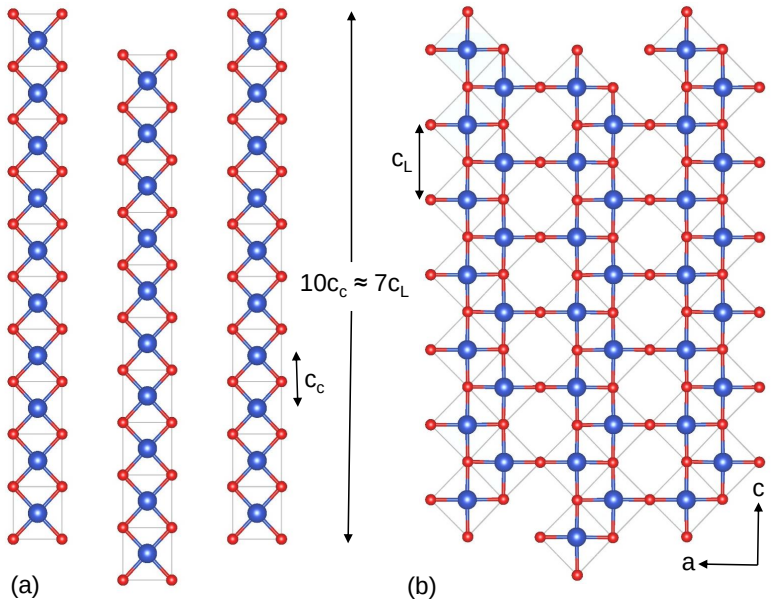

Figure 6.1: The chain (left panel) and ladder (right panel) sublattices in $Sr_{14}Cu_{24}O_{41}$ in the *ac* plane. Blue and red spheres represent Cu and O respectively and Sr is not shown for clarity.

In this regard, the composite crystal $Sr_{14}Cu_{24}O_{41}$ is an ideal system for realizing the gapped sliding modes. As previously mentioned, it has a layered structure comprising an alternating stack of oppositely charged $Sr_2Cu_2O_3$ and CuO_2 sheets. In the $Sr_2Cu_2O_3$ sheet, the Cu ions form a network of weakly interacting 2-leg ladders running parallel to the c-axis; and in the CuO_2 sheet they arrange to form linear chains oriented parallel to the c-axis. In figure 6.1, the chain and the ladder sublattices are shown to elucidate the incommensurate nature of the crystal structure of $Sr_{14}Cu_{24}O_{41}$ or $[CuO_2]_\alpha[Sr_2Cu_2O_3]$. These sheets are however mutually IC along the c-axis with $\alpha = c_l/c_c \approx \sqrt{2} \approx 10/7$, where c_c (~ 2.75 Å) and c_l (~3.93 Å) are the lattice parameters in the chain and ladder sublattices, respectively. In real materials, α exhibits a broad distribution of values which is the hallmark of an IC system [156]. This is also reflected in the high energy x-ray diffraction study where not a single ordering wave vector, but a multitude of Fourier components characterizes the low-temperature modulations of the

chain sublattice [209]. For brevity, however, we will use the notation " $Sr_{14}Cu_{24}O_{41}$" which corresponds to $\alpha = 10/7$.

While the magnetic ground state and spin excitations of $Sr_{14}Cu_{24}O_{41}$ have been extensively investigated in the past [168], the unconventional nature of its phononic ground state started gaining attention only recently. Thorsmølle et al. [210] used Terahertz time-domain spectroscopy and Raman techniques to show the occurrence of new infrared and Raman active modes in the very low energy range between 1 and 2 meV. They conjectured that these modes arise due to the gapped sliding motion of the chain and ladder layers. More recently, new optical phonon modes polarized along the incommensurate axis were reported in the same energy range using inelastic neutron scattering [211]. However, the thermodynamic evidence of these modes and their unambiguous assignment as the sliding phonon modes has remained an open question.

Since the sliding modes are expected to be gapped, they should have a definitive thermodynamic signature in the low-temperature specific heat where the phononic specific heat is expected to exceed the Debye T^3 prediction. In this chapter, we will show that the low temperatures specific heat (C_p) of $Sr_{14}Cu_{24}O_{41}$ exhibits a rather large excess contribution of non-magnetic origin near $T^* = 10$ K. Using a combination of Terahertz time domain spectroscopy (THz-TDS) and specific heat experiments on three different crystals, namely, as-grown, O_2-annealed and Al-doped, we establish that the excess specific heat in $Sr_{14}Cu_{24}O_{41}$ originates from the relative sliding motion of chain and ladder layers predicted previously. We also show that the gap-size associated with these modes is highly sensitive to the stoichiometry.

The chapter has been organized as follows: First, we will give a brief analysis on magnetism of undoped, O_2 annealed and Al-doped crystals in section 6.2.1 and followed by the specific heat data in section 6.2.2. We provide the analysis of THZ-TDS in section 6.2.4 to establish the presence of sliding phonon mode corroborates with the finding from the specific heat data and finally we summarized our findings in the section 6.4.

6.2 Experimental details

Crystalline specimen used for this study are same as reported in the previously in chapter 4 and 5. Details of annealing treatment is as follows: the annealing treatment was carried out in a tubular furnace under flowing O_2 at $T = 850°C$ for 36 hrs. Magnetic and specific heat measurements were performed using a Physical Property Measurement System (PPMS), Quantum Design (QD), USA at IISER Pune. For the specific heat measurements, thin, platelet-like specimens with their largest surface area parallel to the *ac*-plane were mounted on the specific heat puck using the Apiezon N grease. Prior to loading the specimen, addenda was measured to subtract the specific heat of sample holder, and of grease used during the experiment. The Terhertz Time-Domain Spectroscopy (THz-TDS) experiments were performed at IISER TVM, India, For these experiments, polished single crystals were oriented. The THz signals were generated using ultrafast ($\sim$ 80 fs) photoexcitation of low-temperature grown GaAsBi epilayers; and were detected using a photoconductive antenna. Measurements were performed by mounting the sample on the cold-finger of an optical closed-cycle refrigerator. Transmittance were obtained by taking the ratio between magnitude of fast-Fourier transformed sample and the reference amplitudes.

6.2.1 Magnetic susceptibility

For completeness sake, the temperature dependence of spin susceptibility (χ) for H $\parallel c$ is shown in figure 6.2. These are the same data (of undoped crystal) as shown in figure 4.2 in chapter 4. Since the ladder sublattice has a spin-singlet ground state with the singlet-triplet energy gap exceeding $\sim$ 35 meV [166, 167], the low-temperature χ is practically due to the chain sublattice. $Sr_{14}Cu_{24}O_{41}$ is self-hole doped with six holes per formula unit. If all six holes are assumed to be present in the chain subsystem, the ground state configuration of the chains can be written as [212]: $\cdots \circ \circ [\uparrow \circ \downarrow] \circ \circ [\downarrow \circ \uparrow] \circ \circ \cdots$, where $\uparrow$ ($\downarrow$) represents a Cu^{2+} spin 1/2, $\circ$ a Zhang-Rice singlet [213], and $[\uparrow \circ \downarrow]$ denotes a spin 1/2 dimer. For this ideal configuration, χ should decrease to zero exponentially as $T \rightarrow 0$. However, in any real $Sr_{14}Cu_{24}O_{41}$ crystal, a small

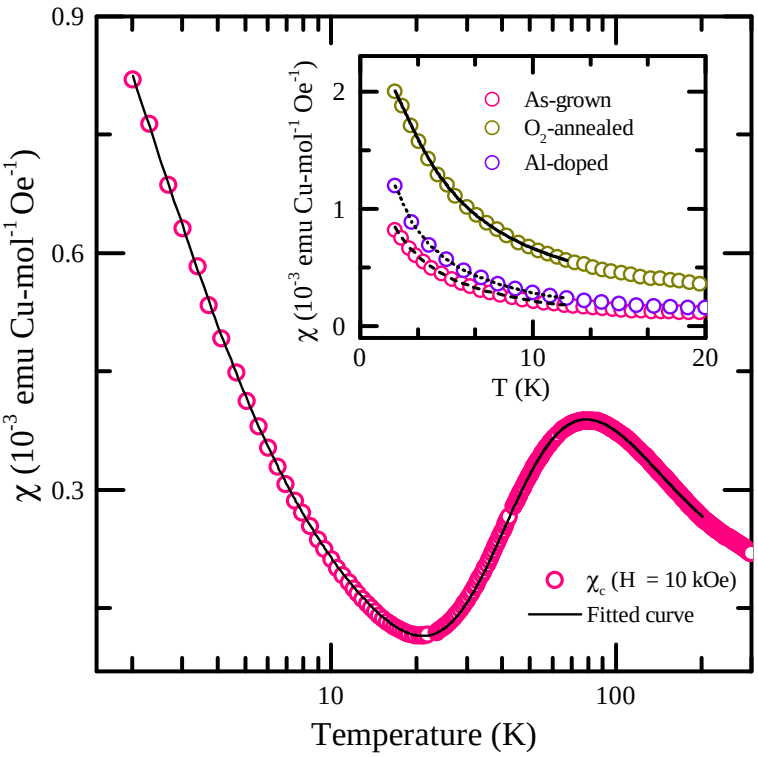

Figure 6.2: Magnetic susceptibility χ of $Sr_{14}Cu_{24}O_{41}$ is shown as a function of temperature for H || c. The black line represents best-fit to the data obtained using eq. 4.3. Inset: Low-temperature χ for an as-grown, annealed and Al-doped crystal. The lines are best-fit to the data using eq. 4.3 in the low-temperature range as described in the text.

fraction of hole transfer from chains to ladders leads to a small number of unpaired spins in the chains that cause $\chi(T)$ to increase at low temperatures ($T < 20$ K) in a Curie-like manner. Recently, it has been shown that at still lower temperatures ($T < 5$ K), these unpaired spins, separated by hundreds of Cu sites along the chain, anti-align to form dimers due to a small antiferromagnetic interaction mediated via the intervening sites [214]. Therefore, χ below $T = 200$ K can be described using a dimer-dimer model represented by eq. 4.3.

As shown in figure 6.2, a satisfactory fit to $\chi(T)$ over a broad temperature range is obtained using eq. (4.3). The best-fit value of J_1 and J_2 is about 132 and 2 K, respectively, in good agreement with previous reports (see Ref. [215] for J_1 and Ref. [214] for J_2). The number of free spins N_s, calculated from C, is ~0.069/f.u., and N_{d1} and N_{d2} are 1.89/f.u. and 0.04/f.u. respectively. Here, however, our interest primarily

Table 6.1: The fitting parameters for the as-grown, O_2 annealed and Al-doped crystals using eq. 4.3; N_s is obtained from the Curie constant C

Sample	N_{d2} ($f.u.^{-1}$)	J_2 (K)	χ_0 (10^{-5}) (emu Cu-mol^{-1}Oe^{-1})
As-grown	0.04	4.3	-3.0
O_2-annealed	0.16	4.0	-1.2
Al-doped	0.045	3.5	-2.8

is to obtain the low-temperature parameters: N_s, N_{d2}, J_2 in eq. (4.3), and to compare these to a similar fitting for the low-temperature specific heat (*vide infra*). Therefore, in figure 6.2 (inset), we show $\chi(T)$ for as-grown, O_2 annealed and Al-doped crystals along with the corresponding low-temperature fits, where the fits are performed using eq. 4.3 after excluding from it the high-temperature $i = 1$ dimer term whose contribution at low-temperatures ($T \lesssim 20$ K) becomes exceedingly small. The values of the fitting parameters thus obtained are summarized in table 6.1. For a more elaborate discussion on the analysis of $\chi(T)$ using various models, including eq. 4.3, we refer the reader to Ref. [216].

6.2.2 Specific heat

In figure 6.3 where the specific heat (C_p) is shown as a function of temperature for the as-grown crystal. When plotted as C_p Vs. T (panel a), the data, otherwise smooth down to 2 K, showed a slight blip near $T^* = 10$ K. This feature becomes clearly discernible in the C_p/T Vs. T^2 (panel b), where data in the presence of an applied magnetic field of 50 kOe are also shown. The small deference between the zero-field and in-field data is due to the presence of a small fraction of free or defect spins in the chains. As the sample is cooled, these spins tend to align along the field direction thus giving rise to a small excess field dependent contribution. At still low-temperatures, a gradual onset of long-distance dimerization takes place which leads to an upturn in C_p/T, which also depends on the strength applied magnetic field. These contributions should be subtracted from the measured C_p in order to examine if the $T^* = 10$ K feature, which has no counterpart

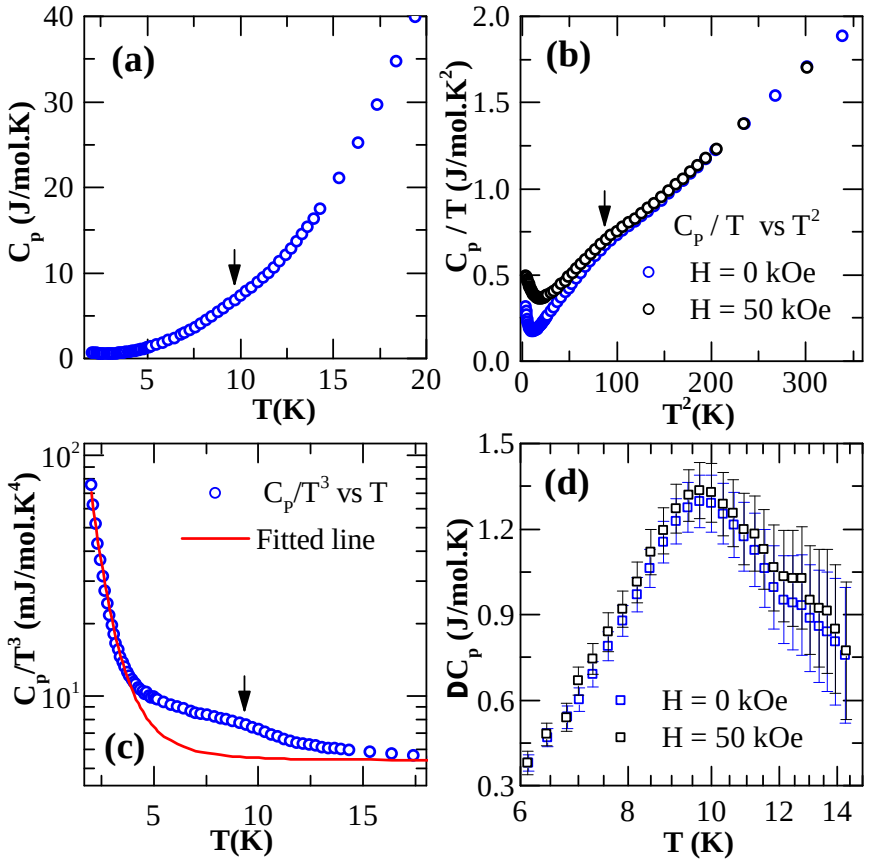

Figure 6.3: (a) Specific heat (C_p) of an as-grown $Sr_{14}Cu_{24}O_{41}$ crystal show as a function of temperature. (b) Specific heat plotted as C_p/T versus T^2 in zero-field, and under a field of 50 kOe; (c) C_p/T^3 is shown as a function of T. The solid line is a fit in the range T = 2 to 3 K using eq. 6.1 (see text for details); (d) ΔC_p is plotted as a function of temperature for H = 0 and 50 kOe. The error bars are taken directly from the PPMS data file.

in $\chi(T)$, has any field dependence. For this purpose, the low-temperature data in the temperature range from $T = 2$ to 3 K, which is sufficiently away from T^*, is fitted using eq. 6.1:

$$C_p(T) = RN_{d_2}(J_2/k_BT)^{\frac{3}{2}}e^{-J_2/k_BT} + \beta T^3 + AT^{-2}, \tag{6.1}$$

here, the first term is due to the long-distance dimers (R here is the gas constant), βT^3 is the phononic contribution, and the term A/T^2 represents the Schottky-tail due to a small number of unpaired spins, i.e., the spins that remain undimerized down to 2 K. The fitted curve (shown in figure 6.3(panel c) where C_p is plotted as C_p/T^3 vs.

Table 6.2: The fitting parameters for the as-grown, O_2 annealed and Al-doped crystals using eq. 6.1. In the C_p fits from the coefficient A of the AT^{-2} term. The value of β was fixed by first fitting the measured C_p in the temperature range T = 12 to 15 K using the expression $C_p = C_0 + \beta T^3$, where C_0 is some constant.

Sample	N_s ($f.u.^{-1}$)	N_{d2} ($f.u.^{-1}$)	J_2 (K)	β (mJ mol^{-1} K^{-4})	N_s ($f.u.^{-1}$)
As-grown	0.08	0.06	2.7	5.3	0.13
O_2-annealed	0.12	0.16	2.0	5.8	0.29
Al-doped	0.10	0.05	4.5	5.4	0.04

T) is extrapolated to higher temperatures. The values of parameters N_{d2}, J_2 and A are summarized in table 6.2, these values are in good agreement with corresponding values obtained from the $\chi(T)$. The value of β is found to be ~5.5 J mol^{-1} K^{-4} in agreement with a previous report where C_p at low-temperatures is reported [217].

The excess specific heat (ΔC_p), estimated by taking the difference between the experimental data and the fitted curve, is shown in the figure 6.3(d) for H = 0 and 50 kOe. ΔC_p exhibits a well-defined peak at T^* whose non-magnetic or phononic origin can be inferred from the insensitivity of ΔC_p to the applied magnetic field; which also agrees with the absence of any anomalous feature in $\chi(T)$ at or around T^*. The peak height exceeds 1 J mol^{-1} K^{-1} at T^*, which is rather large given its non-magnetic origin. A comparable excess C_p is previously reported in the pyrochlore $Bi_2Ti_2O_7$ where the quenched configurational disorder among the Bi lone pairs results in departure from the Debye T^3 law [218].

In figure 6.4, C_p is shown for the O_2 annealed and 0.25% Al doped crystals; the corresponding data for as-grown crystal is also included for comparison. Below $T \approx 4$ K, where the long-distance dimerization of the unpaired spins is expected to set-in, C_p is enhanced due to O_2 annealing but suppressed for Al doping. However, in both cases, C_p exhibits a strong suppression in the region around T^*, which is what we are primarily interested in. The measured C_p of annealed and Al-doped crystals is also fitted using the eq. 6.1 to extract ΔC_p. The fitted curves are also shown in figure 6.4. In the inset, estimated ΔC_p is shown. In both cases, the phononic anomaly in ΔC_p decreases

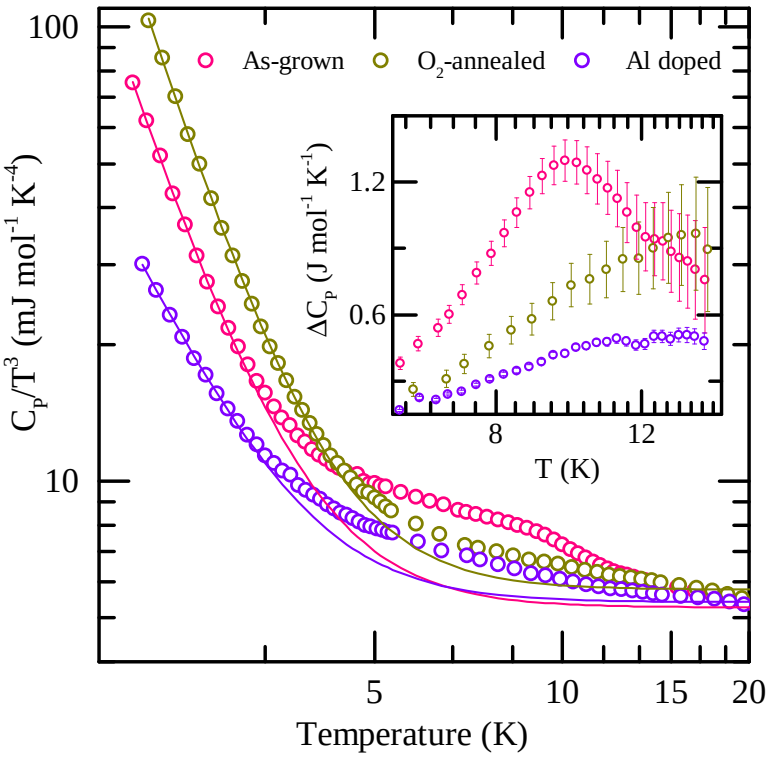

Figure 6.4: Specific heat (C_p) of as-grown, O_2 annealed and Al-doped crystals shown as a function of temperature in the C_p/T^3 representation. The solid lines in the main panel are the fitted lines that are extrapolated for $T > 3$ K. In the inset ΔC_p is plotted as a function of temperature (see text for details). The error bars are taken directly from the PPMS data file.

in magnitude and shifts towards higher temperatures. To investigate this further, we studied THz-TDS for all three specimens which is presented next.

6.2.3 Dependence of excess C_p on crystal growth experiments and annealing treatments

In figure 6.5, the specific heat (as-measured data) of several single crystalline specimens is shown in the low-temperature range. The samples are designated as G_iS_jm, where the subscript j refers to the j^{th} specimen from the growth experiment labeled i. 'm' is the mass of sample measured in mg. The figure emphasizes small variations in C_p in the low-temperature range, which suggests that excess C_p is highly sensitive to the stoichiometry as expected of an IC composite crystal. In the O_2 annealed specimen the

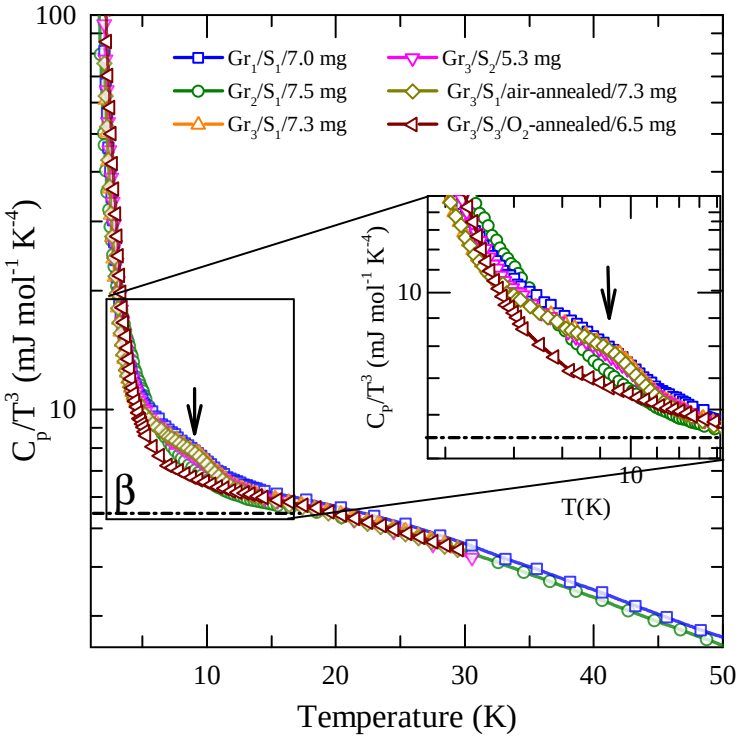

Figure 6.5: Specific heat (C_p) of several as-grown single crystalline specimens plotted as C_p/T^3 Vs. temperature (T). The excess specific heat is marked by an arrow. The dashed horizontal line corresponds to the βT^3 contribution of the three *acoustic* modes. Small variation in the magnitude of excess C_p between Gr_1S_1, Gr_2S_1 and Gr_3S_1 suggest that the excess C_p is highly sensitive to the stoichiometry as expected for an IC composite crystal.

excess C_p has diminished considerably, presumably due to a significant change of the oxygen stoichiometry. Interestingly, air-annealing at the same temperature and for the same duration has a negligible effect on C_p (see Gr_3S_1 and Gr_3S_1/air-annealed); this suggests that the excess C_p is suppressed due to a change in the oxygen stoichiometry rather than homogenization due to annealing.

6.2.4 Terahertz time-domain spectroscopy (THz-TDS)

In figure 6.6(a), the THz signal transmitted through the sample is shown for the as-grown, oxygen annealed and Al-doped crystals at $T = 14$ K and with electric field (**E**) polarized along the c-axis (E $\parallel$ c). The reference signal without the sample is also shown. The THz electric field of the as-grown crystal can be broadly characterized by

the presence of two types of oscillations having periods ~ 1 and ~ 4 ps. For E || a (not shown), the THz signal showed no oscillations in line with the data reported earlier by Thorsmølle et al. [210]. As shown in figure 6.6, for E || c, the annealed and doped crystals show a significantly different behavior compared to the as-grown crystal. To assess this difference quantitatively, THz transmittance for all three samples is shown in figure 6.6(b). The transmittance drops by more than an order of magnitude within a sharply defined window between ~ 0.3 THz to ~ 1 THz (1 THz = 1 ps = $33.3cm^{-1}$ = 4.1 meV) in agreement with Ref. [210]. The lower and upper cut-offs near 0.3 and 1 THz correspond to the slow and fast oscillations, respectively.

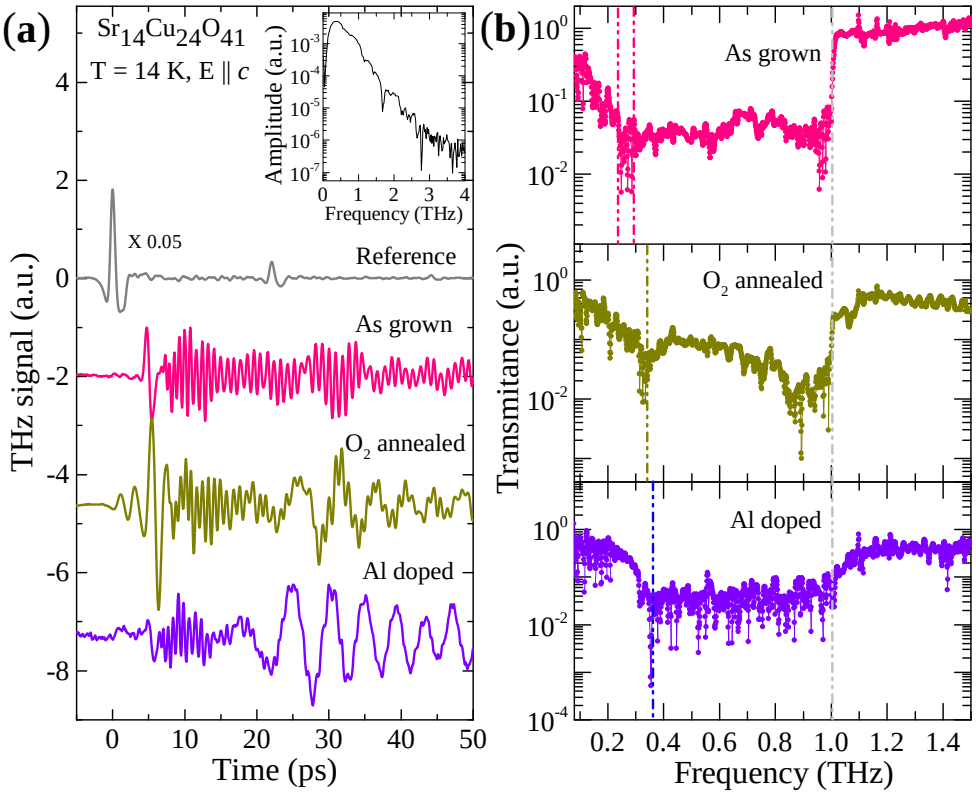

Figure 6.6: (a) Transmitted THz electric field (E) at T = 14 K, and for E || c; (b) THz transmittance for E || c at T = 14 K for the as-grown, oxygen annealed (O_2 ann) and Al-doped $Sr_{14}Cu_{24}O_{41}$ crystals. Inset in the left panel shows the fast-Fourier transform amplitude spectrum of the THz electric field for the reference.

As mentioned earlier, $Sr_{14}Cu_{24}O_{41}$ has an IC structure with oppositely charged layers whose relative sliding motion gives rise to new gapped phonon modes. New IR modes were previously reported near 0.3 THz (lower cut-off) [210]. In the inelastic

neutron scattering investigations also low-lying optical phonon modes were revealed in the same energy range [211]. In Ref. [210], it was conjectured that these modes are due to the relative sliding motion of oppositely charged chain and ladder sheets. In the THz transmittance data of our as-grown crystal, we also see absorption modes near the lower cut-off in the frequency range 0.25 to 0.30 THz. In order to find out if these modes are indeed due to the sliding motion as conjectured earlier or not, we measured THz transmittance of an O_2 annealed crystal. Interestingly, upon O_2 annealing, these modes merged to yield a sharper absorption band whose center shifted to a higher frequency near 0.35 THz. In the following we show that this dramatic shift is consistent with the sliding motion scenario.

6.3 Discussion

We recall that the degree of incommensurability in the IC systems depends sensitively on it stoichiometry [219]. In the present case, one can expres the stoichiometry in terms of parameter α as $[CuO_2]_\alpha[Sr_2Cu_2O_3]$, where $\alpha = 10/7$ for an ideal formulation. However, as shown by Hiroi et al., as-prepared $Sr_{14}Cu_{24}O_{41}$ samples exhibit a broad distribution of α values around the commensurate point $\alpha = 10/7$. Interestingly, by oxidizing or reducing the sample, the distribution width of α narrows considerably [156]. In another words, the as-prepared samples exhibit a high and varying degree of incommensurability, which can be reduced by annealing. We believe that oxygen annealing has a similar effect in our crystal; i.e., it reduces the degree of misfit between the chains and ladders, which results in the suppression of the excess specific heat associated with sliding motion that results from this misfit. In the appendix, we show C_p for several as-grown and annealed crystals. It is shown that unlike O_2 annealing, due to air annealing the excess C_p diminishes only negligibly, which reinforces the point that oxygen stoichiometry is important.

The effect of Al doping is more complex as it not only affects the oxygen stoichiometry as discussed next but also acts as a pinning center owing to its different ionic radius and charge state compared to the host ion. In Ref. [216], it has been shown that the

effect of Al-doping on $\chi(T)$ can only be correctly accounted for if one assumes that Al is doped in the ladder sheets. Since Al concentration is very small, to understand its effect on the sliding motion we first consider the effect of Al doping on the oxygen stoichiometry. Since Al^{3+} replaces Cu^{2+} in the ladders, the charge neutrality requires an equivalent quantity of oxygen absorption by the sample unless some Cu^{2+} reduces to Cu^{1+} which is unlikely due to an oxygen rich crystal growth atmosphere; in that sense the effect of Al doping is analogous to O_2 annealing. However, Al^{3+} impurities are also expected to *pin* the sliding DW in a manner analogous to impurity pinning in charge and spin DW systems.

An equally dramatic effect of Al doping is also seen on the upper cut-off of the transmittance near ~4 meV energy (1 THz), which shows a much higher sensitivity to Al doping compared to O_2 annealing. This can be understood by assuming that the upper cut-off in THz transmittance arises due to the CDW ordering in the ladder sheets. The doping of Al in the ladders probably destroys the CDW ordering to some extent, resulting in a smearing of the upper cut-off. Oxygen annealing, on the other hand, as shown by Hiroi et al. [156], results in an increase in number of free spins due to breaking of the dimers in the chains. It, therefore, has a little or no effect on the CDW ordering in the ladder sheets, which explains why the upper cut-off remains sharp and unshifted upon O_2 annealing. Further work to understand the role of impurities on the upper cut-off is currently under progress.

We now discuss the excess C_p near T^* and its subsequent suppression upon lightly doping or annealing the sample. The temperature variation of χ shows no anomalous feature around T^*, and it is well-fitted using the dimer-dimer model. This suggests a non-magnetic or phononic origin of the excess C_p. The assignment of excess C_p is also consistent with the field independent feature of ΔC_p. The conventional low-dimensional CDW systems [221], for example, $K_{0.3}MoO_3$ [222], $(TaSe_4)I$ [223], also show excess specific heat at low temperatures but this arises due to the collective phase (phason) and amplitude (amplitudon) modes of the IC modulation below the CDW transition [206]. Though $Sr_{14}Cu_{24}O_{41}$ also undergoes a CDW ordering in the ladders below $T \approx 200$ K, the CDW in this case is not accompanied by a lattice distortion, and is believed

to arise from the many-body electronic effects [224]. Therefore, a similar scenario as operative in conventional CDW systems seems inconceivable in the present case. Our experimental results suggest that the excess specific heat in $Sr_{14}Cu_{24}O_{41}$ arises from the relative sliding motion of the oppositely charged chain-ladder sheets, which is manifested in the form of THz modes near the lower cut-off of the transmittance window. The temperature $T^* = 10$ K of the peak in ΔC_p, and an almost exponential rate of decrease at lower temperatures are consistent with a gapped scenario with a gap size close to 1 meV. C_p and THz of the annealed and Al doped crystals also lend support to this interpretation. In the annealed sample, the peak in ΔC_p shifts to higher temperatures from $\sim$ 10.5 K to $\sim$ 13.5 K, this is in line with the observed stiffening of the lower cut-off from $\sim$ 0.28 THz (average ω for the as-grown crystal) to 0.35 THz upon oxygenation. In the case of Al-doped sample, the stiffening of the lower cut-off is even more pronounced, which is not unexpected since Al impurities besides changing the oxygen stoichiometry in a manner analogous to O_2 annealing also act as pinning centers impeding the sliding motion.

6.4 Summary

The sliding motion is manifested as 'new' normal mode in the phononic dispersion [225]. However, what makes these new modes, which were also previously observed in a few other incommensurate systems, highly interesting is the fact that the two types of sheets CuO_2 and $Sr_2Cu_2O_3$ are oppositely charged rendering the new modes quasi-acoustic or very low-lying optical modes. We investigated this gap using the specific heat probe to show the presence of rather large 'excess' specific heat (i.e., in excess of the Debye (T^3) contribution) associated with the gapped mode. We also show that these gapped sliding modes are highly sensitive to small structural changes introduced either by annealing the sample or by doping it with 0.25 % of a trivalent Al impurity. In both cases, we found a huge suppression of the excess specific heat, and simultaneously the THz probe tracked the changes in the oscillations associated with the sliding modes.

The presence of excess specific heat is generally associated with glassy or disordered solids, in the glass literature this is often referred to as the 'Boson peak' [226]. The excess specific heat has also been observed in a few other systems, including, conventional charge density wave (CDW) systems, and $Bi_2Ti_2O_7$ where the configurational disorder of the Bi ions in the pyrochlore lattice is responsible for the excess specific heat. To the best of our knowledge, our work provides the first example of a crystalline solid showing 'excess' specific heat due to the gapped sliding motion. The sensitive of it to very small structural changes make it a very interesting case to investigate further as a candidate material with the unconventional phononic ground state. We believe that this work will initiate a search for new materials with an unconventional phononic ground state, and in particular, systems where very low-lying optical branches with controllable phonon gap can be realized. Such systems may prove useful in understanding a wide range of behaviours including the disordered and glassy systems, and strong coupling superconductors [208].

In Summary, we showed the presence of a large excess specific heat in the IC chain-ladder compound $Sr_{14}Cu_{24}O_{41}$ around $T^* = 10$ K. However, no magnetic anomaly could be detected in the $\chi(T)$ data in this temperature range, which suggests that the excess C_p is of non-magnetic origin. The insensitivity of ΔC_p to the applied magnetic field further corroborates this conclusion. By using THz-TDS in the range from ~0.2 to ~1.4 THz, we argued that the excess C_p originates from the sliding phonon modes. Experiments on O_2 annealed and Al doped crystals revealed significant suppression of the excess C_p, and concomitant changes in the THz response associated with the sliding modes. A very high sensitivity of the THz response to minor structural changes suggest that $Sr_{14}Cu_{24}O_{41}$ has a highly unconventional phononic ground state which invites further investigations. Since Ca-doping at Sr site in $Sr_{14}Cu_{24}O_{41}$ is known to transfer holes from chains to ladders, in future, it will be interesting to perform a systematic THz and specific heat study on variously Ca-doped $Sr_{14}Cu_{24}O_{41}$ samples.

Chapter 7

Investigation of magnetic phase transitions, spin-reorientation and magnetization reversal in orthoferrite $HoFeO_3$

7.1 Introduction

Orthoferrites $R\mathrm{FeO_3}$, R being a tripositive rare-earth ion or Y^{3+}, constitute an important class of materials crystallizing with a distorted perovskite structure of orthorhombic *Pbnm* symmetry [227]. They feature two types of magnetic sublattices: R^{3+} where $4f$ electrons contribute to the magnetic moment (exceptions being La^{3+}, Lu^{3+} and Y^{3+} that are non-magnetic) and Fe^{3+} where the magnetism arises due to the $3d^5$ electrons. In their temperature dependent response $R\mathrm{FeO_3}$ compounds exhibit multiple phase transitions due to exchange coupled R^{3+} and Fe^{3+} sublattices.

Here, we report on a relatively less studied member $HoFeO_3$ (HFO) of this series. The crystal structure of HFO is shown in figure 7.1 and the crystallographic parameters are discussed in chapter 3. Analogous to other members of $R\mathrm{FeO_3}$ family with a magnetic R sublattice, HFO exhibits a cascade of magnetic phase transitions. The Fe^{3+} moments order antiferromagnetically (AFM) along the a-axis (G-type) below $T_N = 643$ K. Due to weak f-f exchange the AFM ordering of the Ho^{3+} moments takes place at a

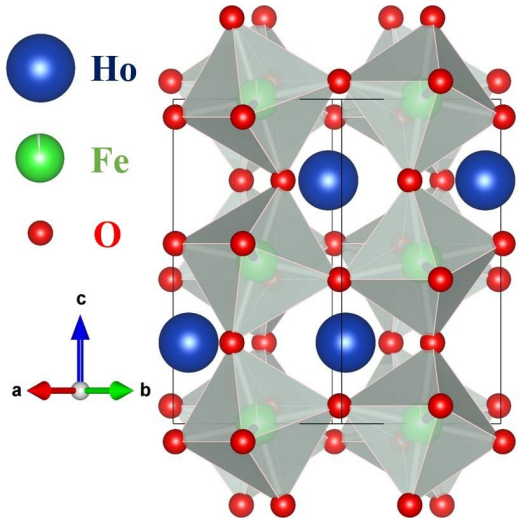

Figure 7.1: Crystal structure of HFO is shown. The figure is produced using VESTA.

much lower temperatures (T < 5 K). However, their role in spin-reorientation, via the *f-d* coupling, is supposedly important, but not fully understood. The Ho^{3+} ion, in particular, has one of the largest ionic magnetic moments (10 μ_B), which combines with its strong single-ion anisotropy, derived from the crystal electric field splitting of the lowest J = 8 multiplet to give rise to several interesting magnetic properties.

In the antiferromagnetic (AFM) state below T_N, the Dzyaloshinskii-Moriya (DM) interaction induced canting of the Fe^{3+} moments results in a weak ferromagnetic (WFM) moment along the *c*-axis of the unit cell. At low temperatures, below T ≈ 60 K, the AFM axis rotates from *a*- to *c*-axis, which results in a reorientation of the WFM moment ($\Delta\mathbf{m}_{Fe}$) from *c* to *a*. The exact manner in which the spin reorientation occurs is not very clear. It is generally believed that the *a*- to *c*-axis rotation occurs in the ≈ 60 - 50 K temperature range along the *ac*-plane[227]. However, using M*ö*ssbauer spectroscopy, Nikolov et al. suggested that during reorientation upon cooling below 60 K, the AFM axis leaves the *ac*-plane around 50 K to turn towards the *b*-axis, and thereafter it continues turning until aligned completely along the *c*-axis around 40 K [228]. A recent M*ö*ssbauer study by Ryan et al. also found a similar behavior but showed that the reorientation completes at 35 K [229]. Zeng et al. used the Terahertz time domain spectroscopy (THz-TDS) to investigate the spin reorientation region [120]. They also proposed two intermediate steps in the spin reorientation region extending from ≈60 to

35 K range (see figure 1.21 in chapter 1 [120]). More recently, Chatterji et al. revisited the magnetic phase transitions in HFO using neutron diffraction on single crystalline specimens [121]. They proposed a *G*-type ordering of the Fe moments in the temperature range $T_N \leq T < 55$ K, an abrupt rotation of the AFM axis below 55 K to point along the *b*-axis, and finally an abrupt rotation along the *c*-axis below T = 35 K to complete the process. Apart from this, two more *new* transitions were reported at lower temperature near 20 and 10 K due to switching of a component of Ho moments along the *c*-axis.

Here, we first show the presence of spin-reorientation transition (T_{SR}) by using the magnetic susceptibility and specific heat probes. We then examine in details the spin-reorientation region using the highly-sensitive torque magnetometry to search for the additional phase transitions previously reported. We also report here the presence of spin-switching in HFO above room-temperature, which has not been previously reported to the best of our knowledge.

7.2 Magnetization

7.2.1 Magnetization below room-temperature

In figure 7.2, we show the temperature dependent magnetization of both the air grown (HFO SC1) and argon grown (HFO SC2) crystals from temperature 2 K to 100 K in the presence of 100 Oe magnetic field. The measurements were carried out as follows: the sample was cooled down to the lowest temperature at 2 K under zero magnetic field and then a magnetic field of 100 Oe was applied. The measurements were then carried out while heating the sample. This is denoted as *ZFW* (zero-field-warming). We also measured the *FCW* (field-cooled-warming) data where the sample was cooled down in a magnetic field and measurements were taken while warming. The *ZFW* and *FCW* data overlap over the entire temperature range for HFO (not shown) and hence all the data reported here are measured under the *ZFW* condition. The temperature dependence of magnetization (*M*-*T*) along *a* - and *c* - axis of two crystals is shown in

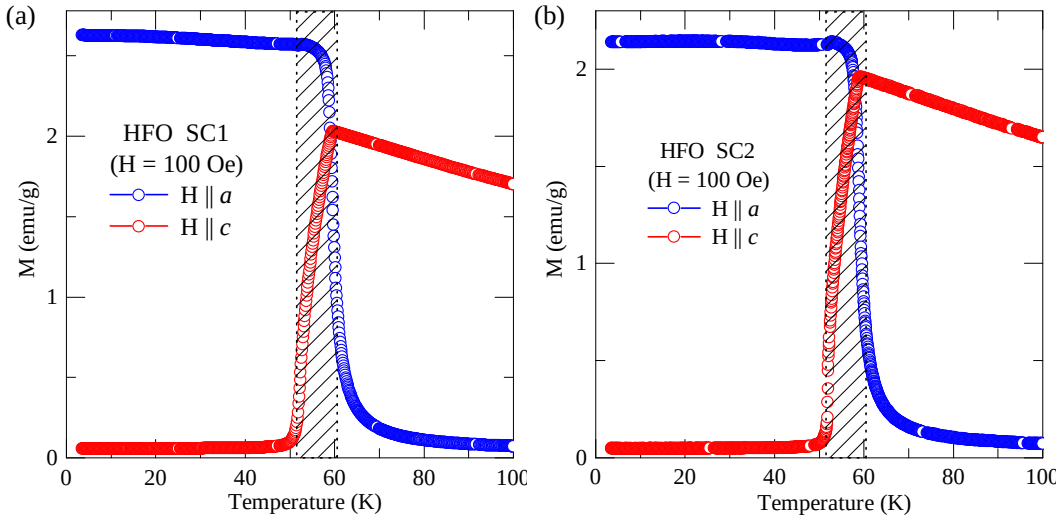

Figure 7.2: Spin reorientation from c-axis to a-axis is observed for both the (a) air grown HFO SC1 and (b) Ar grown HFO SC2 crystals in ZFW measurement.

figure 7.2. It shows the spin-reorientation in the range 50 K - 60 K. In this range, while M_c diminishes to a very small value (nearly zero on the scale bar shown), M_a shows an opposite trend. This is often interpreted as orientation of the AFM axis from *a* to *c* or rotation of *WFM* moment ($\Delta\mathbf{m}_{Fe}$) from *c* - to *a* - axis. Both the samples (HFO SC1 and HFO SC2) showed exactly the same behaviour. However, there is a slight mismatch in magnitude of the moments (see table 7.1), which can be due to small differences in the stoichiometry of the two samples.

Table 7.1: Comparison of magnetizations between air grown (HFO SC1) and Ar grown (HFO SC2) crystals (values are in emu/g).

Sample	T = 3.5 K	T = 52.6 K	T = 59 K	T = 100 K
HFO SC1 (H || *a*)	2.63	2.57	–	0.07
HFO SC2 (H || *a*)	2.14	2.13	–	0.07
HFO SC1 (H || *c*)	0.06	–	2.03	1.7
HFO SC2 (H || *c*)	0.05	–	1.95	1.65

On the other hand, M_b shows a monotonic increase upon cooling with no signs of any anomaly in the spin-reorientation region (figure 7.3). The peak in M_b at very low-temperatures is due to the AFM ordering of the Ho^{3+} moments. The data were taken under the applied magnetic fields of H = 200 and 500 Oe and for both field values the low temperature anomaly due to Ho^{3+} moments ordering is observed below 5 K. The

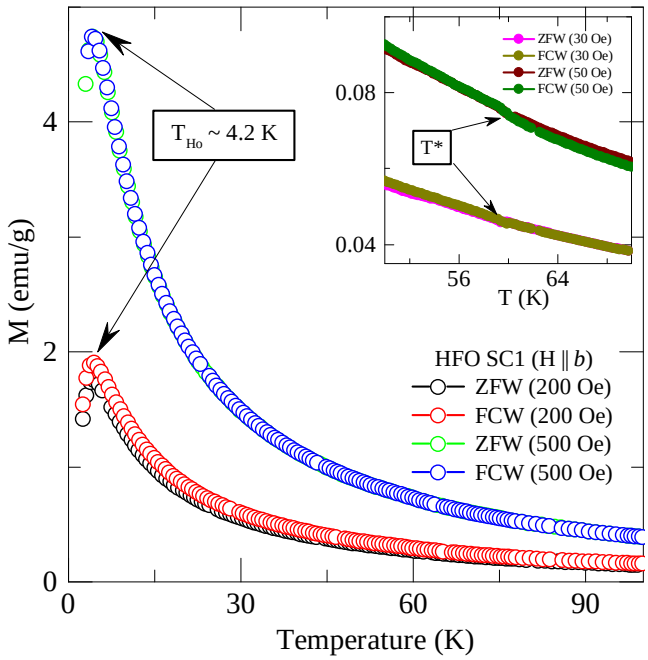

Figure 7.3: The magnetization of HFO SC1 crystal along *b*-axis shows the Ho-Ho ordering (T_{Ho}) below 5 K and inset shows the spin reorientation region (T^*) in presence of low magnetic fields.

absence of any anomalous feature in M_b in the spin-reorientation region suggests the bulk magnetization is not sensitive enough to have any observable effect in the spin-reorientation region. However, in the presence of a small applied magnetic field (30 and 50 Oe), a weak anomaly can be seen while cooling and heating the sample across the spin reorientation (T_{SR}) region (see the inset of figure 7.3).

We measured the isothermal magnetization at different temperature along different crystallographic axes of HFO crystals. We show field dependent magnetization, below and above the spin reorientation region, and for applied magnetic field along the *a*-axis (shown in figure 7.4) and *c*- axis (shown in figure 7.14(a)). Since below T_{SR}, the Fe spins are aligned along the *a*-axis (Γ_2 phase), the magnetization increases once the sample is cooled below T_{SR}. The field dependent magnetization along the *c*-axis shows hysteresis and will be discussed later.

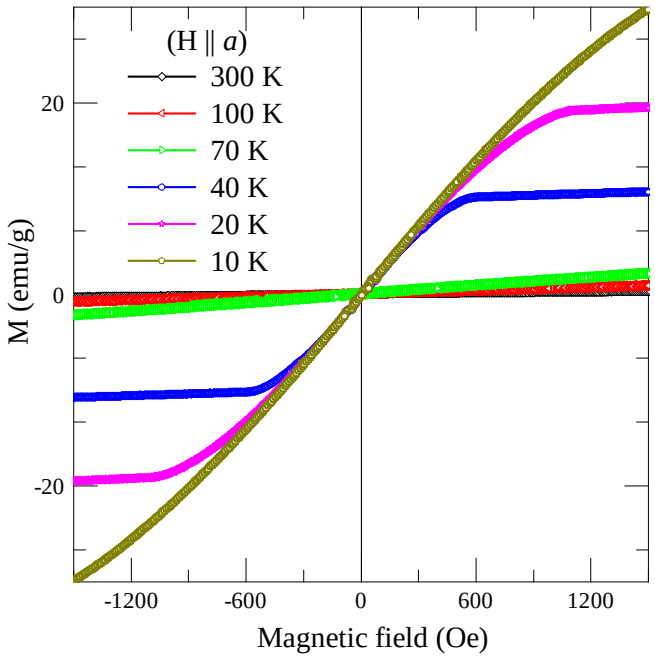

Figure 7.4: Isothermal magnetization (*M-H*) of HFO for H || *a*, do not show any hysteresis below room temperature.

7.2.2 Magnetization above room-temperature

The high temperature magnetic measurements were carried out in a VSM Oven (300 K to 750 K) attached to the PPMS. In the high temperature magnetic studies, the measurement protocol is important. The temperature dependent magnetization were measured using the following procedure: (i) samples were heated upto 750 K (above T_N); and thereafter the magnetic field was set to zero in oscillation mode. Following this, the sample was cooled-down to room temperature under zero field; and, measurement was then taken while heating (denoted as *ZFW*) after applying the desired magnetic field; after reaching the highest temperature (750 K), the measurement was stopped; and waited for 2 minutes and then again started the measurement while cooling the sample down to room temperature in the presence of a magnetic field (denoted as *FCC*); (ii) In this case, the sample was cooled down to room temperature in presence of a magnetic field and measurement was taken while heating the sample (denoted as *FCW*) in the presence of desired magnetic field. We also measured the isothermal magnetization (*M-H*). These were done at different temperatures (in a descending order from or above T_N) and after

measuring *M-H* at each temperature, the magnetic field was set to zero in the oscillatory mode to reduce any remnant magnetization in the superconducting magnet.

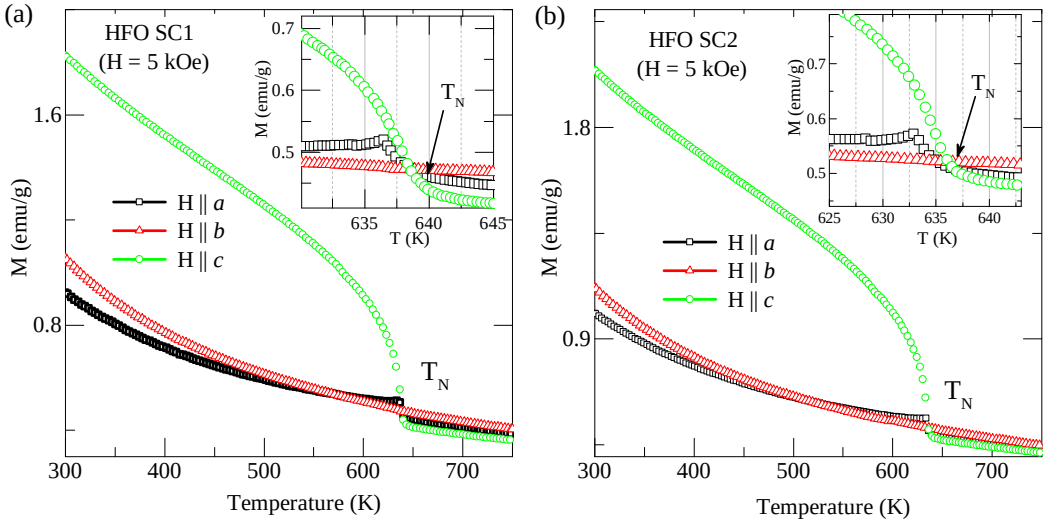

Figure 7.5: High temperature magnetic data (ZFW, H = 5 kOe) along three crystallographic directions show the presence of T_N of (a) air grown (HFO SC1) and (b) Ar grown (HFO SC2) crystal.

In figure 7.5, we have shown the presence of Néel ordering temperature along all the three crystallographic directions under a magnetic field of 5 kOe. We observed an anomaly along *a*-axis for both the HFO SC1 (~ 636 K) and HFO SC2 (~ 633 K) crystals, which corresponds to the Néel ordering. Below the Néel temperature, a weak ferromagntism appears along the *c* - axis, which is evident from a sharp increase in the c - axis magnetization below the Néel ordering temperature (T_N). The magnetization along the *b*- axis also shows a weak anomaly near T_N for both the crystals. Under 5 kOe applied field, these were the only informations that one could gather from the bulk magnetization. However, in the presence of a magnetic field H $\leq$ 1000 Oe, we found a surprisingly rich behaviour along the *c* - axis which is described in section 7.5.

7.3 Specific heat

Along with the magnetic measurement, we also carried out the specific heat study on HFO SC1 (mass = 35.5 mg). The specific heat C_p is shown in figure 7.6. The anomaly

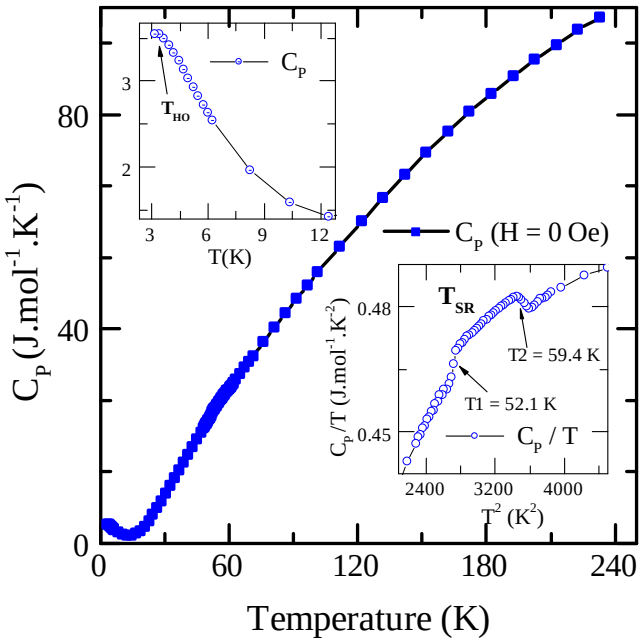

Figure 7.6: Heat capacity data of HFO SC1; insets show low temperature Ho-Ho ordering (T_{Ho}) and the spin-reorientation region (T_{SR}).

at low-temperatures (upper inset) is due to long-range ordering of the Ho^{3+} moments. A careful inspection of the measured specific heat shows two anomalies around the re-orientation region. In the lower inset of figure 7.6, C_P/T vs T^2 plot clearly reveals the presence of anomalies at $T_1 \sim 52.1$ K and $T_2 \sim 59.4$ K, consistent with the magnetization data. The sharpness of these anomalies suggests a high-quality of the single crystal used in our study. Our magnetization and specific heat data show a good overall agreement with previous reports [103, 230, 231].

7.4 Torque magnetometry

The torque magnetometry (TqMAG) is a very sensitive technique for probing magnetically anisotropic material, which exerts a torque when the magnetization ($\vec{M}$) is not aligned along the applied magnetic field ($\vec{H}$). In the presence of a weak magnetic field, the magnetization ($\vec{M}$) can be expressed in term of the susceptibility tensor (χ_{ij}) as:

$$M_i = \chi_{ij} H_j \tag{7.1}$$

For a HFO crystal, the torque ($\vec{\tau} = \vec{M} \times \vec{H}$) about the orthogonal $\vec{a}$, $\vec{b}$ and $\vec{c}$ - axis can be expressed as follows [232]:

$$\tau_a = \pm\sigma_0 H sin\theta - \frac{(\chi_c - \chi_b)}{2} H^2 sin(2\theta) \tag{7.2}$$

for $\vec{H}$ in the bc - plane;

$$\tau_b = \pm\sigma_0 H sin\theta - \frac{(\chi_c - \chi_a)}{2} H^2 sin(2\theta) \tag{7.3}$$

for $\vec{H}$ in the ac - plane; and,

$$\tau_c = -\frac{(\chi_a - \chi_b)}{2} H^2 sin(2\alpha) \tag{7.4}$$

for $\vec{H}$ in the ab - plane,

where, σ_0 is the spontaneous magnetization, which we assume to be along the c - axis; while driving eqns 7.2, 7.3 and 7.4; χ_a, χ_b, and χ_c are the susceptibilities along a, b and c - axis, respectively; θ is the angle between magnetic field H and c - axis; and α is the angle between H and a - axis.

One of the drawbacks of bulk magnetizations in the present case is that any minor spin reorientations remain hard to detect due to an overwhelming paramagnetic background of the Ho^{3+} moments. Similarly, due to an increasingly growing phonon background at higher temperatures (typically temperatures exceeding one-tenth of the Debye temperature which is close to 300 K for orthoferrites), C_p also becomes insensitive to minor spin reorientations. In such cases, TqMAG is a very effective probe due to its insensitivity to the paramagnetic background or phonon or either of which exerts no torque.

The detailed working principle of this technique is described in section 2.3.4 in chapter 2. However, here, before proceeding further it will be useful to introduce the notations used in the subsequent text. A photograph of the torque-lever arrangement along with a schematic of the torque-lever chip on which a single-crystal specimen is loaded is shown in figure 7.7. Here, $\hat{\eta}$ is the axis about which the chip rotates in a

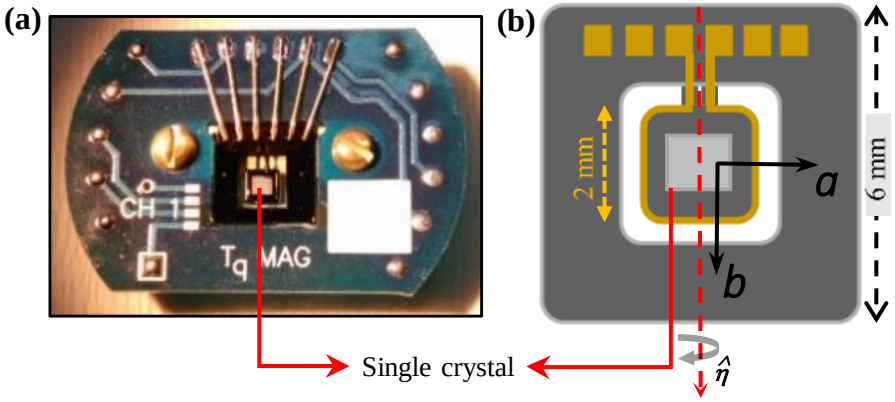

Figure 7.7: (a) Crystal is mounted on torque-lever assembly (H $\perp$ *b*) (b) schematically *ac* - plane rotation (τ_b^{ac}) is shown; $\hat{\eta}$ is the rotational axis along *b*.

vertical rotator with $\vec{H}$ always perpendicular to the axis of rotation $\hat{\eta}$. It lies in the plane of the chip between the two lever arms as shown in figure 7.7(b). The chip can be turned either manually or in an automated mode using a goniometer (not shown) located outside the cryostat.

In figure 7.7, which serves to illustrate a representative case, the crystal specimen is mounted with its *ab*-plane glued to the chip. The *b*-axis is along the rotation axis $\hat{\eta}$. The angle of rotation θ is the angle that the normal to the chip (*c* - axis) makes with respect to the field $\vec{H}$ that acts along the vertical direction. Hence, $\theta = 0°$ corresponds to the horizontal position. Consider the configuration shown in figure 7.7(b); if the crystal is magnetized along the *a*-axis, the torque $\vec{\tau} = \vec{m} \times \vec{H}$ will tend to twist the chip anti-clockwise about the *b*-axis. We shall designate such a twisting moment (independent of its direction) using τ_b. However, in the same $\theta = 0°$ configuration, if the crystal happens to be magnetized along the *b*-axis then a bending moment will be produced about the *a*-axis which will tend to *bend* the lever arms either up or down resulting in an equal compression or elongate of both the lever arms; and, therefore, the differential change that measures the torque will be nearly *zero*, as $\Delta(R_1 - R_2) \simeq 0$. Similarly, in $\theta = 0°$ configuration, the magnetization is along *c* - axis, and so is $\vec{H}$, hence no torque will be produced.

7.4.1 Field-dependent torque

In figure 7.8, we show the isothermal TqMAG data at T = 100 K. This data is obtained for the same configuration as shown in figure 7.7(b) except that the angle θ = 45 ± 5° (θ is the angle between $\vec{H}$ and c- axis). From the M-T data, we know that at 100 K the *WFM* associated with the Fe sublattice (Δm_{Fe}) points along the c-axis. In a vertical field $\vec{H}$, it will produce a torque τ about b (τ_b). The field variation of τ_b is shown in figure 7.8(a). The arrows show the measurement sequence. For comparison, M-H (for H ∥ c) at 100 K is also shown in figure 7.8(b). The isothermal magnetization is

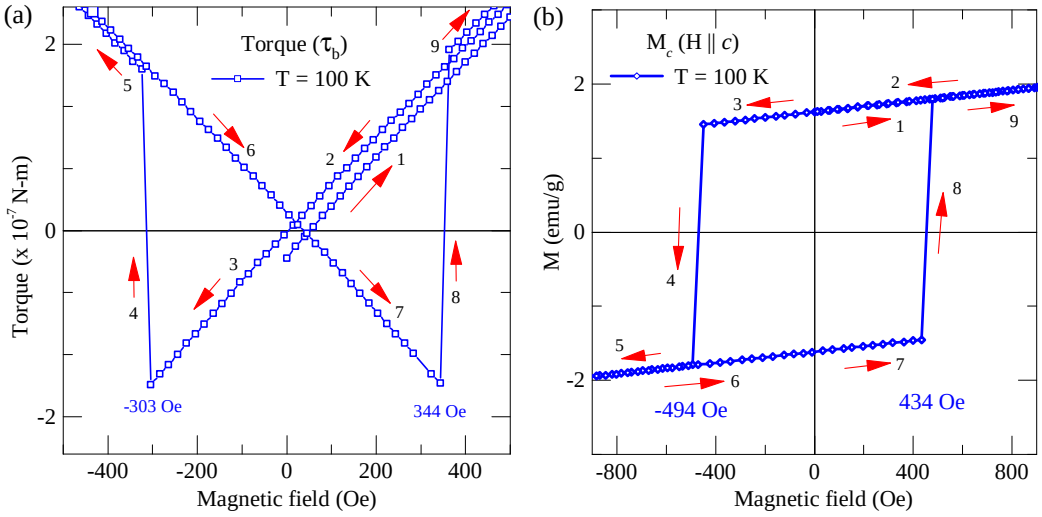

Figure 7.8: (a)Torque (τ_b^{45}) vs magnetic field at 100 K shows a sharp switching from negative to positive torque. The angle between applied field $\vec{H}$ and c - axis is 45°. (b) Magnetic reversal in the isothermal magnetization (M-H) at 100 K corroborates the switching in torque data. The arrows are used to guide the measurement sequences.

characterized by the presence of a rectangular M-H loop with very *sharp* magnetization switchings at - 494 Oe and 434 Oe. The remnant magnetization (M_r) is close to 1 emu/g. A small linear increase in the magnetization with field can be attributed to the paramagnetic response of the Ho sublattice. The leftward shift of the loop indicates the presence of an exchange bias field of about 100 Oe. Recently, large EB fields have also been reported for single-crystals of $ErFeO_3$ [107, 108] and $SmFeO_3$ [109]. As shown in figure 7.8(a), τ_b also shows a field-induced switching consistent with the M-H loop. The τ_b loops are shifted rightward which is due to an opposite direction of the magnetic

polarization while loading the specimen. The experimental field at which τ_b flips is -303 and 343 Oe. Theoretically, we expect this field to be $H_c cos45°$, where H_c is the coercive field obtained from the *M-H* loop (- 494 and 434 Oe) shown in panel (a); and we see that there exists an excellent agreement between the two techniques.

Having established this equivalence, we now proceed to investigate the magnetic behavior of HFO using TqMAG. First we will discuss the angular dependent torque magnetometry at different temperatures, which will be followed by temperature dependent TqMAG.

7.4.2 Angular-dependent torque

In the configuration shown in figure 7.7(b), the rotational axis $\hat{\eta}$ is along *b* - direction. First, we will discuss the angular dependent magnetometry at room temperature (300

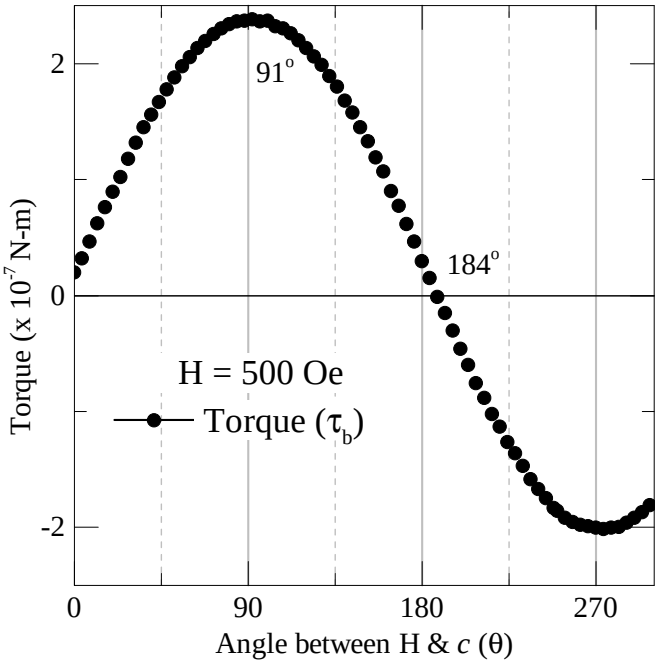

Figure 7.9: Torque magnetometry measurement (τ_b vs θ) in the *ac* plane in presence of H = 500 Oe shows sinusoidal behaviour at room temperature (300 K). No switching in the torque is observed.

K) in presence of different applied field (H) strengths. In figure 7.9, we have shown the torque (τ_b) while rotating the crystal in the presence of a 500 Oe field. The torque

data shows a sinusoidal behaviour with a period of 2π, in agreement with eq. 7.3. The contribution of second term to τ_b is expected to small due to a nearly saturated magnetization. We also measured torque in the presence of higher magnetic fields and observed torque switching above a field of 1000 Oe (figure 7.10) which nearly coincides with the coercive field at this temperature (see figure 7.14). As expected, with increasing

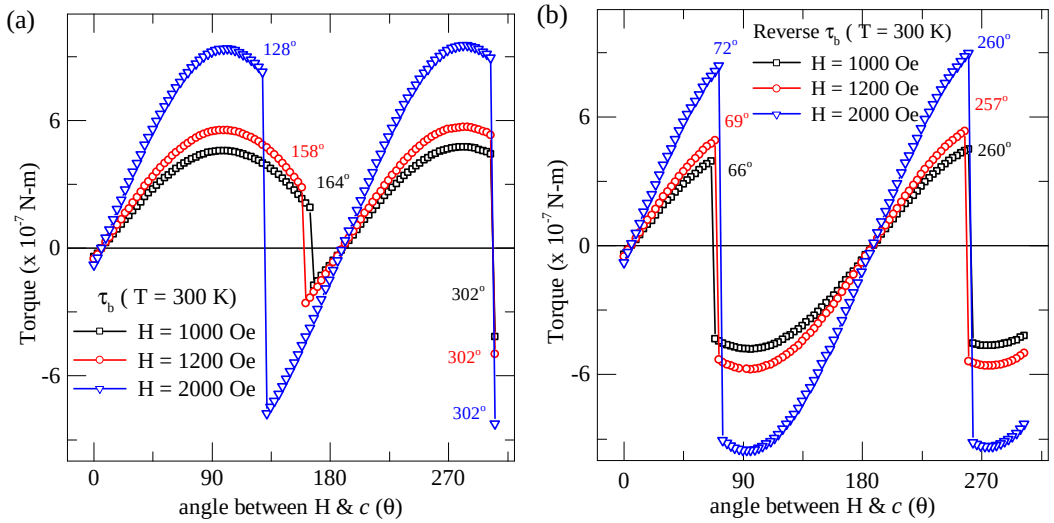

Figure 7.10: (a)Torque (τ_b) vs θ at room temperature in presence of different magnetic field strengths. The switching angle shifted towards lower angle with increasing field. (b) For reverse direction, the angle difference between first and second switching is 188-190 ° for all magnetic fields.

field strength, the angle θ_{SW} at which the torque switches shifts towards lower angles. In figure 7.10(b), we have also measured the torque while rotating the crystal in the reverse direction and observed a constant difference between the two switching values.

7.4.3 Temperature-dependent torque

In figure 7.11, we have shown the temperature dependent torque under an applied magnetic field (H = 1000 Oe) from the temperature range 2 - 300 K. The measurements were carried in the similar configuration as shown in figure 7.7. For θ = 0 ° and $\vec{H} \parallel c$,

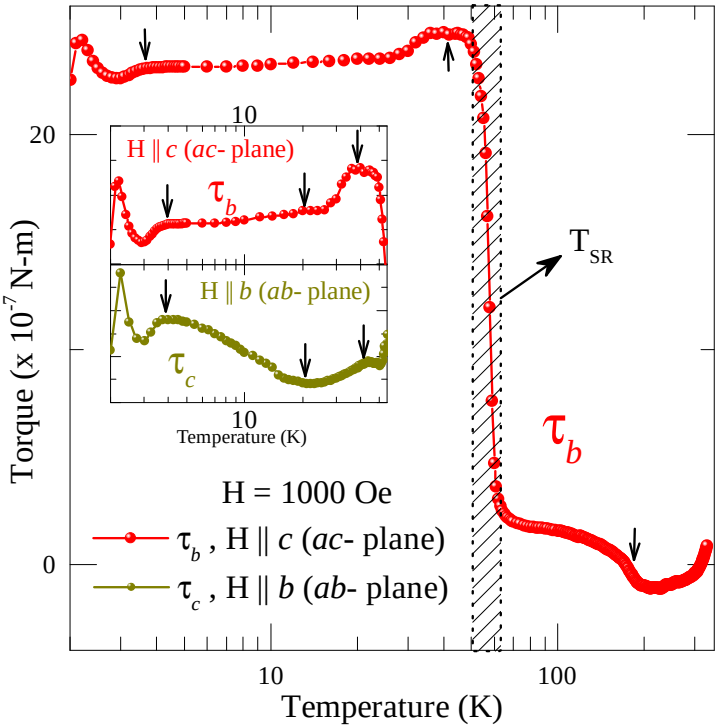

Figure 7.11: Temperature dependence of τ_b for $\vec{H} \parallel c$. The spin reorientation (T_{SR}) region is shown as the hashed region. Insets show the magnified τ_b (*ac*- plane) and τ_c (*ab*- plane, see figure 7.12) below the spin reorientation temperature. Arrows are used to show the presence of new weak transitions along with the previously reported transitions [121] (see the text for details).

the measured torque is defined as τ_b. At room temperature, since *WFM* of Fe spins are along the *c*- direction, hence, one would expect no torque (measured $\tau_b \simeq 10^{-8}$ N-m). Upon cooling the torque data shows the spin-reorientation region (50 K to 60 K), where τ_b increases rapidly as Δm_{Fe} (*WFM*) rotates from *c*- axis to *a*-axis while cooling.

Apart from the spin-reorientation region, the TqMAG data also show the presence of other transitions above and below T_{SR}. These are shown by arrows in figure 7.11. The temperature dependent torque τ_b reveals a step-like change around T = 35 K, which corroborates the recent neutron study by Chatterji et. al. [121], where a change of

magnetic structure from Γ_1 to Γ_2 was reported. Chatterji et. al. also reported further changes as degree of Ho order increases upon cooling below T = 35 K. These changes occur near T = 20 K and T = 10 K where the weak FM of Ho moments changes sign relative to $\mathbf{M}_{Ho} \times \mathbf{M}_{Fe}$ as shown in figure 1.22 in chapter 1.

In our TqMAG data (τ_b), we do see a very weak anomaly near T = 20 K (as shown in the upper inset of figure 7.11). Since the ordered Ho- moments is along the *b*-axis [121, 122], with a very weak ferromagnetic component along the *a*- axis, which changes sign from positive to negative at 20 K and again from negative to positive near 10 K; its signatures will also be expected in τ_c measurements ($\hat{\eta} \parallel c$ and H $\parallel$ *b*- axis ($\theta = 0^\circ$); see figure 7.12). Indeed, in τ_c we see a clear minimum around 20 K which confirms the 20

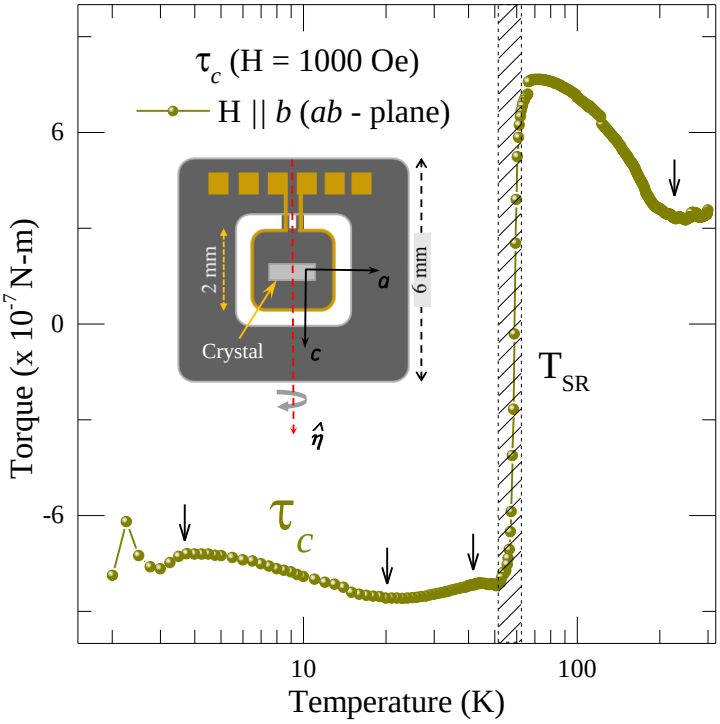

Figure 7.12: The measured torque τ_c ($\vec{H} \parallel b$) in the *ab* - plane reveals the presence of new transitions along with T_{SR}. Inset shows the configuration during the torque measurement.

K transition reported by Chatterjee et al. [121]. Additionally, in all the measurement configurations, we observed anomalies near T = 5 K and 200 K. These anomalies were not previously reported. However, no anomaly is found near T = 10 K. Finally, the peak

in τ_b and τ_c at low-temperatures (T $\simeq$ 2.5 K) is presumably due to ordering of the Ho - moments.

7.5 Spin-switching transition

In figure 7.13(a), we have shown the temperature dependent magnetization along the crystallographic *c*- direction in the presence of magnetic field (H = 100 Oe) for T > 300 K. The measurements were carried out as follows: the sample was heated above the Néel ordering temperature ($T_N \sim 643$ K) and then cooled down to room temperature (300 K) under zero field. Then, after applying a magnetic field (H = 100 Oe), the measurement is carried out while heating from 300 K to 750 K (named as *ZFW* in figure 7.13(a)). At room temperature, the *ZFW* data shows negative magnetization;

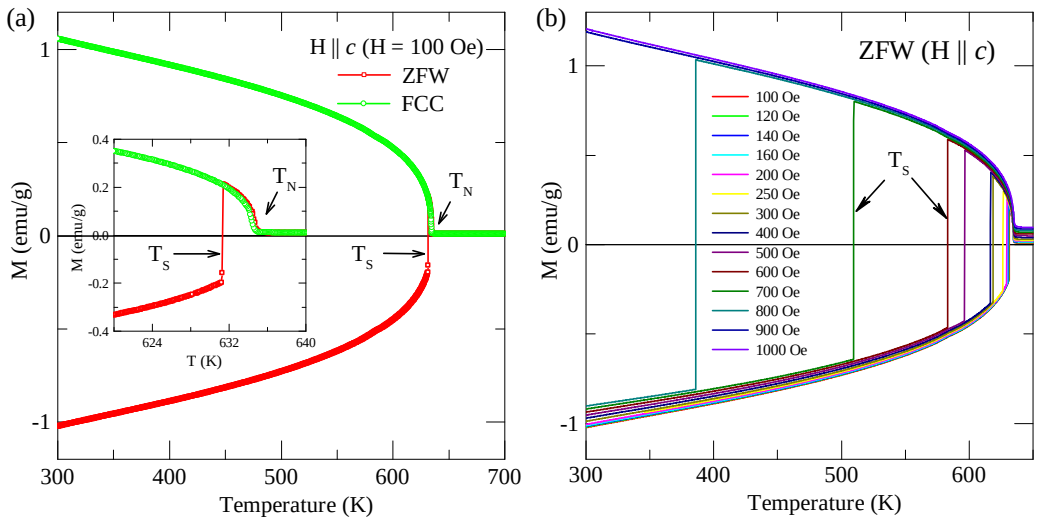

Figure 7.13: (a) *ZFW* (zero-field-warming) data along the *c*- axis of $HoFeO_3$ revealed the temperature induced sharp spin switching transition (T_S) above room temperature, the arrows guided the switching mechanism (H = 100 Oe) (b) Switching transition (T_S) can easily be tuned by varying the magnetic field strength. Above 800 Oe, the switching transition disappeared above room temperature.

and, interestingly, the negative magnetization switches to positive value around 630 K. The inset of figure 7.13(a) shows the spin switching region along with the Néel ordering temperature (T_N). The magnetization undergoes a sudden change in sign from negative to positive value, showing a mirror-like symmetry with respect to zero magnetization at

the transition point. However, the *FCC* data shows only positive magnetization down to room temperature (300 K).

Recently, a similar magnetization has been reported for $SmFeO_3$ crystals below room temperature [12]; and the origin of that has been explained as due to the presence of two magnetic sublattices Sm and Fe, as shown in figure 1.20 in chapter 1. Here, in the case of $HoFeO_3$, the spin switching is more surprising for two reasons, firstly, it occurs above room temperature and secondly, its origin can not be explained using the two sublattice model since Ho spins behave para-magnetically above room temperature [121]. This is further established from the fact that the switching transition (T_S) shifts towards lower temperatures upon increasing the applied field strength. In figure 7.13(b), we have shown the *ZFW* data in presence of various applied magnetic fields. The spin switching transition (T_S) is observed upto H = 800 Oe magnetic field above room temperature. It is worth to mention here that in the presence of higher fields (H = 900 Oe and 1000 Oe) no switching transition is observed above room temperature and the magnetization data show a similar behaviour as field cooling (*FCC*) data as shown in figure 7.13(b).

To understand the origin of this switching behaviour, we measured the isothermal magnetization (*M-H*) along *c* - axis at various temperatures (T > 300 K) as shown in figure 7.14(b). Above Néel ordering (T_N), the *M-H* isotherms are linear as expected in the paramagnetic state. But below T_N, rectangular shaped hysteresis loops are observed. The width of the hysteresis increases with reducing the temperature down to 300 K as shown in figure 7.14(b). In figure 7.15(a), we have plotted the spin-switching temperature (T_S) for different magnetic field strengths. It is observed that with increasing the applied magnetic field strength, T_S decreases (for H = 100 Oe, T_S = 631 K and for H = 800 Oe, T_S = 385 K). From the *M-H* loop, the coercive field (H_C) is plotted as T vs H_C as shown in figure 7.15(b). The coercive field (H_C) increases with reducing the temperature from 630 K to 300 K. Interestingly, there exists a one-to-one correspondence between the manner in which T_S varies with H and H_c varies with T; this clearly suggests that the magnetization reversal is controlled by the coercive field.

Thus, at a given temperature T (< T_N), one should expect a coherent flipping of

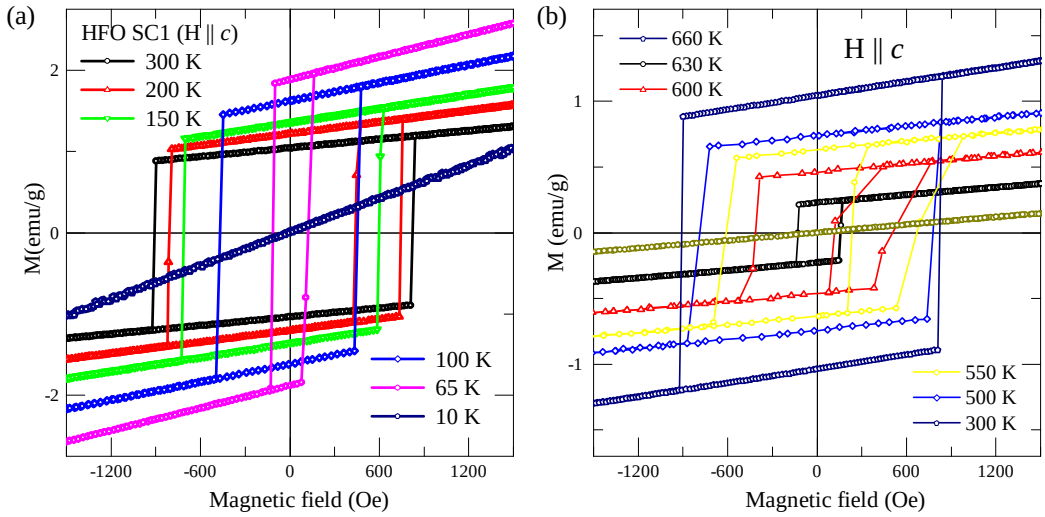

Figure 7.14: (a) *M-H* data for H || *c* show hysteresis above spin-reorientation (T_{SR}). (b)The isothermal magnetization (*M-H*) data below Néel temperature showed sharp rectangular hysteresis down to 300 K.

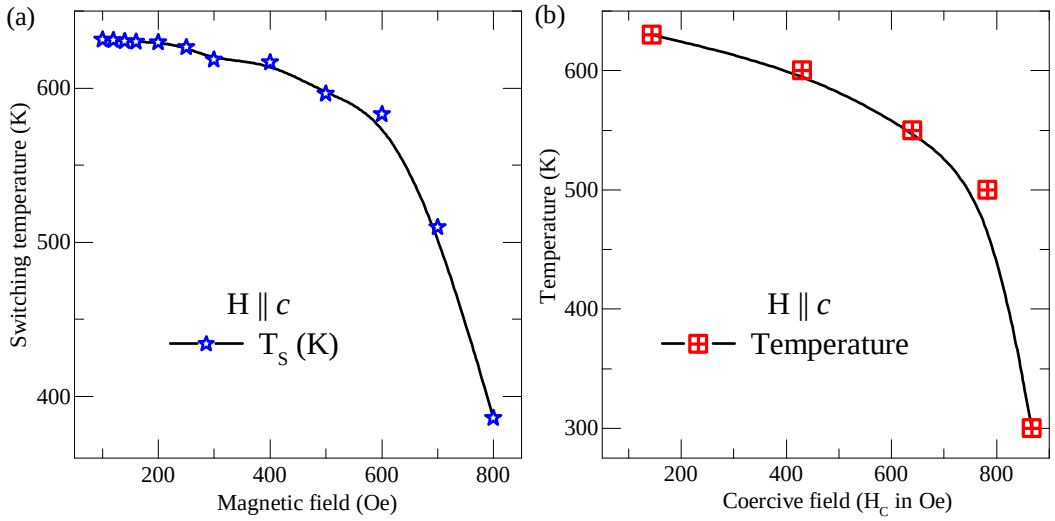

Figure 7.15: (a) Switching transition,T_S, reduces with increasing the field strength (b) Coercive field (H_C) is plotted as a function of temperature.

the Fe domains if the applied magnetic field is higher than the coercive field (H_C). In figure 7.16, we have shown the temperature dependent magnetization in the presence of a negative magnetic field (H = - 100 Oe). The data shows negative magnetization

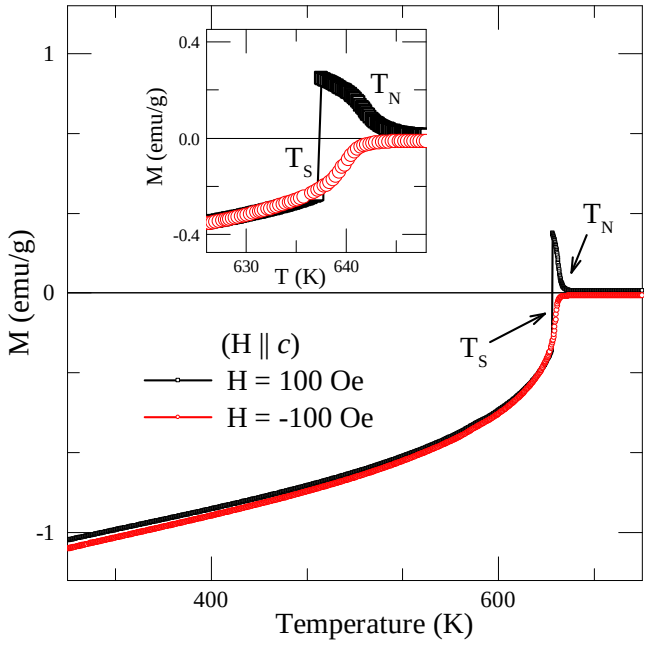

Figure 7.16: Effect of negative magnetic field (-100 Oe) on switching transition: inset shows no T_S is observed and the magnetization remains negative upto 750 K.

while warming the sample from 300 K to T_S, where it flips to positive value. This is due to fact that at room temperature the Fe spins were perhaps aligned in the opposite direction of the applied magnetic field when we loaded the crystal, thus showing negative magnetization. But in presence of negative magnetic field (-100 Oe), magnetization remains negative from T = 300 K to T > T_N as expected.

We also observed that for a fixed field direction, depending on the positive (+ *c*) or negative (- *c*) crystallographic orientation, the magnetization reverses, as shown in figure 7.17. The magnetization reversal shown by HFO could be used in potential application as it is observed above room temperature and can be switched both by magnetic field and temperature.

In figure 7.18, we have shown the temperature dependent magnetization in the temperature range from 2 - 750 K in presence of 100 Oe. Low temperature magnetic study

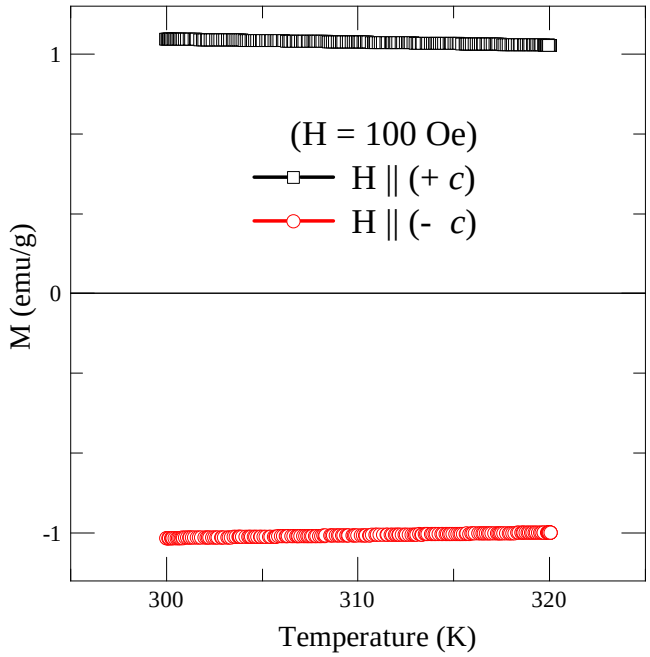

Figure 7.17: The magnetization data is carried out on a HFO crystal specimen along both the crystallographic (+ *c* and - *c*)- axis in presence of 100 Oe magnetic field. For a fixed magnetic field (magnitude and direction), depending on the crystallographic orientation (+ *c* or - *c*), magnetization (M_c) shows mirror image with respect to zero magnetization. This suggests that the Fe spins are robust in a particular direction below the coercive field.

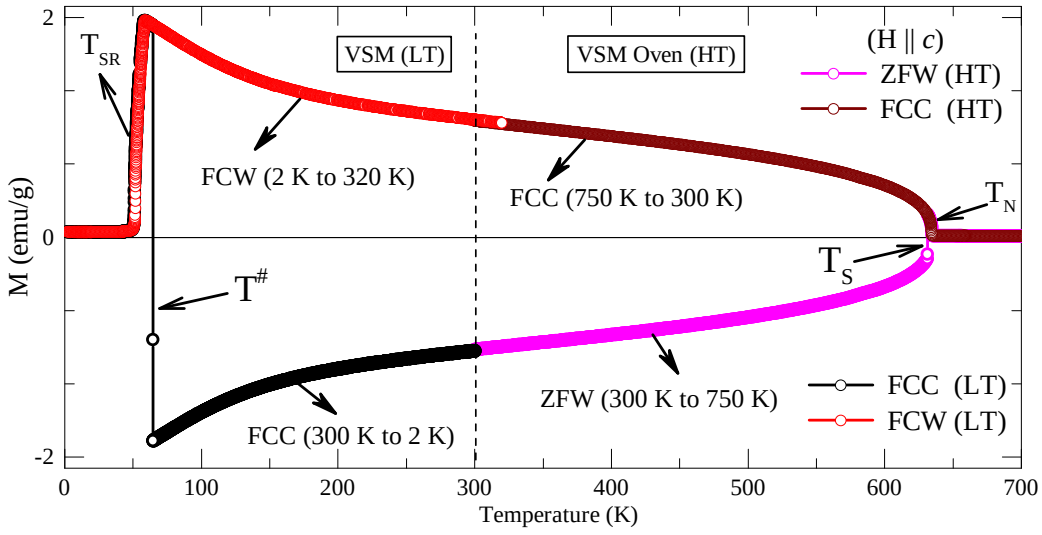

Figure 7.18: (a) Temperature dependent magnetic study (VSM + Oven) is shown in the temperature range (2 - 750 K). At 300 K, low and high temperature data show equal magnetization. Low temperature *ZFC* data revealed a new switching like transition around 65 K ($T^{\#}$) along with spin reorientation transition (T_{SR}).

were performed on the same crystal specimen and we observed the spin-reorientation temperature region from 50 K - 60 K (T_{SR}). We performed low temperature study on the similar measurement configuration including the direction of magnetic field and crystallographic *c* - axis as used for measuring high temperature magnetic study. Both the low and high temperature data are nicely matching at the room temperature (T = 300 K). While cooling down the system from 300 K to 2 K, *FCC* data is taken in presence of magnetic field of 100 Oe along the *c* - direction. Interestingly, the *FCC* data reveals a new transition (negative to positive magnetization) around 65 K ($T^{\#}$) while cooling down the system from 750 K in presence of 100 Oe of magnetic field. And below this temperature, the data shows spin-reorientation (T_{SR}) region as discussed previously. This observation suggests that the spin-reorientation region is unique, independent of crystallographic direction (+ *c* or - *c*) and temperature induced transition. The heating data (*FCW*) also follow the spin-reorientation region and at room temperature it overlaps the high temperature data as shown in figure 7.18(a). Above $T^{\#}$ = 65 K, *FCW* data is a mirror image of the *FCC* data.

To understand the behaviour of coercive field (H_C) and remnant magnetization (R_M) of $HoFeO_3$, we have calculated from the isothermal magnetization (*M-H*) data taken along the crystallographic c - axis of HFO crystal as shown in figure 7.14(a) (below 300 K) and in figure 7.14(b) (above 300 K). The *M-H* data show a rectangular shaped hysteresis loops above spin reorientation temperature (60 K) and a linear behaviour for $T < T_{SR}$ and $T > T_N$. The linearity in *M-H* is expected as the *WFM* moment rotates towards the crystallographic *a* - axis below T_{SR}. Since below T_{SR}, the Fe spins are aligned along the *a*-axis (Γ_2 phase), the magnetization increases once the sample is cooled below T_{SR}. The field dependent magnetization along the *c*-axis shows hysteresis but with coercivity decreasing upon cooling down the sample. In Table 7.2, we show the coercive field and remnant magnetization at various temperatures. As the coercive field decreases upon cooling the remnant magnetization increases, which conserves the hysteresis loss. The hysteresis along *c*-axis is consistent with the presence of the *WFM* moment along the *c* - axis. However, below T = 300 K, the coercive field decreases down to 65 K. This is the opposite of the behaviour observed above room-temperature. Thus, when plotted

over the whole temperature range, 'H_C versus T' plot exhibits a maximum near room temperature (T = 300 K), whereas remnant magnetization increases with lowering the temperature, as shown in figure 7.19. The values of coercive field (H_C) and remnant

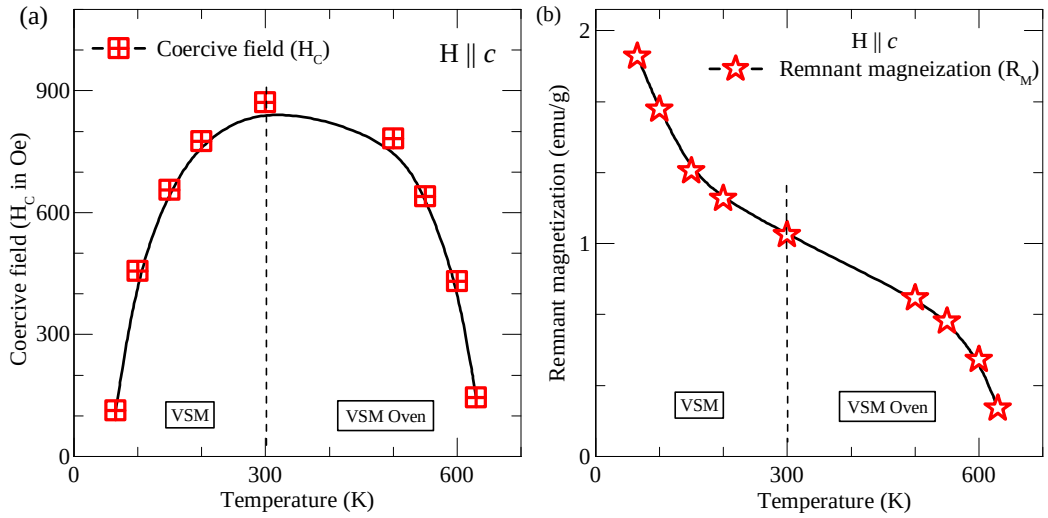

Figure 7.19: (a) The temperature dependent coercive field (H_C) and (b) remnant magnetization (R_M) calculated from the isothermal magnetization (*M-H*) along *c* - axis are shown.

magnetization (R_M) at various temperatures are given in Table 7.2. The unusual behaviour of temperature dependence coercive field is expected either in thin films [233] or in alloy [234]. A similar non-monotonic variation of H_C with temperature has been previously reported for thin-film samples of varying film thickness, and also for nanopowders of magnetic alloys with a large distribution of the particle size [233, 234]. However, in the bulk crystals a similar behavior has not been reported to the best of our knowledge. Since the $f - d$ exchange comes into play around the same temperature where H_C vs. T plot exhibits a maximum, one can tentatively attribute it to the interlattice interaction.

In case of HFO, below the Néel ordering temperature (T_N) as the *WFM* developed while cooling down the system, the increment of H_C is expected as the domain size increases in presence of magnetic field along the *WFM* direction (i.e. *c* - axis for Fe spins). However, the opposite behaviour of H_C below room temperature could be due to presence of single ion anisotropy of Ho spins. This behaviour suggests that although

the *WFM* is along the *c* - axis, this anisotropy becomes stronger while cooling down the system further and below T_{SR} ($T < 65K$) no hysteresis is observed along both *c* - and *a* - axis.

Table 7.2: Coercive field (H_C) and remnant magnetization (R_M) obtained from the *M-H* data shown in figure 7.14.

Temperature	Coercive field (H_C in Oe)	Remnant magnetization (R_M in emu/g)
T = 65 K	113	1.88
T = 100 K	457	1.63
T = 150 K	656	1.34
T = 200 K	776	1.21
T = 300 K	871	1.04
T = 500 K	783	0.75
T = 550 K	640	0.64
T = 600 K	431	0.46
T = 630 K	145	0.23

7.6 Summary

We have successfully grown $HoFeO_3$ (HFO) single crystals under two different growth atmospheres (air and argon). Both the crystals exhibit orthorhombic *Pbnm* space group independent of the growth atmosphere. The anisotropic magnetization of the grown crystals was probed over the temperature range extending from 2 K to 750 K. The data confirm the presence of spin-reorientation transition (T_{SR}) of the Fe^{3+} spins in the temperature range 50 K - 60 K. At low-temperatures (close to 4 K) Ho^{3+} antiferromagnetic ordering ($T_{Ho} \sim 4K$) was also confirmed. We performed highly sensitive torque magnetometry measurements. In addition to the spin-reorientation transition previously reported we found evidence for new weak transitions in agreement with the recent neutron data [121, 122].

High-temperature magnetic measurements were also carried out on the high-quality crystal specimen of $HoFeO_3$. The study revealed a sharp temperature induced spin-switching transitions above room temperature and which can be tuned by magnetic field. Isothermal magnetizations (*M-H*) show perfectly rectangular shaped loops below

the Néel ordering temperature (~ 643 K) with large coercive field of about 1 kOe at 300 K. The presence of tunable spin-switching transitions above room temperature makes $HoFeO_3$ a candidate for potential practical applications in spin switching devices.

Chapter 8

Summary and Outlook

The main focus of this thesis work had been to investigate two different classes of transition metal oxides (TMOs): a low-dimensional quantum magnet $Sr_{14}Cu_{24}O_{41}$ and a member of the perovskite orthoferrite family $HoFeO_3$. We investigated the effects of magnetic and non-magnetic impurities on the magnetic and vibronic ground state of $Sr_{14}Cu_{24}O_{41}$ and examined how small impurities at the Cu-site can alter these properties in unexpected ways. To understand the effect of dilutely doped impurities, it is essential to perform experiments on high-quality single crystalline materials, thus, a major part of this thesis work deals with the crystal growth and characterization.

Being incongruently melting, we used the travelling-solvent floating-zone (TSFZ) technique associated with a four mirror optical zone furnace to grow crystals of $Sr_{14}Cu_{24}O_{41}$ and its doped variants comprising Co, Zn, Ni and Al impurities. We found that 3 bar oxygen pressure is required to achieve a stable growth condition during the doping of Co, Ni, Zn and Al. The grown crystals were characterized by several complementary techniques including optical microscopy under polarized light, scanning electron microscopy, powder x-ray diffraction and Laue diffractions. We also report crystal growth of $HoFeO_3$ and investigated the magnetic phase transitions, and report the presence of sharp magnetization reversal transitions above room-temperature.

A detailed analysis of χ(T) and M(H) of the pristine $Sr_{14}Cu_{24}O_{41}$ crystal confirmed the occurrence of long-distance dimerization (*LDD*) at low temperature (T < 2 K), and the nucleation of Zhang-Rice dimers (*ZRD*s) near 100 K.

The non-magnetic Zn impurity (S = 0) is found to dope at the site of an interdimer

ZR singlet without affecting the *ZR* dimers for dilute concentration of 0.25 %. However, at a higher concentration (1% Zn), we inferred breaking of *ZR* dimers. We also investigated the effect of magnetic impurity (Ni) on the two types of dimers (*LDD* and *ZRD*). We observed that for lower doping concentration (0.25 % Ni), while the *ZRD*s are unaffected, the *LDD*s are severed significantly. However, for higher doping concentration (1 % of Ni), both the dimers are severed significantly. The case of trivalent Al^{3+} impurity turned out to be different from the divalent impurities Zn and Ni. We found that unlike Zn or Ni, the solid-solubility of Al in the crystal is very limited. The crystal with 1 % nominal Al concentration is found to contain about 0.25 % of Al. However, what makes it different from the divalent Zn and Ni impurities is that Al prefers to dope the ladders than the chains.

We investigated the effect of Co impurity up to 10 % of Co doping. The bulk behavior in the presence of Co is found to be highly anisotropic even for the lowest Co doping in stark contrast with a nearly isotropic behavior of the undoped $Sr_{14}Cu_{24}O_{41}$. We also suggest that upon increasing the Co concentration beyond to ~ 3 %, the population of Co in the chain sublattice reaches a saturation level. The effect of Co impurity in the high temperature *ZR* dimer is also investigated and found that the dimerization gap associated with the *ZRD*s showed an anisotropic suppression. Which means that with Co impurity, the suppression rate of intra-dimer interaction in the *ac* - plane is much higher than along the *b* - axis. In short, unlike Zn, Ni and Al impurities the effect of Co impurity turned out to be most unusual displaying a strongly anisotropic response. Further experimental studies are required to understand how the single-ion anisotropy of Co affects the bulk behaviour even for a very dilute doping.

We show that the low temperature specific heat of $Sr_{14}Cu_{24}O_{41}$ is enriched with a rather large excess contribution of non-magnetic origin. We investigated the presence of a gap which was previously manifested as 'new' normal mode in the phononic dispersion due to the sliding motion between the incommensurate chain (CuO_2) and ladder (Cu_2O_3) sublattices. We used the specific heat probe to show the presence of rather large 'excess' specific heat, which deviates from the simple Debye (T^3) law due to the presence of a hump around T = 10 K due to the sliding mode. We also investigated the

effect of impurities on this gapped sliding mode and found it to be highly sensitive to annealing or impurities in the sample. We performed terahertz time-domain spectroscopy (THz-TDS) on these crystals to substantiate that the excess specific heat indeed arises due to sliding mode.

We investigated the magnetic phase transitions, spin-reorientation and magnetization reversal in orthoferrite $HoFeO_3$ by performing magnetization, specific heat and highly sensitive torque magentometry measurements. Being congruently melting the crystals of $HoFeO_3$ readily grown using the floating-zone method. We performed magnetic measurements on oriented crystals to confirm the presence of various magnetic phase transitions including the Néel ordering temperature (T_N), spin-reorientation transition (T_{SR}), and Ho moments ordering (T_{Ho}). We also performed highly sensitive torque magnetometry measurements and in addition to the T_{SR} (from 50 - 60 K), we found evidence of weak transitions in agreement with recently reported neutron data [121].

We also performed high-temperature magnetic measurements above 300 K and found sharp temperature induced magnetization reversal transition, which was not previously reported. We further investigated on this new finding and showed that T_S can easily be tuned by changing the magnetic field strength. We argue that the presence of sharp switching in magnetic hysteresis above room temperature causes the magnetization reversal in the temperature dependent measurements. We believe that the presence of tunable magnetization reversal transition above room temperature in $HoFeO_3$ makes it as a useful candidate for potential practical applications in spin switching devices.

In future, to understand the effect of Co impurity in $Sr_{14}Cu_{24}O_{41}$ in further details advanced experimental techniques such as INS (inelastic neutron scattering) or NMR (nuclear magnetic resonance) will be useful. The low temperature specific heat (below 2 K) on the various doped (Zn, Al and Co at the Cu site) $Sr_{14}Cu_{24}O_{41}$ crystals under different magnetic fields will be useful in order to understand the effect of impunity on the long distance dimers (*LDD*s). Moreover, the low temperature (below 2 K) dc magnetic susceptibility measurements would also provide a direct experimental probe to understand the effect of these impurities on the *LDD*s. Since Ca - doping at Sr site

in $Sr_{14}Cu_{24}O_{41}$ is known to transfer holes from chains to ladders, in future, it will be interesting to perform a systematic THz and specific heat study on variously Ca-doped $Sr_{14}Cu_{24}O_{41}$ samples. It would be also interesting to study the specific heat and THz-TDS in order to understand how a Co impurity affects the low energy sliding mode.

In $HoFeO_3$, THz-TDS spectroscopy around the new transitions reported here (180 K, 35 K and 20 K) will be useful to carry out in future to understand their origins. The effect of impurity in $HoFeO_3$ has not been studied in this thesis. It will be interesting to study the effect of impurities at both Ho and/or Fe site so that the temperature and field range over which the magnetization reversal transition has been observed can be extended further.

Bibliography

[1] E. Dagotto and Y. Tokura, MRS Bulletin **33**, 1037 –1045 (2008).

[2] Y. Tokura, Physics Today **56**, 50 (2003).

[3] M. Imada et al., Rev. Mod. Phys. **70**, 1039–1263 (1998).

[4] J. Ngai et al., Annual Review of Materials Research **44**, 1–17 (2014).

[5] H. Alloul et al., Rev. Mod. Phys. **81**, 45–108 (2009).

[6] K. Karmakar et al., Cryst. Growth Des. **14**, 1184 (2014).

[7] K. Karmakar et al., Crystal Growth & Design **15**, 4843–4853 (2015).

[8] K. Karmakar et al., Phys. Rev. B **95**, 235154 (2017).

[9] K. Karmakar et al., Phys. Rev. Lett. **118**, 107201 (2017).

[10] M. Azuma et al., Physical Review B **55**, R8658–R8661 (1997).

[11] M. Azuma et al., Phys. Rev. Lett. **73**, 3463–3466 (1994).

[12] S. Cao et al., Scientific Reports **4**, 5960 (2014).

[13] S. J. Yuan et al., Phys. Rev. B **87**, 184405 (2013).

[14] P. Mandal et al., Phys. Rev. Lett. **107**, 137202 (2011).

[15] J. A. de Jong et al., Phys. Rev. B **84**, 104421 (2011).

[16] Y. Tokunaga et al., Phys. Rev. Lett. **101**, 097205 (2008).

[17] A. V. Kimel et al., Nature **429**, 850–853 (2004).

[18] N. D. Mermin and H. Wagner, Phys. Rev. Lett. **17**, 1133–1136 (1966).

[19] L. Onsager, Phys. Rev. **65**, 117–149 (1944).

[20] L. de Jongh ed., *Magnetic Properties of Layered Transition Metal Compounds* (Kluwer Academic Publishers, Dordrecht, 1990).

[21] J. M. Kosterlitz and D. J. Thouless, Journal of Physics C: Solid State Physics **6**, 1181 (1973).

[22] B. Lake et al., Phys. Rev. B **71**, 134412 (2005).

[23] H. Yoshizawa and K. Hirakawa, Journal of the Physical Society of Japan **46**, 448–454 (1979).

[24] J. des Cloizeaux and J. J. Pearson, Phys. Rev. **128**, 2131 (1962).

[25] S. Blundell, *Magnetism in Condensed Matter*, Oxford Master Series in Condensed Matter Physics 4 (OUP Oxford, 2001).

[26] F. D. M. Haldane, Physical Review B **25**, 4925–4928 (1982).

[27] F. D. M. Haldane, Physical Review Letters **50**, 1153–1156 (1983).

[28] I Affleck, Journal of Physics: Condensed Matter **1**, 3047 (1989).

[29] R. M. Morra et al., Phys. Rev. B **38**, 543–555 (1988).

[30] J. P. Renard et al., EPL (Europhysics Letters) **3**, 945 (1987).

[31] Z. Tun et al., Phys. Rev. B **42**, 4677–4681 (1990).

[32] J. Darriet and L. Regnault, Solid State Communications **86**, 409 –412 (1993).

[33] M. Hase et al., Phys. Rev. Lett. **70**, 3651–3654 (1993).

[34] J. W. Bray et al., Phys. Rev. B **20**, 2067–2072 (1979).

[35] R. Swietlik, Solid State Communications **45**, 27 –29 (1983).

[36] S. Deonarine and S. J. Joshua, physica status solidi (a) **20**, 595–600.

[37] P. Ganguly and C. Rao, Journal of Solid State Chemistry **53**, 193 –216 (1984).

[38] S. ichi Uchida et al., Japanese Journal of Applied Physics **26**, L445 (1987).

[39] E. Dagotto, Reports on Progress in Physics **62**, 1525 (1999).

[40] S. J. Blundell, Contemporary Physics **40**, 175 (1999).

[41] N. Motoyama et al., Phys. Rev. Lett. **76**, 3212 (1996).

[42] H. Rosner et al., Physical Review B **56**, 23 (1997).

[43] G. Simutis et al., Phys. Rev. Lett. **111**, 067204 (2013).

[44] K. Karmakar et al., Phys. Rev. B **95**, 235154 (2017).

[45] M. Hase et al., Phys. Rev. Lett. **71**, 4059–4062 (1993).

[46] S. B. Oseroff et al., Phys. Rev. Lett. **74**, 1450–1453 (1995).

[47] N. Fujiwara et al., Phys. Rev. Lett. **80**, 604–607 (1998).

[48] S. Ohsugi et al., Phys. Rev. B **60**, 4181–4190 (1999).

[49] E. McCarron III et al., Materials Research Bulletin **23**, 1355 –1365 (1988).

[50] M. Matsuda and K. Katsumata, Phys. Rev. B **53**, 12201–12205 (1996).

[51] P. Abbamonte et al., Nature **431**, 1078–1081 (2004).

[52] G. Blumberg et al., Physica C: Superconductivity **388 - 389**, 227 –228 (2003).

[53] M. Uehara et al., Physica C: Superconductivity **255**, 193 –203 (1995).

[54] M. Uehara et al., Journal of the Physical Society of Japan **65**, 2764–2767 (1996).

[55] K. Naruse et al., Solid State Communications **154**, 60 –63 (2013).

[56] C. Hess et al., Phys. Rev. B **73**, 104407 (2006).

[57] S. Sahling et al., Nature Physics **11**, 255–260 (2015).

[58] J. Etrillard et al., Physica C: Superconductivity **403**, 290 –296 (2004).

[59] Z. Hiroi et al., Phys. Rev. B **54**, 15849–15855 (1996).

[60] T. Ohta et al., Journal of the Physical Society of Japan **66**, 3107–3114 (1997).

[61] A. F. Jensen et al., Acta Crystallographica Section B **53**, 113–124 (1997).

[62] K. Ukei et al., Acta Crystallographica Section B **50**, 42–45 (1994).

[63] Y. Gotoh et al., Phys. Rev. B **68**, 224108 (2003).

[64] G. Deng et al., Phys. Rev. B **84**, 144111 (2011).

[65] T. VuletiÄĞ et al., Physics Reports **428**, 169 –258 (2006).

[66] M. Kato et al., Physica C: Superconductivity **258**, 284 –292 (1996).

[67] S. A. Carter et al., Phys. Rev. Lett. **77**, 1378–1381 (1996).

[68] M. Isobe and E. Takayama-Muromachi, Journal of the Physical Society of Japan **67**, 3119–3124 (1998).

[69] Y. Mizuno et al., Phys. Rev. B **58**, R14713–R14716 (1998).

[70] N. Nücker et al., Phys. Rev. B **62**, 14384–14392 (2000).

[71] R. S. Eccleston et al., Phys. Rev. Lett. **81**, 1702–1705 (1998).

[72] S. Katano et al., Phys. Rev. Lett. **82**, 636–639 (1999).

[73] M. Matsuda et al., Phys. Rev. B **59**, 1060–1067 (1999).

[74] T. Osafune et al., Phys. Rev. Lett. **78**, 1980–1983 (1997).

[75] Ruzicka, B. et al., Eur. Phys. J. B **6**, 301–305 (1998).

[76] M. Braden et al., Phys. Rev. B **69**, 214426 (2004).

[77] D. E. Cox et al., Phys. Rev. B **57**, 10750–10754 (1998).

[78] K. Kumagai et al., Physica C: Superconductivity **282 - 287, Part 3**, 1343 –1344 (1997).

[79] F. C. Zhang and T. M. Rice, Physical Review B **37**, 3759–3761 (1988).

[80] M. Matsuda et al., Physica B: Condensed Matter **246 - 247**, 516 –519 (1998).

[81] L. P. Regnault et al., Phys. Rev. B **59**, 1055–1059 (1999).

[82] R. Klingeler et al., Phys. Rev. B **73**, 014426 (2006).

[83] R. Bag et al., Journal of Crystal Growth **458**, 16 –26 (2017).

[84] S. Tsuji et al., Journal of the Physical Society of Japan **65**, 3474–3477 (1996).

[85] and, Proceedings of the Royal Society of London A: Mathematical, Physical and Engineering Sciences **214**, 451–465 (1952).

[86] T. Vuletic, Phys. Rev. Lett. **90**, 257002 (2003).

[87] A. Rusydi et al., Phys. Rev. B **75**, 104510 (2007).

[88] A. Rusydi et al., Phys. Rev. Lett. **97**, 016403 (2006).

[89] A. Rusydi et al., Phys. Rev. Lett. **105**, 026402 (2010).

[90] R. Fukaya et al., Journal of the Physical Society of Japan **82**, 083707 (2013).

[91] T. Vuletic, Phys. Rev. B **71**, 012508 (2005).

[92] Z. Hiroi, Journal of Solid State Chemistry **123**, 223 –235 (1996).

[93] E. Dagotto et al., Phys. Rev. B **45**, 5744–5747 (1992).

[94] E. Dagotto and T. M. Rice, Science **271**, 618–623 (1996).

[95] C. Hess et al., Physical Review B **64**, 184305 (2001).

[96] N. Ashcroft and N. Mermin, *Solid State Physics* (Harcourt Brace College Publishers, 1976).

[97] M. Matsuda et al., Phys. Rev. B **54**, R15626–R15628 (1996).

[98] M. Matsuda et al., Phys. Rev. B **57**, 11467–11471 (1998).

[99] J. Wang et al., Journal of Physics: Condensed Matter **21**, 075601 (2009).

[100] C. Lin et al., Phys. Rev. B **64**, 104517 (2001).

[101] Y. Lin et al., Physica B: Condensed Matter **400**, 93 –98 (2007).

[102] J.-H. Lee et al., Phys. Rev. Lett. **107**, 117201 (2011).

[103] M. Shao et al., Solid State Communications **152**, 947 –950 (2012).

[104] S. E. Nikitin et al., Phys. Rev. B **98**, 064424 (2018).

[105] P. Suresh et al., Phys. Rev. B **97**, 184419 (2018).

[106] K. Grishunin et al., ACS Photonics **5**, 1375–1380 (2018).

[107] I. Fita et al., Phys. Rev. B **93**, 184432 (2016).

[108] X.-x. Wang et al., Phys. Chem. Chem. Phys. **20**, 3687–3693 (2018).

[109] C. De et al., Applied Physics Letters **111**, 182403 (2017).

[110] M. Das et al., Phys. Rev. B **96**, 174405 (2017).

[111] U. Staub et al., Phys. Rev. B **96**, 174408 (2017).

[112] L. M. W. Daniels, "Structures and Properties of Perovskites and Pyrochlores from Hydrothermal Synthesis", PhD thesis (University of Warwick, 2015).

[113] X. Liu et al., Journal of Materials Science: Materials in Electronics **20**, 323 (2008).

[114] I. Dzyaloshinsky, Journal of Physics and Chemistry of Solids **4**, 241 –255 (1958).

[115] T. Moriya, Phys. Rev. **120**, 91–98 (1960).

[116] T. Yamaguchi, Journal of Physics and Chemistry of Solids **35**, 479 –500 (1974).

[117] S Bujko et al., Journal of Physics: Condensed Matter **7**, 8099 (1995).

[118] L. T. Tsymbal et al., Phys. Rev. B **72**, 052413 (2005).

[119] L. T. Tsymbal et al., Low Temperature Physics **32**, 779–782 (2006).

[120] X. Zeng et al., Opt. Express **23**, 31956–31963 (2015).

[121] T Chatterji et al., AIP Advances **7**, 045106 (2017).

[122] T Chatterji et al., Journal of Physics: Condensed Matter **29** (2017).

[123] B. D. Cullity, *"Elements of X-ray diffraction"*, Addison-Wesley metallurgy series (Addison-Wesley Pub. Co., 1956).

[124] T. J. B. Holland and S. A. T. Redfern, Mineralogical Magazine **61**, 65 –77 (1997).

[125] J. R. Carvajal, Abstracts of the Satellite Meeting on Powder Diffraction of the XV Congress of the IUCr (1990).

[126] K. Momma and F. Izumi, Journal of Applied Crystallography **41**, 653–658 (2008).

[127] B. Hafner, *Scanning Electron Microscopy Primer*, tech. rep. (Characterization Facility, University of Minnesota, Twin Cities, 2007), pp. 1–29.

[128] ICP-AES, Sophisticated Analytical Instrument Facility, IIT Bombay, India.

[129] *Vibrating Sample Magnetometer (VSM) Option User's Manual*, Physical Properties Measurement System, Quantum Design, USA ().

[130] *VSM Oven Option User's Manual*, Physical Properties Measurement System, Quantum Design, USA ().

[131] *Heat Capacity Option User's Manual*, Physical Properties Measurement System,Quantum Design ().

[132] *Torque Magnetometer Option User's Manual*, Physical Properties Measurement System, Quantum Design, USA ().

[133] L. D. J. F. M. G. E. M. C. D. Wagner, W. M. Riggs, *Handbook of X-ray Photoelecton Spectroscopy* (Perkin Elmer corporation, 1979).

[134] E. Kaldis, *Crystal growth of electronic materials* (North-Holland, 1985).

[135] D. T. J. Hurle, *Handbook of Crystal Growth*, v. 3, pt. 2 (North-Holland, 1994, 1994).

[136] W. D. Lawson and S Nielsen, *Preparation of single crystals*, English (Butterworths Scientific Publications, London, 1958).

[137] W. Pfann, Journal of Metals **4**, 747 (1952).

[138] H. Theuerer, US Patent 3,060,123 (1962).

[139] J. Liang et al., Solid State Communications **75**, 247 –252 (1990).

[140] W. Wong-Ng et al., Physica C: Superconductivity **299**, 9 –14 (1998).

[141] R. S. Roth et al., Journal of the American Ceramic Society **72**, 1545–1549 (1989).

[142] B. V. Slobodin et al., Sverkhprovodimost: Fiz. Khim. Tekh **3**, 523–526 (1990).

[143] N. M. Hwang et al., Journal of the American Ceramic Society **73**, 2531 (1990).

[144] U. Ammerahl and A. Revcolevschi, Journal of Crystal Growth **197**, 825 –832 (1999).

[145] U. Ammerahl et al., Journal of Crystal Growth **193**, 55 –60 (1998).

[146] K. Karmakar et al., Crystal Growth & Design **14**, 1184–1192 (2014).

[147] K. Karmakar et al., Crystal Growth & Design **15**, 4843–4853 (2015).

[148] N. M. Hwang et al., Journal of the American Ceramic Society **73**, 2531–2533 (1990).

[149] N. Wizent et al., Journal of Crystal Growth **401**, 596 –600 (2014).

[150] S. Vanishri et al., Journal of Crystal Growth **311**, 3830 –3834 (2009).

[151] S Watauchi et al., Journal of Crystal Growth **229**, 423 –427 (2001).

[152] M. Azuma et al., Phys. Rev. Lett. **73**, 3463–3466 (1994).

[153] J. M. Tarascon et al., Phys. Rev. B **37**, 7458–7469 (1988).

[154] J. Wang et al., Journal of Physics: Condensed Matter **21**, 075601 (2009).

[155] R. Bag, Unpublished.

[156] Z. Hiroi et al., Phys. Rev. B **54**, 15849–15855 (1996).

[157] K. Karmakar, "Disorder in the Quantum Spin-Chains Sr2CuO3 and SrCuO2", PhD thesis (IISER Pune, India, 2016).

[158] P. M. R. Ribeiro, "Einkristallherstellung und magnetischer Wärmetransport von niedrigdimensionalen Kupraten", MA thesis (Diploma Thesis, RWTH-Aachen, 2003).

[159] A. Zheludev and T. Roscilde, Comptes Rendus Physique **14**, 740 –756 (2013).

[160] D. Bounoua et al., Phys. Rev. B **95**, 224429 (2017).

[161] M. Azuma et al., Physical Review B **55**, R8658–R8661 (1997).

[162] M. Hase et al., Phys. Rev. Lett. **70**, 3651–3654 (1993).

[163] B. Grenier et al., Phys. Rev. B **58**, 8202–8205 (1998).

[164] K Uchinokura, Journal of Physics: Condensed Matter **14**, R195 (2002).

[165] R. Klingeler et al., Phys. Rev. B **73**, 014426 (2006).

[166] K. Magishi et al., Phys. Rev. B **57**, 11533–11544 (1998).

[167] R. S. Eccleston et al., Phys. Rev. Lett. **81**, 1702–1705 (1998).

[168] E. Dagotto, Rep. Prog. Phys. **62**, 1525–1571 (1999).

[169] F. C. Zhang and T. M. Rice, Physical Review B **37**, 3759–3761 (1988).

[170] M. Takigawa et al., Phys. Rev. B **57**, 1124–1140 (1998).

[171] V. Kataev et al., Phys. Rev. B **64**, 104422 (2001).

[172] M. Sigrist et al., Phys. Rev. B **49**, 12058–12061 (1994).

[173] J. Wang et al., Physica B: Condensed Matter **441**, 6 –11 (2014).

[174] E. S. R. Gopal, in *Specific heats at low temperatures* (Plenum Press, New York, 1966).

[175] T. R. Kirkpatrick and D. Belitz, Phys. Rev. Lett. **76**, 2571–2574 (1996).

[176] C. Dasgupta and S.-k. Ma, Phys. Rev. B **22**, 1305–1319 (1980).

[177] C. Lin et al., Phys. Rev. B **64**, 104517 (2001).

[178] Y. Lin et al., Physica B: Condensed Matter **400**, 93 –98 (2007).

[179] H. Xie et al., Physica B: Condensed Matter **381**, 168 –173 (2006).

[180] J. C. Slonczewski, Journal of Applied Physics **32**, S253 (1961).

[181] A. Abragam and M. H. L. Pryce, Proceedings of the Royal Society of London A: Mathematical, Physical and Engineering Sciences **206**, 173–191 (1951).

[182] C. CalderÃşn et al., Microelectronics Journal **39**, 1324 –1326 (2008).

[183] B. J. Tan et al., Journal of the American Chemical Society **113**, 855–861 (1991).

[184] J Haber and L Ungier, Journal of Electron Spectroscopy and Related Phenomena **12**, 305–312 (1977).

[185] T. J. Chuang et al., Surface Science **59**, 413–429 (1976).

[186] N. Motoyama et al., Phys. Rev. B **55**, R3386–R3389 (1997).

[187] M. Kato et al., Physica C: Superconductivity **258**, 284 –292 (1996).

[188] S. A. Carter et al., Phys. Rev. Lett. **77**, 1378–1381 (1996).

[189] J. Wang et al., Journal of Physics: Condensed Matter **21**, 075601 (2009).

[190] T. Adachi et al., Solid State Communications **105**, 639 –642 (1998).

[191] N. Ashcroft and N. Mermin, *Solid state physics*, HRW international editions (Holt, Rinehart and Winston, 1976).

[192] J. D. Axe and P. Bak, Phys. Rev. B **26**, 4963–4973 (1982).

[193] R. Zeyher and W. Finger, Phys. Rev. Lett. **49**, 1833–1837 (1982).

[194] W. Finger and T. M. Rice, Phys. Rev. B **28**, 340–358 (1983).

[195] M. B. Walker and R. J. Gooding, Phys. Rev. B **32**, 7412–7416 (1985).

[196] I. U. Heilmann et al., Phys. Rev. B **20**, 751–762 (1979).

[197] J. M. Hastings et al., Phys. Rev. Lett. **39**, 1484–1487 (1977).

[198] X. Chen et al., Nature comm. **6**, 6723 (2015).

[199] I. Loa et al., Phys. Rev. Lett. **99**, 035501 (2007).

[200] B. Toudic et al., Phys. Rev. Lett. **107**, 205502 (2011).

[201] J. Etrillard et al., EPL (Europhysics Letters) **55**, 201 (2001).

[202] J. Etrillard et al., EPL (Europhysics Letters) **66**, 246 (2004).

[203] G. Theodorou and T. M. Rice, Phys. Rev. B **18**, 2840–2856 (1978).

[204] J. Etrillard et al., Phys. Rev. Lett. **76**, 2334–2337 (1996).

[205] A. Cano and A. P. Levanyuk, Phys. Rev. Lett. **93**, 245902 (2004).

[206] G. Reményi et al., Phys. Rev. Lett. **114**, 195502 (2015).

[207] C. H. Lee et al., Journal of the Physical Society of Japan **75**, 123602 (2006).

[208] P. Brown et al., Science Advances **4** (2018) 10.1126/sciadv.aao4793.

[209] M. v. Zimmermann et al., Phys. Rev. B **73**, 115121 (2006).

[210] V. K. Thorsmølle et al., Phys. Rev. Lett. **108**, 217401 (2012).

[211] X. Chen et al., Phys. Rev. B **94**, 134309 (2016).

[212] M. Takigawa et al., Phys. Rev. B **57**, 1124–1140 (1998).

[213] F. C. Zhang and T. M. Rice, Physical Review B **37**, 3759–3761 (1988).

[214] S. Sahling et al., Nature Physics **11**, 255–260 (2015).

[215] R. Klingeler et al., Phys. Rev. B **73**, 014426 (2006).

[216] R. Bag et al., Journal of Physics: Condensed Matter **31**, 035801 (2018).

[217] M. W. McElfresh et al., Phys. Rev. B **40**, 825–828 (1989).

[218] B. C. Melot et al., Phys. Rev. B **79**, 224111 (2009).

[219] S. V. Smaalen, Crystallography Reviews **4**, 79–202 (1995).

[220] G. Theodorou, Solid State Communications **33**, 561 –563 (1980).

[221] G. Grüner, *Density waves in solids*, Advanced book program: Addison-Wesley (Perseuss Group, 2000).

[222] J. Odin et al., The European Physical Journal B - Condensed Matter and Complex Systems **24**, 315–322 (2001).

[223] K. Biljakovic et al., Phys. Rev. Lett. **57**, 1907–1910 (1986).

[224] P. Abbamonte et al., Nature **431**, 1078–1081 (2004).

[225] V. K. Thorsmølle et al., Phys. Rev. Lett. **108**, 217401 (2012).

[226] W. Phillips, *Amorphous solids low-temperature properties* (Springer, New York, 1981).

[227] R. L. White, Journal of Applied Physics **40**, 1061–1069 (1969).

[228] O. Nikolov et al., Hyperfine Interact **54**, 623 (1990).

[229] D. H. Ryan et al., IEEE Transactions on Magnetics **53**, 1–5 (2017).

[230] A. Bhattacharjee et al., Journal of Physics and Chemistry of Solids **63**, 569 – 574 (2002).

[231] M. Shao et al., Journal of Crystal Growth **318**, The 16th International Conference on Crystal Growth (ICCG16)/The 14th International Conference on Vapor Growth and Epitaxy (ICVGE14), 947 –950 (2011).

[232] R. C. Sherwood et al., Journal of Applied Physics **30**, 217–225 (1959).

[233] Q.-L. Ye et al., Journal of Applied Physics **98**, 013906 (2005).

[234] W. C. Nunes et al., Phys. Rev. B **70**, 014419 (2004).